SUBMONOLAYER GROWTH OF COBALT ON METALLIC AND INSULATING SURFACES STUDIED BY SCANNING TUNNELING MICROSCOPY AND KINETIC MONTE-CARLO SIMULATIONS

THÈSE N^{O} 3944 (2007)

PRÉSENTÉE LE 16 NOVEMBRE 2007

À LA FACULTÉ DES SCIENCES DE BASE

Laboratoire de nanostructures superficielles

SECTION DE PHYSIQUE

ÉCOLE POLYTECHNIQUE FÉDÉRALE DE LAUSANNE

POUR L'OBTENTION DU GRADE DE DOCTEUR ÈS SCIENCES

PAR

Philipp BULUSCHEK

ingénieur physicien diplômé EPF
et de nationalité allemande

acceptée sur proposition du jury:

Prof. G. Meylan, président du jury
Prof. H. Brune, directeur de thèse
Prof. T. Michely, rapporteur
Prof. J. Osterwalder, rapporteur
Prof. A. Pasquarello, rapporteur

ÉCOLE POLYTECHNIQUE
FÉDÉRALE DE LAUSANNE

Lausanne, EPFL
2008

Abstract

Submonolayer epitaxial growth is obtained by the deposition of less than a complete layer of atoms on a single crystal surface. It is of fundamental interest for industrial applications (e.g. in the semiconductor industry) as well as from the point of view of basic research. For example, it is known that nanometer-sized atomic structures (nanostructures) exhibit remarkable physical and chemical properties which can differ greatly from those of bulk matter. In order to investigate these properties, it is often necessary to create large quantities of well defined and possibly spatially ordered nanostructures. One way to achieve this result is self-organized growth where one deposits atoms on a clean crystalline surface and lets the growth process evolve freely. Here, nanostructures result from the atomic diffusion and aggregation processes taking place at the surface. Understanding the exact nature of these processes is of ongoing interest in the field of nanostructure growth.

In this thesis we report about submonolayer growth experiments of the ferromagnetic transition metal *cobalt*. Cobalt was chosen because it exhibits remarkable magnetic properties. These experiments were performed in an ultra-high vacuum chamber and molecular beam epitaxy was used to grow the nanostructures. Observations of the surface were made using a variable-temperature scanning tunneling microscope (STM). In order to get a better understanding of the atomic processes happening at the surface, we developed two adapted computational simulation methods. Kinetic Monte-Carlo (KMC) simulations were used to get an atomistic picture of the surface while mean field rate equations were integrated numerically to yield cluster densities.

We study the growth of cobalt on three different surfaces. By depositing Co on a clean Pt(111) crystal surface, we observe that the platinum surface reconstructs by forming star-shaped partial dislocations for sample temperatures above 180 K (-93°C). We also observe that island densities deviate from predictions of all known models towards higher values for these same temperatures. By simulation we are able to show that insertion of Co into the topmost platinum layer creates a repulsive network of dislocations. We show that these dislocations act as diffusion inhibiting barriers and thus influence the island density by constraining the free movement of atoms at the surface. We also show that the Co dimer and trimer diffuse on Pt(111) before dissociating and are able to extract corresponding activation barriers.

We also study the deposition of Co on a Ru(0001) surface which shows a more conventional temperature dependence. By comparing simulation and experiment we extract all relevant diffusion activation barriers and show that at high temperatures the Co dimer and trimer dissociate.

Finally, we investigate the growth of Co on the hexagonal boron nitride superlattice which forms on a Rh(111) surface. On this surface Co clusters form three-dimensional hemispherical dots. We show how the substrate corrugation influences diffusion of Co atoms and that clusters up to the size of the pentamer can diffuse. By simulation, we also extract the relevant migrations and desorption barriers.

Keywords: Scanning tunneling microscopy (STM), kinetic Monte-Carlo (KMC), rate equations, self-assembly, nucleation, growth, cobalt, Pt(111), Ru(0001), *h*-BN/Rh(111) nanomesh

Version abrégée

La croissance épitaxiale sous-monocouche est obtenue par le dépôt de moins d'une couche d'atomes sur une surface d'un monocristal. Ce procédé est d'intérêt dans les applications industrielles (p.ex. dans l'industrie des semi-conducteurs) ainsi que dans la recherche fondamentale. Par exemple, il est bien connu que des structures à l'échelle du nanomètre (nanostructures) présentent des propriétés physiques et chimiques remarquables qui peuvent être très différentes de celles de la matière volumique. Afin d'étudier ces propriétés, il est souvent nécessaire de produire de grandes quantités de nanostructures bien définies et si possible présentant un alignement spatial. Une méthode pour atteindre ce résultat est la croissance auto-organisée qui consiste à déposer des atomes sur une surface cristalline propre et de laisser le processus de croissance évoluer librement. Dans ce cas, les nanostructures sont le résultat de processus de diffusion et d'agrégation qui ont lieu à la surface. Dans l'étude de la croissance de nanostructures, la compréhension de la nature exacte de ces processus est fondamentale.

Dans ce travail de thèse nous présentons des résultats de croissance sous-monocouche de *cobalt* qui est un métal de transition ferromagnétique. Le cobalt a été choisi pour ses propriétés magnétiques remarquables. Les expériences ont été effectuées dans une chambre à ultra-haut vide et on utilise l'épitaxie par jet moléculaire (MBE) (angl."molecular beam epitaxy") pour le dépôt de cobalt. La surface a ensuite été étudiée en utilisant un microscope à effet tunnel à température d'échantillon variable. Afin de mieux comprendre les processus atomiques qui ont lieu à la surface, nous avons développé deux méthodes calculatoires de simulation. La simulation Monte-Carlo cinétique nous a permis d'obtenir une vision de la surface à l'échelle atomique alors que l'intégration numérique d'équations de taux obtenue dans l'approximation de champ moyen nous a donné des informations sur les densités d'îlots.

Nous avons étudié la croissance de cobalt sur trois surfaces distinctes. Après le dépôt de Co sur une surface monocristalline propre de Pt(111) à des températures de dépôt au dessus de 180 K(-93°C) on a observé que le platine reconstruit en formant des dislocations en forme d'étoile. Pour des températures semblables, on a aussi observé que la densité d'îlots diverge des valeurs prédites par tous les modèles connus vers des valeurs plus élevées. Des résultats de simulations ont montré que l'insertion d'atomes de Co dans la couche supérieure du platine forme un réseau de dislocations répulsives. Ces dislocations agissent comme des barrières, empêchant la libre diffusion des atomes à la surface ce qui influence la densité d'îlots. Nous avons de plus montré que les dimères et trimères de cobalt diffusent sur la surface à des températures où ils ne se dissocient pas. Cela nous a permis d'obtenir les barrières d'énergie de diffusion correspondantes.

Nous avons aussi étudié la croissance de Co sur la surface (0001) du ruthénium, qui a un comportement en température plus habituel. Par comparaison entre expérience et simulation nous avons déterminé les énergies d'activations pour la diffusion. Nous avons aussi montré qu'à plus haute température le dimère et le trimère de Co dissocient.

Finalement, Nous avons étudié la croissance de Co sur le super-réseau que forme le nitrure de bore hexagonal sur le Rh(111). Sur cette surface, les agrégats de cobalt forment des demi-sphères. Nous avons étudié comment la corrugation du substrat influence la diffusion des atomes de Co et

avons montré que des agrégats jusqu'à la taille du pentamère diffusent sur la surface. Par simulation nous avons pu déterminer les barrières énergétiques de diffusion et de désorption.

Mots-clés: Microcope à effet tunnel (STM), simulations Monte-Carlo cinétiques (KMC), équations de taux, croissance auto-organisée, nucléation, cobalt, Pt(111), Ru(0001), *h*-BN/Rh(111) nanomesh

Kurzfassung

Epitaktisches Wachstum von Submonolagen wird erreicht durch das Aufdampfen von weniger als einer Schicht Atome auf eine monokristalline Oberfläche. Es ist von hoher Bedeutung für industrielle Anwendungen, z.B. in der Halbleiter Industrie, sowohl wie in der Grundlagenforschung. Es ist zum Beispiel bekannt, dass atomare Strukturen mit Dimensionen im Nanometerbereich (Nanostrukturen) auSSerordentliche physikalische und chemische Eigenschaften aufweisen, die sich stark von denen im Festkörper unterscheiden. Zur Erforschung dieser Eigenschaften ist es oft nötig, groSSe Anzahlen von gut definierten und –wenn möglich– räumlich angeordneten Nanostrukturen zu erzeugen. Dies kann man z.B. durch selbstorganisiertes Wachstum erreichen, in dem man Atome auf eine saubere kristalline Oberfläche aufdampft und den Wachstumsprozess sich frei entwickeln lässt. Nanostrukturen werden dann durch atomare Diffusions- und Aggregationsprozesse auf der Oberfläche erzeugt. Für die Erforschung des Wachstums von Nanostrukturen ist es von anhaltendem Interesse, die Eigenschaften dieser Prozesse genau zu verstehen.

In dieser Doktorarbeit untersuchen wir das Wachstum von Submonolagen des ferromagnetischen Übergangsmetalls *Cobalt*. Cobalt wurde auf Grund seiner hervorragenden magnetischen Eigenschaften ausgewählt. Die Versuche wurden in einer Ultrahochvakuum-Kammer durchgeführt, wobei die nanostrukturen durch Molekularstrahlepitaxie aufgedampft wurden. Die Oberfläche wurde dann mittels eines Rastertunnelmikroskops mit variabler Probentemperatur untersucht. Um die an der Oberfläche stattfindenden atomaren Prozesse besser zu verstehen, wurden zwei entsprechende computergestützte Simulationen entwickelt. Die kinetische Monte-Carlo simulation wurde angewandt, um ein atomares Bild der Oberfläche zu erhalten. Des Weiteren wurden die im Rahmen der "mean-field" Nukleationstheorie aufgestellten Ratengleichungen numerisch integriert und daraus Inseldichten bestimmt.

Wir untersuchten das Wachstum von Cobalt auf drei verschiedenen Oberflächen. Beim Aufdampfen von Cobalt auf eine saubere Pt(111)-Kristalloberfläche bei Probentemperaturen über 180 K (-93°C) stellten wir fest, dass die oberste Atomlage des Platins rekonstruiert und dass sich sternförmige Versetzungen entwickeln. Die Experimente ergaben, dass bei ähnlichen Temperaturen die Inseldichte von den Vorhersagen aller bekannten Modelle abweicht und höhere Werte aufweist. Unsere Simulationen zeigten, dass das Diffundieren von Cobalt-Atomen in die oberste Platin-Atomschicht dazu führt, dass sich ein Netz von abstoSSenden Versetzungen entwickelt. Die Versetzungen agieren als diffusionshemmende Schwellen und beschränken dadurch die freie Bewegung der Atome, was die Inseldichte beeinflusst. Wie zeigten auch, dass die Cobalt-Dimere und -Trimere auf der Pt(111)-Oberfläche diffundieren bevor sie dissoziieren und bestimmten daraus entsprechende Energiebarrieren für die Diffusion.

Im Weiteren untersuchten wir auch das Wachstum von Cobalt auf der (0001) Oberfläche von Ruthenium, welches eine gewöhnlichere Temperaturabhängigkeit aufweist. Durch Vergleiche zwischen Simulation und Experiment bestimmten wir alle wichtigen Diffusionsenergiebarrieren und zeigten, dass Co-Dimere und -Trimere bei höheren Temperaturen dissoziieren.

SchlieSSlich erforschten wir das Co Wachstum auf dem Übergitter, welches hexagonales Bornitrid auf Rh(111) bildet. Auf dieser Oberfläche bildet Co halbkugelförmige Inseln. Wir zeigten wie die

Oberflächenkorrugation die Diffusion von Co-Atomen beeinflusst und, dass Cluster, bestehend aus bis zu fünf Atomen, diffundieren. Den Simulationen entnahmen wir Diffusions- und Desorptionsenergiebarrieren.

Schlüsselwörter: Rastertunnelmikroskop (STM), kinetische Monte-Carlo (KMC) Simulation, Ratengleichungen, selbstorganisiertes Wachstum, Nukleation, cobalt, Pt(111), Ru(0001), *h*-BN/Rh(111) nanomesh

Contents

Chapter 1

Introduction

The physical and chemical properties of nanometer scaled structures depend on their size and shape and can be very different from those of bulk matter. These properties can be investigated by surface integrating techniques, for example by spectroscopy, which requires the fabrication of large quantities of monodisperse structures. Although the possibility of direct atomic manipulation has been shown [1], this method is tedious when applied to produce large quantities of nanostructures. Several techniques have been devised to tackle this challenge. Among them, the size-selected deposition of clusters on a surface [2] and chemical synthesis of colloidal particles [3] are two well-known examples. In this work, we focus on a different technique, namely *self-assembled* growth. The word "self-assembled" indicates that no direct control on the atomic level is applied. The system evolves by atomic transport at the surface while being influenced only by macroscopic parameters (e.g. substrate type and temperature). The success and usefulness of this technique has been demonstrated by recent experiments focused on the size-dependent catalytic [4] and magnetic properties [5] of nanoparticles with narrow size and shape distributions organized in 2D macroscopically phase coherent superlattices.

In this thesis work we are interested in *submonolayer* epitaxial growth on a single crystal surface by molecular beam epitaxy (MBE). Growth is a far-from-equilibrium process. For example, the incoming deposition flux of atoms is not counterbalanced by a desorption process with the same rate as would be expected at thermal equilibrium. Understanding the kinetics of fundamental processes which govern the diffusion and assembly on the surface at the atomic level during this far-from-equilibrium process is an old but ongoing objective whose investigation requires both experimental and theoretical work.

From the experimental point of view, the first available methods capable of investigating surfaces at the atomic level were diffraction methods in the late 20s. Both *low-energy electron diffraction* (LEED) and its cousin the *reflection high energy electron diffraction* (RHEED) have for example brought many successes in understanding atomic surface reconstruction. One of the major disadvantages of these methods is that the surface is represented in the reciprocal space, making interpretation of measured physical data more difficult. The first real space experimental technique capable of imaging atoms at a surface has been the field ion microscope (FIM). While this method has been widely and successfully used to study the diffusion of monomers and clusters at a surface, it is not suited to investigate large areas of nanostructure-covered singular surfaces. The cornerstone of modern growth investigation was laid by the invention of the scanning tunneling microscope (STM) in 1982 by Binnig and Rohrer (nobel laureates in 1986)[6]. This method allowed for the first time to image large areas of a surface at the atomic level, including single atoms. This breakthrough was soon followed by the development of many other scanning probe microscopy (SPM) methods, the most prominent being the atomic force microscope (AFM) which is nowadays widely used in biology and

the industry. In this work, experimental data are acquired using an STM which is described in some detail in Chap. 2.

Interestingly, the theoretical modeling methods followed a similar time evolution going from mean-field global methods towards atomistic simulation methods. In fact, the first theoretical description of growth at a singular surface was made in the late 60s when Zinsmeister [7, 8] and later Venables [9] described the formation of submonolayer clusters by a set of ordinary differential equations (ODE) called *rate equations* (RE). This method was successful at describing the time evolution of cluster densities and, to some extend, their sizes. The technological development of the modern computer in the 70s put new tools in the hands of theorists. The availability of larger quantities of calculation power permitted the development of simulation techniques taking into account each atom on a surface individually, and describing the time evolution by simple rules applicable to each atom. This led to the development of the kinetic Monte-Carlo (KMC) method and molecular dynamics (MD). In this work, we developed and improved the KMC as well as the RE approaches and adapted them to explain experimental observations. The basis of both methods is presented in Chap. 3 while refinements specific to experimental observations are intertwined with results throughout the document.

In this thesis, we focused on the submonolayer growth of the ferromagnetic transition metal *cobalt*. Cobalt clusters, from single atoms to large particles, are of general interest due to their remarkable magnetic properties. For example, when deposited on platinum, Co monomers present a giant magnetic anisotropy energy which is about two orders of magnitude larger than that measured in the bulk state [10]. We have studied the growth of cobalt on three different substrates, namely Pt(111), Ru(0001), and *h*-BN/Rh(111). The interest in the first two systems is due to the strong electronic interaction between Co and substrate atoms which results in spectacular magnetic properties. This interaction is strongly dependent on the cluster size and shape. Thus, a deep knowledge of the surface diffusion barriers is a key element in tailoring the electronic and magnetic properties of these nanostructures. The third system is a potential candidate for the fabrication of long-range phase coherent arrays of monodisperse particles.

- Chapter 4 presents the deposition of Co on the Pt(111) surface. We find that the platinum surface reconstructs in the presence of cobalt monomers at surface temperatures above 180 K. For these same temperatures, we observe a discrepancy between measured cluster densities and homogeneous diffusion models. We review all known models to explain these differences and, upon failure, devise a refined KMC simulation including the dynamic reconstruction of the surface. This model permits to attribute the discrepancy in island densities to the heterogeneous diffusion imposed by the dislocation array generated by the surface reconstruction. We further show that the cohesion energy of Co-dimers and trimers is sufficiently high to allow for their diffusion above 150 K before cluster dissociation sets in. The measured behavior is reproduced in KMC and RE simulations and allows for the determination of dimer and trimer diffusion barriers.

- In Chapter 5, we show results of Co deposited on the Ru(0001) surface. We observe that low-temperature monomer migration is governed by a modified diffusion barrier for attachment (*easy attachment*). At higher deposition temperatures, the measured island densities indicate that the system follows a perfect Arrhenius behavior, enabling the calculation of the migration barrier and the corresponding prefactor. By including data from previous works, we show that the system evolves towards unstable dimers and trimers at temperatures above 300 K.

- Chapter 6 describes Co growth on the hexagonal boron nitride superlattice on Rh(111). On this surface, Co forms three-dimensional islands. We show how the hexagonal superlattice influences monomer diffusion and extract activation energies for diffusion and desorption. By

simulating annealing experiments we are furthermore able to show that clusters up to the pentamer size diffuse at temperatures above 200 K. We also show evidence of the fact that the hexagonal boron nitride layer is continuous over substrate step edges.

Throughout this document experimental and simulation results are intertwined. In each chapter we will propose physical models backed-up by KMC and RE simulations, to explain and understand our experimental observations. In order to facilitate reading, a comprehensive list of the symbols and acronyms used is given as an annexe on p. 131.

Chapter 2

Experimental

2.1 Scanning tunneling microscopy

Since its invention 25 years ago by Binnig and Rohrer [6], the scanning tunneling microscope (STM) has become an important tool for the real space investigation of metal and semiconductor surfaces at the atomic level. The imaging capabilities of the STM are based on the quantum mechanical tunneling effect. This effect allows electrons with an energy E to cross a potential barrier larger than E. In the case of the STM, this allows electrons to tunnel from a tip through vacuum to a sample surface resulting in a tunneling current I_t. Tunneling is observed when the spatial extension of the electronic wave function Ψ is of the same scale as the potential barrier width. Thus in the STM, a sharp tip is brought very close to the sample surface and a bias voltage V_t is applied between the two objects. The tip position on the surface is controlled by piezoelectric actuators. In particular, in the sample-tip z-direction, a feedback loop regulates the tip height to keep the tunneling current constant (*constant current mode*). By scanning the surface plane with the tip and recording its height, a map of the surface can be made and rendered as an image. Below, we introduce the main results of STM theory necessary to interpret images. For a review with complete theoretical treatment see e.g. Ref. [11].

As has been shown by Bardeen [13] in a first-order perturbative treatment of tunneling, the current I_t between two independent planar electrodes for a weak wave function overlap can be written as

$$I_t(V_t) = \frac{2\pi e}{\hbar} \sum_{\mu,\nu} |M_{\mu\nu}|^2 \delta(E_\mu - (E_\nu + e V_t)) \times \Big[f(E_\mu, T)[1 - f(E_\nu, T)] - f(E_\nu, T)[1 - f(E_\mu, T)] \Big] \tag{2.1}$$

where the summation goes over all eigenfunctions of the tip and sample Ψ_μ and Ψ_ν with corresponding eigenenergies E_μ, E_ν. Note that these energies are measured with respect to the corresponding Fermi level $E_{F,t}$ (tip) and $E_{F,s}$ (sample) (see Fig. 2.1). $f(E,T)$ denotes the Fermi-Dirac function which gives the probability of an electronic energy state of energy E to be occupied at temperature T.

The tunneling matrix $M_{\mu\nu}$ evaluates the overlap of the tip and sample wave functions and can be written as

$$M_{\mu\nu} = \frac{-\hbar^2}{2m} \int_S (\Psi_\mu^* \vec{\nabla} \Psi_\nu - \Psi_\nu \vec{\nabla} \Psi_\mu^*) \, d\vec{S} \tag{2.2}$$

where the integral is over a surface S in the tip-sample gap.

A direct application of this approach to the STM was calculated by Tersoff and Hamann [14]. In order to simplify the expression, they made the supposition of a spherical tip of radius R with only

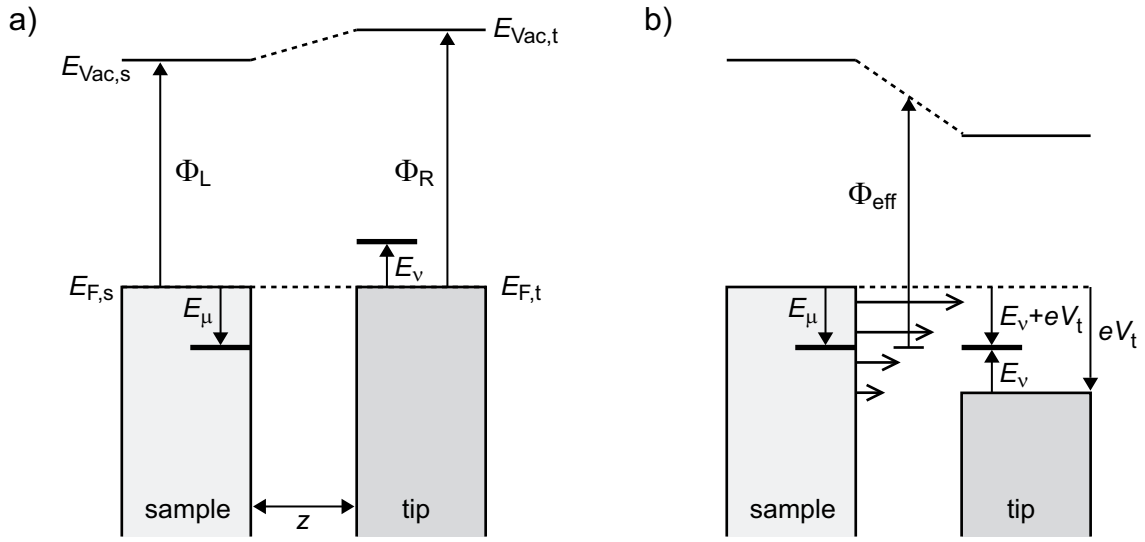

Figure 2.1: Energy diagram of the tip-sample tunnel junction. a) Without an applied voltage. b) With an applied voltage. From [12].

s-type wave functions, low temperatures and small voltages. They find

$$I_t(V_t) = \frac{2\pi e^2}{\hbar} V_t \cdot \sum_{\mu,\nu} |M_{\mu\nu}|^2 \delta(E_\mu - E_F) \cdot \delta(E_\nu - E_F). \tag{2.3}$$

which further simplifies by using explicit wave functions and for a tip position $\vec{r}_0$

$$I_t(V_t) \propto V_t \cdot \rho_t(E_F)\, e^{2\kappa R} \sum_\mu |\Psi_\mu(\vec{r}_0)|^2 \delta(E_\mu - E_F) \tag{2.4}$$

Here, $\kappa = \sqrt{2m\Phi_{eff}}/\hbar$ represents the inverse decay length for the wave functions in vacuum. Φ_{eff} is the effective tunneling potential barrier and $\rho_t(E)$ is the density of states of the tip. Remarkably, this shows that for a constant tunneling voltage V_t, the current is proportional to the local density of states (LDOS) of the sample $\rho_s(\vec{r}, E)$ at position $\vec{r}_0$, i.e.

$$I \propto \rho_s(\vec{r}_0, E_F) \quad \text{with} \quad \rho_s(\vec{r}_0, E) = \sum_\mu |\Psi_\mu(\vec{r}_0)|^2 \delta(E_\mu - E). \tag{2.5}$$

This lets us interpret constant current STM images as a map of the LDOS at the Fermi level. The exponential decay of the wave functions in the z direction normal to the surface yields $|\Psi_\mu(\vec{r}_0)|^2 = e^{-2\kappa(z+R)}$ which we can substitute in Eq. 2.4 to find

$$I_t \propto e^{-2\kappa z} \tag{2.6}$$

Thus, the tunneling current depends exponentially on the tip-sample distance z. This feature gives the STM its remarkable height sensitivity.

2.2 Experimental setup

The experimental results presented in this thesis have been obtained with a home built beetle-type variable-temperature (50–800 K) STM mounted in an ultra-high vacuum (UHV) chamber. This experimental setup (see Fig. 2.2) was developed in a previous Ph.D. thesis by N. Weiss et al. and full details

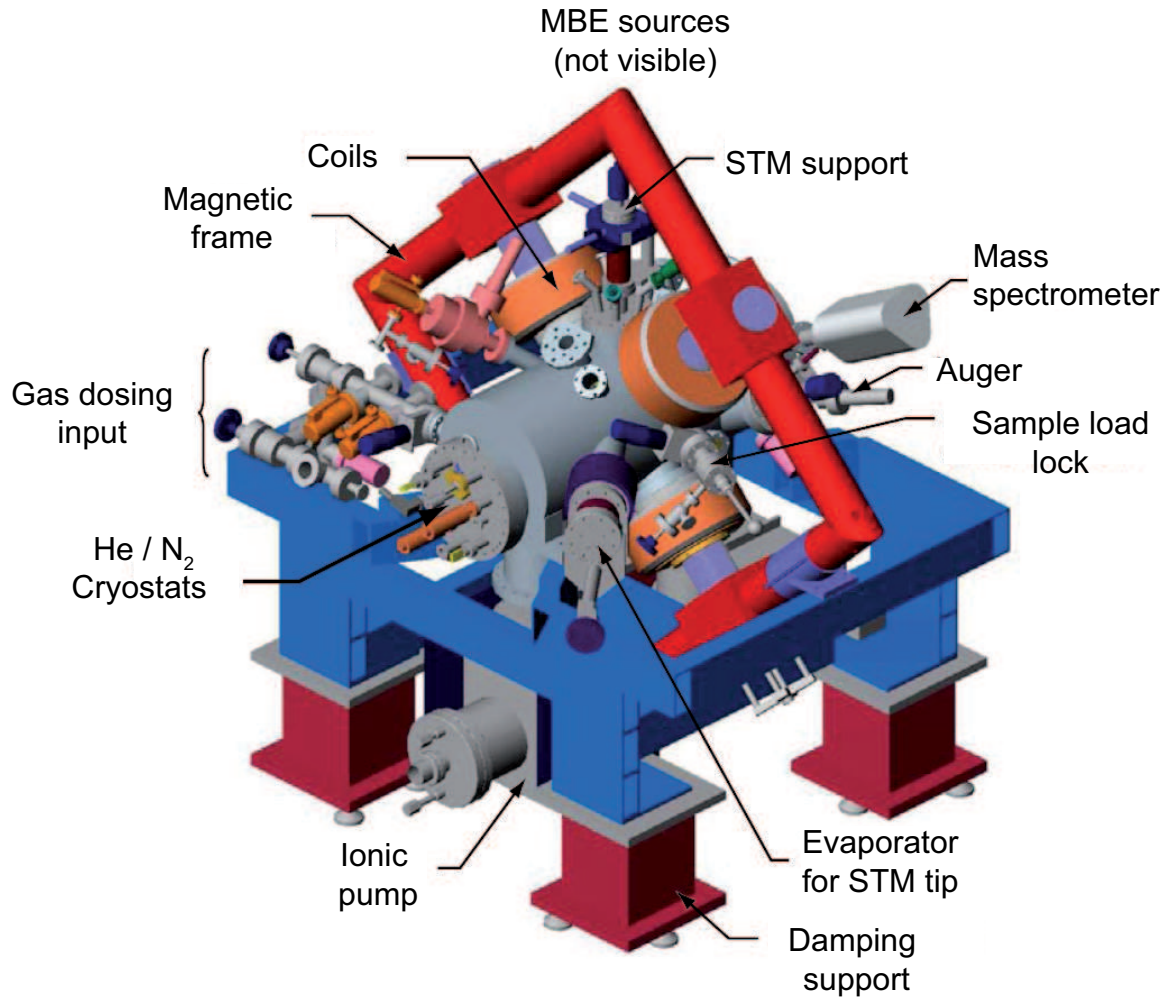

Figure 2.2: Sketch of the experimental setup used in this thesis. The central cylindrical ultrahigh vacuum chamber is surrounded by a four-pole electromagnet. The chamber is equipped with usual surface preparation and analysis tools and features a variable temperature (50–800 K) scanning tunneling microscope (STM).

are given in Ref. [15]. The UHV chamber (base pressure $< 10^{-10}$ mbar) features usual surface preparation and analysis tools, including an Ar^+ ion sputtering gun, electron-bombardment heating of the sample for annealing up to 2000 K and Auger-electron spectroscopy. Deposition of materials on the clean sample surface can be done either by molecular beam epitaxy (MBE) using a commercial triple e-beam evaporator or by using a Knudsen cell. Deposition can also be done by UHV chemical vapor deposition (UHVCVD) as the chamber provides multiple gas inlet points.

2.2.1 Optimization of the STM setup with respect to noise

In the course of this work, special attention was devoted to reducing the mechanical and electronic noise affecting STM imaging. In fact, the original setup showed important mechanical resonances around 300 Hz. These resulted in up to 0.140 Å RMS[1] noise on images.

By systematic measurement and separation of possible causes, we identified two main zones responsible for this noise (see also Fig. 2.4): the mechanical coupling between the cryostat and the sample holder and a coupling between the stacked damping stages.

The cooling of the sample in this setup is provided by a flow-cryostat for liquid helium (ℓHe) or liquid nitrogen. When cooling, the heat flows from the sample to the sample-holder and subsequently through a silver coated copper-braid to the cold finger of the cryostat. The cryostat is directly fixed to the chamber and thus vibrations are not particularly damped. The chamber itself is isolated from low frequency vibrations through active damping platforms. Thus, two possibilities exist to reduce the impact on STM imaging of vibrations in the cooling system. Either, reduce the actual vibrations in the cryostat or reduce the coupling between cryostat and sample holder. We used both approaches. The cryostat was damped with respect to the chamber by mounting on Viton o-rings. At the same time, the copper braid was replaced by a more flexible one. In fact, the actual braid was frayed into single threads to separate the spring effect of each lead. This should result in phase-incoherent vibrations of single threads and an effective loss in transmission of vibrational energy without loss of thermal conduction.

The second point which we identified above was the coupling between plates of the multi-stage damping stack. The coupling resulted from the numerous cables which need to reach the low vibration region, namely:

- Sample contact for tunneling and e-beam heating
- 2 thermocouple
- 2 filament heating
- 4 Kerr-setup motor
- 2 Kerr-setup laser diode
- 2 Kerr-setup photo-diode

In order to address this, we rewired all above-listed leads taking special care to damp each at different stages as often as practical. We reduced direct coupling in-between stages by looping the wires.

We further identified low-level 50 Hz electronic noise in STM images. Part of this noise was produced by lab material which could be switched off during imaging, for example the quadrupole mass spectrometer. The remaining noise was attributed to ground loops and general weak grounding of the chamber. One particular source was identified to be the STM-controlling computer. Separation

[1] Root Mean Square.

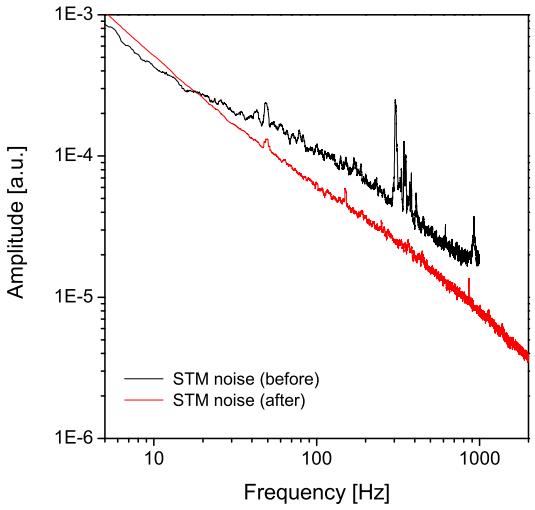

Figure 2.3: Fourier transforms of the static STM z signal recorded before (black) and after (red) modification. In particular, mechanical resonances at ≈ 300 Hz were efficiently reduced by a factor of 5 while electronic noise at 50 Hz was reduced by a factor of two.

of the masses of these elements in addition with a clearer application of the star-shape grounding rule showed some improvement.

Fig. 2.3 compares Fourier transforms of the z signal recorded by the immobile STM. The two curves represent the signal before and after the improvements described above. The mechanical resonances at ≈ 300 Hz were effectively eliminated (reduction by a factor > 5) while the electronic noise peak at 50 Hz was divided by two. The overall noise level in imaging conditions is now below 5 pm RMS.

2.3 Development of an in situ magneto-optical Kerr effect setup

The experimental setup is intended to allow for the measurement of sample magnetization in a continuously variable magnetic field. Four magnetic poles reach inside the chamber to apply a magnetic field up to 350 mT on the sample in any direction of the frame plane (see Fig. 2.2). Magnetization measurements are done using the magneto-optical Kerr effect (MOKE).

MOKE is a magneto-optical effect, that is, an effect induced by a magnetic material on light. The first magneto-optical effect was discovered by M. Faraday in 1845. He observed that linearly polarized light has its polarization direction rotated by an angle θ_F when it goes through a sample which is magnetized in the direction of light propagation. This angle depends on the thickness d and the magnetization M of the material by the relation $\theta_F = \nu M d$ where ν is the Verdet constant. Note that the inversion of the magnetization reverses the rotation angle of the polarization. Another effect is observed simultaneously: the increase of the light's ellipticity. Both observations can be understood when imagining linearly polarized light as the superposition of two circularly polarized beams with inverse rotation directions, namely left and right polarized light. In the material, different complex refraction indices are associated with each polarization direction. Thus, one of the two polarizations has a higher velocity in the material. This modifies the relative phase of the two waves and results in

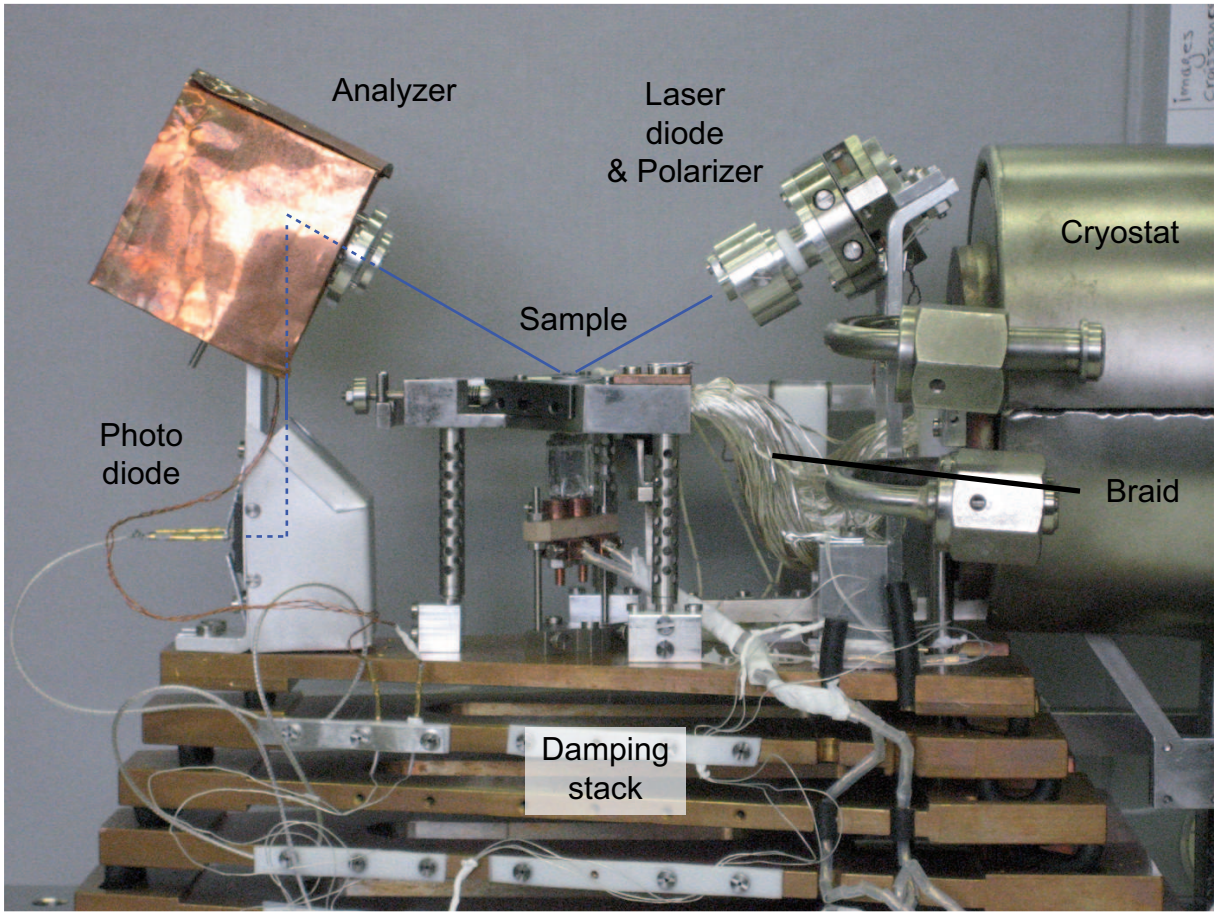

Figure 2.4: Side view of the sample holder on the damping stack. For STM imaging, the beetle type STM-head (not shown) is placed on top of the sample holder. The sample is cooled by a liquid helium cryostat to which it is connected by a silver-coated copper braid. The MOKE setup is mounted directly on the topmost damped plate and thus is insensitive to the UHV chamber deformation. The blue line indicates the path of light used for the MOKE measurements.

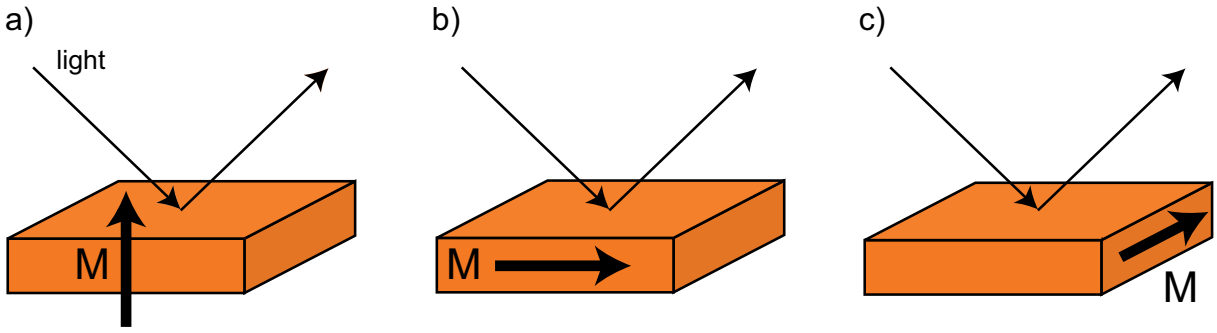

Figure 2.5: The three configurations of the magneto-optical Kerr effect can be categorized by the direction of the magnetization with respect to the plane of the light. a) Polar configuration. b) Longitudinal configuration. c) Transverse configuration.

a change of angle of the linearly polarized light. The ellipticity in contrast depends on the imaginary part of the refraction indices and is the result of different absorptions of the two polarizations. Similar effects have also been observed for liquids (Cotton-Mouton effect) and gases (Voigt effect).

The magneto-optical *Kerr* effect was discovered in 1876 by J. Kerr. He observed comparable effects than Faraday but upon *reflection* of light at a magnetized sample. One generally speaks of three different MOKE configurations depending on the orientation of the material magnetization with respect to the plane formed by the reflected light beam (see Fig. 2.5). In the *polar* configuration, the magnetization is perpendicular to the reflection plane while in the *longitudinal* configuration the magnetization is in the plane of the light and parallel to the surface. In both configurations, after reflection of a beam of linearly polarized light the direction of polarization is rotated by an angle θ and an ellipticity η appears. This effect is the superposition of two separate effects, the one induced by a normal reflection on a surface and the actual Kerr effect. In the third case, the transverse configuration with the magnetization perpendicular to the plane of the light beam, no effect is observed if the incoming light beam is polarized purely in the s direction ($\vec{E}$ perpendicular to the beam plane). For p-polarized light in contrast, a variation in the light's intensity proportional to the magnetization is observed.

The MOKE method is particularly suited to study magnetization of surfaces and it was applied to the study of thin films since the mid-80s. The rotation angle of the polarization is typically of the order of 1 degree for bulk magnetized material. For submonolayer materials, the rotation is typically a few 1/100 of a degree. For a complete review of the theory of MOKE see e.g. Ref. [16].

2.3.1 In situ implementation of the MOKE

In order to use MOKE experimentally, the typical setup is comprised of a laser diode with a high quality polarizer to produce the linearly polarized light. Another polarizer is used as an analyzer after the reflection of the light beam on the sample. A photo-diode finally records the intensity of the light passing through the analyzer. In order to maximize the sensitivity of the setup, the analyzer is crossed with respect to the light source, so that in the absence of magnetization the recorded light intensity behind the analyzer is near zero.

In this work we report on a Kerr setup capable of making polar and transverse configuration measurements. The original design presented in Ref. [15], intended to keep both the light source and the analyzer and photo-diode outside of the UHV chamber. This has many advantages. For example, one can easily access the material to replace or repair and the laser temperature can be stabilized using

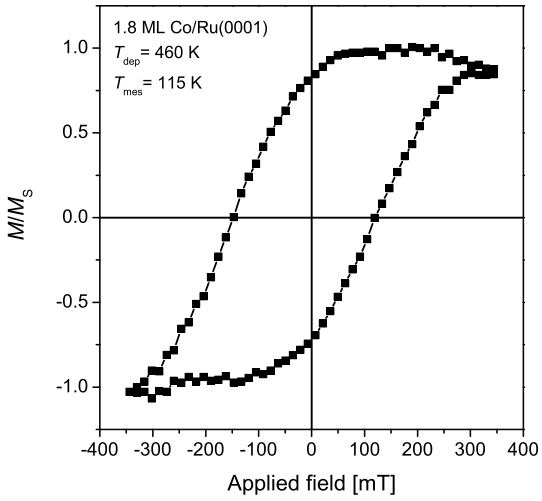

Figure 2.6: Application of the newly developed MOKE setup to the polar Kerr measure of the magnetization of a 1.8 ML Co film deposited on Ru(0001). The hysteresis loop shows that the easy magnetization direction of the thin film is in the out-of-plane direction.

e.g. a Peltier element. Due to the strong magnetic forces which act on the magnetic poles when the maximum field is applied, it was observed that the whole chamber deforms (up to a few mm) resulting in a small torsion of the apparatus. As the polarization rotation angles which are to be measured are of the same magnitude, this introduces large measurement artifacts.

To correct these problems it was decided to build an in situ version of the MOKE, thus including the laser diode, polarizer and analyzer inside the UHV chamber. In fact, by mounting the optical components directly on the main damped stage where also the sample holder is fixed, any relative movements which could take place and falsify the observations are relieved.

The main design was done in collaboration with M. Treier [17] with improvements devised by J. Giesecke [18]. The final setup can be seen on Fig. 2.4. Many incremental improvements were made, whose details can be found in the two references mentioned above. We underline the key features which emerged from this:

- Complete in situ solution: Laser, polarizers and photo diode are in the UHV chamber.
- Usage of non-ferromagnetic laser diodes for which a particular mounting with sub-millimeter features was designed and machined (see Fig. 2.7).
- Usage of UHV compatible stepper motors to rotate the light polarization and align the polarizers.
- Replacement of all stainless steel made sample holder pieces by titanium equivalents.

Preliminary tests showed that the setup is functional. For example, Fig. 2.6 shows a hysteresis loop recorded with the new setup. In this experiment, 1.8 ML of cobalt were deposited on a clean Ru(0001) surface at 460 K. This temperature guarantees step-flow growth (see Chapter 5 for full details on the growth of Co/Ru(0001)) and thus a continuous and flat surface. The hysteresis loop was recorded at a

temperature of $T = 115$ K in the polar Kerr configuration and thus shows the perpendicular magnetization of the sample. The hysteresis loop is open, showing a coercive field of ≈ 150 mT. This indicates that the magnetization easy axis is out-of-plane and that the system is below the blocking temperature. Furthermore, at maximum external field the magnetization reaches its saturation level which lets us plot the relative magnetization instead of arbitrary units. This measure confirms the finding of El Gabaly et al. [19] that a 2 ML film of Co is magnetized out-of-plane.

We thus have developed an innovative solution for the in situ measurement of magnetization of submonolayer ferromagnetic or super-paramagnetic layers. A possible further improvement is still pending. Namely, the usage of a photo-diode with ultra-homogeneous sensitivity. This should open the road towards a further increased sensibility.

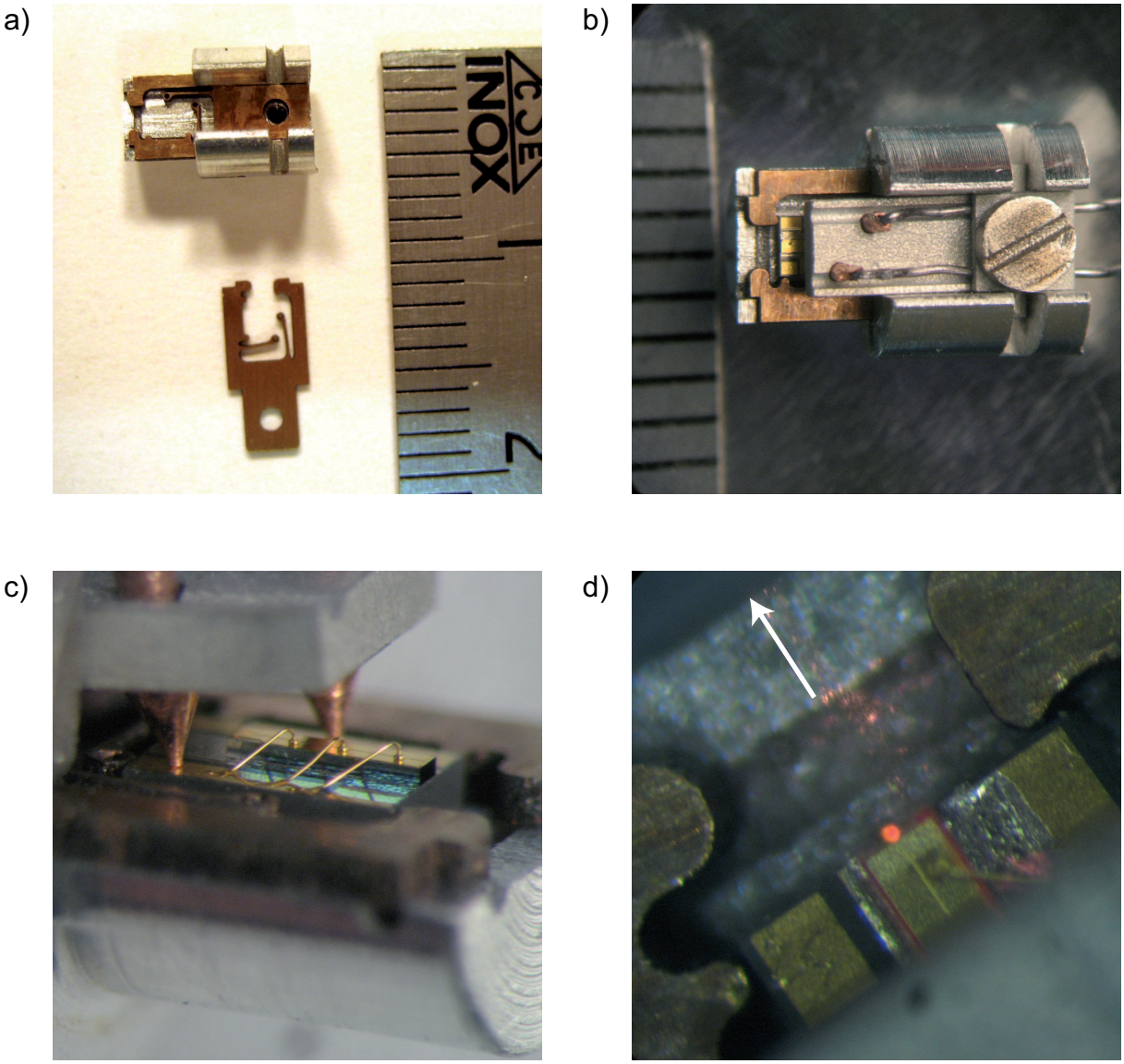

Figure 2.7: Pictures of the non-magnetic laser diode mounting. a) Top-view of main aluminum housing (top) and of the Cu-Be spring system to hold the ceramic-mounted laser diode b) Top-view of the completely assembled laser c) Detail of the electric contacting areas d) Setup when lasing. A light reflection can be seen, the actual light beam is indicated by an arrow.

Chapter 3

Simulating nucleation and growth

Submonolayer deposition is a fundamental process of thin-film growth, with applications in science as well as in technology. The general picture is that adatoms are deposited from the gas phase on a substrate with a flux F which is given in monolayer per second (ML/s). Here a monolayer is defined as the density of atoms in the topmost layer of the substrate. So 1 ML corresponds to the number of atoms covering the substrate equally by a one atom thick layer. Upon deposition, the adsorbed atoms (adatoms) start diffusing *randomly* on the surface by hopping between adjacent adsorption sites with a hopping rate ν. In general, the hopping frequency can be described by a Boltzmann term

$$\nu = \nu_0 \exp\left(\frac{-E}{kT}\right) \tag{3.1}$$

with E an adequate energy barrier and ν_0 a prefactor. Two diffusing adatoms may encounter and nucleate an island or they may aggregate to preexisting islands. In this work, we use the term island and cluster in an indistinct manner. In general, one can define a critical cluster size i. This is the island size which is stable upon incorporation of one additional atom. Stable means that it will not decay by reevaporation of edge atoms. In contrast, islands of size i and smaller are subject to decay.

Several computational means exist to simulate the above processes (for a recent and complete review, see e.g. Ref. [20] or Ref. [21]). The different methods are applicable for different time and length scales. We will only address in more detail the methods which are relevant for the time scale (typically ≈ 100 s) and length scale of our experimental results. The computational methods can be divided into the mean-field approaches and the atomistic approaches. In the mean-field approaches, the exact location of atoms on the surface is replaced by their average effect on the system. This approach thus neglects the inherent stochastic part of the growth process. One mean-field method which has shown considerable successes in explaining growth are the rate equations (RE) developed by Zinsmeister [7, 8] and Venables [9]. These are a set of coupled ordinary differential equations (ODE) describing the time evolution of cluster densities. Using certain approximations, they can be solved analytically while the most general form is addressed by numerical integration.

The atomistic approach in contrast, tracks the position of atoms on the surface and thus explicitly takes into account the stochastic nature of the processes taking place. Two methods are widely used to simulate growth: Molecular dynamics (MD) and kinetic Monte-Carlo (KMC). The MD methods tracks the exact position of substrate and adsorbate atoms. The time evolution is given by applying the equation of motion on each atom in subsequent time steps. The potential at each point is obtained by numerical integration from the position of each atom. Integration time steps are typically of the order of 1 fs and the system may be comprised of several hundred atoms. This approach is well suited to calculate relevant energy activation barriers, but cannot, due to computing power limitation, be applied to large systems.

The KMC approach in contrast, does not track the exact position of atoms, but makes the hypothesis that adatoms can only reside on a grid of well defined adsorption sites. Typically, on a hexagonal close packed surface, these adsorption sites are the fcc or hcp hollow sites of the surface. The time evolution of the system is then described by the rate ν at which an adatom hops from one grid site to a neighboring. Depending on exact parameters, this simplified KMC approach permits to simulate length scales up to a few million surface atoms and time scales of some 100 seconds.

Both, the RE and the KMC approach fit the length and time scales requirements of our experiments. In this thesis work we have adapted the RE approach to understand the experimental results. The basic equations as written for the simplest systems will be given here, while refinements are presented throughout the work when they become relevant for the experimental data. We have also developed a complete KMC simulation framework for which details will given below and application, including refinements, throughout the document. We start this chapter by presenting some key results from nucleation theory.

3.1 Rate equations and scaling laws

Zinsmeister [7, 8] and Venables [9] proposed to write equations describing the time evolution of mean-field quantities such as the density n_s (per surface site) of clusters of size s. For example, two monomers can join to form a dimer with a capture efficiency σ_1. Monomers may also get captured by a stable island (density n_x) with a corresponding capture efficiency σ_x.

We assume complete condensation (i.e. all atoms stay on the surface, no reevaporation occurs) which is applicable in the high supersaturated regime of our MBE experiments. We also suppose that all islands larger than the monomer are stable, and are thus accounted for in n_x. In this case, the density of monomers and stable islands can be written as:

$$\frac{\mathrm{d}n_1}{\mathrm{d}t} = F - 2\sigma_1 D n_1^2 - \sigma_x D n_1 n_x \tag{3.2}$$

$$\frac{\mathrm{d}n_x}{\mathrm{d}t} = \sigma_1 D n_1^2 \tag{3.3}$$

where F is the deposition flux and D is the tracer diffusion coefficient. The tracer diffusion coefficient can be found from the hopping frequency ν via the Einstein relation for 2 dimensions [20]

$$D = \frac{1}{4}\nu\ a^2 = \frac{1}{4}\nu_0 \exp\left(\frac{-E}{kT}\right)\ a^2 \tag{3.4}$$

with a the lattice constant. In this document we generally normalize D to the atomic surface cell c of a hexagonal compact surface ($c = \sin(60)\,a^2$).

The right hand side terms of the first equation (3.2) describe the gain and loss of monomers. F is the gain of monomers due to deposition. Note that the loss by direct deposition on existing islands is neglected here. The second term describes the loss of two monomers by nucleation of a stable dimer and the third term describes the loss of monomers by irreversible aggregation to stable islands. The second equation records the number of stable islands created by nucleation of two monomers (aggregation of monomers to stable clusters does not change its density).

This very simple approach, extended to include critical clusters with sizes > 1, leads to one of the major results of nucleation theory (see Ref. [20] for details), namely that in the steady state regime the density of stable islands can be written as a scaling law

$$n_x = \eta(\Theta, i)\left(\frac{D}{F}\right)^{-\chi}\ \exp\left(\frac{-E_i}{kT(i+2)}\right) \tag{3.5}$$

with $\chi = i/(i+2)$ as the scaling exponent. E_i denotes the binding energy of the critical cluster. Note that in the case of a critical cluster of size 1, the expression is reduced to $n_x = \eta \left(\frac{D}{F}\right)^{-1/3}$. It has been shown that this equation is applicable for temperatures where $D/F > 10^5$ and while the supposition $i = 1$ and complete condensation hold true [22]. The constant factor η linking the island density to D/F is slowly varying with coverage: $\eta \propto \Theta^{1/(i+2)}$ but can be approximated by a constant $\eta = 0.25$ [22].

3.1.1 More refined rate equations

The simplest equations (3.2) can be extended to precisely describe growth in all temperature regimes. Above, we made the approximation that direct landing of adatoms from the deposition flux onto islands and near monomers can be neglected. This is particularly not true for low temperatures (i.e. $D/F \ll 10^5$). A more correct way describing this *direct impingement* accounts for the deposition of monomers on adsorbed monomers by a term $\kappa_1 n_1 F$, where κ_1 describes the propensity of a monomer to nucleate a dimer by landing of an incoming adatom in its direct vicinity. By geometric consideration, one can estimate $\kappa_1 = 7$ (on a hexagonal lattice) as seven adsorption sites yield a dimer when the monomer lands on them. This approach can be extended to all sizes although for $s > 2$ one has to take into account the different conformations of the clusters, and eventually their probability of occurrence. For stable clusters, the direct size information is lost when they are accounted for in the n_x term. A good approach is to estimate the coverage offered by stable islands and their direct surroundings to incoming adatoms by supposing that the islands are circular and monodisperse. The direct impingement term is then

$$-\pi F \left(\sqrt{\frac{Ft - n_1}{\pi n_x}} + 1 \right)^2 \tag{3.6}$$

where Ft is the coverage of deposited adatoms.

Another key point in the correct simulation of the physical growth behavior is the correct determination of the capture numbers σ for the different cluster sizes. Several approaches have been proposed to calculate these capture numbers. Among them the *lattice approximation* [9] has been widely used. Here, the capture numbers are calculated by approximating the stable islands on a regular lattice. In this work, we use the lattice approximation to determine the capture number of stable clusters and, when possible, to determine the capture numbers for other island sizes.

The capture numbers contain a wide range of physical information. In particular, at the beginning of the 90s, KMC simulation have shown that island size distribution are not well reproduced by RE using the above capture numbers. Extensive work by Bartelt et al. [23] has lead to the development of capture numbers taking into account the correlation between island size and its surrounding.

In this work, the rate equations are solved by numerical integration using the Mathematica [24] software package.

3.2 Kinetic Monte-Carlo

In collaboration with M. El Ouali [25] we have developed a new kinetic Monte-Carlo (KMC) simulation framework which will be presented in this section and which will be used to extract activation barriers from experimental data in following chapters. For a general introduction to KMC see Ref. [21]. For a study of the theoretical foundation of this method see Ref. [26].

In contrast to molecular dynamics, simulating growth with the kinetic Monte-Carlo algorithm does not require the tracking of the precise position of atoms. Instead, adatoms are supposed to adsorb only on given sites of a grid, and the tracking is limited to know which site is occupied. In the present work, we suppose that adsorption occurs on a hexagonal close packed surface (typically

an fcc(111) surface). Such a surface has two types of adsorption sites which are called fcc or hcp, depending on what type of stacking the adsorbed atom continues (for a graphical representation see Fig. 5.9, p. 92). In the present KMC simulation, possible adsorption sites are limited to the fcc type. The grid of possible adsorption sites is thus a hexagonal lattice.

The hopping for an adatom from one site to its neighbor is associated with a rate r. When simulating diffusion on a surface with hexagonal symmetry this rate is linked to the total hopping rate v by $r = v/6$. In fact, each site has 6 possible diffusing directions. The KMC method makes the supposition that events on the surface are Markov processes, meaning that the future time evolution of the system is independent of its history but depends only on the present state.

3.2.1 Main algorithm

The basic algorithm of kinetic Monte-Carlo simulations is the following.

1. Create a list of all possible processes available for execution for the present surface configuration
2. Randomly choose one process in the list with a probability equivalent to its rate r
3. Execute the process (i.e. change the configuration according to the chosen process)
4. Update the simulation time
5. Update the process list by taking into account the new configuration
6. Restart at (2)

This cycle is repeated while no interruption condition is true. A possible interruption condition is for example when the coverage of adatoms on the surface has reached a given limit.

3.3 Design & implementation

3.3.1 Design choices

The following general choices were made for the implementation of the KMC simulations:

- Simulating a hexagonal close packed surface
- Adsorption on pseudomorphic fcc sites only
- Simulating a singular surface without steps
- Using periodic boundary conditions for the surface lattice
- Possibility to have two different adatom types on the surface

The following processes were included:

- Deposition of adatoms with a flux F
- Diffusion of adatoms on the surface (see below)
- Other non-diffusion processes which will be detailed later (place exchange, insertion etc.)

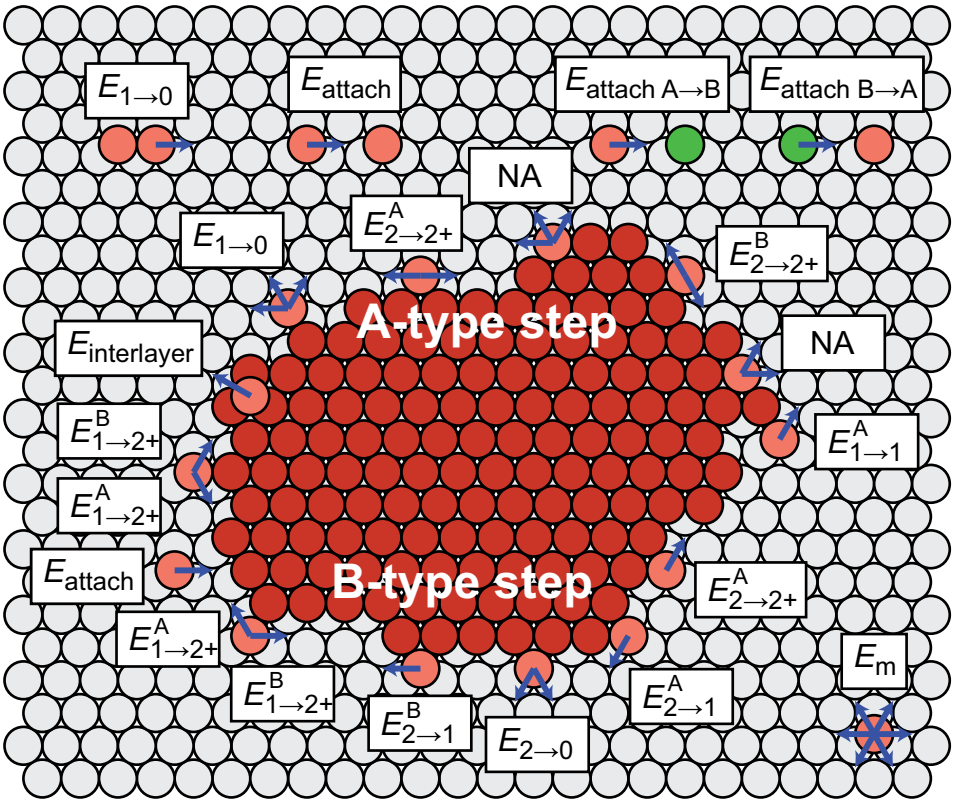

Figure 3.1: Top view of all possible surface diffusion processes implemented in the KMC simulation. All threefold coordinated atom cannot move so they are marked "NA" which stands for "not available".

The possible diffusion processes were chosen following a limited bond-counting model. This means that each adatom move is described by the lateral coordination number at the starting site and at the arriving site. The model is *limited* as all atoms which are threefold or more laterally coordinated are irreversibly attached and cannot move. Each move type has an associated energy barrier which is described by the letter E with a subscript describing the coordination at the start and end point (with "2+" meaning two and more) and a superscript describing if the move is along an A-type step or along a B-type step. The two types of steps which can be found on hexagonal surfaces are characterized by the microfacet which the edge atoms form with the underlying layer: the A-type step forms a (100) microfacet while the B-type step forms a (111) microfacet. This is well shown on the hard sphere model of Fig. 5.9, p. 92.

Fig. 3.1 shows all possible surface moves that are implemented and the corresponding denomination of the activation barrier. To be consistent with the usual notation, the monomer migration on the pristine substrate is not called $E_{0\to0}$ but E_{m}. Furthermore, at this point, the program does not differentiate between the detachment of a laterally onefold coordinated adatom from an island or from a dimer. Dimer dissociation will generally be called E_2 in this document while $E_{1\to0}$ represents all dissociation from onefold coordinated sites. Attachment to a different kind of atom type on the surface has a different barrier ($E_{\text{attach A}\to\text{B}}$) than attachment to the same type of atom (E_{attach}).

3.3.2 Implementation choices

When programming the KMC simulation code, the two main computational implementation goals were:

- A memory and CPU[1]-time efficient implementation
- An easily extensible code structure

The first was addressed by the choice of well adapted algorithms and data structures, some of which are detailed below. The second was addressed by choosing an object-oriented (OO) program structure.

The processes available for execution in the simulation can be classified in three groups

- Time specific events (e.g. deposition)
- Atom specific events (e.g. all single atom surface diffusions)
- Structure specific events (e.g. dimer diffusion)

In this case, *structures* represent islands of different sizes. Thus, structure specific events are those which do not focus on the actual atoms comprising the island, but on the island (structure) as a whole. For example the dimer can diffuse by a concerted move of both atoms; it is thus a structure specific process. In the code, these three groups are represented by classes.

The `Atom` class

The `Atom` class represents single atoms on the surface lattice. Each atom is one instance of this class (or more precisely of a subclass `AtomA` or `AtomB` to differentiate between the two atom types). Atom objects include information about their location (in a `Position` object). They know to what structure they belong (by a pointer to that `Structure`) and they hold a list of all events that are available for execution upon them. Through this list, each atom object has also `static` access to the rates for each process.

The `Structure` class

Structures represent groups of linked atoms (i.e. islands). At the present stage, three types of structures exist which, programmatically, are sub-classes of `Structure`. The `Monomer` represents the structure of a single atom. The `Dimer` class represents two linked atoms and the `StableIsland` class represents all larger groups of linked atoms. All `Structure` objects have in common that they hold a list of the `Atoms` they are made of. They also hold a list of events that can happen to them with static access to the relevant rates.

The `TimeFrame` class

The `TimeFrame` class holds a list of possible time specific events. In the present state, there are only two possible time events, namely the deposition of an A-type atom or a B-type atom.

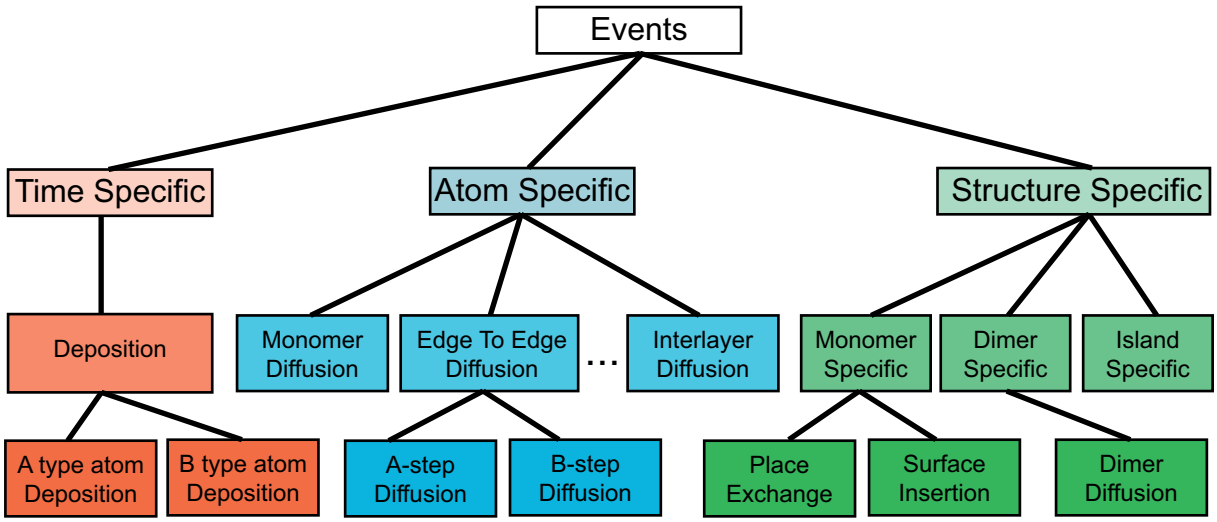

Figure 3.2: Simplified class structure of the processes which can be executed on the surface

Object-oriented structure of possible events

The class hierarchy of all possible processes is shown in Fig. 3.2. The three types of classes described above each have their associated event class from which the actual events are sub-classes. This hierarchical approach has the advantage that large parts of the code can be shared among the possible events. In particular, to implement a new event, one can subclass an existing one and only change the method in which the code changes the surface configuration. This allows for easy development of new events.

3.4 Details on some algorithms and data structures

As we pointed out above, one of the design goals, apart from easy extensibility, was the CPU and memory efficiency. The actual coding of the software was done in the C++ language. C++ is the most widely used programming language in the world. It was designed to allow low level access to the computer's resources while providing a complete OO structure. In particular, due to its large success, C++ has very efficient optimizing compilers. These compilers analyze the code and choose optimizations in order to make a faster executable. We thus believe that C++ is the best choice for this application.

Below, we present some selected algorithms, programming choices and data structures which led to a memory efficient and fast KMC model.

3.4.1 Time

The time is updated in step number 4 of the KMC algorithm presented above. The time increase in one step Δt is calculated using [26]

$$\Delta t = -\frac{\ln(U)}{\sum_i r_i} \tag{3.7}$$

[1] Central Processing Unit

where U is a uniformly distributed random variable and the r_i are the rates of all processes available at that time. From an implementation point of view, one notes that this requires to produce a random number for U and to calculate the natural logarithm of it. When considering many processes, the law of large numbers lets one write a mean time difference as the mathematical expectation of the above expression. The general form of the expected value for f, where f is an arbitrary function of X and X is a random variable with probability density function p(x), can be written as

$$\langle f(X)\rangle = \frac{\int_a^b f(x)p(x)dx}{\int_a^b p(x)dx} \tag{3.8}$$

which in our case ($f(x)=\ln(x)$, $X=U$) gives

$$\langle \ln(U)\rangle = \int_0^1 \ln(x)dx \tag{3.9}$$

$$\langle \ln(U)\rangle = (x\ln(x)-x)|_0^1 + C = -1 + C \tag{3.10}$$

That is, we can replace the exact time increment by a *mean time increment*

$$\Delta t = \frac{1}{\sum_i r_i} \tag{3.11}$$

which is much faster to calculate. By this choice, the simulation loses the stochastic character of the time component (but not of the diffusion component). This can introduce errors in the cases where very few time steps are expected in a simulation. In our application, this does not induce errors as typical simulations have 1×10^{10} time steps which validates the law of large numbers. Consequently, this implementation of a mean time was used.

3.4.2 Process selection algorithm

One of the most time consuming actions in the KMC algorithm is the selection of the process to execute. If there are 10^5 atoms on a surface, and each atom has 6 diffusion directions, one has to choose at each step between the 6×10^5 available processes proportionally to their respective rates. The usual method can be imagined in the following way. One builds a stack in memory of all possible events which can happen, with each process representing a slice of the stack. Each slice has a "thickness" proportional to the rate of the process to which it is linked. One then chooses a random number between 0 and the height of the stack and selects the process which corresponds to the random number height. This is generally done in a cumbersome way. Starting from the bottom of the stack, the random number is compared to the starting height of the next process in the stack. If it is smaller than the chosen random number, one tries the next event above in the stack. This is repeated until the correct process is found. In the simplest case where all processes have the same rate, the above example results in 3×10^5 `if` clauses being evaluated for each diffusion step on the surface.

In this work we introduce a much faster selection algorithm. One can take advantage of the fact that many processes have the same rate. We thus devise a two step selection process. First, the type of event is selected. This is done using the stack approach described above, but each slice represents all processes of a same rate. So each slice has a height $N_i r_i$ where N_i are the number of processes with rate r_i. Having selected the process type j, the programm selects one specific process in the *event list* of all j-type processes. All j-type processes have the same rate and are thus equiprobable, so the selection process can be reduced to choosing a random integer index number and taking the corresponding element out of an indexed list (i.e. a vector).

This two-step process requires two random numbers, but as we will see below, the output of a random number is (now) cheap on computing time.

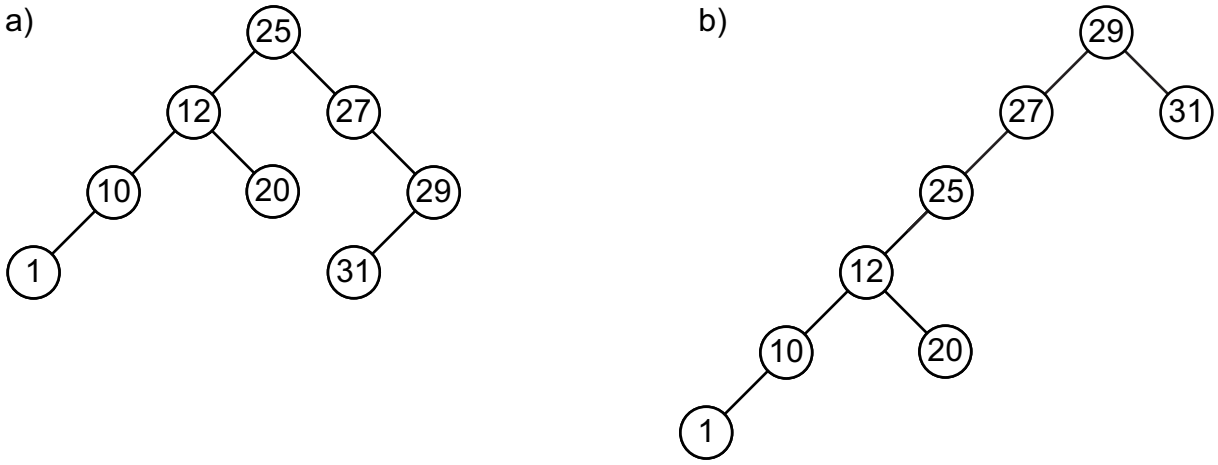

Figure 3.3: An example of binary search tree of integers.
a) A well balanced BST guarantees search times O(log(M))
b) An unbalanced BST has a worst case behavior of O(M)

3.4.3 Choosing a process type in a Binary Search Tree

In the scenario described above, once a process type j is chosen, the corresponding events list of all j-type events must be found in order to execute the second step. This is done using a map as the data structure. A map is a structure like a vector, but instead of linking an index number to each content, it links a *key* to the content. The key can be any type of data. In this case, we use the process rate r (which is simply a `double` precision number) as a key. The content is directly the list of all processes with that particular rate. A map has the particularity that it cannot contain two equal keys. This applies to our case as all rates are unique (otherwise they are counted in the same process list). Different implementations of map structures have been proposed in computer science. In this work, we use a Binary Search Tree (BST) to get the event list corresponding to the rate r_j.

A BST is a structure of nodes that contain useful data and that can each have one right child and one left child, with the particularity that an order relation is defined on the nodes (i.e. for any two nodes N1 and N2, we either have N1 $<$ N2, N1 $>$ N2, or N1 $=$ N2.). Furthermore, any node in the left subtree of a node is always less than the node itself and the node itself is less than any node in its right subtree (see Fig. 3.3). In the case of such a structure, the expected times for operations such as insertion, search and removal are all O(log(M)), where M is the number of nodes (see Refs. [27, 28] for details on the O() notation). Unfortunately, if the BST is strongly unbalanced, it can have a worst case behavior equivalent to a linear search O(M). Although self-balancing trees exist (e.g. a *Red-Black tree*), they tend to be more demanding on computer resources when insertion or removal occurs.

In the KMC case, new nodes (i.e. new rates) are added to the BST mainly at the beginning of the simulation. As soon as all processes have been possible once, the BST does not change anymore. In particular, rates which are not used because no processes are available for it at that time, are not removed from the BST. In order to guarantee a fast search in the tree, we have implemented a cyclic balancing of the BST. The BST is automatically balanced when results are output (default after 50000 moves). This guarantees the fastest search with the least CPU cost.

3.4.4 Mersenne-Twister pseudo-random number generator

The calculations of the KMC are heavily based on random numbers. Producing random numbers on a computer is generally impossible as the computer is a deterministic machine[2]. As a good approximation of a random number on the computer, one can implement an algorithm which produces a sequence of numbers which "seem" random. This method is thus called a pseudo-random numbers generator (PRNG) as the numbers are not really random. A lot of work has been devoted to finding fast algorithms producing well distributed pseudo-random numbers. Among these the algorithm `ran2` from *Numerical Recipes* [29] has for a long time been used for KMC applications.

In 1998, Matsumoto et al. [30] first published a new type of PRNG with an astronomical period of $2^{19937}-1$. This period corresponds to a Mersenne-prime number, so the PRNG was called *Mersenne-Twister*. Dimensionality checks showed that the numbers are equidistributed in 623 dimensions and the PRNG passed the *diehard test* developed by Marsaglia et al. [31]. Besides producing very high quality pseudo-random numbers, it was found to be extremely fast and low on memory usage. Our tests showed a fourfold increase in speed for the pure generation of random numbers when compared with the `ran2` algorithm. We therefore implemented the Mersenne-Twister algorithm in C++ (it was only available in C at the time of development) and gave it an object oriented programming interface. The user can also choose the random seed or use the time of day as a seed for the sequence.

3.4.5 Optimizing simple monomer diffusion

The diffusion of a monomer on the virgin surface is one of the events happening most frequently in the typical KMC simulation of a growth experiment. As has been said, after having changed the surface configuration (i.e. moved the atom), one has to update the list of all possible processes on the surface. In this work, we propose a method which does not require this costly update for the special case of monomer diffusion.

A diffusion process can be either expressed by giving the starting point and ending point of the move, or it can be written as a starting point and a direction vector. In the present KMC architecture, atom specific processes are stored inside each `Atom` object. This means that the starting position is known (as the `Atom` knows its position). A diffusion process on the clean substrate can thus be described by storing only a move direction. This has as a fortunate corollary that the process list must not be updated while the diffusing atom has no second-nearest neighbors. In fact, all diffusion processes in the list remain up-to-date even after a diffusion.

3.4.6 XML output of results

To be completely cross-platform compatible, the program outputs all results as pure text files. These include

- The list and position of all atoms on the lattice
- The list with size and center of mass of each structure (islands)
- A summary of the occurrence of each process type as a function of simulation time
- A summary of structures classified by size as a function of simulation time

In order to easily parse and extract relevant data from these text files, the XML [32] file format was chosen. XML is a text markup language which permits for a computer program as well as for a human being to read the recorded data. XML files in the KMC are written using a free and open-source code

[2] True random number generators exist which for example base their randomness on the electronic noise of a transistor.

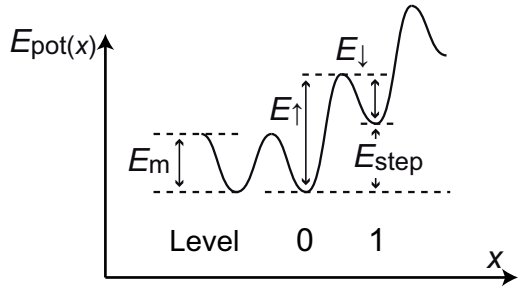

Figure 3.4: Diffusion activation barriers on the pristine substrate (E_{m}) when diffusing towards a site with lower binding energy ($E_{\uparrow}$) and when diffusing towards a site with higher binding energy $E_{\downarrow}$. The binding energy is measured by a level number and the binding energy difference between subsequent levels (E_{step})

library developed by Thomason et al. called TinyXML [33]. Various tools have been developed to calculate the mean size or the island density from output files. Output files containing the position of all atoms can also be used as an input for further simulations, for example to simulate the following three step preparation process

1. Deposition of atoms of type A at temperature T_1

2. Annealing of the previous surface at a temperature T_2 to e.g. activate border diffusion

3. Decoration of previous islands by deposition of atoms of type B at temperature T_3

The tools to render images of the resulting lattice surfaces have also been implemented. Typical results will be shown in later chapters.

3.5 Implementation of a lattice with variable binding energy

It has been shown experimentally (e.g. in Ref. [34]) that strain in the topmost surface layer of a crystal can alter the diffusion behavior of adatoms. It is suggested that the binding energy of a monomer varies on the surface as a function of its position. The effect of this binding energy difference on the diffusing adatoms is that the diffusion barrier is smaller towards stronger bound sites and higher towards more weakly bound sites. In order to account for this, a specific branch of the KMC program was developed.

In this version, each surface site holds an integer value, the binding *level*. When an adatom diffuses from one surface site to its neighbor, the corresponding diffusion rate is calculated by taking into account the difference in binding level between the sites. If this difference is 0, i.e. both sites have the same level, the diffusion happens with the normal rate corresponding to E_{m}. In contrast, if the level of the target site is higher, a higher barrier $E_{\uparrow}$ is used. Conversely, if the level of the target site is lower, a lower barrier $E_{\downarrow}$ is used. Several models can be imagined to calculate these new energy barriers as a function of the binding energy difference between the two sites E_{step} and the actual migration barrier E_{m}. We propose to calculate the two diffusion activation barriers by making the assumption that the surface potential on the pristine substrate can be modeled by a $\sin^2$ function. We also suppose that the binding energy varies locally from one site to the next with the shape of a cosine. We can then write the potential $E_{\mathrm{pot}}(x)$ as a function of the position x ($x = 0$ and $x = 1$ are

adsorption sites) and conclude about the activation barriers.

$$E_{\text{pot}}(x) = \overbrace{E_{\text{m}} \sin^2(\pi x)}^{\text{surface potential}} + \overbrace{\frac{1}{2} E_{\text{step}} (1 - \cos(\pi x))}^{\text{change in binding energy}} \tag{3.12}$$

$$E_{\uparrow} = \max\left(E_{\text{pot}}(x)\right) = E_{\text{m}} \left(\sin\left(\arccos\left(\frac{E_{\text{step}}}{4E_{\text{m}}} \right) \right) \right)^2 + \frac{E_{\text{step}}}{2} \left(\frac{E_{\text{step}}}{4E_{\text{m}}} + 1 \right) \tag{3.13}$$

$$E_{\downarrow} = \max\left(E_{\text{pot}}(x)\right) - E_{\text{step}} = E_{\text{m}} \left(\sin\left(\arccos\left(\frac{E_{\text{step}}}{4E_{\text{m}}} \right) \right) \right)^2 + \frac{E_{\text{step}}}{2} \left(\frac{E_{\text{step}}}{4E_{\text{m}}} - 1 \right) \tag{3.14}$$

Note that a requirement in these equations is that $E_{\text{step}} < 4E_{\text{m}}$. This is not a stringent requirement because the kinetic Monte-Carlo simulation assumes transitions between energetically well defined adsorption sites. If the energy step from one site to the next is so large, this assumption will no longer hold true for the physical system being simulated. These barriers and the corresponding rates are calculated once at the start of the simulation, thus they do not impose any particular cost on the execution time.

By giving E_{step} as a parameter and feeding the program with a preconceived lattice of levels, one can change the potential surface at will and thus simulate any geometry of repulsive or attractive regions.

3.6 Conclusions & Outlook

The goals set out at the beginning of the project, namely CPU efficiency and extensibility, were achieved. The table below shows a speed and memory comparison between different versions of the code, including a previously available KMC code from the Technical University of Denmark (TUD). All codes were compiled using the `icc` *intel* compiler including the `-O3` optimization option and run on a dedicated 2.4 GHz processor Linux machine. The running parameters were those for Ag/Pt(111), namely $E_{\text{m}} = 160\,\text{meV}$, $E_{\text{attach}} = 100\,\text{meV}$, $E_{\text{interlayer}} = 10\,\text{meV}$, $\nu_0 = 1 \times 10^{13}\,\text{Hz}$ on a 2000×2309 lattice with a coverage $\Theta = 0.1\,\text{ML}$ and a deposition flux $F = 0.001\,\text{ML/s}$ at a temperature $T = 116\,\text{K}$ ($k_B T = 10\,\text{meV}$).

	TUD[a] 1.0	TUD[b] 2.1	EPFL[c] 2.55.0	EPFL[d] 2.75.7	EPFL[e] 3.00.17	EPFL[f] 3.03.5	EPFL[g] 3.04.6
Memory [MB]	788	924	124	124	1005	1005	1005
Processes [10^6 proc]	535	530	597	537	538	533	538
Execution time [s]	1513	1295	1240	674	1039	1049	1055
Process speed [10^6 proc/min]	21.2	24.5	28.8	47.8	31.1	30.5	30.6
Islands	1402	1400	1372	1391	1411	1362	1381

[a] Original code from TUD including all border diffusion processes
[b] Code from TUD including all of [a] and additionally exchange
[c] First version of new code (stable and completely ANSI-C++ compatible)
[d] New code including all border diffusion processes, exchange, differentiated attachment to different monomer types, selectable ending condition (deposition, time), new random number generator and diverse speed optimizations
[e] New code including all of [d] as well as a lattice with variable binding energy and insertion process
[f] New code including all of [e] as well as dynamic growth of repulsive dislocations. Dislocation growth takes place by insertion at the dislocation *tip*
[g] As [f] but dislocation growth takes place by insertion at the dislocation *sides*

The table shows that for equivalent simulation features (compare ^{b} and ^{d}), our new code has a 7 times smaller memory footprint and a twofold process speed increase when compared to the previously available program. The implementation of the locally variable binding energy surface (versions $^{e-g}$) heavily increases the used memory but has only a small impact on process speed. These versions also show that the structure is readily extensible as many new features have been added since the original version. The modified versions will be presented in more detail in subsequent chapters when they become relevant from the experimental perspective.

As an outlook, we present here possible extensions to the present code which could be implemented in future versions.

- Inclusion of hcp type sites
- Addition of a desorption process
- Addition of an upwards interlayer process to permit simulation of Volmer-Weber 3D growth
- Parallelization of the code
- Simulating the growth of compact islands without the need for edge diffusion

This last point is particularly interesting when studying e.g. island densities for which the precise morphology is not of interest. In fact, compact clusters are necessary in order to achieve the correct capture behavior of the islands but activating diffusion for all edge atoms is very computing-time intensive with little gain, if the morphology is not a central result. An algorithm could be applied which upon aggregation of an adatom to an island would automatically place this atom in the correct location for a compact island. Obviously, this approach could be extended to 3D clusters to simulate systems at thermodynamic equilibrium. In this case, the equilibrium shape of clusters would be given as an input to the simulation. Equivalently, this same approach could be used to simulate kinetically limited systems by giving the final cluster shape as an input and thus saving the computing time for upward and downward interlayer diffusions. Naturally, this algorithm supposes that the final cluster shape is known or can be extracted from experiment.

Furthermore, KMC is an algorithm which lends itself perfectly to parallelization. With our design choices, it is no longer the lattice size with its large memory which is the limiting factor but rather the computing time. In this case, parallelization means to adapt the algorithm so that several processors can work on a same lattice at the same time.

Chapter 4

Co/Pt(111): Growth and nucleation on a surface unstable towards reconstruction

Due to the broken symmetry at the interface, the (111) surfaces of the fcc transition metals Ir, Au and Pt are known to favor shorter in-plane bond lengths compared with the bulk. This puts the surface under tensile stress [35, 36]. Partially relieving the stress by adding atoms in the first layer tends to lower the surface energy promoting surface reconstruction. This process is in competition with two factors which favor an unreconstructed first layer: 1. The energetic cost of dissociating an atom from a step and inserting it and 2. The lower bonding energy of a reconstructed first layer compared with the pseudomorphic layer [37]. The insertion cost can be substantially reduced by providing a continuous supply of weakly bound adatoms from a supersaturated gas phase, thus increasing the number of potential insertion candidates and saving the energy to dissociate adatoms from a step. In particular, the Pt(111) surface has been observed to reconstruct at 400 K [38] (see Fig. 4.27), instead of 1330 K [39], in the presence of a supersaturated Pt gas and at room temperature in the presence of Co adatoms [40, 41]. As such, Co/Pt(111) is a model system for the study of nucleation and growth on a surface unstable towards reconstruction.

Lately, the system cobalt on platinum (111) has attracted much attention because of its remarkable magnetic properties. Gambardella et al. have demonstrated that single cobalt atoms on a platinum surface have a giant magnetic anisotropy energy (MAE) of 9 meV per atom compared to 0.045 meV/atom for bulk hcp-Co or 0.9 meV/atom for the $L1_0$ CoPt alloy [10]. It has also been shown that monatomic Co chains exhibit long range ferromagnetic order below 15 K while breaking up into domains for higher temperatures [42]. For cobalt islands on the Pt(111) surface, it has been shown that the island border atoms are responsible for the out of plane direction of the easy magnetization axis. The border atoms show a MAE 20 times higher than other surface or bulk atoms [43]. This newly acquired understanding of magnetism gave rise to the large interest in Co/Pt as a model system for investigation of future magnetic recording media.

All nanostructures studied in the results cited above were obtained by self-assembly of Co atoms. Typically one wants to attain a known and predefined spatial ordering, size distribution and morphology of the islands in order to simplify and clearly distinguish among the properties of the system. The main parameters which can be set in order to influence the auto-organized growth are:

- Substrate surface element, crystallographic index and morphology
- Substrate temperature during deposition T_{dep}
- Annealing time and temperature
- Flux F and coverage Θ of deposited adatoms

- Order and type of preparation steps

To choose these parameters efficiently for a given desired morphology, one needs a model of the physical processes taking place at the surface. In this chapter we present submonolayer growth experiments of cobalt on Pt(111) at deposition temperatures T_{dep} between 50 K and 340 K. We show that the topmost Pt(111) surface layer undergoes a transition from pseudomorphic to incommensurate with respect to the bulk for $T_{\mathrm{dep}} \geq 180$ K. At similar deposition temperatures, the island density deviates from all known nucleation models. Using Kinetic Monte-Carlo (KMC) and Rate Equation (RE) models, we show how this reconstruction induced strain affects monomer diffusion and how the reconstruction evolves dynamically in parallel with the growth process.

4.1 Experimental procedure

The experiments were performed in a UHV chamber with base pressure below 3×10^{-11} mbar equipped with a variable-temperature (40–800 K) scanning tunneling microscope (STM). The Pt(111) surface was prepared by repeated cycles of Ar-ion sputtering (1 keV, 0.3 μA) at room temperature and at 800 K followed by annealing in O_2 atmosphere at 800 K and flash to 1300 K. Prior to Co deposition at low temperatures, the sample was flashed to 800 K to desorb any residual gas which may have adsorbed on the surface. Co atoms are deposited by molecular beam epitaxy (MBE) using a commercial e-beam evaporator from a thoroughly outgassed Co rod (purity 99.995%, Alfa-Aesar). The deposition flux was $5\cdot10^{-3}$ ML/s where a monolayer (ML) is defined as the density of atoms in one bulk Pt(111) layer ($=0.15\,\text{Å}^{-2}$). The sample was cooled down to measurement temperature T_{mes} immediately after deposition ($T_{\mathrm{mes}} < 0.9\cdot T_{\mathrm{dep}}$) to quench any post-deposition evolutions. Furthermore, the sample temperature was measured by contacting a K-type thermocouple directly on the sample resulting in an absolute temperature error $\delta T < 0.1$ K. The experimental measurements were performed in collaboration with S. Rusponi and E. Vargoz.

4.2 STM data

In order to study the growth kinetics at the island saturation level we deposited 0.12 ML Co at temperatures $50\,\text{K} < T_{\mathrm{dep}} < 340\,\text{K}$. Fig. 4.1 shows the evolution of island shape and density as a function of deposition temperature T_{dep}. We see that the island density and the morphology changes. For T_{dep} below 100 K, a high density of small, compact and nearly circular islands is observed. For deposition temperatures between 100 K and 200 K, the cobalt islands are more ramified and the density is reduced. For temperatures in the range $200\,\text{K} < T_{\mathrm{dep}} < 310\,\text{K}$, the island get compact and triangular. Finally for higher temperatures, the Co forms dendrites coexisting with compact triangular single and double layer islands as has been observed before [40, 44, 41].

In order to measure the "compactness" of this islands, we can study the perimeter length p (in atom diameters) as a function of island size s (in atoms). The surface area and perimeter length is measured on the STM images at half height between the Pt surface level and the Co island level. To get the perimeter in atoms, the length is divided by the Pt-Pt (111) interatomic distance $a = 2.77\,\text{Å}$.[1] The number of atoms per islands is calculated by dividing the surface (in Å^2) by the Pt(111) atomic cell $c = 6.67\,\text{Å}^2$. For islands with one atom wide regions, like atomic chains or pure diffusion limited aggregation islands, the ratio p/s has a systematic error, because the perimeter is measured as the outer length of the island. For example, a dimer would have $s = 2$ but $p = 6$ (each atom shows

[1] The cobalt islands are supposed pseudomorphic to the Pt surface layer and thus adapt to its interatomic distance. The limit of this supposition is commented below.

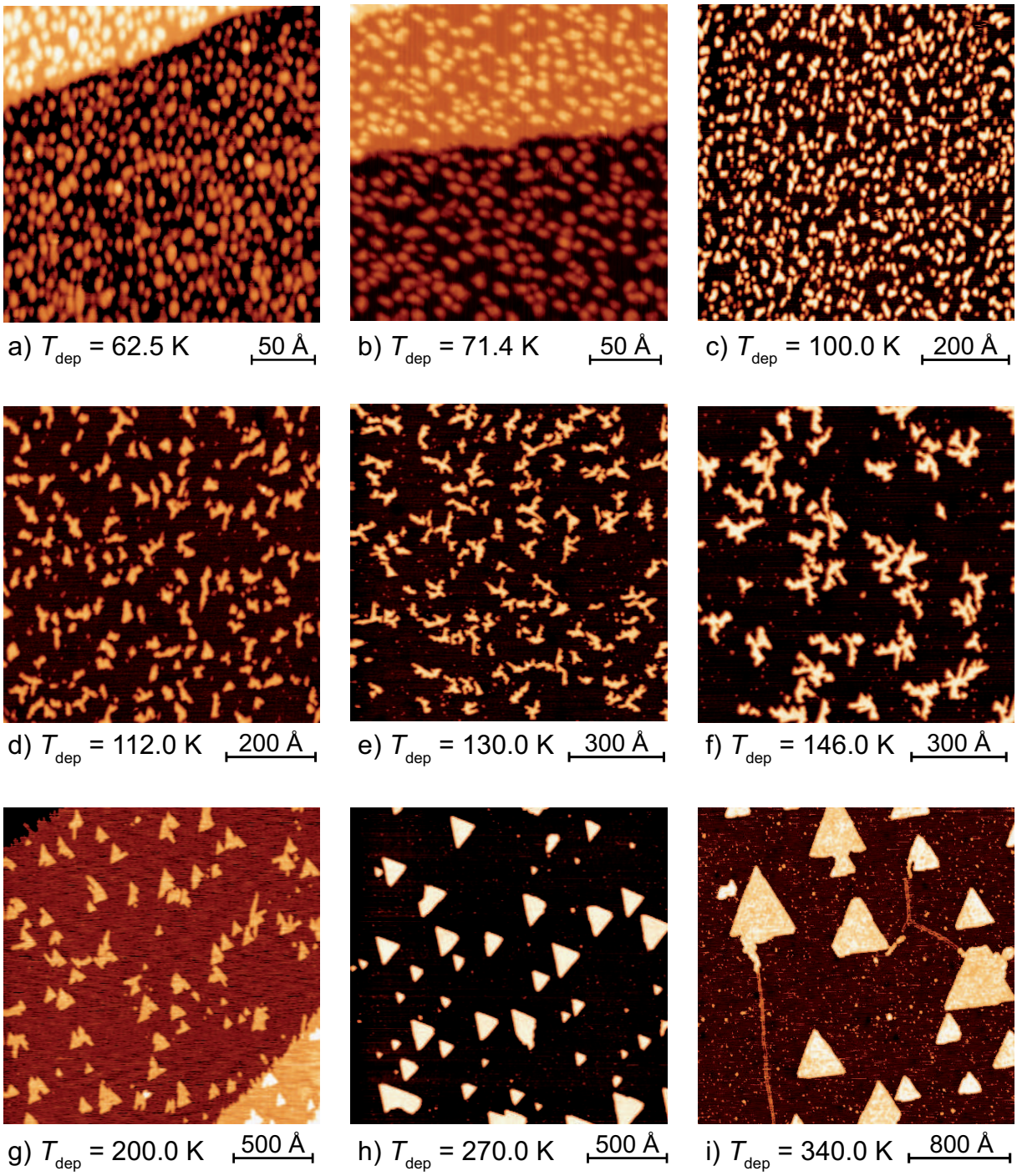

Figure 4.1: STM images of 0.12 ML Co deposited on clean Pt(111) at diverse deposition temperatures T_{dep}. The island morphology evolves from small compact islands for $T_{dep} < 70$ K to ramified islands in the temperature range $100\,\text{K} < T_{dep} < 200\,\text{K}$ to compact triangular islands for $T_{dep} > 200$ K. Above $T_{dep} = 310$ K the deposited cobalt forms dendrites and islands consist of a double layer.

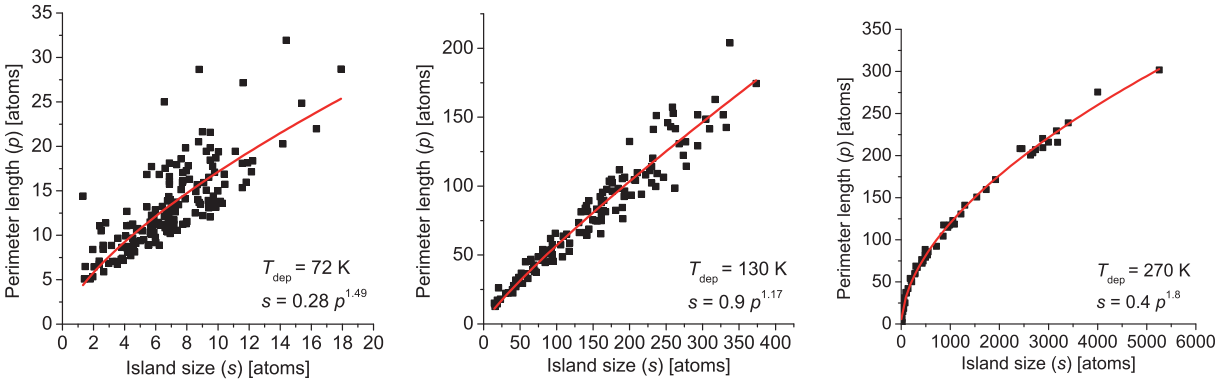

Figure 4.2: Island perimeter length as a function of size for 3 deposition temperatures. Each distribution is fitted with a test function $s = \alpha p^{\beta}$, where β measures the order of ramification ($\beta = 2$ for islands keeping aspect ratio while growing) and α is related to the border atoms proportion.

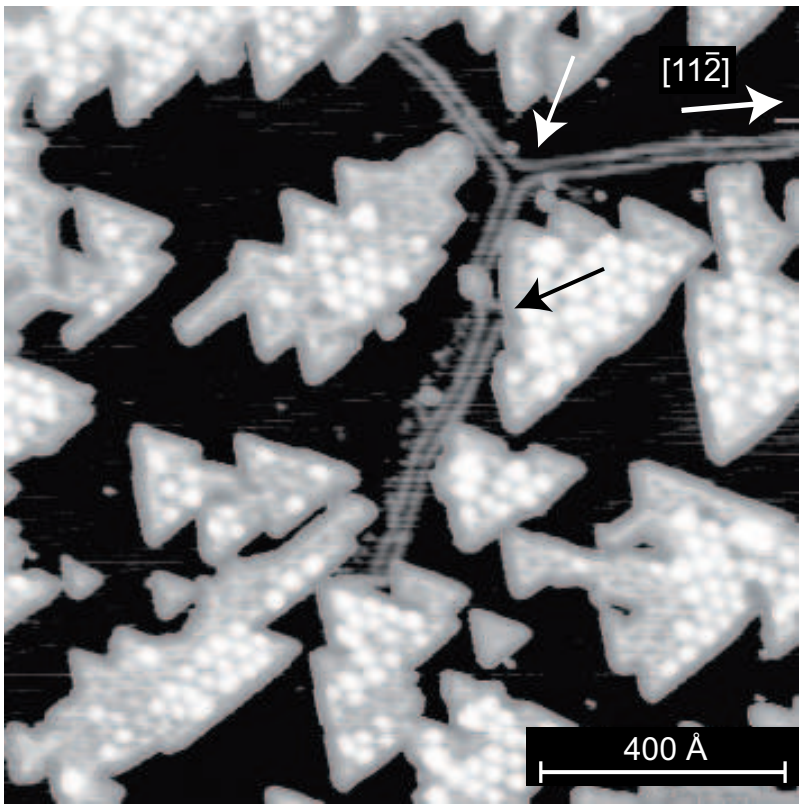

Figure 4.3: STM topograph of 0.7 ML Co deposited on Pt(111) at $T_{\text{dep}} = 200$ K. The image shows the Co induced Pt(111) surface reconstruction appearing as bright double lines. These lines are partial dislocations which extend in the $\langle 1\,1\,\bar{2} \rangle$ directions starting from a center point. Two such centers are indicated by arrows.

three atomic lengths to the perimeter). This error is reduced for islands with no regions of width one. Fig. 4.2 shows the plots of perimeter vs. size distribution for three characteristic temperatures. We can fit this distribution with the test function $s = \alpha p^{\beta}$. The two free parameters, α and β are a good measure for ramification. β measures the power law between perimeter atoms and surface atoms. All shapes which conserve aspect ration, or in other words which "scale", have $\beta = 2$. Typical examples are the circle where $s = \frac{1}{4\pi} p^2$ or the square with $s = \frac{1}{16} p^2$. A corresponding example where the aspect ratio is not conserved is a rectangle with one fixed length side $x = 1$ and one variable side y. In this case, $s = \frac{p}{2} - 1$ and we have a simple linear relationship. α is a measure of the ratio of perimeter atoms to surface atoms.

Using this fit we can quantify the ramification of the three growth stages described above. The small compact islands which form at low temperatures have a relation $s = 0.28\ p^{1.49}$ at 72 K, for the ramified islands we get the relation $s = 0.9\ p^{1.17}$ at 130 K and the triangular, compact islands show a behavior $s = 0.4\ p^{1.8}$ (for 270 K). This measure has the biggest error when fitting low temperatures and thus very small islands. Firstly, because for small islands the STM tip convolution is more relevant, and so the measured perimeter length has an offset versus the actual perimeter length. Secondly, because very small islands may show the systematic error described above in one atom wide regions. This second error decreases very rapidly with larger islands sizes.

Taking into account these two limitations for the value at 72 K, we can conclude that at intermediate temperatures (100 K–200 K) the ramification is maximum, with most atoms on the border. At 130 K, the evolution of size versus perimeter atoms is nearly linear, with exponent $\beta = 1.17$.

Fig. 4.3 shows 0.7 ML Co/Pt(111) deposited at 200 K. At this higher coverage, small Co islands (bright white) nucleate on top of large, one atom layer thick Co islands. We observe that the shape and placement of these second layer islands are not random. They form an approximate trigonal lattice with lattice constant 27 Å. Moreover, the second layer islands seem not to be equally distributed on the area of the underlying island, but to favor growth in bunches. While these island bunches form, coalescence is notably absent. The shape of these islands seems to favor equilateral triangles with faces rotated by 180° with respect to the first layer triangular islands. An analysis of this data is presented below in section 4.11.1.

Fig. 4.3 also shows bright double lines with an apparent height of 0.2 Å on the Pt(111) surface. The two lines are separated by 20 Å and have lengths up to a few hundred Å. They extend like three branched stars in the threefold $\langle 1\,1\,\overline{2}\rangle$ directions starting from a common center and end preferably at a Co island or a step edge, while a few abrupt endings on the flat terrace are also observed. Detailed analysis shows that *two* such star centers appear on the image (see arrows) and that the line pointing to the bottom of the image is not continuous but made of two separate arms belonging to two different stars. These double lines are attributed to the Pt(111) surface reconstruction reported in Refs. [40, 41]. We observe this reconstruction for T_{dep} above 180 K which is well below the 300 K previously published. The shape of the islands which grow close to the dislocation lines is influenced by their presence since the islands do not cross the double lines. This indicates that the dislocations form early in the growth process and that growing islands adapt to them. Presumably the dislocations have a repulsive effect on diffusing species. This idea will be developed in Sect. 4.10. Moreover, the straightness of the lines seems to be little affected by the presence of the islands.

Fig. 4.4 shows a chemically resolved STM image of a double dislocation line taken by Lundgren et al. [41]. The sample has been prepared by depositing 0.1 ML Co/Pt(111) at $T_{\mathrm{dep}} = 400$ K followed by 0.1 ML at $T_{\mathrm{dep}} = 300$ K. Cobalt atoms (see arrows and large part on the upper left corner) on the image have a lower apparent height than platinum substrate atoms and thus appear darker. From this image it becomes clear that one *inserted* Co atom for each Pt atom row in the $\langle 0\,1\,\overline{1}\rangle$ is responsible for the visible dislocation. We also note that inserted atoms are not homogeneously distributed on the surface, but that insertion is preferred near the dislocation. This suggests that the dislocation grows

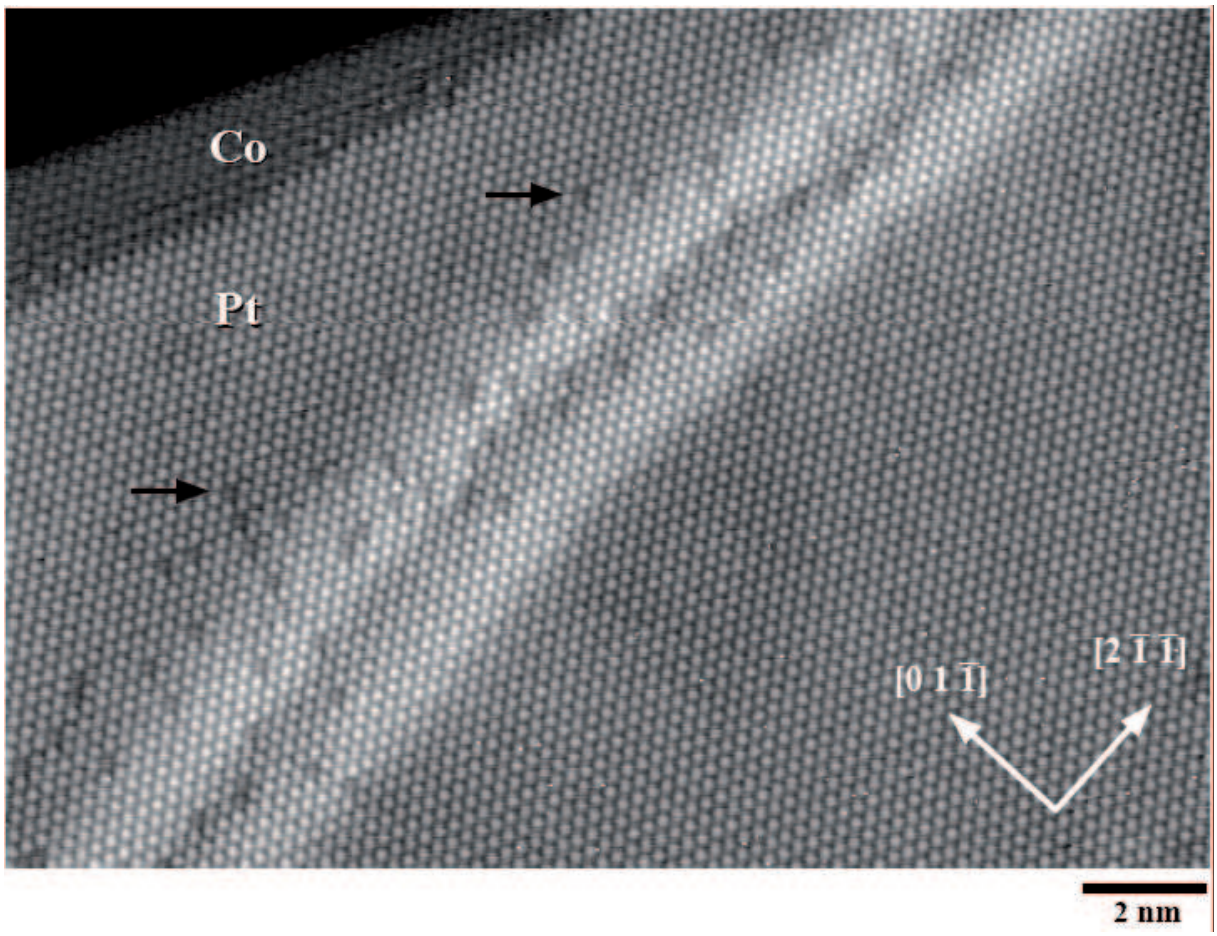

Figure 4.4: 0.1 ML of Co deposited at 400 K followed by 0.1 ML Co deposited at 300 K on Pt(111). Chemically resolved STM image of the double line reconstruction. Darker Co atoms attached to the Pt step edge due to the second Co evaporation can be seen in the upper left corner. Two of the Co atoms in the double line reconstruction are indicated by arrows. The image size is $200 \times 150\,\text{Å}^2$. From [41]

by insertion of atoms at its edge. The reconstruction is formed by pairs of partial dislocation with burgers vector $\frac{1}{2}\langle 0\,1\,\bar{1}\rangle$. The dislocations separate large pseudomorphic fcc stacked regions from hcp stacked regions in between the dislocations.

At deposition temperatures above 310 K, the system changes its growth mode. Long dendrites are observed with an apparent height equal to that of cobalt islands. The dendrites form along the dislocation lines in the Pt substrate. This high temperature regime has been studied before in Refs. [40, 41] so we will concentrate on the lower temperature regime.

We will now study the island densities extracted from the STM data above in order to further understand the growth of Co/Pt(111).

4.3 Island densities

Studying the island density gives insight into the energy barriers involved in the diffusion of species and growth of islands [45]. Fig. 4.5 a) shows the Arrhenius plot of the island density (squares) as a function of inverse temperature as derived from STM images. The plot shows the density of the sum

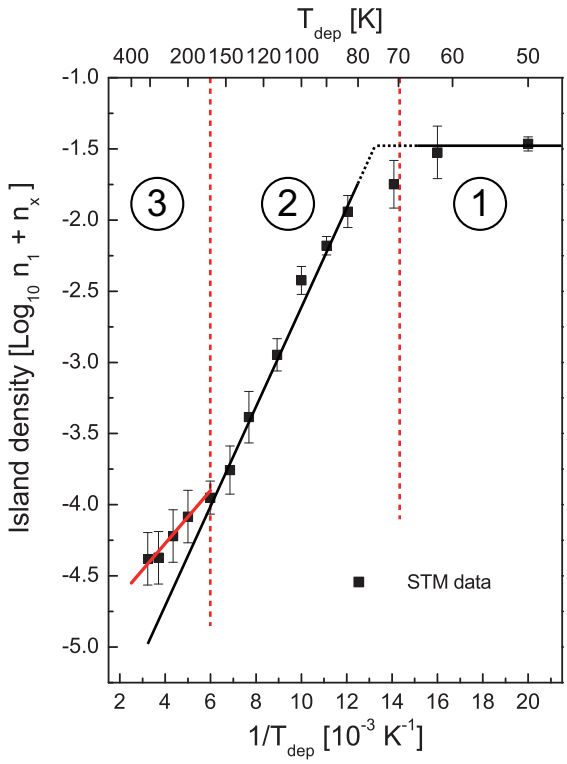

Figure 4.5: Arrhenius plot of 0.12 ML Co deposited on clean Pt(111) with a flux $F = 5 \times 10^{-3}$ ML/s. Data extracted from STM images (squares) represent the density of both, stable islands (n_x) and monomers (n_1), as it is not possible to differentiate between these on the images. The plot shows three regions: 1) At low temperature $T_{\text{dep}} < 70$ K the island density is approximatively constant. 2) Between 70 K and 170 K, the island density follows a constant slope in the Arrhenius representation as expected from nucleation theory. 3) At higher temperatures but $T_{\text{dep}} < 310$ K, the island deviates with a constant, shallower slope. Continuous lines are guides to the eye.

of stable islands and monomers as one cannot easily distinguish between the two on STM images. The plot shows three regions. These are emphasized by the straight lines as a guide to the eye. In the temperature range 50–70 K the island density ($n_x + n_1$) remains roughly constant. The monomer diffusion is frozen on the time-scale of the experiment. Between 70 K and 170 K and between 170 K and 310 K the island density follows a linear behavior with two distinct slopes.

4.4 Behavior below 70 K

At 50 K the mean island size is $\langle s \rangle = \frac{\Theta}{n_x+n_1} = 3.4$ atoms. This should correspond to the *statistical growth* regime. When the deposition temperature is low enough, thermally activated diffusion is frozen and stable islands can only be created by direct impingement of adatoms incoming from the gas phase beside or on top of already adsorbed adatoms. As such the island density and mean island size is purely a function of coverage Θ. This case has been simulated before by KMC and the variable $\langle s \rangle$ has been determined as a function of Θ (see Fig. 7 in Ref. [45]). The expected mean island size for 0.12 ML in the pure statistical growth case is $\langle s \rangle = 1.6$ atoms. However, our experimental value is twice as high as the theoretical calculated value.

The higher mean island size suggests two possible explanations. First, the Co monomer may experience transient mobility while reaching thermal equilibrium with the surface. During deposition, the Co monomers have an intrinsic kinetic energy due to the deposition flux. Adding to this, the monomer gains several eV binding energy upon adsorption. This energy, if thermalization is not immediate, could result in a few non-thermal diffusion steps, leading to a higher mean island size. Up to now, there exists no direct evidence by atomic-scale observations for a metal on metal system that such transient mobility exists. Furthermore, all systems for which such experiments where performed exclude transient mobility suggesting that the energy transfer from the incoming adatom to the surface is nearly immediate [46].

Alternatively, neighbor driven mobility can result in a higher mean island size. Several experiments [47, 48] suggest that diffusion on the flat terrace differs from the diffusion towards a neighboring adatom, step or island. The proposed interpretation is that the binding energy for an adatom in a onefold lateral-coordinated site is higher by the value of the dimer binding energy when compared to the uncoordinated monomer. This higher binding leads to a lowered diffusion barrier for the last or several last steps towards attachment. This has been called *easy attachment*.

From our experimental values it is not possible to distinguish between the two effects. In order to separate between non-thermal transient mobility and thermally activated easy attachment, measurements at lower temperature are required. In this case, if the increased mobility is due to the lowering of the diffusion barrier, the mean island size will eventually reach the value expected for statistical growth.

Supposing a hopping attempt frequency $\nu_0 = 1 \times 10^{14}$ Hz we can calculate an upper bound for the neighbor induced lower diffusion barrier. We perform KMC simulations of the growth of 0.1 ML including a modified diffusion barrier for the last step towards attachment. Normal diffusion on the flat terrace is not activated. As can be seen in Fig. 4.6, the mean island size as a function of attachment barrier makes a transition from pure statistical growth $\langle s \rangle = 1.6$ atoms (67 % monomers, 20 % dimers, 8 % trimers) to easy attachment $\langle s \rangle = 2.7$ atoms (31 % monomers, 25 % dimers, 17 % trimers, 10 % tetramers). The experimental mean island size of 3.4 atoms suggests that at 50 K the system is completely in the easy attachment case. We can thus give an upper-bound for the easy attachment energy barrier: $E_{\text{attach}} < 120$ meV. Effective Medium Theory (EMT) calculations estimate the attachment barrier to 60 % of the terrace diffusion barrier [49, 50, 51]. This is in excellent agreement with our value (see below for the determination of the terrace diffusion barrier, $E_{\text{m}} = 200$ meV). We note from the simulation perspective that the easy attachment model is equivalent to the 1-step transient

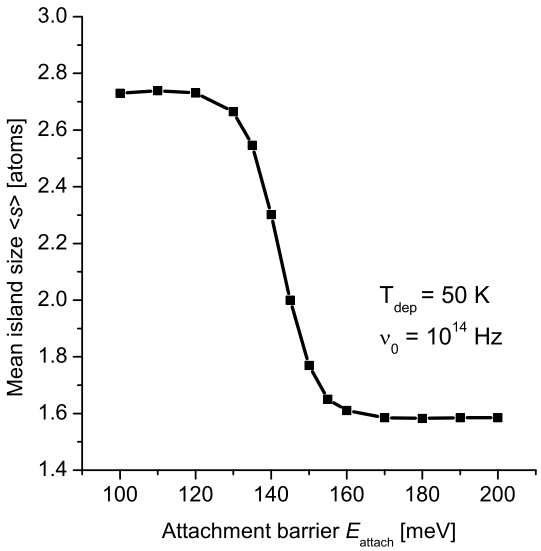

Figure 4.6: KMC simulation of the mean island size as a function of attachment barrier in the case of statistical growth of 0.1 ML Co/Pt(111) at 50 K (frozen monomer diffusion on the flat terrace) with a flux $F = 5 \times 10^{-3}$ ML/s. Only the last step towards an attachment is authorized with an activation energy E_{attach}. Corresponding experimental data indicate a mean size $\langle s \rangle = 3.4$ atoms leading to the conclusion that the easy attachment barrier for Co/Pt(111) has an upper bound at $E_{\text{attach}} < 120$ meV.

mobility.

We note that the experimental mean island size $\langle s \rangle = 3.4$ atoms is still larger than the one obtained in the KMC model $\langle s \rangle = 2.7$ atoms. Two possible explanation come to mind. First, the STM measurements are done during several hours. The 31 % remaining monomers may diffuse during this time, even if the measurement temperature is lower than the deposition temperature, and thus attach to existing islands, which increases the mean island size. Our KMC simulations show that this effect is negligible, the monomer diffusion is really "frozen" and its occurrence probability is very small, even when measuring for several hours. This comes as no surprise as the temperature has an exponential effect on diffusion probability, while the time is only linear. Second, the perturbation of the migration barrier by the higher binding energy at a coordinated site may span more than one site. This is the explanation given by Wang et al. [47] for the monomer vacancy regions observed for Ir/Ir(111) around clusters. Transient mobility with more than one site diffusion, would yield comparable results. To support this claim we model the system by rate equations (RE) without any diffusion term. As we want to model in an exact way island sizes between one and three atoms, we write the equations for

these species. The coupled equations to solve are then:

$$\begin{aligned}
\frac{\mathrm{d}n_1}{\mathrm{d}t} &= F - 2\kappa_1 F n_1 - \kappa_2 F n_2 - \kappa_3 F n_3 - \pi F \left(\sqrt{\frac{Ft - \sum_{s=1}^{3} s\, n_s}{\pi n_x}} + 1 \right)^2 \\
\frac{\mathrm{d}n_2}{\mathrm{d}t} &= \kappa_1 F n_1 - \kappa_2 F n_2 \\
\frac{\mathrm{d}n_3}{\mathrm{d}t} &= \kappa_2 F n_2 - \kappa_3 F n_3 \\
\frac{\mathrm{d}n_x}{\mathrm{d}t} &= \kappa_3 F n_3
\end{aligned} \tag{4.1}$$

where κ_s is the geometric capture cross section of a cluster of size s for a monomer coming from the gas phase. Taking the monomer as an example in the simplest hit&stick model, an adatom coming from the gas phase will form a dimer if it lands directly on previously adsorbed atom or on one of the six sites around it. Thus, the cross section is $\kappa_1 = 7$. In the case of easy attachment, all atoms arriving on second nearest neighbor sites will eventually form a dimer, the corresponding parameter is then $\kappa_1 = 19$ because there are 6 nearest neighbors and 12 second nearest neighbors. By these simple geometric considerations one can find the corresponding κ for the dimer and the trimer in the three cases which are of interest here, namely hit&stick, easy attachment from nearest neighbor and attachment from second nearest neighbor. The trimer has three possible configurations with different κ which are presented below.

	Compact trimer	κ_3 (sum)	In-line trimer	κ_3 (sum)	Angled trimer	κ_3 (sum)	Mean κ_3
Cluster atoms	3		3		3		
Nearest neighbors	9	12	10	13	10	13	13
Second nearest neighbors	15	27	16	29	16	29	28
Third nearest neighbors	21	48	22	51	22	51	50

Table 4.1: Number of nearest neighbor sites for possible configuration of a trimer.

Solving the rate equations for a final coverage of 0.12 ML gives the mean sizes presented in the table below.

	κ_1	κ_2	κ_3	$\langle s \rangle$	KMC $\langle s \rangle$	STM $\langle s \rangle$
Hit & stick	7	10	13	1.55	1.56	
Easy attachment from second nearest neighbor	19	24	28	2.74	2.74	
Easy attachment from third nearest neighbor	37	44	50	**3.65**		3.4

We first note the excellent agreement of the rate equation approach when compared with the *exact* KMC simulation. In both cases, i.e. without any easy attachment (pure statistical growth) and with easy attachment from the second nearest neighbor sites, the difference in mean size is below 1%. This gives us confidence in the rate equation approach when calculating the case with third order nearest neighbor easy attachment. The calculation results in a mean size of 3.65. This is very close to the experimentally measured value of 3.4 which strongly supports that Co adatoms on the surface lower the diffusion barrier for diffusing Co monomers up to the third nearest neighbor site. The remaining difference between the two values can be explained in the following way. In the RE model, all atoms falling in the 2-site vicinity of an existing cluster are funneled to attach to it. This picture is somewhat biased, as in reality the diffusion barrier towards the island is probably distance dependent and

monomers landing on third nearest neighbor sites will still have a lower probability to attach than monomers arriving on second nearest neighbor sites. Also, the rate equation approach as presented above does not take into account island-island correlation. The capture zones of each island is always totally effective, while from atomic simulation we know that close islands will have overlapping capture zones, so capture should be less effective and produce a lower mean size. Finally, in order to exclude any unknown parameters from the equations, we have neglected coalescence. Coalescence could be accounted for in the equation but would require an unknown parameter measuring the effectiveness of coalescence. This approximation introduces only a small bias as coalescence is nearly negligible for a coverage of 0.12 ML.

4.5 Homogeneous monomer diffusion

The lowering of the island density above $T_{\mathrm{dep}} = 70$ K (region 2 in Fig. 4.5) clearly establishes the onset of long range diffusion (as opposed to easy attachment). In order to get a quantitative understanding of the Co migration we apply three different models to the island density: scaling law (Eq. 3.5), kinetic Monte-Carlo (KMC) as well as more elaborate rate equation (RE) simulations. The three models presented are valid only in the complete condensation case.

Complete condensation is generally expected for transition metal heteroepitaxy [46]. We can experimentally confirm complete condensation for Co/Pt(111) in the studied temperature range because the deposited coverage does not depend on deposition temperature. As an alternative argument, DFT calculations in the local density approximation (LDA) estimate the total cohesive energy for Co monomers on Pt(111) to $E = 5.5$ eV [52]. Although this value suffers from systematic errors, we can still use it as a reference. The corresponding desorption temperature is $T_{\mathrm{desorp}} \approx 3600$ K when using a prefactor $\nu_{0\,\mathrm{desorp}} = 10^{14}$ Hz. Further details on how this calculation is done are given in Chapter 6.6.2 on page 109. Needless to say, the realization of this desorption experiment is impossible due to the tendency of Co adatoms to diffuse into the Pt bulk for deposition temperatures above 375 K and to form a bulk alloy [53, 54].

We also assumed irreversible growth which is valid only if the critical cluster size is $i = 1$. The critical cluster size is defined as the size at which a cluster becomes stable upon incorporation of one extra atom. The assumption $i = 1$ is justified for three reasons:

1. The experimental size distribution at $T_{\mathrm{dep}} = 130$ K shown in Fig. 4.7 matches the theoretical one calculated by KMC by Bartelt and Evans [23] for $i = 1$. Particularly, one notes that the mode (i.e. the maximum) of the experimental size distribution has a normalized value of ≈ 0.7, where a value of 1.2 would be expected for $i = 2$.

2. The slope change towards a steeper slope expected at the transition between $i = 1$ and $i > 1$ [45] does not occur in the Arrhenius plot.

3. Annealing experiments presented below in Section 4.12 suggest that the dimer is stable at least up to 200 K [55].

4.5.1 Calculating the migration barrier from the scaling law

In order to extract the relevant parameters, we fit the scaling law equation for stable dimers ($i = 1$) to the STM data island density with the migration barrier E_{m} and the attempt frequency ν_0 as fit parameters. The stable island density using the constant approximation $\eta(\Theta) = 0.25$ is then

$$n_x = 0.25 \left(\frac{D}{F}\right)^{-1/3} \tag{4.2}$$

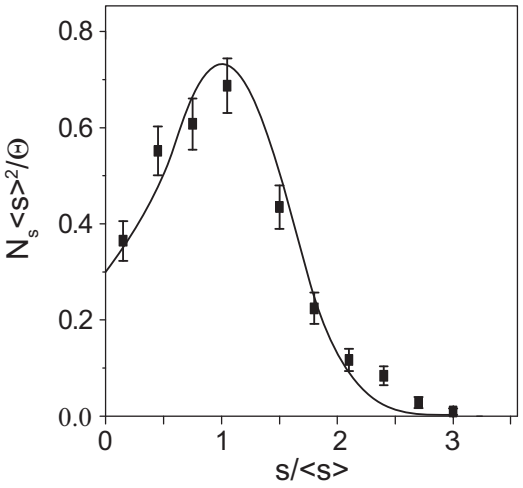

Figure 4.7: Normalized island size distribution for 0.12 ML deposited at 130 K. The island size s is normalized to the mean size $\langle s \rangle$. The count of islands of size s, N_s is normalized to yield a total integral of 1.

with

$$D = \frac{1}{4}\, \nu_0 \exp\left(\frac{-E_\mathrm{m}}{kT}\right) \tag{4.3}$$

The fit is shown in Fig. 4.8 (red continuous line). It is obtained for $E_\mathrm{m} = (200 \pm 10)$ meV with a prefactor $\nu_0 = 3 \times 10^{14\pm0.5}$ Hz. This value for the migration barrier is sensible when compared to $E_\mathrm{m} = 260 \pm 10$ meV [56] and $E_\mathrm{m} = 260 \pm 3$ meV [57] for Pt(111) homoepitaxy or $E_\mathrm{m} = 157$ meV for Ag/Pt(111) [58]. The corresponding prefactor is high when compared with the two other systems. Pt/Pt(111) has a prefactor $\nu_0 = 5 \times 10^{12}$ Hz and Ag/Pt(111) has a prefactor $\nu_0 = 1 \times 10^{13}$ Hz. To demonstrate that this difference is significant and cannot be accounted for in error bars, we show the effect of a prefactor of $\nu_0 = 1 \times 10^{14}$ Hz with the continuous black line in Fig. 4.8.

One could argue that the Arrhenius plot of the STM data does have a knee at $T_\mathrm{dep} = 100$ K and that the behavior is linear between $T_\mathrm{dep} = 60$ K and $T_\mathrm{dep} = 100$ K. In order to investigate this we have fitted the scaling law on these points exclusively (green line in Fig. 4.8). The corresponding parameters– $E_\mathrm{m} = 90$ meV and $\nu_0 = 1 \times 10^8$ Hz– are unusually low. This suggests that this fit does not represent the physical reality, but that the island density in this low temperature regime is determined by easy attachment.

4.5.2 Calculating the migration barrier from kinetic Monte-Carlo and Rate Equations

Kinetic Monte-Carlo and rate equations can both be used to calculate island densities, using the migration barrier and the attempt frequency as parameters. Fig. 4.9 a) shows the results for the simplest KMC model, i.e. diffusion limited aggregation (DLA). The simulation fits the STM data with parameters

$$E_\mathrm{m} = (200 \pm 10)\,\mathrm{meV} \qquad \text{and} \qquad \nu_0 = 1 \times 10^{14\pm0.5}\,\mathrm{Hz} \tag{4.4}$$

For comparison, the graph shows also the calculation from scaling law with the same parameters. Equivalent simulations with $i = 1$ and diffusing monomer were also performed using the mean-field rate equation approach. The migration barrier and prefactor determined from these calculations are both the same as for KMC. A modified barrier for next neighbor attachment influences the island

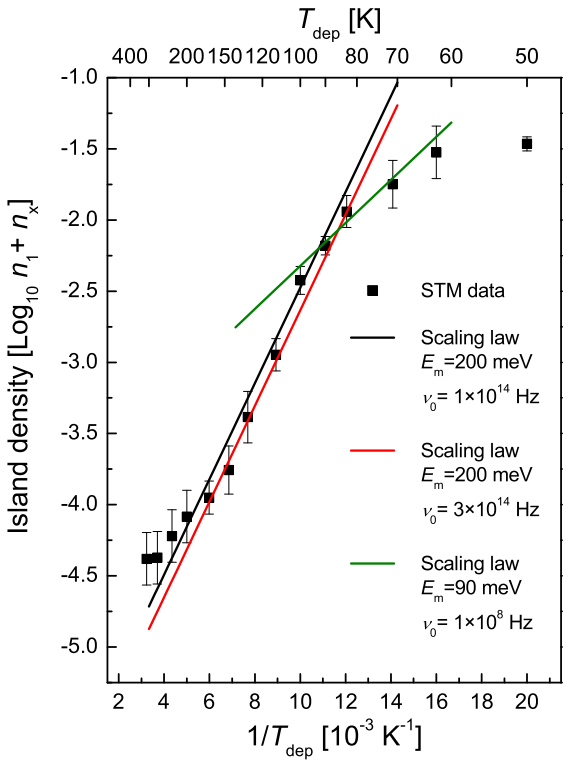

Figure 4.8: Island densities from experiment compared with scaling law. Red line: Scaling law equation with parameters E_m and ν_0 fitted to the experimental data. Black line: Scaling law with parameters equivalent to a kinetic Monte-Carlo simulations fit (see section 4.5.2). Green line: Scaling law equation with fit parameters for the lower temperature part of the graph. The unusually low values for the prefactor and the barrier –as well as annealing experiments (see Section 4.12)– indicate that this last fit is not physically correct.

density as shown by the graphs in Fig. 4.9 b). Based on the arguments presented above, the attachment barrier has been chosen $E_{attach} = 120$ meV. The island density fits the STM data much better. The remaining difference in the T_{dep} range between 50 K and 70 K can be accounted for by an easy attachment active up to the third nearest neighbors.

The results are summarized in the table below:

	STM data fitted with KMC / RE	Molecular Dynamics from Ref. [59]
E_m [meV]	200 ± 10	230 ± 10
E_{attach} [meV]	< 120	
ν_0 [Hz]	$1 \times 10^{14 \pm 0.5}$	2.3×10^{11}

4.5.3 Dimer diffusion

Annealing experiments at low coverage presented in Section 4.12 show that the Co dimer diffuses with a barrier $E_{m2} = 270$ meV which is also supported by corresponding molecular dynamics calculations [59]. Due to the stability of the Co dimer, diffusion takes place while the critical cluster size remains $i = 1$ and the dimer does not break up. The dimer dissociation barrier is calculated in the previous reference to be $E_2 = 410$ meV.

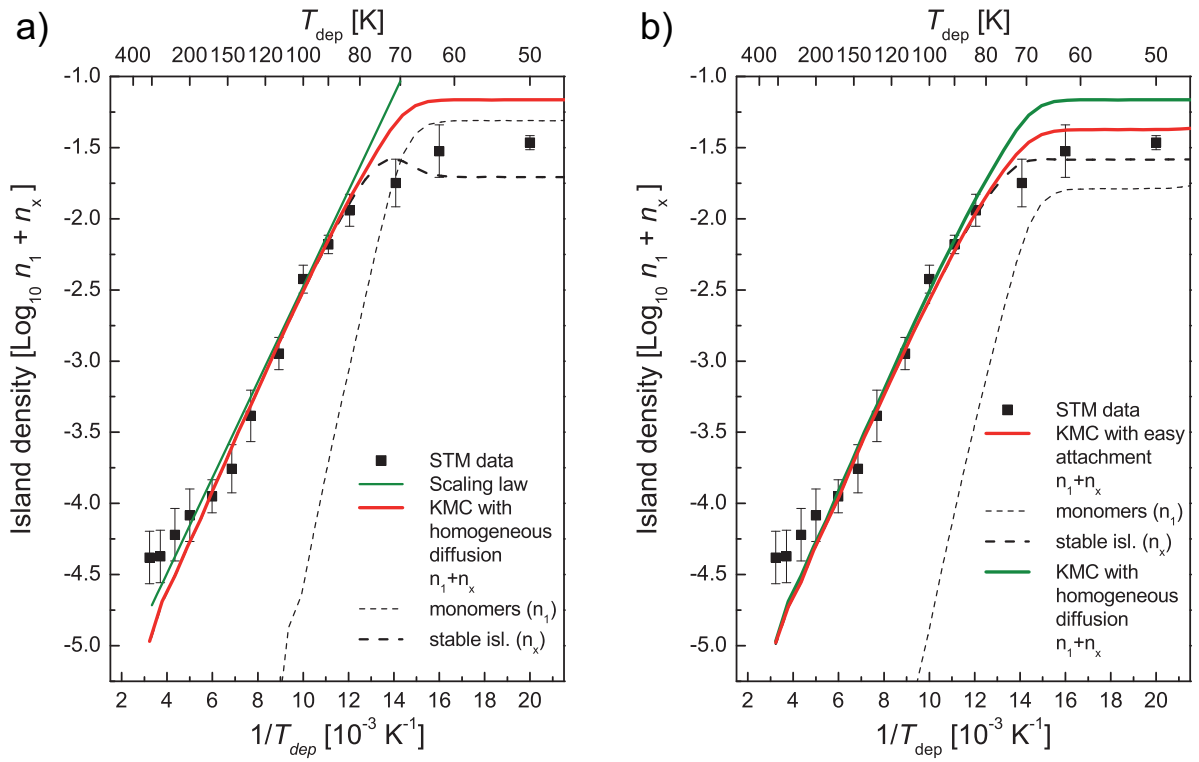

Figure 4.9: Island density for 0.12 ML Co/Pt(111). Comparison between different models.
a) Comparison between scaling law and KMC diffusion limited aggregation (DLA). For the temperature range of homogeneous monomer diffusion (70-170 K) both models give similar results. With the onset of diffusion, the monomer density decreases rapidly and the difference between the stable island density (n_x) and the total island density $n_1 + n_x$ becomes negligible.
b) Comparison of KMC simulation with and without easy attachment to nearest neighbor.

Dimer diffusion on a (111) surface is generally separated into two distinct motions [60]: First, the rotational movement of the dimer around one substrate atom or *intracell* motion which is connected to no net displacement of the dimer center of gravity. Second, the *intercell* motion of the dimer, where the dimer moves from one substrate atom to a neighbor. In the KMC simulation we model dimer diffusion by activating the corner-to-corner processes (see also process $E_{1\text{-}1}$ in Fig. 3.1 on page 19) with isotropic diffusion barriers for A and B type diffusions. This results in the effective displacement of the dimer center of gravity by successive movements of each of the dimer's atoms. Our model neglects the concerted movement of atoms where both dimer atoms make a step simultaneously. The concerted movement is supposed to have a higher activation barrier, which minimizes the effect of that approximation. Both the intracell and intercell diffusion processes were simulated in molecular dynamics by C. Goyhenex [59]. In contrast to Pt homoepitaxy, the activation barrier for the two process are close in the case of Co/Pt(111). As such our KMC model with corner-corner diffusion is presumably close to the physical reality. In the KMC simulation, in order to account for the attachment of the dimer to a pre-existing island, the corner-to-edge ($E_{1\text{-}2+}$) process must also be activated. To keep the model simple and with few degrees of freedom, we chose this attachment barrier to be equivalent to the corner-corner process barrier (no easy attachment for diffusing dimers).

To get a complete picture we also simulated the nucleation with dimer diffusion using rate equations. The modified equations are presented below:

$$\frac{\mathrm{d}n_1}{\mathrm{d}t} = F - 2\sigma_{11}\, D_1\, n_1^2 - \sigma_{12}\,(D_1+D_2)\, n_1 n_2 - \sigma_x\, D_1\, n_1 n_x + U_{\mathrm{di}\,1} \tag{4.5}$$

$$\frac{\mathrm{d}n_2}{\mathrm{d}t} = \sigma_1\, D_1\, n_1^2 - \sigma_{12}\,(D_1+D_2)\, n_1 n_2 - 2\sigma_{22}\, D_2\, n_2^2 - \sigma_x\, D_2\, n_2 n_x + U_{\mathrm{di}\,2} \tag{4.6}$$

$$\frac{\mathrm{d}n_x}{\mathrm{d}t} = \sigma_{12}\,(D_1+D_2)\, n_1 n_2 + \sigma_{22}\, D_2\, n_2^2 + U_{\mathrm{di}\,x} \tag{4.7}$$

where the $U_{\mathrm{di}\,j}$ represent direct impingement terms which have been written out in Eq. 4.1. When numerically solving the above equations, we make the approximation that the capture number for a given cluster size couple i, j is given by the monomer capture coefficient of the larger of two islands. For example, the same σ_2 is used to account for dimers capturing diffusing monomers (term $\sigma_{1,2}\,(D_1+D_2)\, n_1 n_2$) as well as dimers capturing diffusing dimers (term $\sigma_{22}\, D_2\, n_2^2$). This is not true in the most general case, and the capture number σ_{jk} ought to be calculated for each couple of cluster sizes j, k as a function of the density of all species[23]. To our knowledge, no data has been published on the general form of σ_{jk}. Nevertheless, this approximation keeps the solution simple without introducing an important bias in the island densities. In general, RE calculations have been done using the *lattice approximation* for σ_x and either constants or the expression derived by Bales and Chrzan in Refs. [61, 62] for σ_j with $j \neq x$.

Fig. 4.10 presents the island density calculated using the rate equations described above. The dimer diffusion barrier is set to $E_{\mathrm{m}2} = 270\,\mathrm{meV}$ as extracted from the annealing experiments (see Section 4.12). It is not possible to extract the dimer diffusion barrier directly by fitting the simulated island density to the experimental data for two reasons: First, the effect of dimer diffusion on the island density is rather small. The plot shows a comparison between KMC simulation with monomer diffusion only and the RE result. Dimer diffusion becomes relevant above $T_{\mathrm{dep}} = 150\,\mathrm{K}$, but the difference remains small. Thus, even in an ideal system as modeled, the difference would be close to the error margin and not permit much confidence in the extracted barrier. Furthermore, the experimental island density does not behave like the simulated one for deposition temperatures $T_{\mathrm{dep}} > 170\,\mathrm{K}$. In fact, the experimental island density is higher than the one expected from simple monomer diffusion. This effect becomes even more pronounced for higher temperatures. Dimer diffusion, although known to be present in the system, does not explain this behavior.

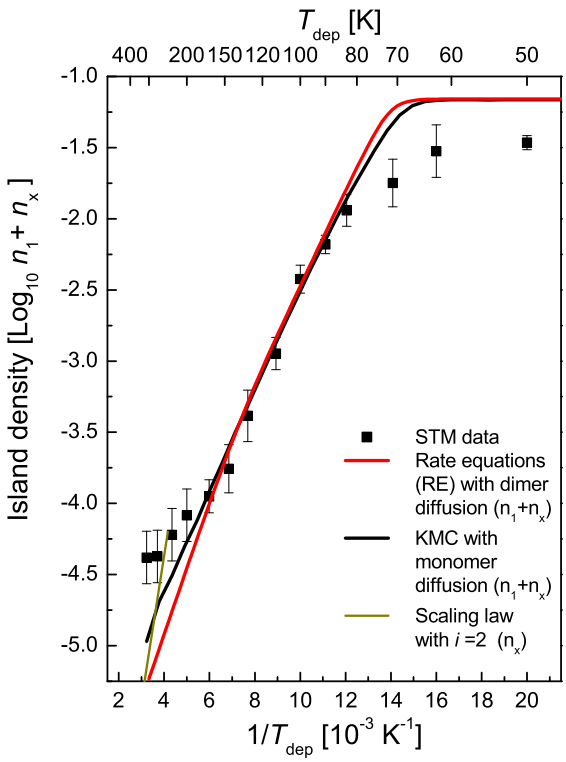

Figure 4.10: Island density in the presence of dimer diffusion. RE calculation compared with KMC and STM data. The effect of dimer diffusion (red line) becomes relevant for deposition temperatures above 170 K. The effect on the island density is small. In contrast, dimer dissociation has a drastic effect and could be easily identified in the experimental data, if present. Dimer dissociation island densities are calculated by scaling law for $i = 2$ (green line).

Another expected high temperature effect is the transition from $i = 1$ to $i = 2$ supposing that the dimer is the least stable specie. Using the dimer dissociation barrier $E_2 = 410$ meV calculated by MD, one can use the scaling law (Eq. 3.5) to calculate the expected island density. This is plotted as a green continuous line in Fig. 4.10. The effect of dimer dissociation on the island density is much more drastic than the effect of dimer diffusion. But the tendency of both effects is to lower the island density with higher deposition temperatures when compared to the monomer diffusion model. The higher island density measured experimentally can thus neither be explained by dimer diffusion nor by dimer dissociation. In following results calculated by KMC, dimer diffusion has been neglected to keep computing time lower. As has been shown above, the bias introduced by this choice is small.

The discrepancy between experimental data and monomer or dimer diffusion models starts at ≈ 170 K and coincides with the appearance of the Pt(111) surface reconstruction. In the next section we will study which physical processes result in the higher island density.

4.6 Cobalt induced surface reconstruction of Pt(111)

The Pt(111) surface experiences tensile stress due to the broken symmetry at the interface. The effect that the tensile stress of the surface favors a reconstruction can be intuitively understood by studying

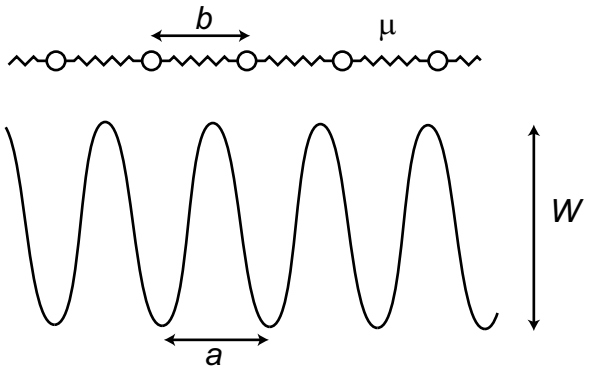

Figure 4.11: The one-dimensional Frenkel-Kontorova model. Each atom is connected to its two neighbors by springs of modulus μ and natural length b. The atoms sit in an external sine wave potential of periodicity a and peak-to-peak amplitude W. Adapted from [63].

the Frenkel-Kontorova model presented in Fig. 4.11. The figure shows the one-dimensional form of the model, although the extension to two dimensions as relevant in our case is straightforward. In the Frenkel-Kontorova model, the topmost surface atomic layer is modeled as atoms connected to their nearest-neighbors by springs with a spring-constant μ and natural length b. This spring chain sits on a sinusoidal potential surface with periodicity a and amplitude W. The potential surface can be interpreted as the combined effect of all underlying bulk atoms on the topmost layer.

This permits a calculation of the total energy of the surface. By energy minimization and depending on the parameters, the model can predict surface reconstruction with either a higher or lower density of surface atoms than in the bulk layer. Corresponding calculations have been performed for the Pt(111) surface [63, 37] and its main prediction is that the unreconstructed Pt(111) surface is close to "an instability towards adding atoms to the surface".

Our experiments show that the Pt surface is unstable towards reconstruction in the presence of a supersaturated cobalt gas at a surface temperature above 180 K. As shown above, the island density deviates from all known models for deposition temperatures above ≈ 170 K. Based on these observation we will develop below several models trying to explain the behavior.

4.7 Exchange and vertical dimers

In order to achieve higher island densities, the system must create more growth nuclei during the nucleation phase than it would in the unperturbed homogeneous monomer diffusion case. One effect which has been shown to result in an increase of nuclei is the adatom-substrate place exchange (hereafter simply called *exchange*)[64]. In the exchange process (see Fig. 4.12 a.), a Co adatom diffusing on the Pt surface replaces one surface Pt atom and gets embedded in the first substrate layer. Simultaneously the Pt atom gets ejected. This creates a substitution point-defect in the uppermost Pt layer. Two possible scenarios may follow:

1. The ejected Pt stays immobile on top of the inserted Co atom. Two factors would contribute to this scenario. 1. The diffusion barrier of Pt on itself is too high for the diffusion process to be activated. 2. The Co-Pt bond in the so created vertical dimer is too strong for thermal break-up.

2. The Pt diffuses on the surface with its own diffusion barrier. At a later time, another Co atom reaches the inserted Co atom and they form a *vertical* Co-Co dimer.

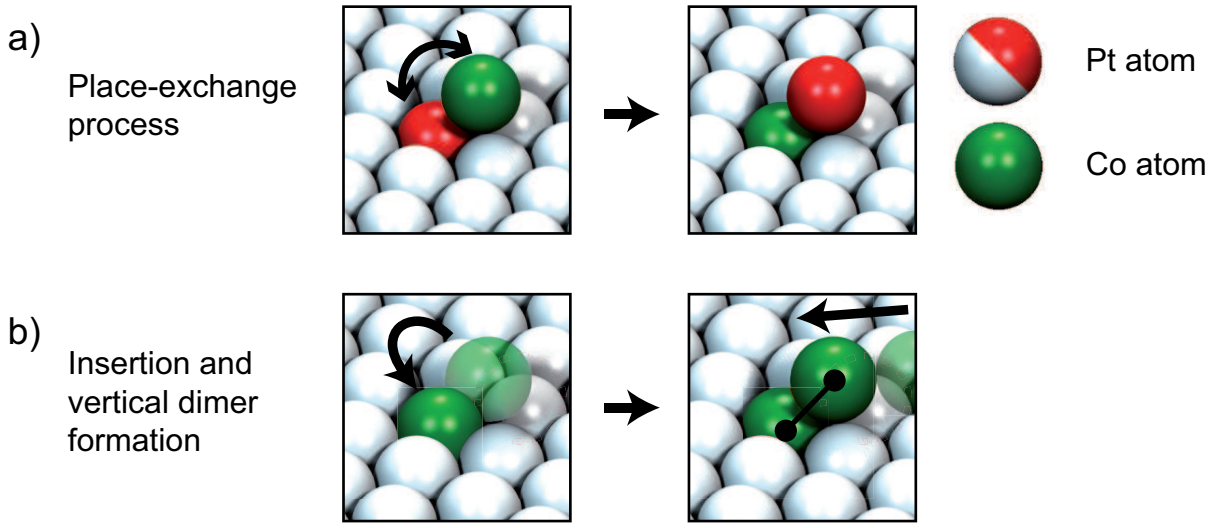

Figure 4.12: Schematic view in the hard sphere model of two processes capable of creating new growth nuclei in the course of deposition. a) Exchange process. A diffusing Co adatom replaces a Pt surface atom. The corresponding Pt atom is ejected and may diffuse on the surface. This creates a substitution point-defect. b) Vertical dimer formation. A diffusing Co adatom is *inserted* in the Pt surface locally creating a strain field. Subsequently another diffusing Co adatom forms a vertical dimer with the inserted one.

Both scenarios result in an irreversibly immobile surface atom which will act as an aggregation point for other adatoms. We thus have a stable island of size 1, which corresponds (by definition) to a critical cluster size $i = 0$. The first scenario seems improbable because the diffusion barrier $E_m = 260$ meV [57] of Pt/Pt(111) –although higher than the corresponding value for Co/Pt(111)– is expected to be activated. This can be shown by a small calculation. For Co/Pt(111) the monomer diffusion becomes relevant at a characteristic temperature $T_{char} \approx 70$ K. We can then calculate a characteristic rate at which a *diffusion process* must happen to be relevant on the timescale of the experiment. This hopping rate is simply:

$$\nu_{char} = \nu_0 \exp\left(\frac{-E_m}{k\ T_{char}}\right) \tag{4.8}$$

which applied to the Co/Pt(111) parameters gives: $\nu_{char} \approx 1$ Hz. Knowing the characteristic rate we can compute a characteristic temperature for Pt/Pt(111) using the parameters measured by Kyuno et al. [57]. One finds that Pt/Pt(111) diffusion becomes relevant for temperatures above 100 K. As we are investigating effects in the range between 180 K and 310 K, we cannot exclude Pt monomer diffusion on the surface.

Still in the first scenario, the second argument is that the Co-Pt vertical dimer has a strong bond which cannot be broken at the thermal energies considered. Although no direct experimental evidence exists in favor or against this, we can use a qualitative argument. When the Co monomers are diffusing on the Pt surface from one threefold coordinated site to the next, the bonds between the Co adatom and the substrate are of the Co-Pt type. Given that for one diffusion step a bond must be transferred from one substrate atom to the next, this transfer has an energy barrier of the order of the diffusion barrier (≈ 200 meV). Thus, the Co-Pt bond is very likely to break. The arguments above favor the second scenario, where the Pt diffuses away from the embedded atom and a Co-Co dimer can form.

Place exchange as described has been observed experimentally on several systems, namely Fe/Cu(100) [65], Co/Cu(100) [66, 67], Ni/Ag(111) [64], Pt/Ni(119) [68] and Pt/Pt(100) [69]. The ex-

change process is supposed to be thermally activated and follow an Arrhenius law.

In the Pt(111) case the surface is under tensile stress, so the ejection of the Pt substrate atom is energetically unfavorable. The chemically resolved STM image in Fig. 4.4 also implies that insertion of Co in the first layer is possible without the ejection of a substrate atom. Although the image suggests that insertion is preferred near previously inserted atoms, insertion on the pristine substrate is isotropic by lack of distinguished sites.

The second scenario of the exchange process can so be extended to the *insertion* of Co. This is schematically shown in Fig. 4.12 b) which is then also a two step process. First a cobalt atom gets inserted in the first substrate layer. At a later time, a diffusing adatom binds to the inserted one and form an irreversible vertical dimer. Again, insertion is supposed to be a thermally activated process.

In order to test the effect of these processes on the island density, we perform KMC and RE simulations. We see that all three cases of exchange or vertical dimer formation result in the irreversible creation of a growth nucleus. Therefore, the three cases can be simulated by one unique model.

4.7.1 Simulating place-exchange

Rate equation approach to exchange

To include exchange or equivalently insertion with vertical dimer formation we add an equation for the density of exchanges atoms n_{ex} to the standard mean-field rate equations:

$$\frac{\mathrm{d}n_1}{\mathrm{d}t} = F - 2\sigma_1\, D_1\, n_1^2 - \sigma_x\, D_1\, n_1 n_x \overbrace{-\sigma_{\mathrm{ex}}\, D_1\, n_1 n_{\mathrm{ex}}}^{\substack{\text{monomers lost by}\\ \text{attachment to}\\ \text{exchanged atoms}}} \overbrace{-\nu_{\mathrm{ex}} n_1}^{\substack{\text{monomers lost}\\ \text{by exchange}}} + U_{\mathrm{di,1}} \tag{4.9}$$

$$\frac{\mathrm{d}n_{\mathrm{ex}}}{\mathrm{d}t} = \nu_{\mathrm{ex}} n_1 - \sigma_{\mathrm{ex}}\, D_1\, n_1 n_{\mathrm{ex}} + U_{\mathrm{di,ex}} \tag{4.10}$$

$$\frac{\mathrm{d}n_x}{\mathrm{d}t} = \sigma_1\, D_1\, n_1^2 + \sigma_{\mathrm{ex}}\, D_1\, n_1 n_{\mathrm{ex}} + U_{\mathrm{di,x}} \tag{4.11}$$

The effective loss of monomers due to exchange is proportional to the monomer density and has a rate:

$$\nu_{\mathrm{ex\,eff}}(T)\, n_1 = \nu_{0\,\mathrm{ex}}\, \exp\left(\frac{-E_{\mathrm{ex}}}{kT}\right)\, n_1 \tag{4.12}$$

where E_{ex} is the energy barrier associated with exchange and $\nu_{\mathrm{ex}\,0}$ is the corresponding attempt frequency. At the same time, monomers are lost by attachment to the already exchanged atoms forming stable islands, at a rate $\sigma_{\mathrm{ex}}\, D_1\, n_1 n_{\mathrm{ex}}$, where σ_{ex} is the capture coefficient of an exchanged adatom. In the following simulations, σ_{ex} was chosen equal to the monomer capture coefficient σ_1. In order to keep the model simple, the attempt frequency has been chosen equal for the diffusion process as for the exchange. This is open to debate, as one could easily imagine a yield associated with exchange which might be different from 1.

Kinetic Monte-Carlo approach to exchange

In order to account for exchange in the kinetic Monte-Carlo model, a corresponding event has been introduced. The event is monomer specific and is thus stored in each `Monomer` object (see section 3.3.2 on page 20 for the KMC implementation details). The associated rate is again an Arrhenius term

$$\nu_{\mathrm{ex}}(T) = \nu_{0\,\mathrm{ex}}\, \exp\left(\frac{-E_{\mathrm{ex}}}{kT}\right) \tag{4.13}$$

Upon realization, the cobalt atom (or more generally an atom of type A) is withdrawn from the surface and replaced by a platinum atom (resp. B atom). The newly created atom is populated with possible events (diffusion, exchange etc.) associated with the new atom type and the simulation carries on. Several scenarios can be simulated in this way. The closest to irreversible exchange is to make the newly created atom immobile, with all event rates equal to 0. Diffusion of Pt after exchange can also be simulated, but then vertical dimer creation is no longer possible as the simulation does not remember at what site exchange took place. This limitation has been addressed in a different model presented below.

4.7.2 General behavior of the system

Fig. 4.13 shows a comparison between KMC simulations without (a) and with (b) exchange. Both simulations have edge diffusion activated to obtain realistic compact islands (discussed in Section 4.11). They simulate the deposition of 0.1 ML Co/Pt(111) at $T_{\mathrm{dep}} = 200$ K. The exchange barrier is $E_{\mathrm{ex}} = 440$ meV and the attempt frequency $\nu_{0\,\mathrm{ex}} = 1 \times 10^{14}$. Atoms shown in red are those which underwent exchange.

In the case with exchange, the island density is much higher and islands are correspondingly smaller. The mean island size without exchange is $\langle s \rangle = 1356$ atoms while in the case with exchange we have $\langle s \rangle = 294$ atoms. Most exchanged atoms are found in the middle of large islands. This indicates that they are present early in the growth process, possibly being responsible for the creation of the original growth nucleus. The growth of an island around an existing exchanged, immobile atom is also possible but several arguments suggest that this effect is negligible. First, only 0.06% of exchanged atoms are not incorporated in a larger island. In the hypothetical case where exchanged atoms would not contribute to island density, one would expect 90% of single, non-incorporated, exchanged atoms. Furthermore, 95% of all islands contain exactly 1 exchanged atom which strongly suggests that this acts as the starting point of the new island.

To investigate this further, we plot the effective exchange frequency $\nu_{\mathrm{ex\,eff}}$ (see Eq. 4.12) as a function of time in Fig. 4.14 a) (black curve). Aggregation to exchanged atoms is close to 100% and nearly immediate so that nucleation of islands due to exchange has the same values. It shows that exchange takes place the fastest at the very early stage of deposition when the mean free path of monomers is the longest. The plot is linear in the log-log representation which indicates that it follows a scaling law. The corresponding fit is $\nu_{\mathrm{ex\,eff}} \approx 2.3 \times 10^{-6}\ \Theta^{-0.56}$. Because ν_{ex} is constant throughout the simulation, we deduce that the monomer density is $n_1 \propto \Theta^{-0.56}$. Bartelt et al. [70, 71] calculate that in the irreversible growth case with isotropic diffusion but *without exchange*, the monomer density takes the scaling form $n_1 \propto \Theta^r$ where $r = -0.34$ from simulation and $r = -1/3$ from rate equation. While the general form of the monomer density as a scaling law of coverage is still valid in the exchange case, the scaling exponent $r = -0.56$ is not constant but a function of temperature and exchange barrier. For $T_{\mathrm{dep}} = 200$ K, the lower exponent in the exchange case indicates that the lifetime of the monomer before aggregation, nucleation or exchange is sensibly reduced when compared with the system without exchange.

To further show the effect of exchange on the creation of new stable growth nuclei, we plot the ratio of nucleations due to exchanged atoms versus the total amount of nucleation (see red curve in Fig. 4.14 b.). In the first 10^{-3} ML of deposition, the ratio goes from 60% to 90%, meaning that 9 out of 10 new islands are created because of exchanged atoms. Our supposition that exchange is at origin of most islands is thus justified. In the homogeneous growth model, most nucleation takes place at the very early stage of deposition. The blue curve shows that at 0.01 ML of deposition, 67% of nucleation has taken place. The following phase is then predominantly a growth phase where existing nuclei acquire more atoms by aggregation. In the exchange case in contrast, nucleation of stable islands continues at a higher rate up to the end of deposition. In this case, at 0.01 ML of deposition time, only

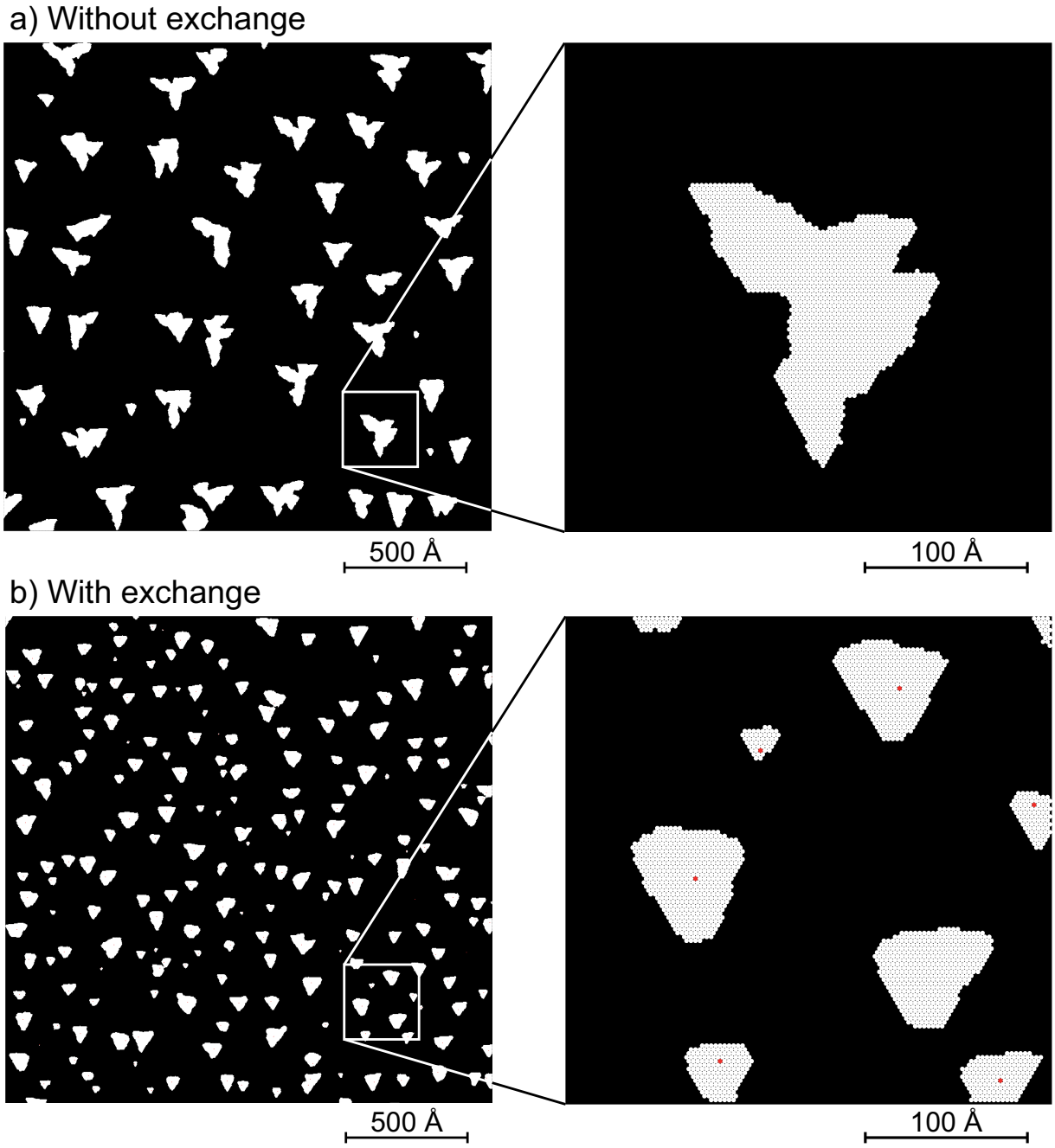

Figure 4.13: Comparison of KMC simulation without (a) and with exchange (b). Simulation of $\Theta = 0.1$ ML Co/Pt(111) at 200 K with flux $F = 5 \times 10^{-3}$ ML/s and activated edge diffusion. b) Exchange is activated with a barrier $E_{ex} = 440$ meV. The red dots indicate exchanged Pt atoms. After realization of this process the atoms are simulated as immobile and offer new growth nuclei. Exchanged atoms are the nuclei for most stable islands and thus can be found mainly in the center of islands.

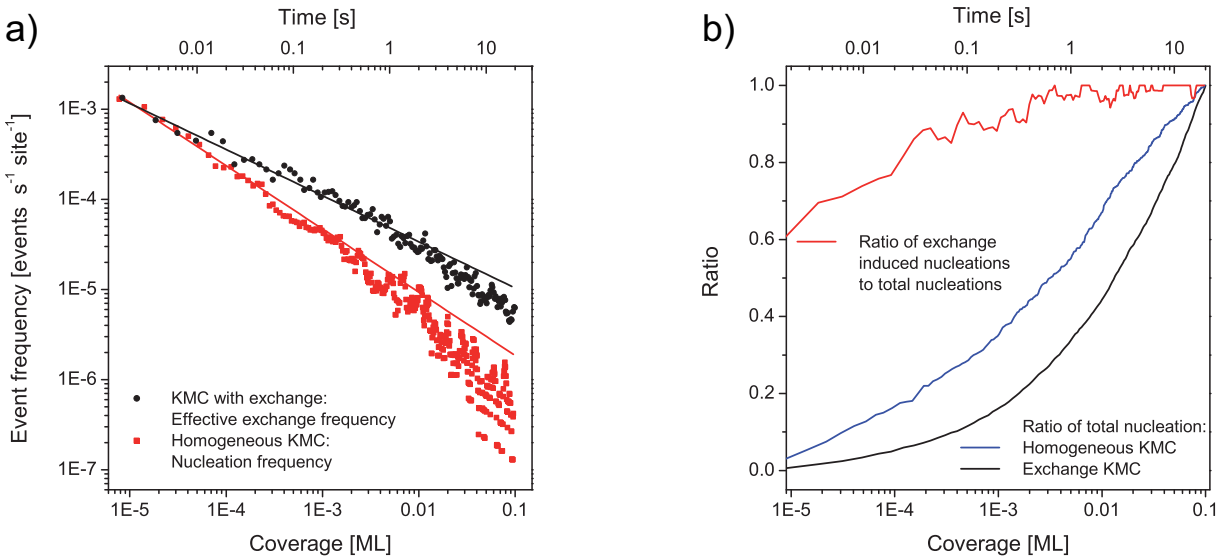

Figure 4.14: KMC simulation, Co/Pt(111), $\Theta = 0.1$ ML, $T_{dep} = 200$ K, $F = 5 \times 10^{-3}$ ML/s, exchange barrier $E_{ex} = 440$ meV.
a) Black dots: Log-log plot of the number of exchange events per second and per surface site during deposition as a function of coverage or time. Most exchange takes place at the very early stage of deposition when the mean free path of monomers is the longest. Exchange is directly proportional to the monomer density.
Red dots: For homogeneous KMC, number of nucleation (two monomers joining) events per second per site.
b) Red line: Rate of nucleation due to Co exchange normalized to total nucleation rate, versus coverage. Starting at ≈60 % for very low coverages it rapidly rises to ≈100 % above 1% of deposition time.
Black line: Sum of nucleation at Θ normalized to the sum of nucleation at 0.1 ML. After 10% of deposition time only 46 % of all nucleation has taken place in the exchange in contrast to 67 % in the homogeneous case. This indicates that a surface experiencing exchange nucleates more islands later in the deposition process.

47% of all finally present islands are already nucleated.

4.7.3 Island size distribution and density

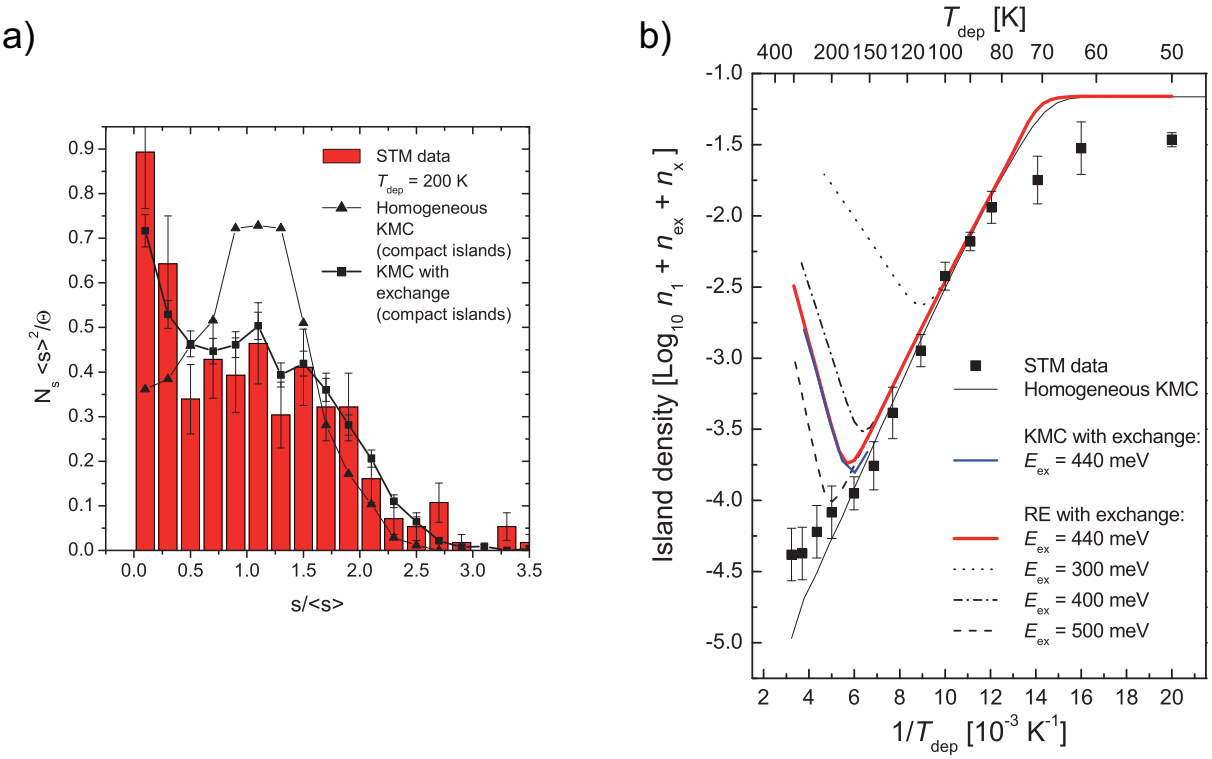

Figure 4.15: a) Comparison of island size distributions at $T_{dep} = 200$ K from experiment, KMC with and without exchange. Exchange introduces a bimodal distribution with a high number of small islands. The distribution from KMC simulation with exchange is in good agreement with the experimental one. This indicates that in the physical system a nucleation process similar to exchange may be active.
b) Arrhenius plot of the island density in the case of exchange (KMC and RE models) compared to STM data. The behavior of the system is not well described by the exchange models.

Fig. 4.15 a) shows the normalized island size distribution obtained from KMC simulation with (squares) and without (triangles) exchange. As already observed by Zangwill et al. [72] the normalized island size distribution in the presence of exchange is bimodal. One mode is located at 0 and another slightly above 1. The high density of small islands can be explained by the remarks above. As nucleation of new islands takes place at high rate up to the end of deposition, these nuclei have little time to aggregate atoms and thus remain small. The second mode, approximatively at the mean island size $\langle s \rangle = 294$ atoms, is created by islands nucleated early in the deposition process.

We also compare these two models to our experimental island size distribution obtained at $T_{dep} = 200$ K. The STM data show a bimodal distribution with modes at 0 and ≈ 1.2. The first peak has height 0.9 while the second is at 0.45. It is evident that the simple homogeneous model with its normalized peak of 0.8 at the mean island size (s/$\langle s \rangle$=1) does not describe the experimental data accurately. In the case of exchange, however, the size distribution is in agreement with the experimental data, showing modes at the same normalized sizes and of correct height.

Fig. 4.15 b) shows the Arrhenius plot of the island densities for the system with exchange. Comparing the simulation models for a given exchange barrier (KMC: blue curve, RE: red curve), we note

the excellent agreement between RE and KMC approaches in the exchange activated, high temperature parts. Both models exhibit the standard behavior for nucleation and growth up to the temperature where exchange becomes relevant. In the case presented where the exchange barrier is $E_{ex} = 440\,\text{meV}$, exchange becomes important for $T_{dep} > 160\,\text{K}$. The island density reaches a minimum for $T_{dep} \approx 175\,\text{K}$ and *increases* almost linearly in the Arrhenius representation for higher deposition temperatures. The higher island density is explained by the creation of new growth nuclei by exchange. Each nucleus thus competes for the aggregation of diffusing adatoms, resulting in a higher density of smaller islands. Dashed lines in the plot show the effect of different exchange barriers. Smaller barriers lower the temperature where exchange becomes relevant.

The high temperature, linear part in the Arrhenius plot asymptotically tends to a limit function which was derived by Meyer et al. [64]. The function describing the evolution of the island density in the exchange activated part is

$$n_x = \Theta^{1/2} \left(\frac{\nu_{ex}}{D} \right)^{1/2} = \Theta^{1/2} \exp\left(\frac{E_m - E_{ex}}{2kT} \right) \tag{4.14}$$

It is notable that the island density in this regime does not depend at all on the deposition flux F nor the attempt frequency ν_0 (when assuming equivalent attempt frequencies for exchange and diffusion). The dependence is on the *difference* between the migration barrier E_m and the exchange barrier only. The parameter $\Theta^{1/2}$ describes the island density at infinite temperature and is ≈ 0.31 for $\Theta = 0.1$ ML which we confirm by both KMC and RE simulation.

From the expression of island density in the exchange regime (4.14) and the scaling law for $i = 1$ (3.5) we can calculate an expression for the temperature of minimum island density:

$$T_{min} = \frac{6(E_m - E_{ex}) - E_m}{k\left(\ln\left(\frac{4F}{\nu_0} \right) - \frac{3}{2} \ln\left(\frac{\eta^2}{\Theta} \right) \right)} \tag{4.15}$$

where $\eta \approx 0.25$ is the same as in the scaling law (3.5). If used with all parameters given above for our system, this equation estimates a minimum temperature $T_{min} = 177\,\text{K}$ which is in very good agreement with 175 K obtained from simulation.

In Fig. 4.15 b), the two exchange models are also compared with the experimental data. The model's exchange barrier was chosen in order to become active at the point where the transition between the slopes occurs in the experimental data. The exchange models predict a rise in island density with increasing deposition temperature. This is not observed experimentally since the island density continues decreasing but with a shallower slope.

Although the exchange models are in good agreement with the experimental data regarding the overall island size distribution, we can exclude the simple exchange mechanism as the island density does not fit experimental behavior at high temperature. As specified above, the exchange model represents two possible physical phenomena, namely adatom-substrate place exchange and irreversible vertical dimer formation. In the latter, it represents the extreme form of a model with attractive local point-defects, where the attractive potential energy well would be infinitely deep. In order to understand the effect of the potential well depth, we present below a model with a finite potential well.

4.8 Attractive point-defects KMC model

In order to account for attractive point-defects created by insertion of diffusing adatoms, the KMC model was modified. The new insertion process is reserved to monomers and thus stored in a `Monomer` object. It is also thermally activated (follows Eq. 4.13) with a corresponding energy barrier E_{insert}. Upon insertion, the reacting atom is withdrawn from the KMC simulation and the adsorption site

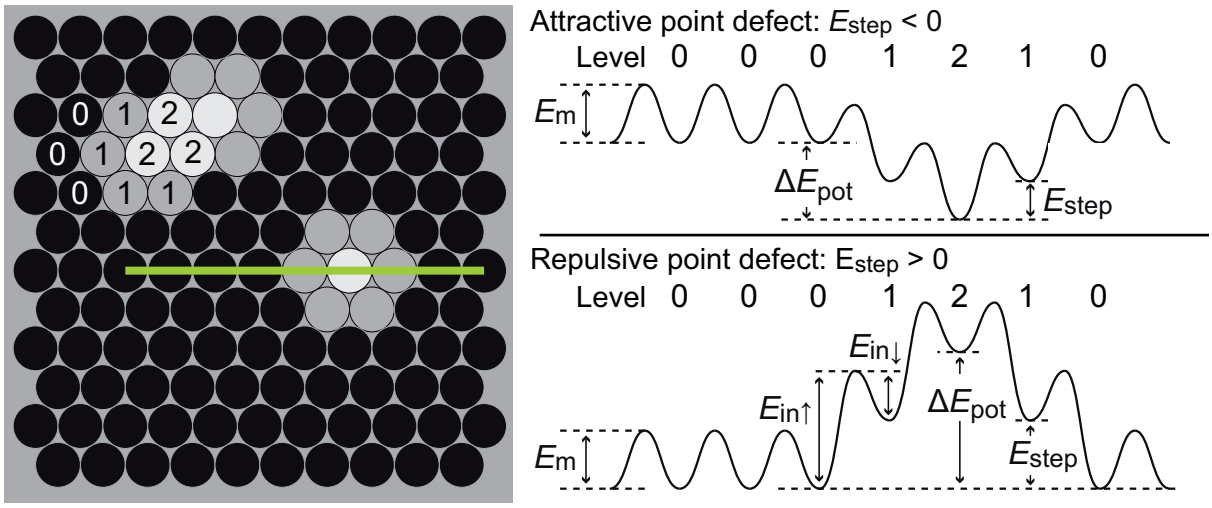

Figure 4.16: Left: Top view of possible fcc adsorption sites in the KMC model. Each site has an associated binding energy indicated by the position's gray level. Insertion locally modifies the binding energy, making the insertion point either attractive or repulsive. Top left: result of two insertions with overlapping effect. The overlapping site's binding energy is modified by both insertions. Right: Potential energy landscape viewed by an atom diffusing along the green line depicted in the left schema for attractive and repulsive cases.

and its surroundings up to a distance d_{insert} is modified. The binding energy of these neighboring sites at a distance d is raised[2] by a multiple of a energy step E_{step}. The potential energy around a site following insertion is at time t

$$E_{\text{pot}}(d,t) = E_{\text{pot}}(d,t-1) - (d_{\text{insert}} - d + 1)E_{\text{step}} \qquad \text{for } d \leq d_{\text{insert}} \tag{4.16}$$

where $d = 0$ stands for the actual insertion site, $d = 1$ for nearest neighbors etc. and $(t-1)$ is the time step before insertion and t the one after. We can thus associate an integer *level* value to each site, depending on how many times E_{step} is added to the binding energy of the pristine substrate.

This is best shown in Fig. 4.16 where $d_{\text{insert}} = 1$ was chosen. The top view of possible fcc adsorption sites indicates in gray levels the binding energy of each site (lighter = more strongly bound in the attractive case). The corresponding binding energy along the green line is depicted in the energy diagram on the right. The integer level describing the modification of the binding energy is indicated above each site in the diagram. Note that new insertions on second neighbor sites will augment the level of the overlapping sites twice (see top left in Fig. 4.16). All presented simulations were performed with $d_{\text{in}} = 1$ as depicted, although the program takes it as a parameter and permits any distance. The total energy well compared to the pristine substrate is $\Delta E_{\text{pot}} = (d_{\text{insert}} + 1)E_{\text{step}}$.

In the model, insertion is only allowed on sites which still have the potential energy level of the pristine substrate (level = 0). Without this condition, the dwelling time of monomers in the attractive well created by a first insertion is so high that a second insertion occurs at the same point with a great probability. Depending on the total energy well and simulation temperature, this can lead to more than five atoms inserting at the same point. This is not realistic from the physical point of view where the insertion creates a local strain field, relieving some of the tensile stress which is itself responsible for insertion. In reality, a second insertion at the same point will certainly be associated with a much higher activation barrier. To account for this, we made insertion impossible on nearest neighbor

[2]When the binding energy is *raised* (the atom is more strongly bound), the potential energy is lower as shown in the diagram meaning that diffusion away from an attractive insertion site is more difficult.

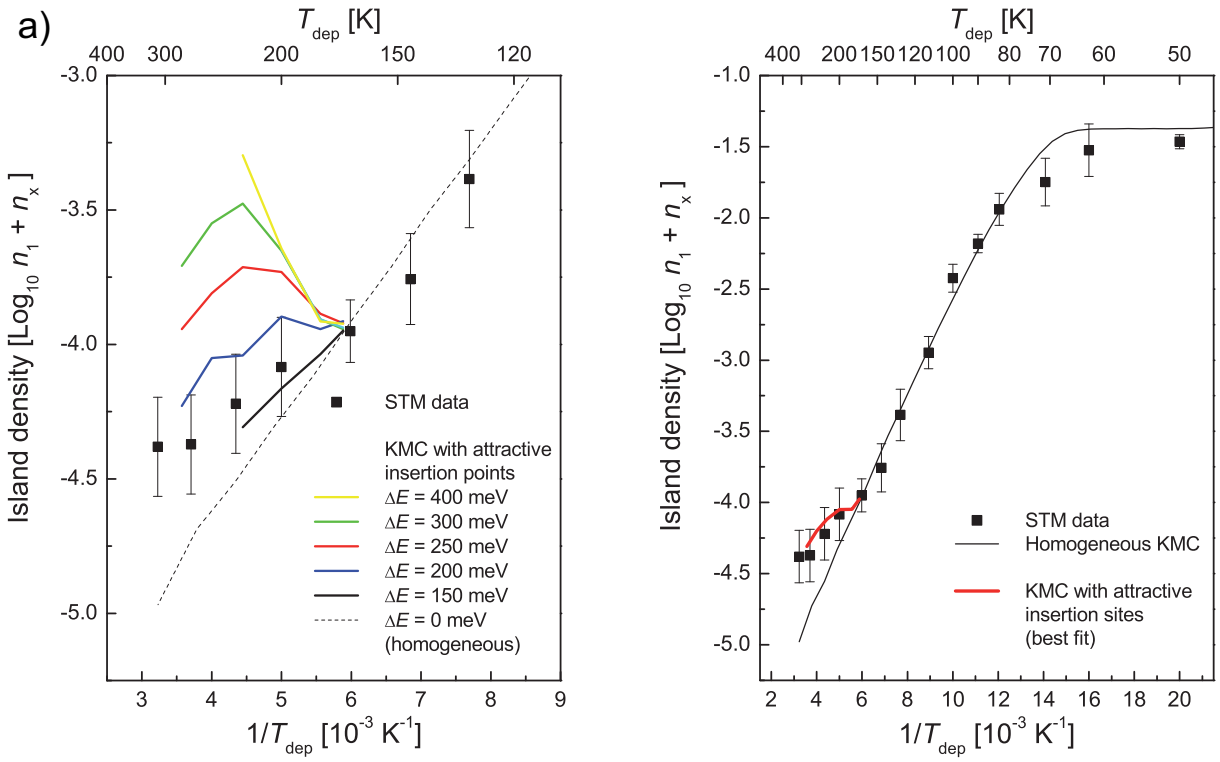

Figure 4.17: Island densities obtained from 0.1 ML Co/Pt(111) KMC simulations with attractive point-defects created by insertion of adatoms.
a) Effect of the attractive potential well depth on the island density for a given insertion barrier ($E_{\text{insert}} = 440$ meV). A deeper well increases the island density and the temperature at which the island density reaches its local maximum.
b) Fit of the experimental data obtained with parameters $E_{\text{insert}} = 460$ meV and $\Delta E_{\text{pot}} = -200$ meV

.

sites around a previous insertion site (i.e. level $\neq 0$). As a corollary, the absolute maximum insertion density in the model is limited to 0.25 ML. If for a new insertion we intentionally chose always the site which minimizes the number of newly modified sites, at least 4 sites are modified for each insertion following that a maximum of 1/4 of all site could experience insertion. Another consequence is that this limit does not act as a hard limit up to which insertion acts unhindered. With more and more sites having a modified binding energy, new insertions become *continuously* less probable. This is very close to the supposed physical behavior of the system.

4.8.1 Island density

Island densities obtained by the deposition of 0.1 ML have been calculated and are presented in Fig. 4.17. The left part (a) shows a detail of the high temperature range where insertion is relevant. Given a constant insertion barrier $E_{\text{insert}} = 440$ meV, the graphs show curbs for potential energy well depths ΔE between 0 meV (homogeneous KMC model) and 400 meV. The island density evolution versus temperature takes the following form: At temperatures below 170 K, the island density in the presence of insertion is indistinguishable from the homogeneous diffusion model. This temperature limit depends on E_{insert}. For temperatures above 170 K and well depth > 200 meV the island density increases to reach a local maximum. For a well depth of 300 meV this maximum is located at ≈ 230 K.

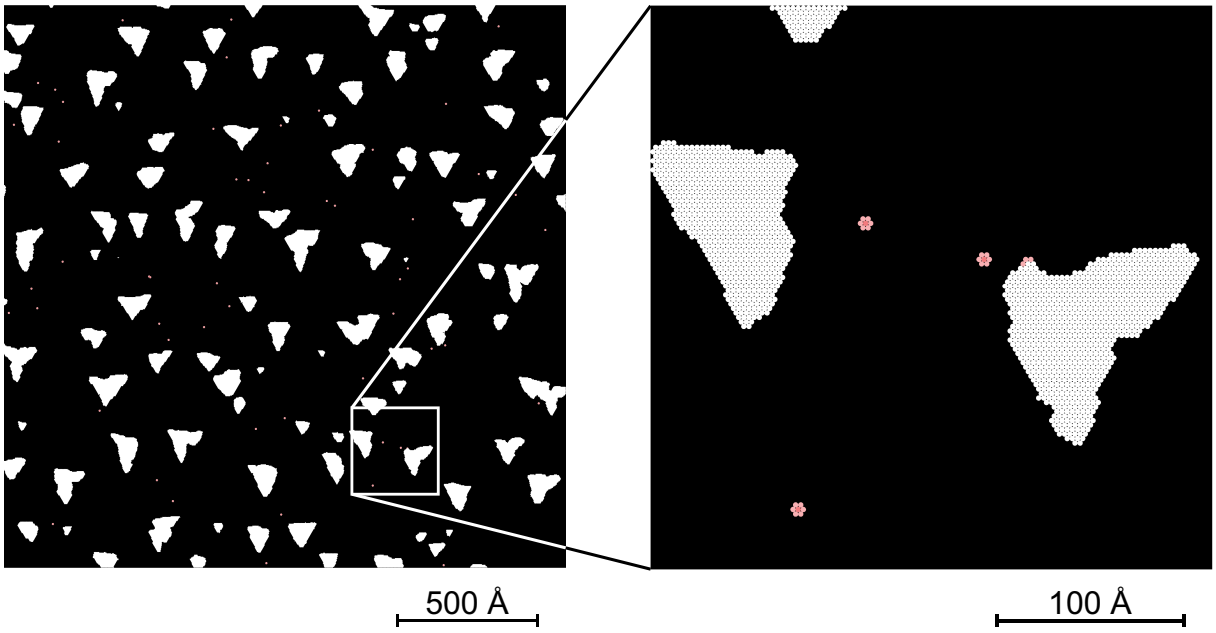

Figure 4.18: Top view of a KMC simulation of 0.1 ML Co/Pt(111) at $T_{\text{dep}} = 200\,\text{K}$ with attractive insertion points ($\Delta E_{\text{pot}} = 200\,\text{meV}$, $E_{\text{insert}} = 460\,\text{meV}$, $d_{\text{insert}} = 1$). Sites where insertion occurred are shown in pink. Insertion sites covered by Co atoms (white) cannot be distinguished.

At higher temperatures, the island density decreases with a steeper slope than for homogeneous diffusion. The island density eventually reaches the island density of the homogeneous diffusion model at very high temperature.

This general behavior can be explained in the following way: At low temperature, insertion is a slow process occurring rarely (3.3×10^{-6} ML at 170 K) so the island density is essentially equivalent to the homogeneous KMC simulations. Above this temperature, the island density diverges from the homogeneous model and for energy wells deeper than $\approx 200\,\text{meV}$, the island density increases. In fact, with increasing temperature, the number of inserted atoms grows exponentially. Because the potential around insertion sites is attractive, the dwelling time for a diffusing adatom there is also increased. For a very deep well, the dwelling time is approximatively infinite while for a shallower well, the dwelling time is just extended. The resulting chance of nucleation is higher than on the homogeneous substrate.

For higher deposition temperatures, the island density reaches a local maximum followed by a decrease. The temperature of the local maximum as well as the island density itself increases with increasing well depth. The existence of the maximum and the transition towards a decreasing function is the result of two competing processes: First, the insertion is thermally activated and becomes exponentially more frequent with increasing temperature, thus creating attractive sites and correspondingly favoring island nucleation and higher island densities. Secondly, with increasing temperature the attractive points created by insertion are less efficient in keeping the adatoms localized and thus favor lower island densities. As explained before, the two extreme cases of the model are the infinitely deep well, equivalent to exchange (when neglecting the atoms lost to insertion), and the 0 depth well, equivalent to homogeneous diffusion.

We thus have a parameter –the well depth– which permits to scale continuously between these two extremes. This has been done to best fit the experimental island densities in Fig. 4.17 b) yielding $E_{\text{insert}} = (460 \pm 20)\,\text{meV}$ and $\Delta E = (-200 \pm 20)\,\text{meV}$. The fit describes the experimental behavior

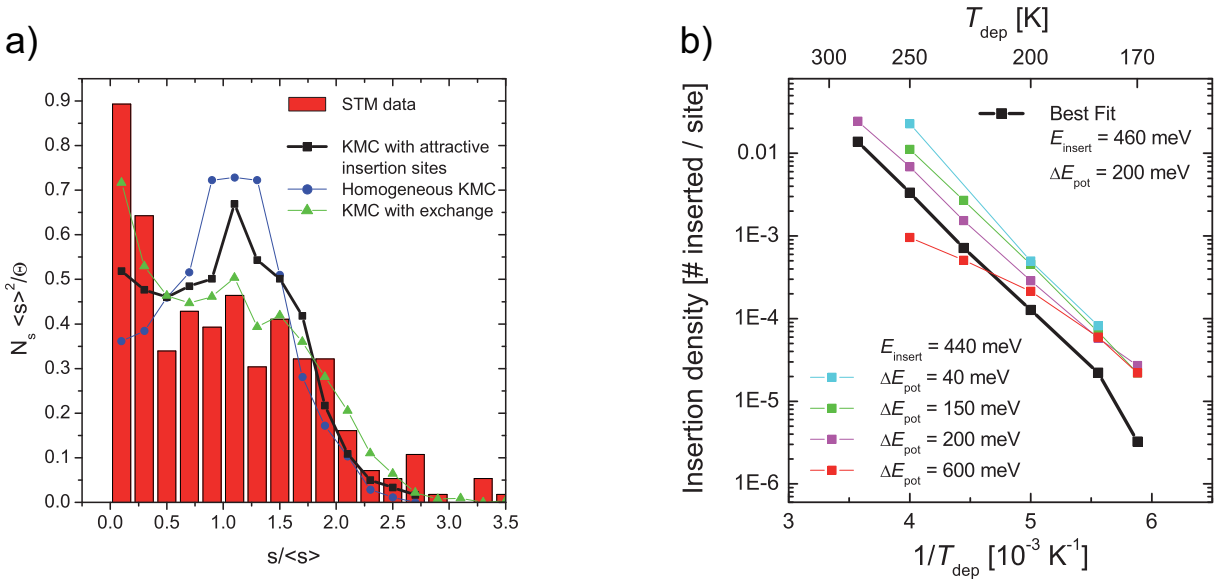

Figure 4.19: Results for KMC simulations with insertions ($\Theta = 0.1$ ML, $E_{\text{insert}} = 460$ meV) and attractive insertion site ($\Delta E_{\text{pot}} = -200$ meV).
a) Normalized island size distribution at 200 K in the presence of attractive insertion (black squares) compared with homogeneous KMC simulation (blue), exchange KMC simulation (green) and STM data (red bars).
b) Density of inserted atoms as a function of deposition temperature. The effect of different attractive well depth from 40 meV to 600 meV is compared. The behavior is nearly linear in the Arrhenius representation (see text for analysis). For the best fit (black curve) parameters ≈ 0.03 ML inserted atoms are expected at 300 K (by extrapolation).

correctly within the error bars. While the tendency of the experimental island density seem to be linear in the Arrhenius plot, the simulated values show the transition from a local minimum to a local maximum followed by decrease. This behavior cannot be resolved in the experimental data with the existing error bars.

A top view of a simulations performed with these optimal parameters at 200 K is shown in Fig. 4.18. Adsorption sites with modified binding energy due to insertion are shown in pink. Attractive sites which are later covered by diffusing adatoms cannot be distinguished from adatoms (shown in white). The morphology is not strongly influenced by the insertion process; size distributions will be discussed below.

4.8.2 Island size distribution

In order to further investigate this model, we compare the normalized island size distribution of the simulation with previous models and the experimental data. Fig. 4.19 a) shows the size distribution obtained at 200 K with the optimized parameters given above. The simulated island density (black curve) has the same overall shape as the one found for exchange (green curve). It shows two modes, one at the minimum size with height 0.52 and one at $\langle s \rangle = 1$ with height 0.66. When comparing to KMC with exchange, we note that the mode at 0 is lower while the mode at 1 is higher. When comparing with homogeneous diffusion, the differences are opposite. This confirms the idea developed for the island density above, that the model with attractive insertion is halfway between the two extremes, homogeneous diffusion and exchange. Again, the attractive well depth ΔE acts as a

parameter shifting from on extreme model to the other.

Comparing the simulated island density with experiment, we note that the agreement is not as good as for the exchange model. In particular the attractive insertion model has fewer small islands than observed experimentally. In contrast, it shows more islands of the mean island size. For normalized sizes above 1.5, the agreement between the model and experimental data is within the experimental error. The physical system thus creates more small islands than the simulation does.

4.8.3 Inserted atom density

Since insertion is restricted by the condition that it can occur only on sites with pristine binding energy level, it is necessary to check whether insertion occurs at a reasonable rate. For the attractive insertion model, we plot the insertions per surface site as a function of deposition temperature in Fig. 4.19 b).

The colored curves show the effect of the attractive potential on insertion. For attractive potentials below ≈ 200 meV (upper curves), when the diffusion of monomers is not remarkably hindered by the insertion sites, the behavior is linear in the Arrhenius representation. This is expected since insertion is both thermally activated and proportional to monomer density. Monomer density is itself a linear function of temperature in the Arrhenius representation (see Fig. 4.9). At high attractive potentials ($\Delta E < 200$ meV) the behavior changes. Particularly at high temperature, less insertions are observed. This is because stronger binding at the insertion sites will favor a lower density of mobile monomers and thus lower insertion. Although insertion is a function of diffusivity D, insertion rate ν_{insert}, attractive potential ΔE, and evidently temperature, no simple analytical relation governing the behavior could be found.

In the case which fits our experimental data (black curve on Fig. 4.19 b.), we note that insertion density reaches 0.014 ML for deposition at 280 K. Using the graph as reference, we can extrapolate to ≈ 0.03 ML insertion at room temperature (at $\Theta = 0.1$ ML). For Pt/Pt(111) homoepitaxy, Bott et al. [38] estimated the saturation insertion value to ≈ 0.04 ML. Although the insertion of Co in the Pt(111) surface cannot be directly compared to Pt insertion, this value can still be used as a reference. Thus insertion densities calculated with our model seem realistic.

4.8.4 Conclusions

We presented a modified KMC code including a thermally activated insertion process. Upon realization, this process creates an attractive point on the surface with a corresponding potential energy well. This model reproduces the experiments with parameters $E_{\text{insert}} = 460$ meV and $\Delta E = -200$ meV. The island size distribution is in good agreement with the experimental data, showing a bimodal distribution with modes at the correct positions, but different heights. We also compared the density of insertions predicted by the model with values obtained experimentally for Pt homoepitaxy. The fact that the insertion densities are of the same order of magnitude strongly supports our model.

Several discrepancies still remain: As seen in the STM images, insertion leads to the creation of dislocations in the Pt surface. It is very probable that the effect of isolated inserted atoms on the adatom diffusion is not the same as the one from dislocations. Our model does not yet take into account the creation of such dislocations.

Furthermore, insertion locally creates a compressive strain field, displacing Pt surface atoms to make room for the Co atom. Density functional theory (DFT) calculations [52] show that the binding energy for an adatom is reduced on a compressively strained site. This means that regions with compressive strain, and therefore insertion sites, should act repulsively on the diffusing adatom. This is in contradiction with the model presented above. In order to investigate this possibility, we show below simulations with repulsive insertion sites.

4.9 Repulsive point-defects KMC model

Submonolayer nucleation and growth on a surface with a constant number of randomly placed repulsive impurities has been studied theoretically by Liu et al. in Ref. [73]. In this publication, the authors show that in the presence of repulsive impurities the density of stable islands does no longer follow the standard scaling law (Eq. 3.5), but that the following new scaling law becomes valid

$$n_x = B(T,c)\,\Theta^{\chi}\left(\frac{D}{F}\right)^{-\chi} \qquad \chi = \frac{\alpha}{1+2\alpha} \tag{4.17}$$

where c is the impurity density and α is the new single particle diffusion exponent. Simulations show that the function $B(T,c)$ is close to 1. Note that this scaling law reduces to the standard law for $\alpha = 1$. The parameter α obeys $0 < \alpha \leq 1$ and decreases monotonically with decreasing temperature as well as with increasing m, the density of impurities. This finding disqualifies the new equation (4.17) to predict island densities correctly, since α is a non-trivial function of temperature. The calculated values for α range continuously from 1 to ≈ 0.2. For a given impurity density (e.g. 6 %) the parameter can vary from $\alpha = 0.4$ for 110 K to $\alpha = 0.8$ for 300 K.

The remarkable result is that the island density in the presence of repulsive impurities is higher than in the homogeneous diffusion case. This leads to the surprising conclusion that both the presence of *attractive* points (see previous section) as well as *repulsive* points increase the island density. The latter can be understood when considering that repulsive impurities hinder the free diffusion of monomers. The mean dwelling time of a monomer on a site is increased and the mean square displacement is reduced. Correspondingly, the island density is higher.

We studied if this model applies to Co/Pt(111) in the case of inserted sites acting repulsively. Particularly, we were interested to know if it could lead to the island density behavior observed experimentally. To get a first idea, we performed simulations with a fixed amount of repulsive points. The KMC code is the same as in the attractive case presented above, but with repulsive potential ($\Delta E > 0$). The thermally activated insertion process is totally prohibited. Instead, a surface with randomly placed repulsive points is taken as a starting point. Each repulsive point affects the center site and its 6 nearest neighbors (see Fig. 4.16 and the corresponding repulsive potential energy diagram). No restriction is put on the site where new repulsive point can be placed. As a result, several repulsive sites overlap. For example, with 0.1 ML of surface sites being repulsive centers, not 0.7 ML but only 0.51 ML of the adsorption sites have a binding energy different from the pristine substrate. The remaining 0.19 ML overlap. For a given repulsive point density (e.g. 0.1 ML), all deposition temperature calculations were performed with the same initial potential energy surface.

Fig. 4.20 shows a typical result of a simulation at 200 K with $\Delta E = 400$ meV and 0.1 ML repulsive sites. Edge diffusion was not activated in this simulation. We observe that the Co atoms avoid the repulsive sites. The diffusion barrier seen by an adatom diffusing towards a repulsive site is $E_{\mathrm{m}} = 310$ meV while the diffusion away has a barrier $E_{\mathrm{m}} = 110$ meV. At 200 K, the corresponding diffusivity values are respectively $D = 3.86 \times 10^5$ sites/s and $D = 4.23 \times 10^{10}$ sites/s compared to the diffusivity on the homogeneous substrate $D = 2.28 \times 10^8$ sites/s. This means that diffusion away from the repulsive site is $\approx 10^5$ times more probable than diffusion towards it. Naturally this difference gets smaller with increasing temperature, but it easily explains the adaptation of the Co monomers to the potential energy surface given by the substrate.

4.9.1 Island density

We have calculated the island densities for 0.02 ML and 0.10 ML repulsive insertion sites. Both simulations, which are shown in the Arrhenius plot in Fig. 4.21, were computed with a total repulsive

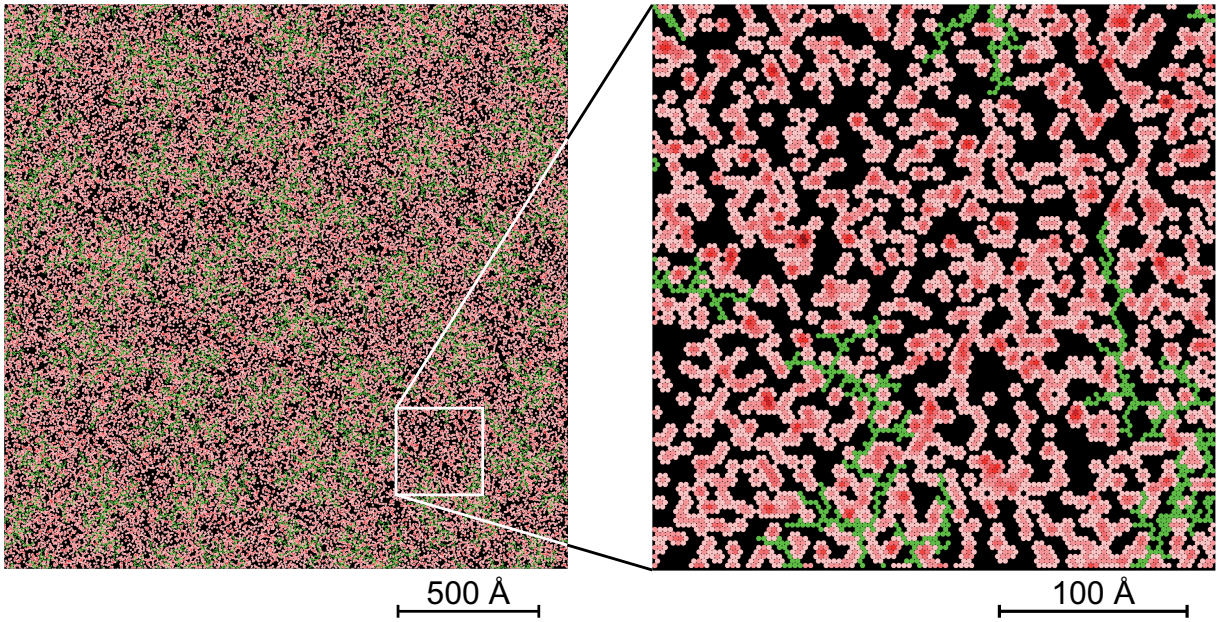

Figure 4.20: Top view of a KMC simulation ($\Theta = 0.1$ ML, $T_{\text{dep}} = 200$ K) with 0.1 ML of random placed repulsive points ($\Delta E_{\text{pot}} = 400$ meV), each reaching to nearest-neighbor sites. Repulsive sites with lower binding energy are shown in various tints of pink (darker = less bound). For contrast and clarity, Co atoms are shown in green as opposed to white on other simulation results.

barrier $\Delta E = 400$ meV. For 0.02 ML repulsive points (black curve), the difference to homogeneous diffusion is small. The overall behavior with a linear decrease of the island density is maintained. The effect of 0.02 ML repulsive impurities is thus negligible.

For 0.1 ML, we observe that the island density is higher than for 2% for deposition temperatures above 80 K. The Arrhenius plot shows two distinct regions. For $80\,\text{K} < T_{\text{dep}} < 130\,\text{K}$, the island density shows a shallower slope than expected for homogeneous diffusion. For temperatures above 130 K, the slope is steeper. The knee in the curve and so the maximum difference is at ≈ 125 K, where 2.7 times more islands are created in the presence of 0.1 ML repulsive impurities than in the 0.02 ML case. The transition at 130 K can be explained by the fact that diffusion towards a repulsive site (i.e. one potential energy level up) becomes relevant at the time scale of the experiment.

In the 0.1 ML repulsive point case, the simulated island density crosses the experimental data at ≈ 170 K. For deposition above this value, the island density derived from STM is even higher. This suggests that even more than 0.1 ML repulsive points are needed to reach the experimental values.

Making the assumption that insertion of one Co atom in the uppermost Pt layer creates one repulsive point implies that more than 0.1 ML of inserted atoms are needed in order to have the desired raise of island density. This can be excluded for two reasons: First, the insertion densities measured by Bott et al. [38] for platinum homoepitaxy show only insertion up to 0.04 ML which makes it highly improbable that more than twice this value is inserted in the Co/Pt(111) case. The second, more crucial argument, is that while the deposited quantity is kept constant for all experiments, the Co coverage observed by STM at different temperatures does not visibly vary. This indicates that the inserted number of atoms must lie below ≈ 0.02 ML for any temperature, which is the error bar of the coverage estimated by STM.

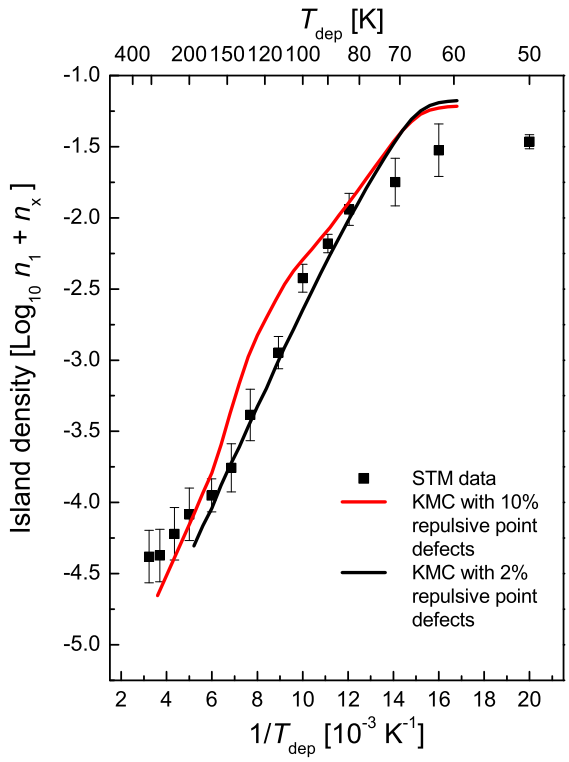

Figure 4.21: Arrhenius plot of island densities as calculated from a KMC model including a constant density of repulsive sites ($\Theta = 0.1$ ML). The presence of 0.02 ML repulsive points on the surface shows no noticeable effect on the island density.

4.9.2 Conclusions

Using a modified KMC code to include repulsive sites on the surface before deposition, we have shown that the presence of this modified potential energy surface yields higher island densities than in the homogeneous diffusion case. Although the higher island density obtained from simulation could point towards a model to explain our experimental data, the very large density of inserted atoms necessary to modify the island density makes it not a viable alternative. Furthermore, the high insertion density should lead to the creation of dislocations. Diffusion in the presence of dislocation has been studied in the next section.

4.10 Repulsive dislocations model

While it was never observed directly, the formation of surface dislocations by the insertion of Co in the uppermost layer of Pt(111) is supposed to be a process taking place in several steps. The starting point is the insertion of a single Co atom in the pristine Pt surface. This results in a circular strain field around the inserted atom. This strained site may act as the starting point of a dislocation which we can also consider as a *dislocation nucleus*. The second step, following the creation of a dislocation nucleus, is the insertion of a second atom near the first one. This will transform the circular strain of the single insertion into a non isotropic strain field with a preferred direction. In effect, this corresponds to the *growth* of a dislocation arm.

The dislocation arms grow in the $\langle 2\bar{1}\bar{1}\rangle$ directions. More precisely, if one arm grows in the $[2\bar{1}\bar{1}]$ direction, then two other arms may grow from the same point in the $[\bar{1}2\bar{1}]$ and $[\bar{1}\bar{1}2]$ direction and not in the 3 other directions, namely $[\bar{2}11]$,$[1\bar{2}1]$,$[11\bar{2}]$. These two sets of three directions cannot be distinguished on a (111) surface, without knowing which sites are the hcp and which the fcc sites. How exactly the atoms auto-arrange to favor reconstruction in these 3 directions remains unclear. From analysis of the STM images presented before (see Fig. 4.4), we note that atoms seem to favor insertion in certain regions. The inserted atoms are not distributed in a homogeneous way but accumulate along the dislocation. This indicates that, although the strained region is acting repulsively on the diffusing adatom, insertion seems to be preferred near a dislocation. From the same image we observe that precisely one atom per row is inserted. This suggests that a limiting mechanism is at work, prohibiting the insertion of a second atom in a row perpendicular to the arm growth direction.

4.10.1 KMC implementation of dislocations

Taking these information into account we have developed a KMC model trying to mimic the physical phenomenon, including the creation (nucleation) and growth of such dislocations. The model uses the following main parameters

- $E_{\text{dl-nucl}}$: the energy barrier for creation of a dislocation nucleus by insertion of a monomer.
- $n^{\text{sat}}_{\text{nucl}}$: the saturation density of dislocation nucleation.
- $E_{\text{dl-grow}}$: the energy barrier for growth of a dislocation.
- $n^{\text{sat}}_{\text{grow}}$: the saturation density of inserted atoms.
- d_{forward}: the free distance in front of the dislocation tip to allow further growth.

The primary insertion and creation of a dislocation nucleus is a thermally activated process with a corresponding energy barrier $E_{\text{dl-nucl}}$. The attempt frequency for all processes is set to the value calculated for monomer diffusion. This insertion event is possible for each monomer diffusing on

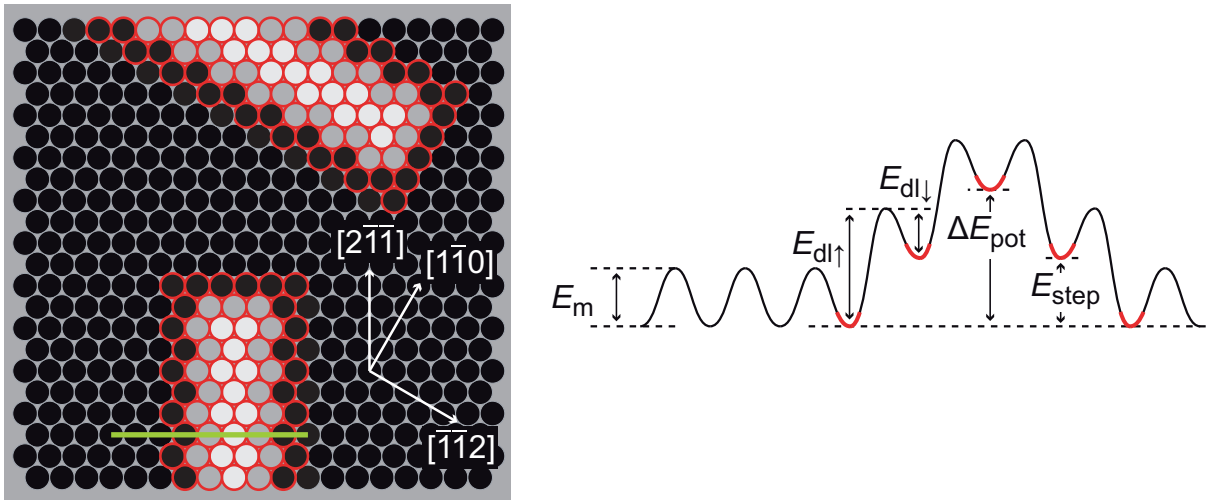

Figure 4.22: Schematic view of the KMC model with repulsive dislocations growing in the $[2\bar{1}\bar{1}]$ direction. Possible adsorption sites for adatoms are shown in black. Adsorption sites with a modified binding energy are shown in levels of gray. The potential energy experienced by an adatom diffusing along the green line is shown on the right. Red circled sites indicate adsorption sites where insertion makes the dislocation grow. The two dislocations depicted cannot cross. The minimum forward distance is set in the simulation. In the example shown, the minimum distance is 10 sites.

the surface, also for those which reside on non-pristine sites. Upon realization, the atom is removed from the surface and the potential energy levels of the sites surrounding the insertion point are modified to make them repulsive. This is very close to the insertion processes discussed in the previous two sections. Subsequently a number of sites around the nucleus are changed to become *active* towards insertion. This means that whenever an monomer is on one of those sites, another thermally activated insertion process is attached to them. This is the dislocation growth process with its own energy barrier $E_{\text{dl-grow}}$. Upon realization, the atom is removed from the surface and the corresponding dislocation is extended by one site distance in the relevant direction. Before the process update of all involved atoms and structures, the active sites are updated. The new dislocation sites are made active for insertion and growth.

Fig. 4.22 shows a schematic view of the dislocation as simulated in the KMC. The sites' gray level shows the binding energy (lighter = less bound) and the red circled sites are those which permit insertion to extend the dislocation. Two versions of the simulation exist: 1. Only the sites at the tip of the dislocation are active 2. All sites of the dislocation and its surroundings are active. The latter is the configuration shown in Fig. 4.22. Besides the potential energy height E_{step}, the code permits to choose the maximum width of the dislocation (4 in the figure) and the width of insertion sensitive (reactive) sites (6 in the figure).

As explained above, the physical system favors insertion as long as it is energetically interesting. This suggests that a saturation density of inserted atoms exist. In order to reproduce this feature correctly in the simulation, we introduce a saturation value for both the dislocation nucleation density $n^{\text{sat}}_{\text{nucl}}$ and the dislocation growth density $n^{\text{sat}}_{\text{grow}}$.

On the STM images we also observe that dislocations do not cross. To account for this, we have introduced a minimum distance which is held between the tip of a growing dislocation and another dislocation. In the schematic view, the distance is 10 sites and the vertical dislocation may not be allowed to grow any more if the minimum distance parameter assumes a value $d_{\text{forward}} > 10$. The fortunate consequence of this is that no diffusing monomer can get trapped in a closed cell surrounded

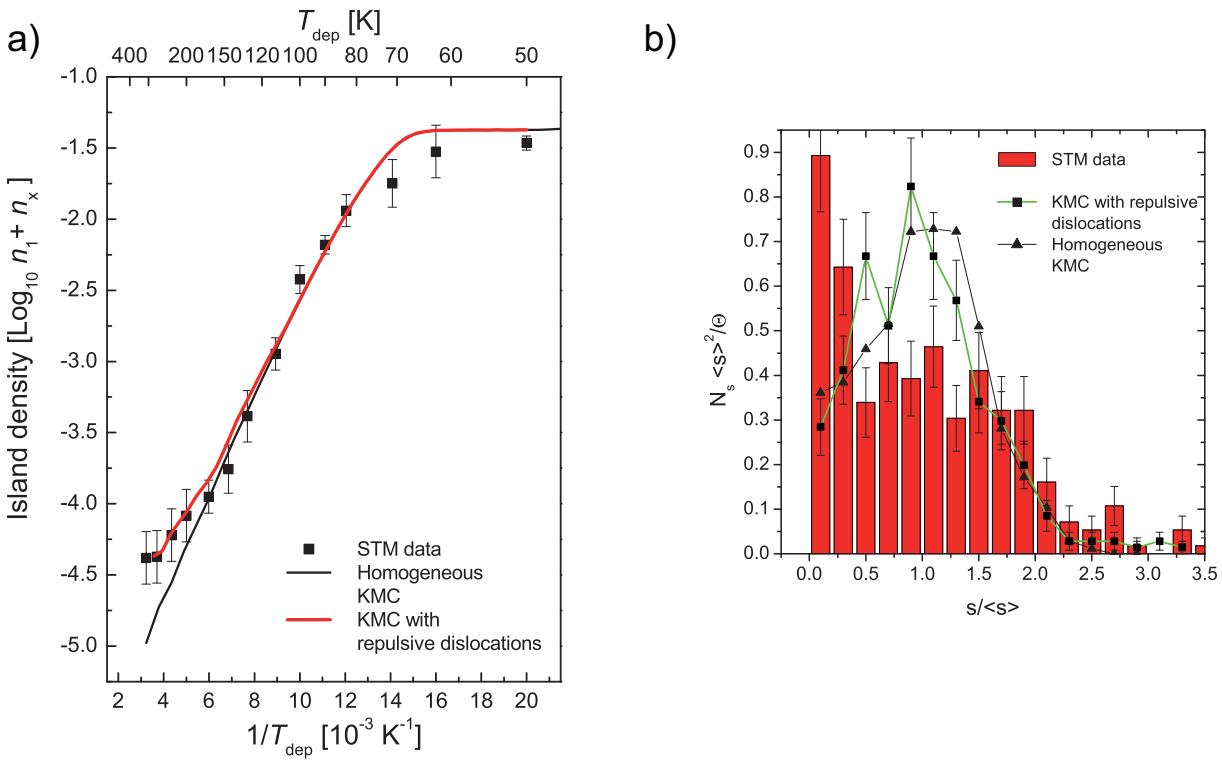

Figure 4.23: a) Red line: Arrhenius plot of the island density obtained by KMC with repulsive and dynamically growing dislocations ($\Theta = 0.1$ ML, $E_{\text{dl-nucl}} = 410$ meV, $E_{\text{dl-nucl}} = 10$ meV, $n^{\text{sat}}_{\text{grow}} = 0.02$ ML, $n^{\text{sat}}_{\text{nucl}} = 7 \times 10^{-5}$ ML). b) Corresponding island size distribution at $T_{\text{dep}} = 200$ K compared to experimental data and the homogeneous KMC model.

by repulsive dislocations. Simulations have shown that in the case where a monomer gets trapped in such a cell, the calculation time is drastically increased. Normally the diffusion of a monomer is limited because it meets an existing island or another adatom (diffusion limited by aggregation). In the case where a monomer gets trapped in a cell and the repulsive barrier is high enough to practically block all diffusion across it, the probability for the monomer to meet another monomer is limited to the deposition of another monomer inside the cell. This is naturally proportional to the cell surface C. The mean time between two depositions inside a cell is $\tau = F^{-1}C^{-1}$. Assuming a cell of 100 sites and using the experimental flux $F = 5 \times 10^{-3}$ ML/s yields $\tau = 2$ seconds. Further assuming a deposition temperature of 250 K and the usual Co/Pt(111) diffusion parameters given above, this results in $\approx 2 \times 10^{10}$ monomer diffusions. The monomer will simply wander randomly inside the cell without contributing to the final result. Evidently, this enormous number of diffusion processes makes it impossible to execute such simulations in a reasonable timescale even on the fastest computers. One could imagine possible optimizations. By checking for example if the monomer is in such a cell, and simply blocking its diffusion if a second atom is absent. However, such approaches are error-prone and difficult to code. Thus this road was not followed.

4.10.2 Simulations parameters

Island densities obtained from calculations with this model are shown in Fig 4.23. A very good agreement with the experimental island densities is observed when using the following values for the different parameters:

$E_{\text{dl-nucl}} = 410$ meV, $E_{\text{dl-grow}} = 10$ meV, $n^{\text{sat}}_{\text{grow}} = 0.02$ ML, $n^{\text{sat}}_{\text{nucl}} = 7 \times 10^{-5}$ ML,
$d_{\text{forward}} = 10$ atomic sites and $\Delta E_{\text{pot}} = 2 \times E_{\text{step}} = 700$ meV.
These values can be inferred from the following arguments: The dislocation nucleation barrier $E_{\text{dl-nucl}} = 410$ meV is determined by the onset temperature T_{dep} at which dislocation formation is experimentally observed (≈ 180 K). The island density is not very sensitive to the dislocation growth barrier $E_{\text{dl-grow}}$. This is not surprising because the sites where dislocation growth can occur are rare on the surface. Thus, the growth kinetics are governed by the geometry and the mean free path of the monomer to reach an insertion site, while the insertion barrier has a smaller influence. The latter only needs to be smaller than E_{m} so that insertion is more probable than diffusion away from the insertion site). Therefore, we chose to make this process immediate with a negligible barrier to emphasize its small effect.

The saturation insertion value $n^{\text{sat}}_{\text{grow}} = 0.02$ ML gives the best fit and is in agreement with experiment. $n^{\text{sat}}_{\text{nucl}}$ is chosen so that the saturation case corresponds to a mean dislocation arm length of ≈ 300 Å in agreement with STM images. Finally, it was determined that the total potential energy barrier for crossing a dislocation needed to be high enough for the dislocation to act as total diffusion barrier up to 310 K ($\Delta E > 700$ meV). This is fully supported by the following calculation. We observe in Fig. 4.4 that two quasi-pseudomorphic regions are separated by 20–25 atomic rows forming the dislocation. Having one inserted atom per row thus yields a compressive strain between 1/25 and 1/20 or 4–5 %. For comparison, the herringbone reconstructed Au(111) surface has a compressive strain of 4.5% [74]. Strain dependent calculations of binding energies done by DFT calculations [52] for Co/Pt(111) show that the binding energy difference across a dislocation should be in the range of $640\text{ meV} < \Delta E < 840$ meV with the above calculated strain values (using a linear extrapolation of the data in Fig. 3 of Ref. [52]). The very good agreement with our value strongly supports our model. The DFT calculations also show that the migration barrier is reduced in regions with compressive strain. However, in our case the rate limiting factor for diffusion across a dislocation is not the migration barrier but the binding energy in the potential energy landscape. Fig. 4.24 shows a top view of a simulation with repulsive dislocations at 180 K. The figure shows the evolution in time and coverage. We observe that at the early stage of deposition (a) the first dislocations get created and concurrently the first islands nucleate. The creation of new dislocation nuclei happens very fast at the beginning of deposition up to the dislocation nucleation saturation level $n^{\text{sat}}_{\text{nucl}}$. This level is typically reached after a deposition of 1.25×10^{-3} ML at $T_{\text{dep}} = 180$ K. In the following stage, dislocations grow simultaneously with the nucleation and growth of islands. The saturation of insertion which prohibits any further growth of the dislocations is reached after ≈ 0.022 ML. Subsequent to the creation of all dislocations, the growth and nucleation of islands continues on the heterogeneous substrate.

At lower temperatures, e.g. 140 K, the creation of dislocation nuclei is rare, but as the growth energy barrier is held low (10 meV in the above simulation), these few dislocations will grow rapidly and create a network of a few very long dislocations.

4.10.3 Island densities

Using the above mentioned parameters we have calculated the corresponding island densities which are presented in Fig. 4.23. When comparing the dislocation model results (red curve) with the homogeneous diffusion model (black curve), one notices that the Arrhenius plot is divided in three parts. For deposition temperatures below 140 K, no noticeable difference between the two models can be detected. For depositions between 140 K and 170 K, the slope becomes slightly shallower and higher island densities than for the homogeneous model are measured. Finally, for deposition temperatures above 170 K, the simulated island density diverges from the homogeneous model. The island density is higher, with a *constant* and remarkably shallower slope compared to the simple monomer diffu-

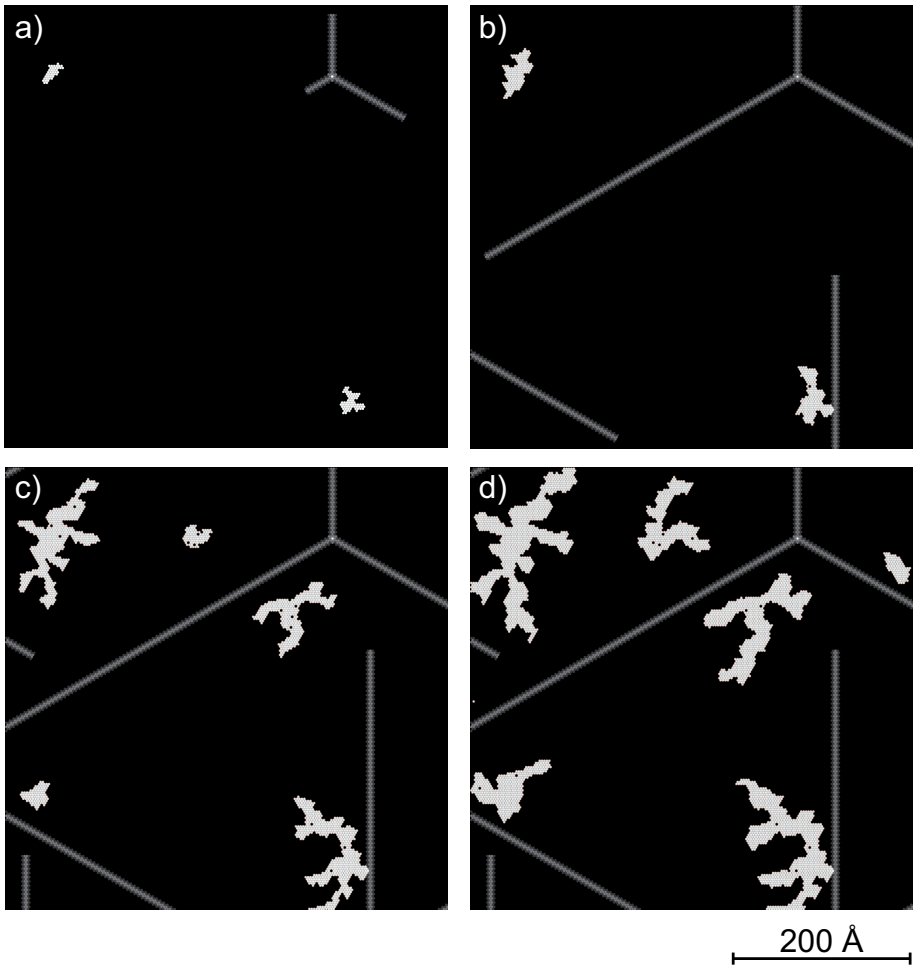

Figure 4.24: Time evolution of the surface during deposition, calculated by KMC simulation with reconstructing substrate at $T_{\mathrm{dep}} = 180\,\mathrm{K}$ ($E_{\text{dl-nucl}} = 410\,\mathrm{meV}$, $E_{\text{dl-nucl}} = 10\,\mathrm{meV}$, $n^{\mathrm{sat}}_{\mathrm{grow}} = 0.02\,\mathrm{ML}$, $n^{\mathrm{sat}}_{\mathrm{nucl}} = 7 \times 10^{-5}\,\mathrm{ML}$) . Co islands are shown in white. Dislocations are shown as gray lines.
(a) $\Theta = 0.005\,\mathrm{ML}$ (1 s)
(b) $\Theta = 0.02\,\mathrm{ML}$ (4 s)
(c) $\Theta = 0.05\,\mathrm{ML}$ (10 s)
(d) $\Theta = 0.10\,\mathrm{ML}$ (20 s)
Creation of dislocation nuclei takes place at the very early stage of deposition. Island nucleation and dislocation growth happen concurrently up to the saturation of insertion (0.02 ML inserted atoms). Above 0.02 ML inserted atoms, the evolution is dominated by growth and nucleation on the anisotropic substrate.

sion model. As explained below, a fourth regime would be expected for even higher temperatures ($T_{dep} > 310$ K). However, this is not relevant from the physical point of view, as the system changes its growth behavior radically at these temperatures by nucleating double-layer islands and Co dendrites.

These three regions can be explained in the following manner: In the low temperature regime, the insertion process which creates dislocation nuclei is effectively inhibited. As no dislocation nuclei are created, their growth cannot take place and the island nucleation of the system is practically homogeneous. Insertion and thus creation of dislocation starts at ≈ 140 K. This process rapidly creates the randomly placed dislocation nuclei. Growth of those dislocations is limited by the short mean free path of diffusing monomers. The dislocation network grows simultaneously while island nucleation and growth take place. The simulation results show that islands cross dislocations. However, in accordance with DFT calculations, the repulsive energy barrier of the dislocations is chosen high enough to act as insurmountable barrier on the complete temperature range studied. This proves that dislocations have grown below already nucleated islands on the surface. Most monomers will not interact with a repulsive dislocation before nucleating an island. Therefore, the impact on island density is small. At temperatures above 170 K, the higher island density is the combined result of a higher dislocation density and a longer mean free path of the monomer. The dislocation nuclei form as soon as deposition starts and the mean free path of monomers is long enough to reach these nuclei, causing a fast development of the dislocation network. As an example, at 180 K (see Fig. 4.24) the dislocation network is finished after deposition of 0.022 ML. While 0.02 ML of this coverage are inserted in the surface to create the dislocations, only the remaining 0.002 ML are involved in the nucleation and growth of the islands on the heterogeneous substrate. Nucleation on this reconstructing surface can thus be understood as a two step process. First, the dislocation network is created followed in a second step by nucleation and growth of the islands. As the mean free path is long enough, nearly all monomers will interact with at least one dislocation before nucleating and forming an island. The result is a reduced mean square displacement of the monomer and higher island density.

Fig. 4.23 a) also compares the simulated island density with the STM results. We note the excellent agreement between the model and measured data. Both the low temperature regimes as well as the high temperature *linear* behavior are well reproduced. This strongly supports the model with rapidly growing, repulsive dislocations.

Fig. 4.23 b) shows the island size distribution obtained by the model at 200 K (green curve). The results are noisy due to a lack of statistics. This affects particularly the size distribution as the total number of islands is divided into ≈ 14 sizes categories, thus augmenting the relative error of each category. To quantify the error we have included error bars relative to a Poisson process. The results show that the model with dynamic dislocation growth produces a mono-modal sizes distribution. The mode is somewhat shifted to lower sizes (0.8) when compared with the distribution obtained by homogeneous diffusion (1.0). The height of both modes is comparable. However, the fit does not agree well with the experimental data which show a majority of small islands whereas the simulation produces mainly islands around the mean size. The bi-modal form of the data obtained from STM is not reproduced. Explaining the presence of a such a high density of small islands remains a challenge for the model.

As an overview of the simulation results, Fig. 4.25 shows side-by-side comparisons of STM versus KMC for the complete temperature range studied. At 62.5 K (Fig. 4.25 a.), when diffusion is not yet activated, we can precisely see the diversity of island sizes present in the KMC simulation. Elongated clusters form due to the easy attachment discussed above. They coexist with monomers, dimers and larger islands. The comparison with the STM image confirms that the island density is well reproduced. From the experimental data it is difficult to extract exact island sizes and morphologies due to tip convolution, but the diversity of dot sizes points towards a relatively large island size distribution in accordance with simulation. At $T_{dep} = 130$ K (Fig. 4.25 b.), the islands are ramified. Again,

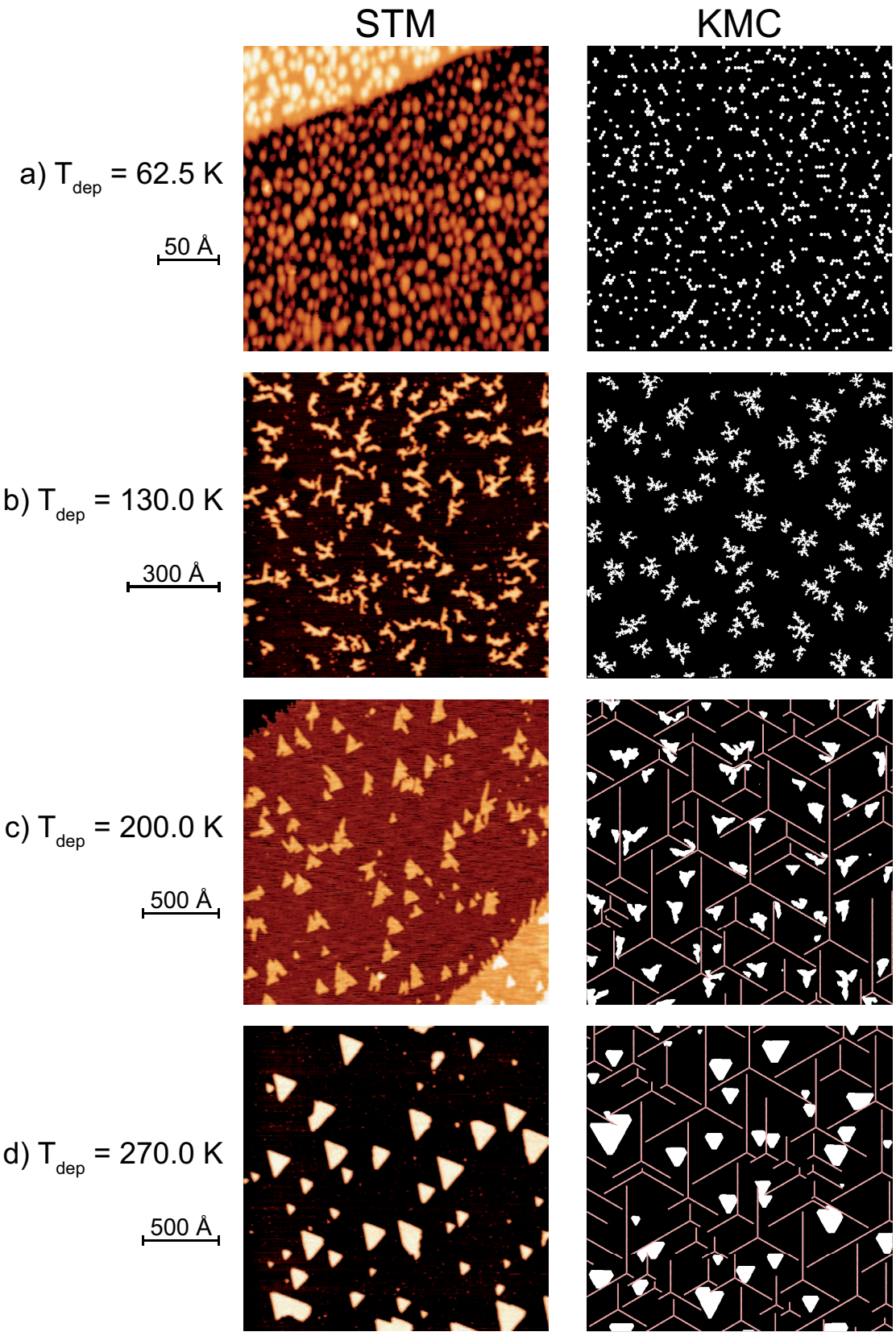

Figure 4.25: Direct on scale comparison of STM data with KMC simulations including dynamic dislocation creation. The simulated density and morphology of the islands, as well as the size distribution (right) are in excellent agreement with the experimental data (left). For each temperature, experimental images and simulation results are of the same size.

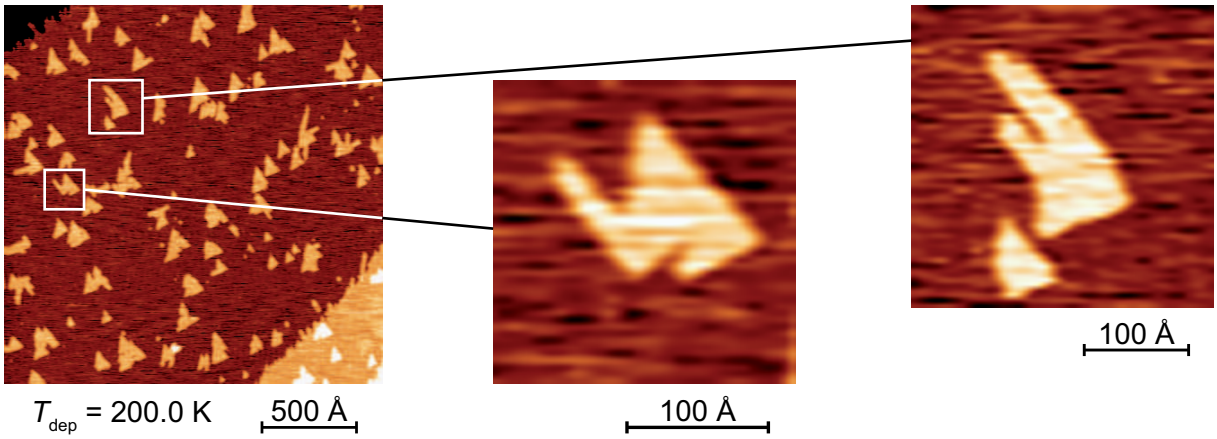

Figure 4.26: Detail view of 0.1 ML Co/Pt(111) islands grown at 200 K. The detail shows that some islands feature long Co arms. It is suggested that these shapes form by growth around the repulsive barrier of a dislocation. Simulation reveals that dislocations present during growth may be responsible for these shapes (e.g. see island on the left of the KMC image in Fig. 4.25 d.).

the density and morphology of the islands, as well as the size distribution are well reproduced by the simulation. For depositions at 200 K (Fig. 4.25 c.), the experimentally observed island shapes are more compact than those obtained at 130 K. This experimentally measured island morphology is –as well as the overall island density– very well reproduced by the KMC simulations. Particularly, we note that some islands in the STM images show arms or dendrites (see enlarged view in Fig. 4.26). Those features are well reproduced in the simulation by islands growing around dislocations (e.g. see large island on the left side of the simulation in Fig. 4.25 d). The KMC image at 200 K shows a completely developed dislocation network. However, the STM image does not exhibit those dislocations (this finding will be addressed below). The deposition at 270 K (Fig. 4.25 d.), results in the formation of compact triangular islands. The corresponding simulation shows that the density and morphology of the islands are again in good agreement with the experiments, although STM images show a wider island size distribution than obtained from simulation. As for 200 K already, the KMC simulation shows a fully developed dislocation network which cannot be seen in the experimental images.

Simulations suggest that more dislocation lines might be present during deposition than the ones visible on the STM images. As pointed out above, some islands feature long arm shapes (Fig. 4.26) which are not expected to form by simple growth and edge diffusion. Such morphologies are reproduced by simulation when an island has grown around an existing dislocation. This finding suggests the existence of dislocations during island growth of those islands. Moreover, homoepitaxy deposition experiments on Pt(111) show a dense dislocation network (see Fig. 4.27 a.) which is very similar to our KMC simulated dislocation network of Co/Pt(111) (see Fig. 4.25 d.). In addition, an island density by a factor ≈ 10 times higher is reported on these densely reconstructed regions [75] with a bimodal island size distribution [76]. A similar behavior, even at lower temperature, can be expected for Co/Pt(111). This brings up the question why only a few dislocations can be seen in the STM images. A tentative explanation is that the creation of Co islands on Pt introduces an additional stress on the surface due to the 10.6 % lattice mismatch. This may relieve or move the dislocations subsequent to the deposition. An additional argument for the existence of a complete dislocation network is the work of Kalousek et al. [77] in which a dense network of Co/Pt(111) dendrites is observed at higher temperature (310 K). As it has been shown previously [40, 41], the dendrites grow on top of the Pt surface dislocations. This implies that, before the development of the dendrite network, a corresponding

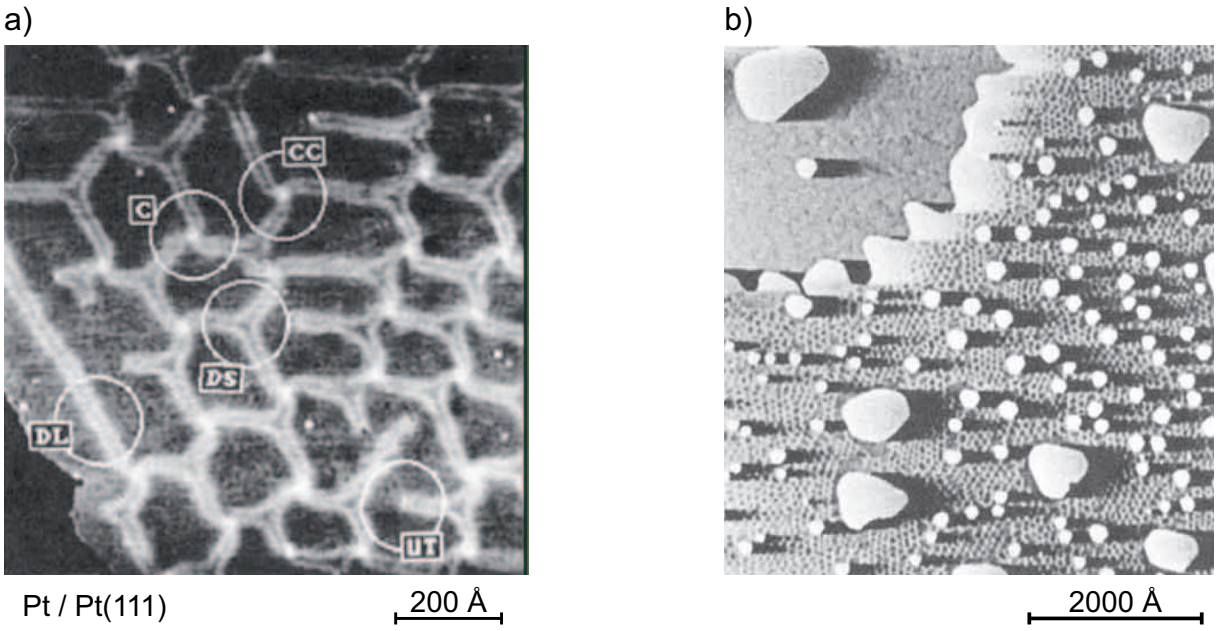

Figure 4.27: a) STM image of 0.3 ML of Pt/Pt(111) deposited at 630 K. The Pt surface reconstructs into a complete dislocation network very similar to the one simulated by KMC for Co/Pt(111). b) Pt islands show a bimodal growth behavior. The absence of a lattice mismatch between the Pt islands and the Pt substrate explains the stability of the dislocations even after deposition, thus influencing nucleation and growth (Both images from Ref. [38]).

dislocation network was present, although this cannot be seen on the STM images. Island nucleation and growth would then be a three step process: 1. Insertion and development of a complete dislocation network; 2. Nucleation and growth of Co islands on the heterogeneous substrate; 3. Relief of dislocations by the additional stress introduced by the Co islands.

4.10.4 Conclusions

We have shown KMC simulations including the dynamic creation of repulsive dislocations in the course of deposition. The model's main parameters are the insertion barrier for the creation of dislocations and the overall density of inserted atoms. The former value is determined experimentally to $E_{\text{dl-nucl}} = (410 \pm 30)$ meV by the lowest T_{dep} at which dislocations in the Pt surface are observed. The large error bar is due to the fact that the effect of the dislocations is small at this temperature and that it is convoluted with the effect of the mean free path of the diffusing monomers. The latter parameter, the overall density of inserted atoms, is the actual fitting parameter with the largest effect on the island density. The optimal value is $n_{\text{grow}}^{\text{sat}} = 0.02$ ML which is in agreement with estimations derived from Pt/Pt(111) experiments and our own experimental observations.

The fact that dislocations act repulsively on diffusing monomers is corroborated by DFT calculation which predict repulsive strained regions with energy barriers in the range of those found in our simulation. Particularly, growth experiments of Pt/Pt(111) [38] show that the dislocation network of the Pt(111) surface inhibits diffusion of the adatoms and thus promotes a higher island density and smaller islands.

The KMC model results in a relatively dense repulsive dislocation network which is not observed in this form in the STM images. Although such a high density of dislocation cannot be seen exper-

imentally, several arguments point toward the fact that the dislocations are indeed present during nucleation and growth of the islands. The excellent agreement of the island density in simulation and the experiment over the complete temperature range strongly supports the proposed model. Furthermore, the island shape indicates that islands grow by adapting to repulsive straight regions on the surface. Finally, a comparable dislocation network is observed in homoepitaxy experiments. The absence of a visible dislocation network on the STM images is ascribed to the additional stress induced by Co islands on the strained reconstructed surface. The partial reconstruction relief in the presence of Co islands can tentatively be explained by the following suggestion: The additional stress may distribute the strain more uniformly so that it is no longer visible as apparent height differences in STM images.

4.11 Island morphology

All main simulation results presented above are calculated using activated edge diffusion (also called perimeter diffusion in the literature, to differentiate it from diffusion along a substrate step). As described in section 3.3.2, p. 20 presenting the KMC algorithm, several processes are available for adatoms with finite lateral coordination. These are classified by the number of nearest neighbors at the starting site and the final site. Furthermore, a difference is made between diffusion along A and B type step edges and corners.

In the calculations presented above, re-evaporation from the island edge is forbidden. We are in the irreversible growth case and the edge diffusion barriers will mainly influence the cluster shape. The effect on the island density is limited. In fact, only the capture coefficient of an island is modified by the shape. The capture cross section of a ramified island of a given size s might be somewhat larger than the same island with a compact shape, but the overall effect on the island density is small.

Several previous studies [78, 79] were focused on the concerted effect of these edge diffusion processes on the island shape. They reveal that the anisotropy between A and B type *corner crossing* processes is responsible for the triangular shape of islands at high temperature. This is in contrast with the intuitive image that diffusion along the straight island edge, differentiated by the A and B type, is the decisive factor. Applying the insights acquired in those studies, we have determined optimal edge diffusion parameters which reproduce the experimental data. The comparison with experimental result has already been shown in Fig. 4.25. The corresponding energy barriers are shown in the table below.

Diffusion type	Energy barrier
$E^A_{1\to1}$	not authorized
$E^B_{1\to1}$	not authorized
$E^A_{1\to2+}$	290 meV
$E^B_{1\to2+}$	290 meV
$E^A_{2\to1}$	430 meV
$E^B_{2\to1}$	470 meV
$E^A_{2\to2+}$	415 meV
$E^B_{2\to2+}$	445 meV

Table 4.2: Activation energy barriers for edge diffusion processes of Co/Pt(111). Note that in contrast to Ref. [78], the E in the table stands for *energy barrier* and not *edge diffusion*.

The results show that the anisotropy resulting in the compact, triangular form at deposition temperatures above 200 K is distributed on the edge-to-corner ($E_{2\to1}$) and the edge-to-edge ($E_{2\to2+}$) dif-

fusions. The corner-to-corner crossings are totally inhibited, principally to forbid dimer diffusion. The sole effect of this choice is that compact islands cannot reduce to a pure triangular shape surrounded exclusively by A (or B) steps as the corner crossing from one A step edge to another A edge is not possible. In order to properly account for this, a distinction between a dimer corner-to-corner and larger island corner-to-corner diffusion would have to be introduced.

4.11.1 Second layer nucleation on strained Co islands

An additional finding while studying the STM image in Fig. 4.3 of Section 4.3 concerns the second layer nucleation. Second layer islands are small and ordered on a triangular lattice with a periodicity of 27 Å. This growth behavior can be explained by noticing that the first layer Co islands relieve the stress due to the 10.6 % lattice mismatch with the Pt substrate by creating dislocations. These dislocations, which are present in the first-layer Co islands, separate hcp and fcc (pseudomorphic) stacked regions forming a triangular network of cells. The selective nucleation of second layer islands in those cells suggests that the dislocations act repulsively on the diffusion of Co/Co/Pt(111).

Using the expression for the characteristic hopping rate which was introduced above (see Page 46), we can estimate a lower bound for the diffusion energy barrier that the dislocation imposes on a Co adatom. Taking $\nu_{\text{char}} \approx 1$ Hz and using

$$\nu_{\text{char}} = \nu_0 \exp\left(\frac{-E_{\text{char}}}{k\ T_{\text{dep}}}\right) \tag{4.18}$$

with $T_{\text{dep}} = 200$ K, we find $E_{\text{Co/Co/Pt(111) dislocation}} > 550$ meV. As a reference, we recall that Co diffusion across a Pt(111) surface dislocation has a barrier of ≈ 700 meV.

4.12 Annealing experiments

It has been shown by field ion microscope (FIM) experiments by Wang and Ehrlich [80] for Ir/Ir(111) or Kyuno and Ehrlich [81] for Pt/Pt(111), that the bond energy of the dimer can be strong enough to permit dimer diffusion at lower temperatures than dimer dissociation. This is in contrast to 2D Ostwald ripening observed for example on Ag/Pt(111) [82, 45] where immobile small islands re-evaporate their border atoms and thus disappear in favor of larger islands before their diffusion is activated.

The difference between these two behaviors is particularly evident in ripening experiments, where one deposits adatoms at low temperature and monitors by means of STM the mean island size after annealing steps at increasing temperatures. This gives insight into activation temperatures of diffusion or dissociation processes, and thus allows estimations of energy barriers.

4.12.1 STM study

In order to establish a consistent, reproducible and well known initial condition, experiments with a low density of Co monomers on the clean Pt(111) surface have been performed.[3] This is done by statistical growth of 0.01 ML Co at 50 K. As has been explained in Ref. [45] and above in Section 4.4, in the case of statistical growth the mean island size depends on the coverage and on the easy attachment behavior. Using the relevant parameters, KMC simulations show that islands have a mean size $\langle s \rangle = 1.1$ atoms. A size analysis reveals that 91.4 % are monomers, 7.8 % are dimers and the remaining 0.8 % are mainly trimers (see also brown bars in Fig. 4.28 b.).

Following deposition, the sample is heated up to the annealing temperature T_{ann} and kept there for 30 min. After annealing, STM images are recorded in order to determine the size of the islands.

[3] Experiments were performed by S. Rusponi et al.

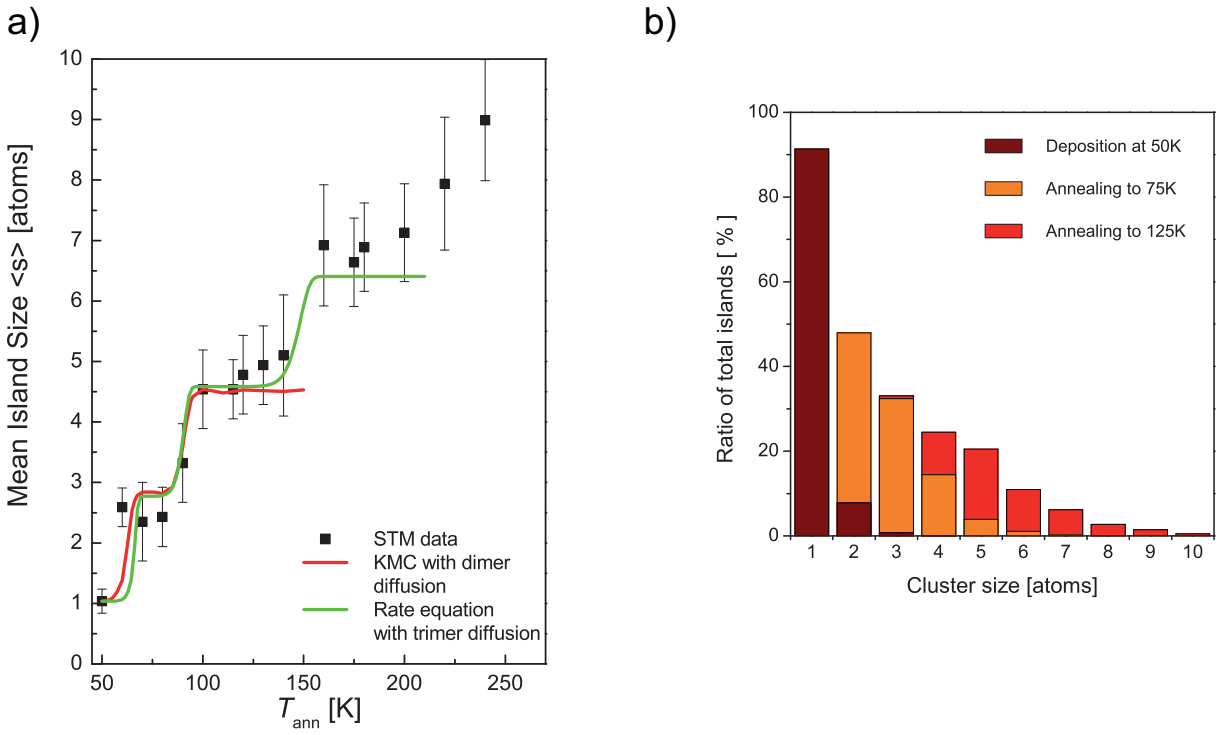

Figure 4.28: Evolution of the island size as a function of annealing temperature. A low density of Co monomers is deposited at 50 K on the Pt(111) surface and subsequently annealed at increasing temperatures.
a) Mean island size versus annealing temperature. The mean island size shows three steps indicating the onset of monomer (70 K), dimer (90 K), and trimer diffusion (160 K). Red curve: KMC simulation with monomer and dimer diffusion. Green curve: RE simulation with monomer, dimer and trimer diffusion.
b) Simulated island size distribution calculated using KMC. Brown bars: Original deposition at 50 K including easy attachment. Orange: After annealing at 75 K which activates monomer diffusion. Red: After annealing at 125 K which activates dimer diffusion.

By repeating this process for a large range of annealing temperatures and recording the mean island size, a complete ripening profile could be produced. The mean island size as a function of annealing temperature is shown in Fig. 4.28 a), where the squares indicate experimental data.

The plot shows that the mean island size increases monotonically with annealing temperature. It reveals a *stepwise* increase with the first level starting at 60 K with a mean size $\langle s \rangle = (2.45 \pm 0.15)$ atoms. The second level starts at 90 K and exhibits a mean island size $\langle s \rangle = (4.78 \pm 0.2)$ atoms, while the third has an onset at 160 K with a size $\langle s \rangle = (6.0 \pm 0.25)$ atoms. This last plateau lasts up to 200 K. For higher annealing temperatures, the mean sizes increase continuously with temperature.

It is evident that this behavior cannot be explained by 2D Ostwald ripening which predicts an exponential increase of the mean size above an onset temperature [82]. In order to explain this result simulations including small cluster diffusion have been performed.

4.12.2 Simulating annealing by KMC

KMC simulations including monomer and dimer diffusion have been performed using the monomer diffusion barrier and attempt frequency determined by the growth experiments shown above. Using the same attempt frequency for dimer diffusion and an energy barrier $E_{m2} = 270$ meV we obtain the red curve on Fig. 4.28 a). As seen in the graph, the simulation reproduces the stepwise size increase

very well. This fact can be explained in the following way:

Up to ≈ 70 K the Co monomer does not diffuse at all and the mean size stays constant at $\langle s \rangle = 1.1$ atoms as obtained by statistical growth. With the onset of monomer diffusion above 70 K, the simulated mean size augments to $\langle s \rangle = 2.8$ atoms which is in good agreement with the experimental value. Note that this part of the calculation was done with the previously determined parameters E_m and ν_0. The good agreement in the onset temperature of monomer diffusion in the annealing experiment further confirms the previously obtained values. The increased island size results from diffusing monomers which join to form dimers, trimers and also tetramers which represent 14 % of all islands. The complete size distribution (orange bars in Fig. 4.28 b.) shows that subsequent to the annealing process, no monomers are left on the surface since they all have aggregated into stable islands. Analysis of the process time evolution in the KMC simulation shows that at 75 K, 98 % of all diffusions (monomer & dimer) take place in the first 5 minutes of annealing.

The second step at 90 K is attributed to the onset of dimer diffusion. The energy barrier of dimer diffusion is extracted by fitting the onset temperature at which the size increase is experimentally observed. The extracted barrier $E_\mathrm{m2} = 270$ meV is in very good agreement with the dimer diffusion barrier $E_\mathrm{m2} = 250$ meV calculated from molecular dynamics in Ref. [59]. In this second step, the simulated mean size increases to $\langle s \rangle = 4.5$ atoms which is also in remarkable agreement with the experimental value. This mean size after the onset of dimer diffusion is not dependent on any free parameters. The excellent agreement between experiment and simulation thus supports the supposition that the mean size increase in the physical system is caused by dimer diffusion.

The size distribution simulated after the onset of dimer diffusion (red bars in Fig. 4.28 b.) indicates that all dimers have aggregated into larger islands. The distribution spans island sizes up to 10 atoms, but ≈ 80 % of islands are trimers, tetramers and pentamers. The time evolution reveals that at 125 K, 99.9 % of diffusions take place in the first 15 seconds of annealing.

4.12.3 Simulating annealing by RE

In analogy to the previous results, the third plateau which starts at a temperature of 160 K is attributed to trimer diffusion. The present form of the KMC does not permit trimer diffusion.[4] To cope with this fact, we adapted the rate equation approach to include trimer diffusion. We write the equations in a more general form, suitable for diffusion to a size s_max. As a consequence, the equations need be written with k taking values from 2 to s_max:

$$\frac{\mathrm{d}n_1}{\mathrm{d}t} = F - \sum_{j=1}^{s_\mathrm{max}} \sigma_j \, (D_1 + D_j) \, n_1 n_j - \sigma_x \, D_1 \, n_1 n_x + U_{\mathrm{di}\,1} \tag{4.19}$$

$$\frac{\mathrm{d}n_k}{\mathrm{d}t} = \sum_{j=1}^{\lfloor k/2 \rfloor} \sigma_{j,k-j} \, (D_j + D_{k-j}) \, n_j n_{k-j} - \sum_{j=1}^{s_\mathrm{max}} \sigma_{j,k} \, (D_j + D_k) \, n_j n_k - \sigma_{k,x} \, D_k \, n_k n_x + U_{\mathrm{di}\,k} \tag{4.20}$$

$$\frac{\mathrm{d}n_x}{\mathrm{d}t} = \sum_{j=1}^{s_\mathrm{max}} \sum_{l=s_\mathrm{max}+1-j}^{s_\mathrm{max}} \sigma_{j,l} \, (D_j + D_l) \, n_j n_l + U_{\mathrm{di,x}} \tag{4.21}$$

where $\lfloor x \rfloor$ represents the *floor* function describing the closest integer equal or smaller than x and U_di is the direct impingement term.

The solution is now a two step process: First, a solution of the deposition part at 50 K is calculated which leads to the initial densities of monomers (n_1), dimers (n_2), trimers (n_3) as well as larger stable and immobile islands (n_x). These values are taken as an initial condition for the second calculation,

[4] Trimer diffusion has been implemented in a branch of the KMC framework by S. Berning [83] during an internship in our labs.

where the deposition flux is set to 0 and the temperature is chosen according to the annealing point. In this second part, the differential equations are integrated for a time corresponding to a annealing of 30 min, as in the experiment. The resulting densities permit the calculation of the mean island size $\langle s \rangle = \frac{\Theta}{\sum_{j=1}^{x} n_j}$.

The mean island size calculated from these equations is shown as the green curve in Fig. 4.28 a). For equivalent energy barriers we note the excellent agreement between the two simulation methods, KMC and RE. While after the onset of dimer diffusion the mean size extracted from KMC stays constant for higher temperatures, the mean size extracted from solving RE yields an additional step with the onset of trimer diffusion. The energy barrier ($E_{\mathrm{m3}} = 440\,\mathrm{meV}$) associated with this diffusion is extracted by fitting the step to the experimental data. This is again consistent with the corresponding ($E_{\mathrm{m3}} = 480\,\mathrm{meV}$) value calculated by MD [84]. The mean island size obtained with activated trimer diffusion is $\langle s \rangle = 6.4$ atoms. A corresponding island size distribution cannot be extracted from the RE since these equations have not been written for all larger sizes. Moreover, it is known [23] that correct size distributions are hard to obtain using RE. The above mentioned reference emphasizes the dependence of capture numbers on the island sizes and densities. To our knowledge, capture coefficients for diffusing clusters have not been determined up to now.

4.12.4 Conclusions

A novel and easy method for manufacturing small-sized clusters by ripening which has been developed in our lab was presented. We focused on understanding the processes underlying the stepwise increase of mean island size during annealing at increasing temperatures. Our simulations show that cluster diffusion is responsible for the observed behavior. From this data, we were able to extract both dimer and trimer diffusion activation barriers in good agreement with theoretical *ab initio* calculations.

The narrow and easily reproducible size distribution at the steps is promising for research applications. As an example, the study of physical properties of very small clusters by integrative methods (e.g. Kerr effect, XMCD etc.) demands the controlled creation of large quantities of these islands. Our models give insight into the mean size and the exact size distribution expected from annealing.

Both methods, the experimental as well as the simulation approach can be extended to other systems with high dimer binding energies as for example Pt/Pt(111) [85]. The corresponding annealing experiments also show a stepwise increase in mean size and permit the extraction of the relevant diffusion energy barriers [55]. G. Moulas et al. have performed similar experiments for Fe/Pt(111) [86]. Preliminary analysis of the results using our simulation indicate that dimer and trimer diffusion have undistinguishable activation barriers of only 285 meV (supposing an attempt frequency $\nu_0 = 1 \times 10^{13}\,\mathrm{Hz}$).

4.13 Conclusions

We have presented a complete analysis of the submonolayer growth of cobalt on the Pt (111) surface at temperatures below 310 K. A thorough understanding of the nucleation and growth properties of this system is of great interest because it is a model system for the development of novel magnetic recording materials. The system is also appealing with respect to the subject of island nucleation and growth since it allows an investigation of the heteroepitaxial nucleation on a surface subject to reconstruction. We show that the Pt(111) surface reconstructs by insertion of Co adatoms in its topmost layer for substrate temperatures above 180 K.

By comparing experimental data with KMC and RE simulation we were able to show that at low temperatures, where the monomer diffusion is frozen, Co/Pt(111) is subject to easy attachment or

transient mobility. We argue that this easy attachment is effective to the third neighbor sites. A similar behavior was previously observed experimentally for Ir/Ir(111).

The joint analysis of island density measurements and annealing experiments permit to extract all relevant activation energy barriers like the diffusion of monomers (200 meV), dimers (270 meV) and trimers (440 meV) as well as the corresponding attempt frequency 1×10^{14} Hz. Edge diffusion barriers have also been obtained by detailed analysis of the island shape as a function of deposition temperature.

Understanding the exact processes involved at deposition temperatures above 180 K where the Pt surface reconstructs has been a major part of the work. With the onset of reconstruction, the island density and the island size distribution are both modified with respect to the known monomer diffusion models. The measured island density is larger than the one expected by homogeneous diffusion, while exhibiting a linear curve in the Arrhenius plot. The island size distribution shows a bimodal distribution with a majority of small islands.

We have presented four different models in order to understand the physical phenomenon responsible for this evolution:

1. A place exchange model which is known to yield higher island densities than homogeneous diffusion. We show that the exchange model does indeed produce a very well fitting island size distribution. However, above a threshold temperature, the island density augments with increasing temperature in contrast to the experimentally observed behavior. This model is also unfavorable from an energetic point of view because the Pt surface is under tensile stress which can be relieved by incorporating new atoms.

2. In the second model, Co adatoms can insert in the topmost Pt layer. By adding a localized circular strain field, the inserted sites attract diffusing monomers. Fitting the experimental data, using as parameters the insertion activation barrier (460 meV) and the potential well (200 meV) created by insertion, leads to a convincing fit of the island density versus deposition temperature. While in this model a high density of small islands is still present, this approach does not reproduce the experimental bimodal size distribution. Furthermore, the fact that negative strain induces an attractive potential is in contradiction with *ab initio* DFT calculations for Co/Pt(111) which predict a repulsive effect.

3. Taking the considerations of the second model as a lead, we developed an approach with repulsive impurities which also results in higher island densities than a simple homogeneous monomer diffusion model. Our simulations show that a density of inserted atoms above 0.1 ML is necessary to have noticeable effect on the island density. This is not compatible with our experimental observations and previous work on the insertion of Pt in Pt(111) limiting the density of inserted atoms to less than 0.04 ML.

4. We finally proposed a model which mimics the creation of repulsive dislocations on the Pt(111) surface. The most important free parameter of the model is the saturation density of inserted atoms which are responsible for the dislocations. This density has been tuned to fit the experimental data and yields 0.02 ML inserted atoms. This value is in good agreement with the insertion density expected from experiments. The relatively dense dislocations network visible in the KMC simulations is not observed experimentally in the STM images. With respect to this observation we propose that the deposition of Co islands relieves the dislocations after deposition by inducing an additional stress on the Pt surface. Besides, we note that the simulated island size distribution does not exactly reproduce the high density of small islands observed experimentally. A possible process would be that inserted atoms are ejected from the substrate

surface subsequent to the deposition; maybe under the influence of the additional stress induced by Co islands. This explanation is also tentatively proposed by Lundgren et al. [41] for the creation of Co dendrites. However, the island density is in perfect agreement with experimental data. In addition, the shape of the islands observed in STM images points towards growth on a substrate with repulsive line regions. These two findings strongly supports the validity of our model.

The repulsive dislocation model applies (with adapted parameters) to all epitaxy on reconstructing surfaces. In particular, it would be interesting to model the nucleation of Pt on Pt(111) at temperatures above 400 K, when the Pt surface reconstructs in a dense dislocation network. In fact, the work of Bott et al. [38] has shown that the island density is highly influenced by the presence of these dislocations.

Chapter 5

Growth and nucleation of Co/Ru(0001)

In the previous chapter we have shown a complete study of the submonolayer growth of Co/Pt(111) below room temperature. The reason for keeping temperatures low in this system is that the growth mechanism changes at higher temperatures. In particular, the Co diffuses into the Pt bulk at temperatures above 375 K. The tendency for two metals to intermix is measured by the segregation energy of the one specie versus the other. This is the difference in total energy between the systems with the impurity atom in the host's bulk and at its surface. Using DFT methods, Ruban et al. [87] have calculated the segregation energies for 24 transition metals acting respectively as impurity and as host. The host is represented by a close-packed surface of the elements. The calculated segregation energy for the couple Co/Pt(111) is 460 meV which, by its positive value, denotes a tendency to create a bulk alloy. In order to study the growth of Co on a substrate with which it doesn't intermix, a substrate must be chosen which shows a negative segregation energy. From those available in the calculation of Ruban et al. [87], chromium, titanium, tungsten and ruthenium would fit the bill.

We chose Ru (0001) as a substrate for this study. The calculated -370 meV segregation energy predicts by its negative value a strong segregation of the Co on the surface. Furthermore, the Co/Ru(0001) system shows interesting magnetic properties. Spin polarized low energy electron microscopy (SPLEEM) measurements done by El Gabaly et al. [19] show that the magnetization of a Co film on Ru(0001) changes twice its magnetic easy axis, the direction of preferred magnetization. The Co film was grown at temperatures and deposition flux conditions assuring a Frank-van der Merwe (layer-by-layer) growth. The 1 ML thick film is measured to have in-plane magnetization, meaning that the magnetization vector can take any direction in the surface plane. The 2 ML film in contrast shows out-of-plane magnetization, with a magnetization vector perpendicular to the substrate surface. Finally, for three and more layers of cobalt, the easy axis settles back in the in-plane configuration.

The easy axis of thin ferromagnetic (FM) films is determined by the spatial anisotropy of the magnetization energy function and is measured by the magnetic anisotropy energy (MAE). This MAE is comprised of several contributions. The convention is that positive MAE contributions are those that favor out-of-plane magnetization, while negative contributions favor in-plane magnetization. In thin FM films, the dominating term is generally the *shape anisotropy*, which stems from the long-range dipole-dipole interaction. This term favors the in-plane magnetization. Other contributions to the MAE include bulk, interface and surface magnetocrystalline anisotropy energies as well as film strain and relaxation terms which give rise to film thickness dependent anisotropy energies (see e.g. Ref. [88] for a complete review). A combination of these terms can favor out-of-plane magnetization both in bidimensional islands as well as in films.

In the case of Co/Ru(0001), calculations [19] have shown that it is a balance between these contributions, namely of strain, interface and surface terms, which promotes the easy axis to an out-of-plane direction for 2 ML Co. Out-of-plane magnetization is generally regarded as the most promising

development for magnetic recording media. Understanding the growth of submonolayer Co/Ru(0001) as well as eventually the magnetic properties, is thus of interest for magnetic recording media applications as well as for basic research of nucleation and growth.

In the present chapter we present growth experiments of submonolayer Co/Ru(0001) and extract relevant energy barriers for the system.

5.1 Experimental methods

The experiments were performed in a UHV chamber (not the same as in the previous chapter) of base pressure below 1×10^{-10} mbar using a variable-temperature (50–800 K) STM. The Ru(0001) surface was prepared by repeated cycles of Ar-ion sputtering (1.3 keV, 1.2 μA) at room temperature and at 1000 K followed by annealing in 2×10^{-8} mbar of O_2 atmosphere at 1700 K and flash annealing to 2000 K. This preparation procedure and a previous long term anneal above 1800 K resulted in atomic terrace width up to 2500 Å. We note that these high temperatures impose an important strain on the sample preparation stand. In particular the high bias voltage (550 V) which was necessary to reach 2000 K can cause sparks between the filament and the sample. This conditions, together with the strong emission current ($\approx$ 120 mA) required to heat the sample, lead to a faster aging of the heating filament. The sample temperature is measured by a C-type thermocouple pair spot-welded directly on the sample. While this ensures a high accuracy in the temperature measurement ($\delta T <$ 0.1 K) it also introduces limitations. The thermocouple is insulated by Al_2O_3 tubes. Upon heating the thermocouple partially sublimates metal on the insulating tubes. This may lower their resistance to a few kΩ and provide a path for the current to the ground, effectively reducing the heating power and disturbing STM measurements.

Prior to Co deposition at low temperatures, the sample was flashed to 800 K to desorb any residual gas which may have adsorbed on the surface. Co atoms are deposited by molecular beam epitaxy (MBE) using a commercial triple e-beam evaporator from a thoroughly outgassed Co rod (purity 99.995 %, Alfa-Aesar). The deposition flux was $4.2 \cdot 10^{-3}$ ML/s which has been determined by STM imaging after deposition of $\approx$ 0.5 ML Co at 450 K, assuring large islands and step-flow growth conditions. The error of the deposition flux, and thus of the reproducibility of coverage is estimated to be less than 10 %. The deposition amount was electronically monitored in the MBE source by integrating the flux meter over deposition time. During deposition the pressure in the chamber remained below 2×10^{-10} mbar. The sample was cooled down immediately after deposition ($T_{\mathrm{mes}} < 0.9 \cdot T_{\mathrm{dep}}$) to quench any post-deposition evolutions.

5.2 STM data

In order to study island nucleation and growth we deposited 0.12 ML of Co on the clean Ru(0001) surface. As has been described above and in detail in Ref. [45], studying the island density in the island density saturation regime offers insight into the diffusion barriers and attempt frequencies of the adsorbed monomer. Fig. 5.1 shows STM topographs of the Ru(0001) surface with 0.12 ML Co deposited at different temperatures. Images are taken in constant current mode with a typical sample-tip bias voltage $-2.0 < V_{\mathrm{t}} < 2.0$ and tunneling currents 100 pA $< I_{\mathrm{t}} <$ 10 nA. in the images, the Co islands appear as brighter regions with an apparent height of 1.9 Å above the Ru terrace while the ruthenium atomic steps have an apparent height of 2.2 Å.

At 100 K (Fig. 5.1 a.) the very small Co islands are compact, mainly circular and have a mean size of $\langle s \rangle = 3.9$ atoms. At 130 K (Fig. 5.1 b.), the island size is already much larger with $\langle s \rangle = 9.7$ atoms but the island shapes are still compact. At temperatures up to 250 K (Fig. 5.1 c) and d.) the islands, while

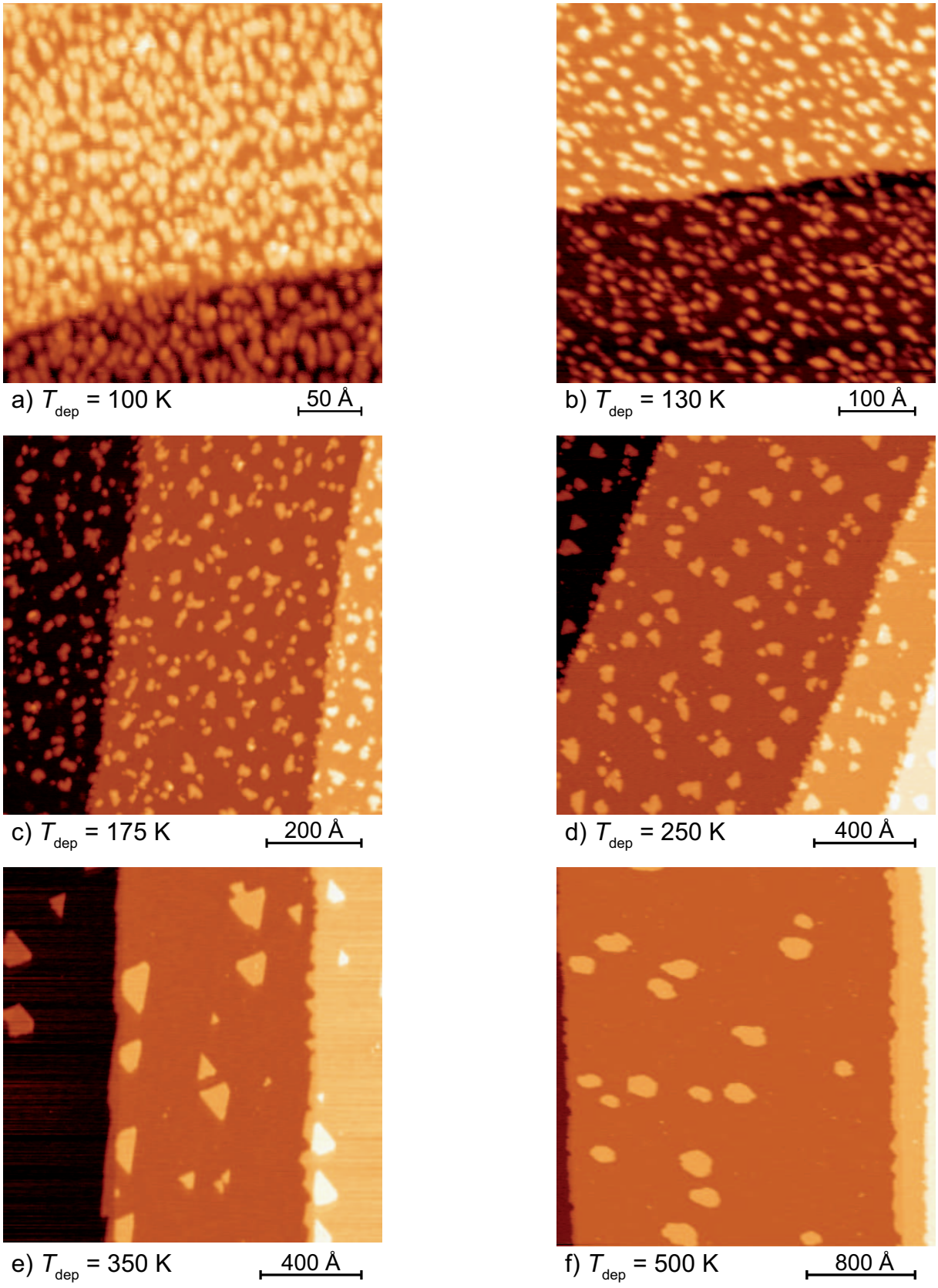

Figure 5.1: STM topographs of 0.12 ML Co deposited on Ru(0001) at different deposition temperatures.

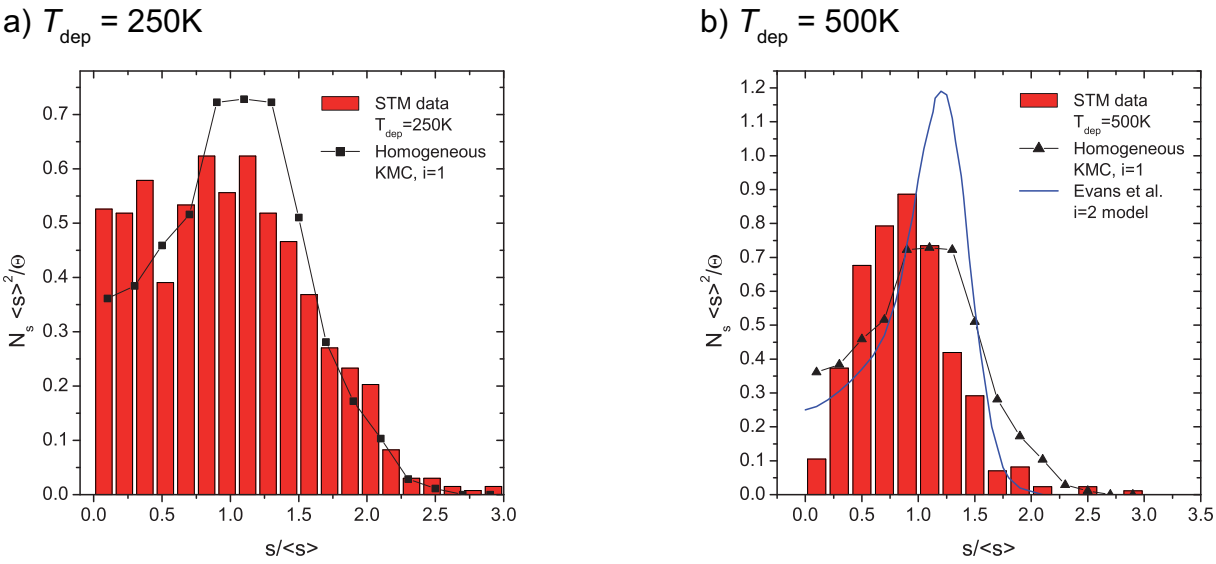

Figure 5.2: Normalized island size distributions obtained from a collection of STM images at deposition temperatures of 250 K (a) and 500 K (b). The data are compared with an $i = 1$ KMC model for compact islands (a) and (b), and with the theoretical curve for $i = 2$ published by Evans et al. (Ref. [20], p. 28) for point-islands at $D/F = 10^7$.

remaining compact, get irregular and the mean size grows further. We also notice a higher island density along the substrate's atomic steps. At 300 K (not shown) and 350 K (Fig. 5.1 e.) the island shape becomes triangular. We notice that the triangles on the same terrace are not all pointing in the same direction. This question will be addressed in Section 5.8. At the highest measured temperature, 500 K (Fig. 5.1 f.), the islands have a compact, nearly hexagonal shape. We observe that there is a region along the ascending Ru step (right-hand side of image) with a lower island density. This *depletion region* and its effect on the overall island density will be discussed in Section 5.7.

5.3 Island size distribution

As has been pointed out in the chapter on Co/Pt(111), the island size distribution gives important information on the processes happening at the surface during deposition. In particular, simulations and calculations show that the island size distribution changes dramatically when the system makes a transition from critical cluster size $i = 1$ to $i = 2$ where dimers can dissociate. Comparisons are easily made between systems with different growth conditions by normalizing the island size distribution. In fact, the work of Evans and Bartelt [89] shows that the normalized island density is almost insensitive to a large change of D/F, which in our case reduces to a dependency on the temperature since the values E_m, ν_0 and F are supposed to be constant.

In Fig. 5.2 we show normalized size distributions obtained from several STM images for $T_{dep} = 250$ K and $T_{dep} = 500$ K. The distribution for 250 K corresponding to $D/F = 2 \times 10^9$ (see below for the determination of E_m and ν_0 required for this calculation) shows a mode at 1 ± 0.2 mean size with a normalized height of 0.6. When compared with homogeneous kinetic Monte-Carlo (KMC) simulation with $i = 1$ performed at $D/F = 5 \times 10^{10}$, we see that the distribution shows a higher density of small islands than expected from simulation results but that the behavior at larger sizes is well reproduced. In particular, we note that the mode is correctly placed and that the height is only marginally smaller. The higher density of small islands may indicate that surface impurities have trapped diffusing adatoms.

In summary, the island distribution at 250 K indicates nucleation in the $i = 1$ regime.

At $T_{\mathrm{dep}} = 500$ K ($D/F = 2\times10^{12}$), the experimental distribution mode is at $0.8\langle s\rangle$ with a peak height of 0.9. In contrast to the distribution at 250 K, the mode is narrow and the island density at small size is low. In order to compare the island density with theoretical predictions, the KMC simulation for $i = 1$ is also plotted. Furthermore, the blue curve shows the result of the calculation for $i = 2$ done by Evans and Bartelt [89]. We emphasize that this calculation is done for point-islands, meaning that this calculation is valid for islands which do not show any spatial extension. Moreover, the calculation is performed at $D/F = 10^7$. This is different from our experimental conditions by five orders of magnitude but unfortunately no corresponding calculations have been made for higher diffusivity values. Although no corresponding distribution is published in the literature for $D/F = 10^{12}$, we can still conclude that the behavior is of the $i = 1$ type. As a matter of fact, for $i = 2$ the trend is to obtain a narrower island distribution with a higher normalized island count at the mode when going towards higher D/F values. Thus, we expect the mode for $i = 2$ and $D/F = 10^{12}$ to be even higher than the value of 1.2 predicted by Evans. A comparison with our experimental result shows that the curve for $i = 1$ best fits the experiment.

In conclusion, analyzing the island size behavior up to the maximum deposition temperature permits to conclude that the critical cluster size remains 1 up to $T_{\mathrm{dep}} = 500$ K. This is of particular interest when applying KMC and rate equation approaches to simulate the island density.

5.4 Island density

The island density has been measured as a function of deposition temperature. At low T_{dep}, the thermalization of the STM recording head and the associated dilatation or contraction of the movement piezos may make the tip move across the surface. This effect disappears when a dynamic equilibrium between the room temperature (RT) radiation and a constant heat flow from the cold sample and sample holder to the STM is achieved. This tip movement due to the temperature difference between the STM and the sample holder is called *thermal drift* and results in deformations of the recorded images with respect to reality. In fact, the drift speed which is considered constant on the time-scale of an image scan, is added to the scan speed. Thus, scanning the surface in a direction when the two speeds have reverse signs will result in a contracted image, while when the two speeds have the same sign, the image will appear dilated. Evidently, this affects the measured island density. To counter this measurement artifact, we record the images by pairs of inverse scan directions. The island density is then calculated as the average of two consecutive images of the same region.

The measured island density as a function of inverse temperature is shown as squares on the Arrhenius plot in Fig. 5.3. As for Co/Pt(111), it is not possible to distinguish between monomers and larger clusters in the STM images at very low temperatures. Consequently, the plot shows the logarithm of the sum of stable islands (n_x) and monomers (n_1). The highest island density is obtained for the lowest deposition temperature which was 85 K. In this temperature range the measured mean island size is $\langle s\rangle = 1.8$ atoms which corresponds to the statistical growth discussed previously, with the surface containing a mix of monomers and dimers. At 100 K, the island density is already reduced giving $\langle s\rangle = 4.0$ atoms. This observation could be interpreted as an effect of the onset of monomer diffusion. In fact, one observes that the island densities at 130 K and 166 K seem to fall on a straight line with the two previous points in the Arrhenius representation, which would be in accordance with the hypothesis of monomer diffusion. By fitting these 4 points with the scaling law for $i = 1$ (see Eq. 3.5) we get $E_{\mathrm{m}} = 100$ meV for the monomer migration barrier E_{m} and $\nu_0 = 2\times10^6$ Hz for the corresponding attempt frequency ν_0. It is particularly the very low prefactor which indicates that the hypothesis of monomer diffusion is incorrect at these low temperatures.

This conclusion as well as our previous finding that $i = 1$, even at the highest $T_{\mathrm{dep}} = 500$ K con-

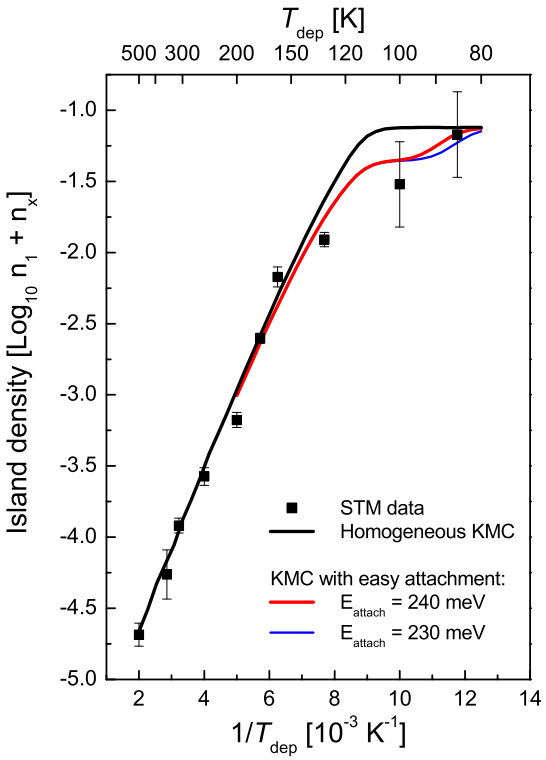

Figure 5.3: Arrhenius plot of the stable island density for $0.12\,ML$ Co deposited on Ru(0001) at deposition temperatures between 85 K and 500 K. Continuous lines show KMC models with $i = 1$ fitted to the experimental data using $E_{\mathrm{m}} = 310$ meV and $\nu_0 = 5 \times 10^{13}$ Hz. Black line: Homogeneous model with monomer diffusion. Red and blue line: Homogeneous model with easy attachment with an attachment barrier of 240 meV and 230 meV , respectively.

sidered, lets us fit the whole range of experimental data using the corresponding scaling law, KMC simulation and RE simulation. The three methods give similar results as shown in the table below:

	Scaling Law	Kinetic Monte-Carlo	Rate Equations	Mean
E_m	305 meV	310 meV	310 meV	(310 ± 10) meV
ν_0	2×10^{13} Hz	5×10^{13} Hz	5×10^{13} Hz	$5 \times 10^{13\pm0.5}$ Hz

The KMC fit is shown as a black continuous line in Fig. 5.3. While the model reproduces the high T_{dep} behavior well, a discrepancy with experiment is observed in the low temperature regime. The drop in island density between 85 K and 100 K is a clear signature that the system follows an easy attachment behavior. Here, in contrast to the system Co/Pt(111), the mean island size $\langle s \rangle = 1.8$ atoms observed at the lowest deposition temperature ($T_{dep} = 85$ K) is the one expected by simple statistical growth (black line in Fig. 5.3). In this regime, dimers and larger stable islands form only when two or more atoms are deposited on adjacent sites. The island size distribution determined by KMC is 67 % monomers, 20 % dimers, 8 % trimers. The good agreement between experiment and statistical growth furthermore excludes transient mobility which would result in a larger $\langle s \rangle$. When T_{dep} is slightly increased, the easy attachment process becomes thermally activated. By simulating the thermally activated easy attachment in the KMC simulation and using the attempt frequency determined above, we can extract the diffusion barrier for attachment to next-nearest neighbor atoms. Fig. 5.3 shows calculations for two barriers in order to evaluate the effect of the attachment barrier on the island density. Naturally, with a higher barrier, easy attachment is activated at a higher temperature. The best fit is obtained with $E_{attach} = (240 \pm 15)$ meV. This value corresponds to 75 % of the surface migration barrier, which is reasonably close to the estimated 60 % for easy attachment in Ref. [45].

5.5 Comparison with previous work

Previous works on the submonolayer growth of the Co/Ru(0001) system were focussed on deposition temperatures above RT. A comparison of the island densities obtained in these works with our results is shown in Fig. 5.4. Note that a scaling to our deposition flux was applied following the scaling law (Eq. 3.5) for $i = 1$:

$$n_x = n_{exp} \left(\frac{F}{F_{exp}} \right)^{1/3} \tag{5.1}$$

where n_{exp} and F_{exp} are the island density and deposition flux in the original experiments, respectively. $F = 4.2 \times 10^{-3}$ ML/s is our deposition flux and n_x is the scaled island density which is plotted on the graph. The island densities are published for coverages ranging from 0.12 ML to 0.23 ML. This guarantees that we are still in the island saturation regime and that island densities can be compared with confidence.

The results obtained by Bartelt et al. (purple stars in Fig. 5.4) are taken from Ref. [90]. Two island densities are given for 300 K and 323 K. A drop in the density by a factor of 6.5 is observed by the authors in this small temperature range which raises their surprise (see footnote in the publication). We observe that the value at 300 K is very close to the one we measured, while still being lower. The value at 323 K is notably lower. Unfortunately, no STM images of the pure, un-annealed Co on Ru(0001) are published in this reference so the only information about island morphology is given in the text as "(...) a distribution of pseudomorphic Co islands with irregular, threefold symmetric growth shapes (...)". Upon annealing to 625 K, the island shape becomes hexagonal.

The island density obtained by Vrijmoeth et al. (cyan pentagons in Fig. 5.4) is published in Ref. [91]. We are a bit surprised by the fact that the STM image published in this article seems to be

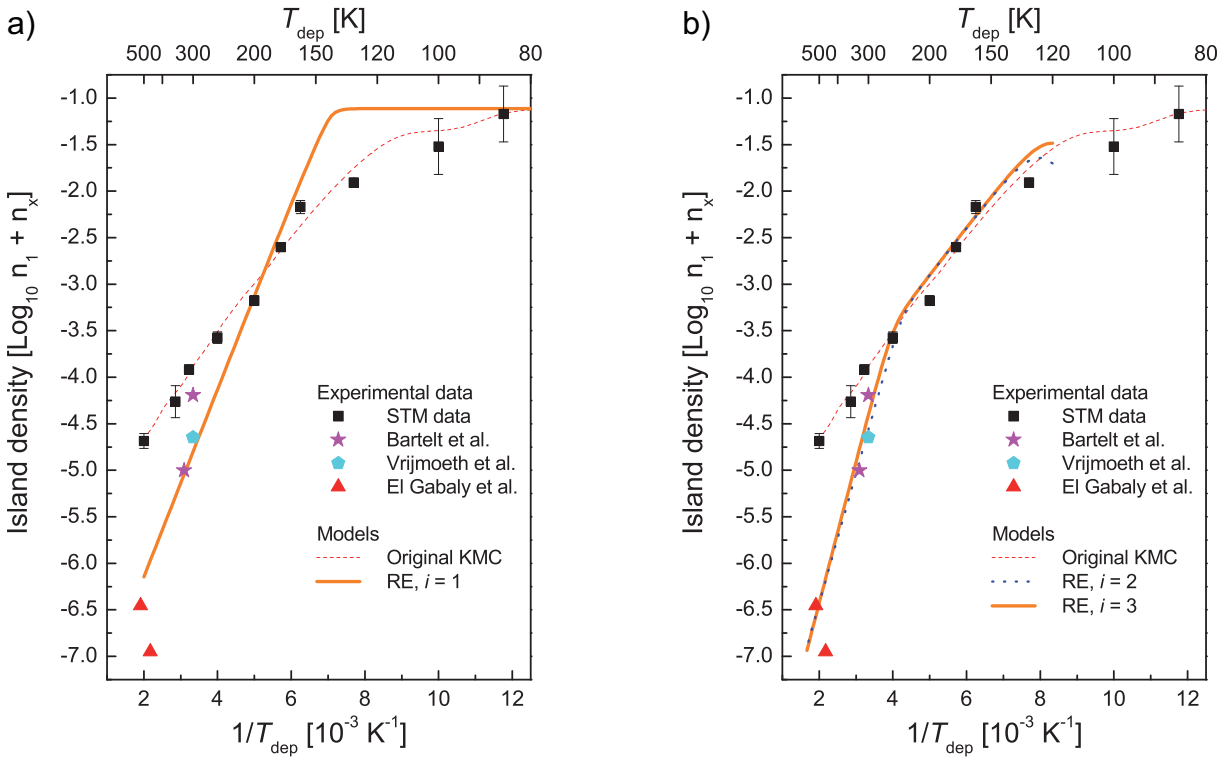

Figure 5.4: Arrhenius plots of the measured island density compared with results from other groups (see text for full references). a) Fit of the results from other research groups by a homogeneous diffusion RE model with critical cluster size $i = 1$. b) Fit of the results from other research groups by a RE model with $i = 2$ and $i = 3$. See text for parameters.

also published by Günther et al. in Ref. [92] as well as by Hwang et al. in Ref. [93] but with differing coverages (0.19 ML, 0.17 ML and 0.2 ML, respectively) and differing deposition fluxes (2.5×10^{-3} ML/s, 1.8×10^{-3} ML/s and 2.5×10^{-3} ML/s, respectively). We are aware that the impact on the island density is small. The density given by Vrijmoeth is measured at 300 K and falls halfway between the two values of Bartelt et al. Islands are clearly triangular but annealing to 600 K yields hexagonal islands [91, 92].

Finally, El Gabaly et al. published two papers with SPLEEM images at 460 K (Fig. 1 a. in Ref. [19]) and 523 K (Fig. 2 a. in Ref. [94]) showing triangular islands (red triangles in Fig. 5.4). Unfortunately, the island density is not given in these references and thus had to be extracted by counting from the single images available at each temperature. We are aware of the lack of statistical information and the inherent error, but with 147 and 444 islands, respectively, this error should be below 10 % which represents only a difference of 0.04 on the log scale of the plot. The field of view in the SPLEEM images is given as 10 μm but no uncertainty for this value can be estimated. The island densities extracted with this method are well below our experimental results for the same temperatures. They also show a surprising trend, namely that the island density measured at 460 K is *lower* by a factor of 3 than the density at 523 K. In homogeneous diffusion a decreasing island density with augmenting deposition temperature is expected (for special cases where this is reversed see Section 4.7, p. 45). Island shapes are clearly triangular but the measurement at 460 K shows triangles with slim waists indicating that the kinetic equilibrium shape with activated edge diffusion is not yet reached.

Comparing these values to our own work we notice that all island densities from other sources are below values found in our own measurements. Three possible explanations come to mind: 1. Impurities on our sample may capture diffusing adatom. 2. An adsorbed gas lowers the diffusion barrier in the other works. 3. An adsorbed gas increases the diffusion barrier on our sample. Although the first suggestion seems a good candidate to explain the difference in island density, two arguments work against it. We observe a linear decrease of the island density in the Arrhenius representation. In the case of capturing impurities, one would expect a nearly constant island density given by the density of attractive impurities up to a transition temperature. Above this temperature, the effect of impurities would become negligible and the island density would drop sharply (see also the previous chapter for remarks on attractive point defects). This is not the behavior observed in the plot. Furthermore, the analysis of the island size distribution suggests that the regime $i = 1$ with a mono-mode distribution reaches up to 500 K while, in the presence of attractive impurities, this would lead to a bimodal distribution.

The second possible explanation is that an adsorbed gas lowers the diffusion barrier for the monomer which results in a higher diffusivity and therefore in a lower island density. This explanation thus applies to the results of the other groups, assuming that our results are free of artifacts. A corresponding effect has been observed previously for several systems. Particularly the presence of minute amounts of hydrogen has been observed to enhance the diffusivity in homoepitaxy experiments in Rh/Rh(100) [95], Be/Be(0001) [96], Pt/Pt(110) [97] or Si on H-terminated Si(001)-(2×1) [98]. This suggests that the presence of residual gas of the UHV chamber adsorbed on the surface may increase the diffusivity and artificially lower the island density.

Finally, the third suggestion is that the presence of adsorbed gas on the surface lowers the diffusivity. This could explain why we measure higher island densities. Several observation of similar effects have been reported, notably diffusion inhibition by the presence of hydrogen [99] or CO [100] in the Pt/Pt(110) system.

It is not possible to discriminate between these two last possibilities simply basing on the reported UHV quality. All groups report similar values for the base vacuum pressures ($< 1\times10^{10}$ mbar) and, if published, similar pressures during deposition ($< 4\times10^{10}$ mbar). The surprising result from Bartelt et al. that the island density decreases so rapidly in a small temperature range as well as the unusual result from El Gabaly et al. that the island density increases with increasing temperature strongly

suggests that the Co/Ru(0001) system is very sensitive to preparation and deposition conditions.

In order to give a complete picture of Co/Ru(0001) with all the available data, we performed simulations disregarding our high temperature results and using the data of the other groups instead. Unfortunately, no island size distribution is available for any of the results. The rare STM images presented do not give a sufficient statistical sample to conclude if the size distribution is of the $i = 1$ or $i > 1$ type. We thus performed simulations using rate equations for $i = 1$ which are presented in Fig. 5.4 a) (thick orange line). The result is fitted in order to be coherent both with our lower temperature measurements as well as with high temperature values from other groups. The fit's migration barrier is $E_m = 600\,\text{meV}$ and attempt frequency $\nu_0 = 1 \times 10^{21}\,\text{Hz}$. This prefactor is eight orders of magnitude above the typically expected values excluding the $i = 1$ assumption. Note that the low temperature behavior is not well reproduced because no easy attachment term was introduced in the RE. To recall the correct low temperature behavior simulated by KMC, the dashed red line shows the original KMC model. In order to address the discrepancy between the expected and actual attempt frequencies we propose a $i = 2$ model where dimers can dissociate. The monomer diffusion parameters are taken from our study above $E_m = 310\,\text{meV}$ and $\nu_0 = 5 \times 10^{13}\,\text{Hz}$. Fitting the data using the dimer dissociation barrier E_2 as well as a corresponding attempt frequency $\nu_{0,2}$ yields the following results: $E_2 = 800\,\text{meV}$, $\nu_{0,2} = 1 \times 10^{18}\,\text{Hz}$. Although the dimer dissociation barrier is reasonable, the corresponding prefactor is still five orders of magnitude above expected values. Fitting the experimental data using a reasonable attempt frequency requires the extension of the model to $i = 3$ where even the trimer can dissociate to a dimer and a monomer. A good fit of the data is obtained with $E_2 = E_3 = 600\,\text{meV}$ and $\nu_{0,2} = \nu_{0,3} = 1 \times 10^{13}\,\text{Hz}$. The knee of the curve in the Arrhenius representation at the transition from $i = 1$ to $i > 1$ cannot be resolved precisely enough to separate between the onset of $i = 2$ and the onset of $i = 3$. This leads us to set both dissociation barriers to the same value. With these energy barriers, the attempt frequency is in the expected range.

In conclusion, our deposition results show that the monomer migration barrier of Co/Ru(0001) has a value of 310 meV with an attempt frequency $\nu_0 = 5 \times 10^{13}\,\text{Hz}$. Explaining previously published growth results implies that both the dimer and the trimer can dissociate with close energy barriers of approximatively 600 meV. The large discrepancy in island densities between our work and previous results can be attributed to the presence of residual gas on the surface during deposition inhibiting or enhancing the diffusion of the monomer. It is not possible to determine which of the studies is affected by the presence of these gases. The growth behavior needs to be addressed by a specific study with the controlled presence of impurity gases, namely H and CO.

5.6 Morphologies

The morphology of the Co islands in our images evolve depending on deposition temperature. In contrast to Co/Pt(111) no clearly discernable temperature with ramified islands is present. The islands are always compact. For T_{dep} between 160 K and 250 K the compact islands have irregular shapes. At temperatures above 300 K, the islands acquire a regular triangular shape. At 500 K finally, the islands takes a hexagonal shape.

The fact that the islands remain compact throughout the complete temperature range indicates that already at low temperatures the edge diffusion processes are activated. Bartelt and Evans have estimated an edge diffusion barrier for Co/Ru(0001) in Ref. [101]. They base the calculation on the island edge growth instability observed in the images of Günther et al. [92]. The edge migration barrier is estimated to $E_e = 300\,\text{meV}$ using a supposed attempt frequency of $\nu_0 = 5 \times 10^{11}\,\text{Hz}$. Because we have determined the correct attempt frequency at $\nu_0 = 5 \times 10^{13}\,\text{Hz}$ we can adapt the migration barrier which yields $E^B_{2\to 2+} = (420 \pm 10)\,\text{meV}$. We specify that this is valid for the B type step as this is the expected majority step in pseudomorphic triangular islands. The calculated barrier corresponds

to an onset of island-edge diffusion at ≈ 150 K which is in good agreement with our observations. The corner crossing anisotropy which results in the triangular islands cannot be easily determined from our data.

We present a comparative table of the shapes as observed by the different groups. All measurements agree on the fact that at 300 K the islands are triangular. A discrepancy between our hexagonal island shape and the triangular shape observed by El Gabaly et al. at 500 K still needs to be explained. It is possible that this corresponds precisely to the transition temperature between the triangular and hexagonal shapes. In this case, a small temperature difference could yield the observed difference in shape.

T_{dep}	This work	Bartelt et al.	Hwang, Vrijmoeth Günther et al.	El Gabaly et al.
< 300 K	Irregular compact			
300 K	Triangular	Triangular	Triangular	
500 K	Hexagonal			Triangular
600 K		Hexagonal[a]	Hexagonal[a]	

[a] Morphology obtained by annealing from deposition at RT.

5.7 Effect of the terrace width on island densities

At a growth temperature of 500 K, where the mean square displacement of the monomer is large, it is well known that the substrate step edges can influence the island density on a terrace. This is well exemplified on Fig. 5.1 f. where it is obvious that only few islands are found close to the step, thus creating a depletion zone. This can produce artifacts when comparing with theoretical models or simulations where the substrate is always assumed free of steps. To measure island densities from STM images coherently with calculations, one has to take into account the terrace width on which the island counting is made and possibly remove the depletion zone near a step edge. In order to quantify this effect and develop a procedure to measure island densities at high T_{dep}, we have performed a short study on the effect of the step edge. A similar study was done by Bales in Ref. [62]. The calculations in this reference extend only up to $D/F = 10^9$ while we are in the case of $D/F = 10^{12}$. These three orders of magnitude difference do not allow an extrapolation in confidence. Our experimental terrace width at 500 K is approximatively 2100 Å or ≈ 800 sites. We perform KMC simulation on a terrace with width varying from 100 sites to 3200 sites.

We model the substrate terrace in the KMC simulation as a surface with a totally repulsive descending step. This is equivalent to an infinite Ehrlich-Schwoebel [102, 103] barrier at the step edge. We are aware that this is only a crude approximation. In fact, experimental evidence shows that the descending barrier, or more precisely the transition from Co diffusing on the Ru terrace towards Co diffusing on the Co strip which is adsorbed along the step edge, has not an infinite barrier. In the case of an infinite barrier, the total amount of Co adsorbed on each terrace would be directly proportional to the terrace's width. This is not the case but we nonetheless use this simplified model convinced that the effect on the island density is small. The ascending step is modeled as an irreversibly attaching strip. In the model, the step edges run along the high density direction of the substrate surface.

Fig. 5.5 shows KMC simulations of 0.12 ML Co growth on terraces with three different widths. Calculations are done for surfaces with approximatively 4×10^6 sites to get a good statistical sample of islands. We present simulations for dendritic diffusion limited aggregation (DLA) as well as compact islands. The compact islands are obtained by activating edge diffusion. The edge diffusion barriers chosen do not reproduce the island morphology correctly at high temperature. Nonetheless, the

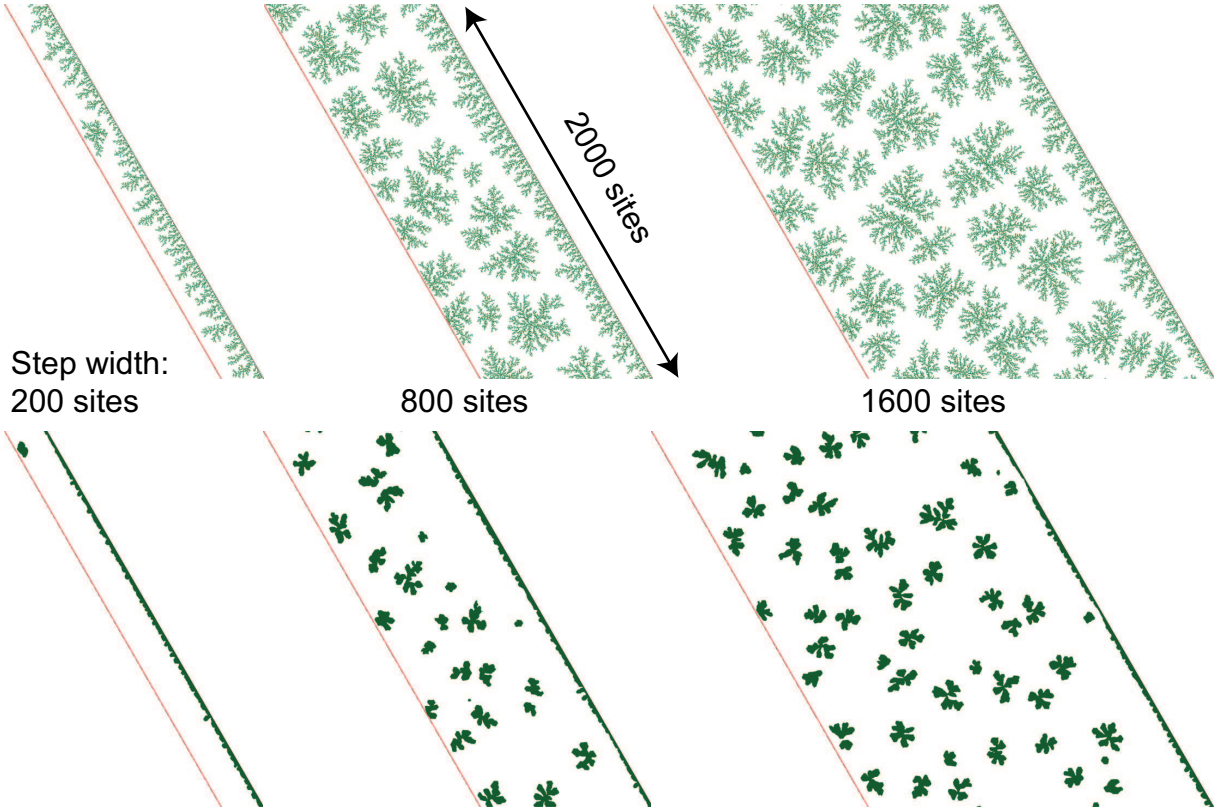

Figure 5.5: KMC simulation of growth of 0.12ML Co on a Ru(0001) terrace for three different widths. Simulations were performed on surface with $\approx 4 \times 10^6$ sites. The images show details with a constant step length of 2000 sites. The descending step (left side) is modeled as totally repulsive while the ascending step (right side) has irreversible attachment for the diffusing monomer. The upper row shows simulations with pure DLA while the lower row shows simulation with edge diffusion activated to assure a compact shape. Note that the experimental island morphology is not faithfully reproduced with these activation barriers.

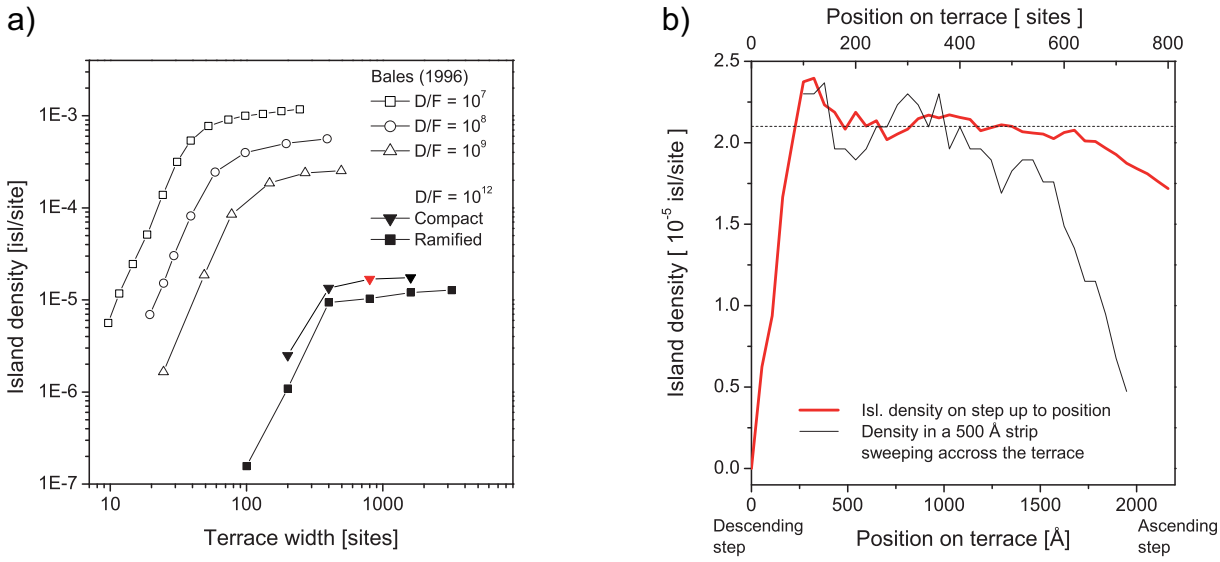

Figure 5.6: a) Island density as a function of step width calculated for different values of D/F. The results for D/F equal to 10^7, 10^8 and 10^9 are taken from Ref. [62]. We present results for both, compact and ramified (DLA) simulations for $D/F = 2\times10^{12}$ which corresponds to our experimental conditions. The red triangle indicates the result corresponding to an experiment at $T_{\text{dep}} = 500$ K.
b) Red line: Density of compact islands inside a strip extending from the descending step edge (left) to a given point on the terrace. Black line: Island density measured in a 500 Å wide strip swept across the terrace. Fluctuations are due to lack of statistics.

compacting of the shape result in the expected difference in island capture capacity. Particularly the compact step edge strip has a reduced adatom capture area when compared with the long dendrites extending on the terrace in the DLA simulation. Simulating compact islands is much more processor time demanding than simulating DLA as atoms keep on moving along the island edges during the complete simulation time. As a consequence, only DLA results are available for the extreme cases (terrace width of 100 sites and 3200 sites).

We observe that the simulation faithfully reproduces the depletion region close to the ascending step edge. The full effect of the width of the terrace on the island density is shown in Fig. 5.6 a). In this graph, the density is calculated on the complete terrace width. The graph shows previous results as calculated by Bales [62] for lower D/F values as well as our results for $D/F = 10^{12}$. We note that a factor of ≈ 1.8 separates the compact and DLA results. More precisely, this ratio is not constant but increases with smaller terrace width. This underlines the importance of simulating the system with compact islands to faithfully reproduce the island density.

For each D/F value, the graph shows a clear transition between two scaling regimes with the crossover marked by a characteristic terrace width ℓ_0. If the terrace width $\ell \gg \ell_0$, the nucleation and growth happens in the same manner as on an infinite terrace. In contrast, if $\ell \ll \ell_0$ the island density is dominated by step edge interactions [62]. For the D/F relevant in our experiment, this characteristic width is $\ell_0 \approx 400$ sites. Thus, we are confident that the 800 site wide experimental terraces do not introduce a large error on the island density. In order to minimize the effect of the depletion zone on the measured island density one can remove a strip of the surface and the corresponding islands at the ascending step edge.

The black curve in Fig. 5.6 b) shows the island density measured in a strip of 500 Å width sweeping across the terrace. This results in an approximation of a local island density as a function of the po-

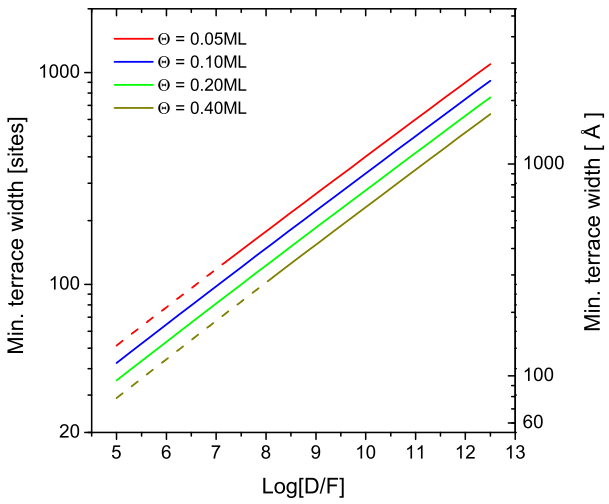

Figure 5.7: Minimum terrace width necessary to render step edge effects negligible when measuring island densities on STM images. The plot gives values for a large range of coverages and D/F values in the island density saturation regime and for $i = 1$ and immobile clusters. The parts where the assumption of island density saturation is not valid are plotted as dashed.

sition on the terrace (for a complete treatment of this problem see e.g. Ref. [20], p.71 and references therein). The presence of the depletion zone can be readily seen by the sharp drop in island density starting at ≈ 500 sites towards the ascending step edge. The effect on the island density of the whole terrace is shown by the red curve in Fig. 5.6 b). This result shows that the island density measured in a strip extending from the descending step to a given point on the terrace seems stable up to width of ≈ 600 sites. Taking the whole terrace, an error due to the depletion zone is introduced which represents ≈ 20 % of the island density on the infinite terrace. This lets us conclude that ≈ 200 sites or ≈ 540 Å of the terrace towards the ascending step must be discarded when counting islands on experimental images in order to obtain the best measure of the island density. The experimental island densities presented here have been calculated according to this procedure.

We have extracted from the paper of Bales [62] a result particularly relevant for the experimentalist, namely the minimum terrace width at a given D/F above which the effect of the step edge is negligible. This is done using the island density n_0 as a function of terrace width in the step edge dominated regime calculated in Eq. (9) of Ref. [62]

$$n_0(\ell) = \pi \frac{\sqrt{3}}{36} \left(\frac{D}{F}\right)^{-1} \ell^3 \frac{K_1(\sqrt{12}/\ell)}{K_0(\sqrt{12}/\ell)} \Theta \tag{5.2}$$

where ℓ is the terrace width, Θ the coverage and K_j are modified Bessel functions of order j. The transition point between the two extreme growth regimes takes place at their meeting point $n_0 = n_\infty$. We use the scaling law for $i = 1$ to calculate

$$n_\infty = \eta \left(\frac{D}{F}\right)^{-1/3} \tag{5.3}$$

with $\eta = 0.25$ chosen according to Ref. [22] (in contrast to $\eta = 0.315$ given by Bales). The terrace width which can be extracted from these three equations for a given D/F is not sufficient to guaran-

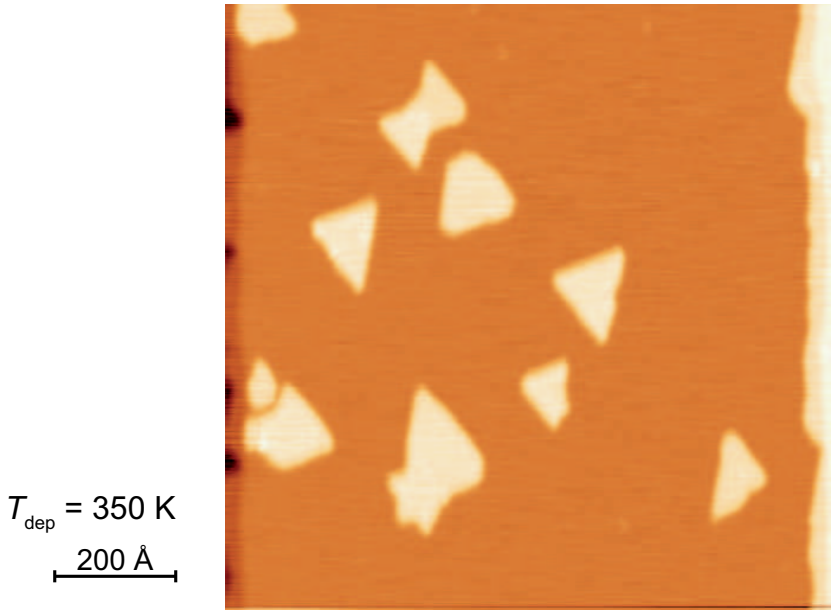

Figure 5.8: STM image of 0.12 ML Co/Ru(0001) deposited at 350 K. The image shows coexistence of pseudomorphic, stacking faulted and mixed stacking islands on a same substrate terrace.

tee a negligible effect of the step edge. It defines the crossover terrace width. We use the criterion $N_0/N_\infty > 10$ to determine the region where the step edge influence becomes negligible. This permits to extract a corresponding minimum terrace width for a given D/F and coverage Θ. The results are plotted in Fig. 5.7 and are valid for all types of surfaces with growth conditions assuring $i = 1$. The terrace width in Å is given for the Ru(0001) surface closest neighbor distance ($a = 2.71$ Å) so that the graph can be readily used in experiment as a reference with any surface with comparable interatomic distance.

5.8 Stacking faults

When depositing Co on Ru(0001) in the temperature range of 350 K – 400 K, the island shape is triangular. As can be seen in the STM image in Fig. 5.8, not all islands on a same terrace point in the same direction. Some are rotated by 180°. We also observe large islands which seem to be the result of a coalescence of two types of triangular clusters. As has been said before, the triangular shape of islands is the result of anisotropic border diffusion [78, 79]. The anisotropy lies in the activation energy for A-type and B-type edge and corner diffusions. The reversal of some triangles on a close-packed hcp(0001) surface indicates that some triangles grow in a pseudomorphic stacking, while others grow in stacking fault. Here, stacking faulted means that between the two types of sites available for adsorption, the one which does not continue the periodicity of the substrate crystal is chosen. The difference between the two stacking types is schematically shown in Fig. 5.9. Since ruthenium is an hcp crystal, a switch in the orientation of the A and B steps and thus of triangle orientation is expected for subsequent substrate terraces. On a single terrace, stacking faulted islands will result in reverse oriented islands.

Our analysis shows that at 350 K we have 76.6 % pseudomorphic stacked islands, 8.8 % mixed or indeterminate stacking and 14.6 % stacking faulted islands of a total of 171. The stacking ratio is then $P_{\mathrm{fcc}}/P_{\mathrm{hcp}} = 0.19$. To determine for two different images which stacking is pseudomorphic (hcp), we

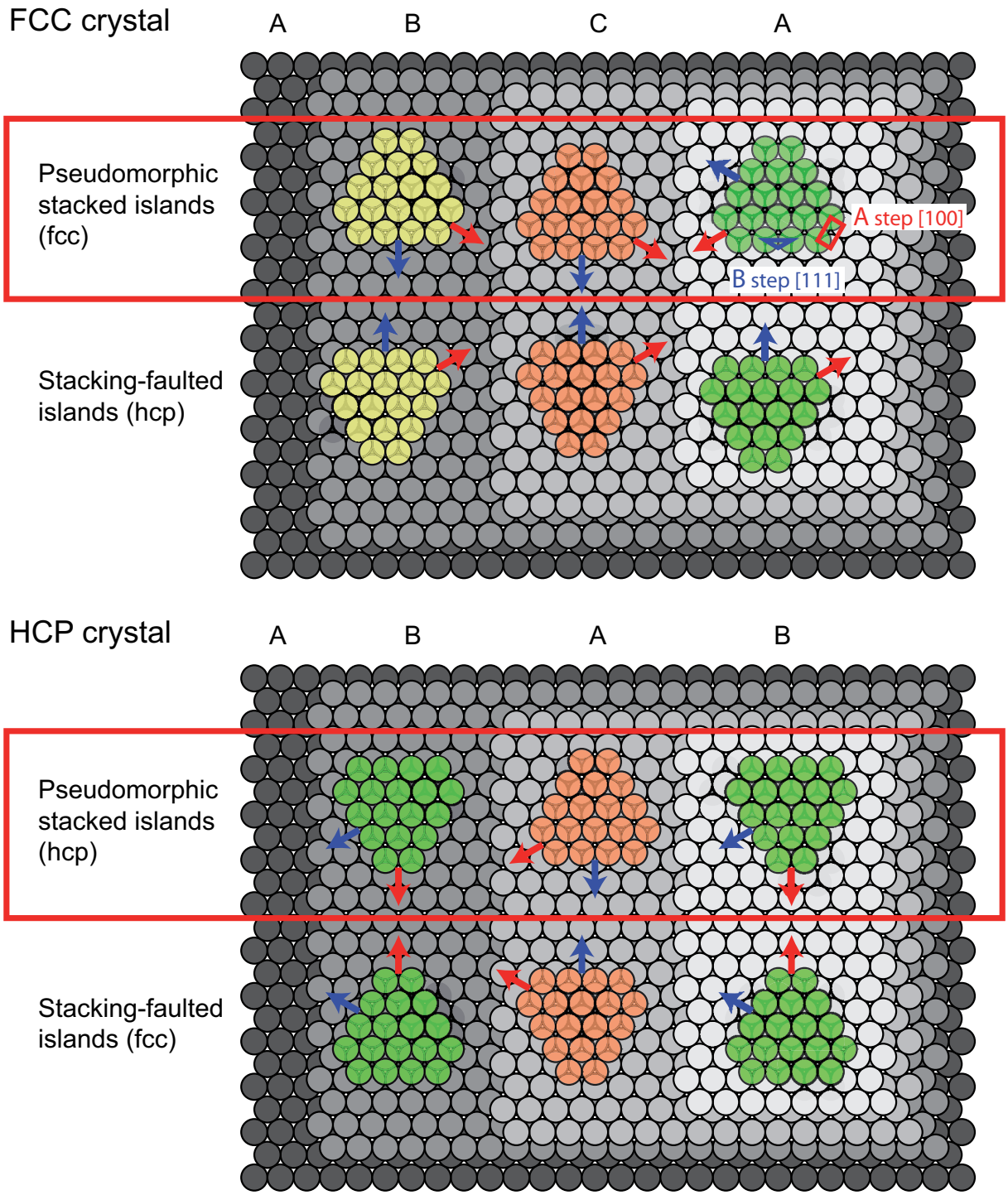

Figure 5.9: Sphere model of a fcc and hcp crystal with pseudomorphic and stacking faulted adsorbed islands. In the fcc crystal the orientation of A (red arrow) and B (blue arrow) steps on pseudomorphic adsorbed islands is maintained from one substrate terrace to the next. In the hcp crystal the orientation of A and B steps switches for each substrate terrace. Islands with a stacking fault always have the reverse orientation compared with pseudomorphic islands.

compared the relative occurrence of the two types of triangular islands. The more frequent island direction was arbitrarily assigned to the pseudomorphic stacking. This method did never give ambiguous result as one direction was always approximatively five times more frequent than the other. We did not obtain atomic resolution across a substrate step which would be necessary to determine which stacking was really pseudomorphic, but both, Bartelt et al. [90] and El Gabaly [94] describe the stacking as pseudomorphic in the studied temperature range.

Busse et al. [104] have reported on the stacking fault behavior of Ir/Ir(111). In this publication the stacking fault behavior is explained by the difference in binding energy for the two different sites. This influences the dwelling time of the monomer on each site. The working assumption is that pseudomorphic (stacking faulted) islands are nucleated by the encounter of two adatoms on pseudomorphic (stacking faulted) sites. The ratio of stacking faulted islands versus pseudomorphic is then given by the probability for a monomer to be on each type of site (we do not consider mobile clusters in this case). The ratio of these two probabilities is described by a Boltzmann term:

$$\left(\frac{P_{\mathrm{fcc}}}{P_{\mathrm{hcp}}}\right) = \exp\left(\frac{\Delta F}{k\,T}\right) \tag{5.4}$$

where $\Delta F = F_{\mathrm{hcp}} - F_{\mathrm{fcc}}$ is the difference in free energy of the system of a monomer on each of the two types of sites. In our case $\Delta F = -50$ meV. The free energy is related to the binding energy E_{b} and entropy ΔS by $\Delta F = \Delta E_{\mathrm{b}} - T\Delta S$. Unfortunately, the determination of ΔS requires a study over large temperature ranges [105] which was not possible in this case (see below). For reference, the entropy term is $\Delta S = 0.64\,k$ in the case of Ir/Ir(111) (with k the Boltzmann constant).

Polop et al. [106] propose a beautiful rate equation approach to model the stacking fault behavior as a function of temperature in the Ir/Ir(111) case. This approach cannot be applied to our case for the following two reasons: First, being on a hcp crystal, we cannot determine unambiguously which stacking is faulted and which is pseudomorphic on different terraces of the sample. The fcc case of Ir(111) guarantees that pseudomorphic islands always have the same orientation with respect to the microscope head. This permits to show the transition from a stacking fault majority to a pseudomorphic majority on this substrate. In our case, the only way to distinguish between the two stacking without atomic resolution across a step is to rely on the relative occurrence count. This method is error-prone (to say the least) in the case where the two probabilities become close. The second, and more important limitation, is that the observed islands are only triangular in a small temperature range. At lower temperature ($T_{\mathrm{dep}} < 300$ K), the shape is irregular and compact, but does not reflect a clear preferred direction. At higher temperatures, the islands become hexagonal or rounded which again does not permit determination of a preferred direction. In both cases, differentiating between the two types of stacking based on the island shape is impossible.

None among the previous experimental works shows triangular islands with stacking faults. Furthermore, we observe that stacking faulted (minority) islands have a mean size of 520 atoms while pseudomorphic (majority) islands have $\langle s \rangle = 1460$ atoms. This suggests that the same effect responsible for the different island densities may be responsible for the nucleation of stacking faulted islands. Several publications show the possibility that impurities [107] or surface strain [108] could lead to stacking faults. As has been said before, studying the effect of impurity gases on the nucleation of Co/Ru(0001) is a prerequisite to enable a complete understanding of the stacking fault behavior observed here.

5.9 Conclusions

In this chapter we have presented an extensive growth study of submonolayer Co/Ru(0001) for deposition temperatures in the range of 85 K to 500 K. We were able to extract the monomer migration

barrier $E_m = 310$ meV and the corresponding hopping attempt frequency $\nu_0 = 5 \times 10^{13}$ Hz. Both values appear reasonable when compared to other transition metal on metal growth experiments in the literature. Our data further show evidence of a lowered migration barrier for the last step towards attachment (*easy attachment*). We calculated the corresponding activation energy $E_{attach} = 240$ meV. This value is also in good agreement with theoretical predictions found in previous publications.

Our experimental data suggests that the critical cluster size remains 1 for the whole range of studied temperatures. Based on the island density behavior at high temperature, we can furthermore exclude cluster diffusion. Comparing these results with previous works done by other groups reveals an important discrepancy. In fact, our simulations show that previous results require a model with dissociation of dimers as well as trimers. Assuming that our high temperature data are biased, we can still extract relevant activation energies for the dimer and trimer dissociation $E_2 = 600$ meV and $E_3 = 600$ meV.

The island morphology undergoes a transition from irregular compact islands below 300 K to triangular below 400 K and hexagonal at 500 K. This observation is in accordance with the low edge-diffusion energy barrier calculated by Bartelt et al., which we adapted to the correct attempt frequency. This yields an activation energy for diffusion along the B-type island edge of $E^B_{2\rightarrow 2} = 420$ meV.

In the temperature range of 300 K to 400 K we observe the nucleation of stacking faulted islands. The assumption that this stacking fault is due to the difference in binding energy of hcp versus fcc sites leads to the conclusion that the difference in free energy of the two type of sites is ≈ 50 meV. The stacking fault behavior could also be ascribed to the presence of impurities or strain in the substrate. In fact, the discrepancies between previously published results of Co/Ru(0001) growth could be explained by the presence of adsorbed residual gases. The presence of hydrogen and carbon-monoxide has been shown to alter the diffusion behavior of monomers on other types of surfaces. This work thus acts as a first approach and should be complemented by an extensive study of the effects of adsorbed gases on the diffusion of the cobalt monomer on the Ru(0001) surface.

Chapter 6

Volmer-Weber type island growth on the *h*-BN *nanomesh*

One of the major challenges in self-organized growth is the fabrication of a well ordered superlattice of nanoparticles with a narrow size distribution. One route is to deposit atoms from the vapor phase onto a template, i.e. a substrate characterized by a periodic array of cluster nucleation sites. For example, a regular strain-relief pattern has been used as a template for nucleation for Fe/2 ML Cu/Pt(111) or Ag/1.5 ML Ag/Pt(111) in Ref. [34]. Weiss et al. [5] have used a Au(788) vicinal surface. The intrinsic stress of the surface triggers a reconstruction into partial dislocations running perpendicular to the atomic steps. The reconstructed areas act as traps for the diffusing adatoms, eventually producing a phase coherent macroscopic rectangular lattice of Co dots. Oxide superstructures on metal surfaces have also proven efficient as nucleation templates, for example when depositing Pd on the alumina/Ni_3Al superstructure [109]. A different approach, used by N'Diaye et al. [110] is to use a one monolayer thick graphite layer (graphene) on an Ir(111) surface as a template. Graphene forms a hexagonal moiré pattern with a lattice constant of 25 Å on the iridium surface. The deposition of iridium adatoms on this surface produces a hexagonal lattice of clusters with a remarkably narrow size distribution.

A surface structure which has lately drawn much interest and which could be a candidate as a template for the growth of metal clusters is the hexagonal boron nitride (*h*-BN) deposited on Rh(111) or Ru(0001). On these surfaces, a *h*-BN layer produces a hexagonal lattice with a parameter of 32.2 Å [111] which has been called "nanomesh". In this chapter, we present an extensive study on the growth of Co cluster on the *h*-BN/Rh(111) surface. A similar study about Co/*h*-BN/Ni(111) has been performed by W. Auwärter et al. [112]. The main difference is that on the nickel substrate the hexagonal boron nitride does not form a superlattice. We will refer to this publication to point out differences and similarities between both systems throughout this chapter.

6.1 Hexagonal boron nitride

The BN compound, made of one boron and one nitrogen atom, is isoelectronic to a pair of carbon atoms. Due to this particularity, BN can form polymorphic crystal structures like carbon, including the hexagonal boron nitride (*h*-BN) which is graphite-like or cubic boron nitride (*c*-BN) which is diamond-like (see Fig. 6.1). In the latter structure (*c*-BN), it is one of the hardest materials known. Other carbon-like structures, as concentric onion-like fullerene shells [114] as well as nanotubes [115, 116] have been reported for BN. The compounds are thermally stable, electrically insulating but good thermal conductors. This makes boron nitrides an interesting material for numerous industrial applications. Hexagonal boron nitride is for example used for high temperature lubrication.

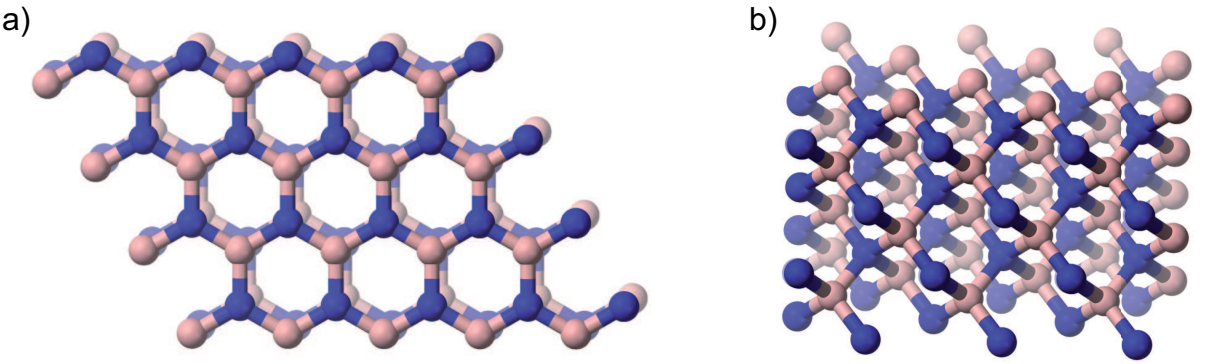

Figure 6.1: Atomic structure of BN compounds (boron: pink, nitrogen: blue)
a) Hexagonal boron nitride (*h*-BN), B and N atoms alternatively assume positions on a hexagonal lattice. The structure resembles graphite with carbon atoms replaced by B and N.
b) Cubic boron nitride (*c*-BN) has the same crystallographic structure as diamond with carbon atoms replaced by alternating B and N. From [113].

Hexagonal boron nitride can be grown on metal surfaces by chemical vapor deposition (CVD) of $B_3N_3H_6$ (*borazine*). The boron nitride structure is formed by thermal decomposition at the surface of this molecule at $T \approx 1050$ K. Extensive studies have been performed for *h*-BN/Ni(111)[117, 118, 119] where a self-limiting monolayer of commensurate *h*-BN forms.

Upon growth of *h*-BN on Rh(111), Corso et al. [111] have reported the formation of a corrugated hexagonal layer with a lattice constant of 32.2 Å [120] (see Fig. 6.2 a.). This mesh appears as circular holes with ≈ 0.5 Å depth. As we will see, this value depends on the tunneling conditions. Recent works [121, 122] have confirmed that the mesh is the result of a coincidence lattice or moiré pattern of 13×13 *h*-BN unit cells on 12×12 Rh(111) substrate sites. The formation of the characteristic hole/bridge pattern as visible on STM images has been explained by force field calculations [121]. They show the formation of the strongly corrugated *h*-BN layer due to the lattice mismatch, with the boron atoms closer to the rhodium surface than nitrogen atoms. A corrugation of ≈ 0.55 Å is predicted by these calculations. The σ-bands splitting reported in the original publication is ascribed to the different positions the B and N atoms take with respect to the Rh atoms. Recent results indicate that a similar pattern appears upon deposition of *h*-BN on Ru(0001)[123] and Pd(111)[124].

6.2 Experimental

The experiments were performed in the same UHV chamber as for Chap. 5. The single crystal Rh(111) surface was prepared by repeated cycles of Ar^+ ion sputtering ($E = 1.3$ keV, $I = 1.2\,\mu$A) at room temperature, followed by annealing in O_2 atmosphere at 800 K ($P_{O2} = 2 \times 10^{-8}$ mbar, $t = 10'$). The sample was then flash annealed to 1500 K. On day-to-day work this preparation cycle was performed twice. In fact, monitoring the UHV chamber's residual gas level with a mass spectrometer shows a pressure peak during the first flash-anneal. This suggests that the first sputtering cycle does not remove the *h*-BN completely, but only the high temperature (≈ 1300 K) thermal desorption does. The Rh(111) surface after two complete preparation cycles showed terraces of width $\ell > 5000$ Å. The *h*-BN was deposited by exposure of the clean rhodium surface to 100 L (1 Langmuir $= 10^{-6}$ Torr s) borazine at $T_{dep} = 1040$ K. The exposure was typically done at a borazine partial pressure of 6×10^{-7} mbar during 180 s followed by an additional 60 s at the deposition temperature before cooling down. The sample temperature was monitored by a K-type thermocouple pair spot-welded to the Rh(111) sample. After

deposition of *h*-BN and recovery of the chamber pressure to values $< 3 \times 10^{-10}$ mbar, the sample was cooled to the expected deposition temperature. Cobalt deposition was performed using an e-beam evaporator with a flux of $F = 5.3 \times 10^{-3}$ ML/s. The flux was determined by depositing ≈ 0.5 ML of Co on the clean Rh(111) surface at $T_{\mathrm{dep}} = 400$ K followed by measurement of the coverage by STM imaging. Pressure during deposition was below 2×10^{-10} mbar

The measurement were done in collaboration with the group of Prof. J. Osterwalder who provided the ultra-pure borazine and the CVD source. We acknowledge the kind help of T. Brugger [125] and A. Lehnert [126] for the experimental work.

6.3 Cobalt on *h*-BN/Rh(111)

The study of the growth behavior of Co/*h*-BN/Rh(111) was divided in three steps. First we studied the island size behavior and shape as a function of cobalt coverage for a fixed deposition temperature $T_{\mathrm{dep}} = 200$ K. By identifying the growth regime from these experiments, we can acquire the island densities at the saturation level as a function of temperature and obtain diffusion barriers. We finally studied Co cluster diffusion by annealing experiments.

Fig. 6.2 a.–e. show STM images of the deposition of cobalt at $T_{\mathrm{dep}} = 200$ K for coverages ranging from 0.013 ML to 1.17 ML. At low coverage (Fig. 6.2 b.), small, circular, Co dots are visible on the STM topographs. The dots exhibit diameters in the range from ≈ 8 Å to ≈ 16 Å and seem randomly placed with respect to the underlying *h*-BN structure. The typical height above the mesh bridge sites is between ≈ 2 Å and ≈ 4 Å, meaning the coexistence of mono and bilayer islands. With increasing Co coverage (Fig. 6.2 c.), the dots become more numerous, higher and their diameter gets larger (≈ 12 Å). Most clusters are still clearly separated. At a coverage closer to 1 ML, (Fig. 6.2 d.) the cluster diameter has grown and islands seem to touch while avoiding each other. At coverages over the monolayer (Fig. 6.2 e.) the whole surface is covered by clusters of different heights. In contrast to the work of Auwärter et al. [112], we did never observe bidimensional islands, neither on, nor below the *h*-BN layer. Furthermore, we did not see equivalent defect lines to those reported in this publication.

Even at the smallest coverages, Co does not wet the *h*-BN surface but follows a Volmer-Weber growth mode, with creation of 3D islands. Assuming thermodynamic equilibrium, the growth model is determined by the free energy of the substrate surface (F_{s}), the interface free energy (F_{i}) and the surface free energy of the deposited material (F_{f}). Strain can also influence the growth mode, but in our case the lattice mismatch between Co and the *h*-BN layer is small (1.3 %). In the case where strain effects can be neglected, the condition for Volmer-Weber growth reads: $F_{\mathrm{s}} < F_{\mathrm{f}} + F_{\mathrm{i}}$.

At higher coverages, the STM tip is unable to resolve the mesh surface in between Co islands. Thus we cannot determine if coalescence occurs at the bottom level of the Co islands or if the Co dots are separated. Furthermore, in this case the simple island recognition algorithms fail because of the very disparate cluster heights. We thus developed an ad-hoc image processing tool which permits to automate recognition and extraction of height, location and surface data also for these results. The tool is presented in Annexe A.2.

The location of the Co islands seems random. In particular, no dot chains form in contrast to observations on *h*-BN/Ni(111) [112]. The dots neither clearly align to the hexagonal lattice of the boron nitride. However, the mesh surface has been shown to yield preferred adsorption sites for the deposition of C_{60} molecules [111]. We can thus expect a difference in Co binding energy between hole and bridge sites. In order to quantify this energy we have counted the occurrence of Co dots inside holes and on bridge regions. The count was made on images of 0.05 ML Co deposited at $T_{\mathrm{dep}} = 200$ K. Because the cobalt appears with a relatively large diameter, 34.2 % of all islands cannot be clearly classified. For the purpose of our calculation, we temporarily discard these indeterminate dots. We count $N_{\mathrm{h}} = 31.8$ % of clusters inside mesh holes and $N_{\mathrm{b}} = 68.2$ % on bridge sites (total sample: 380

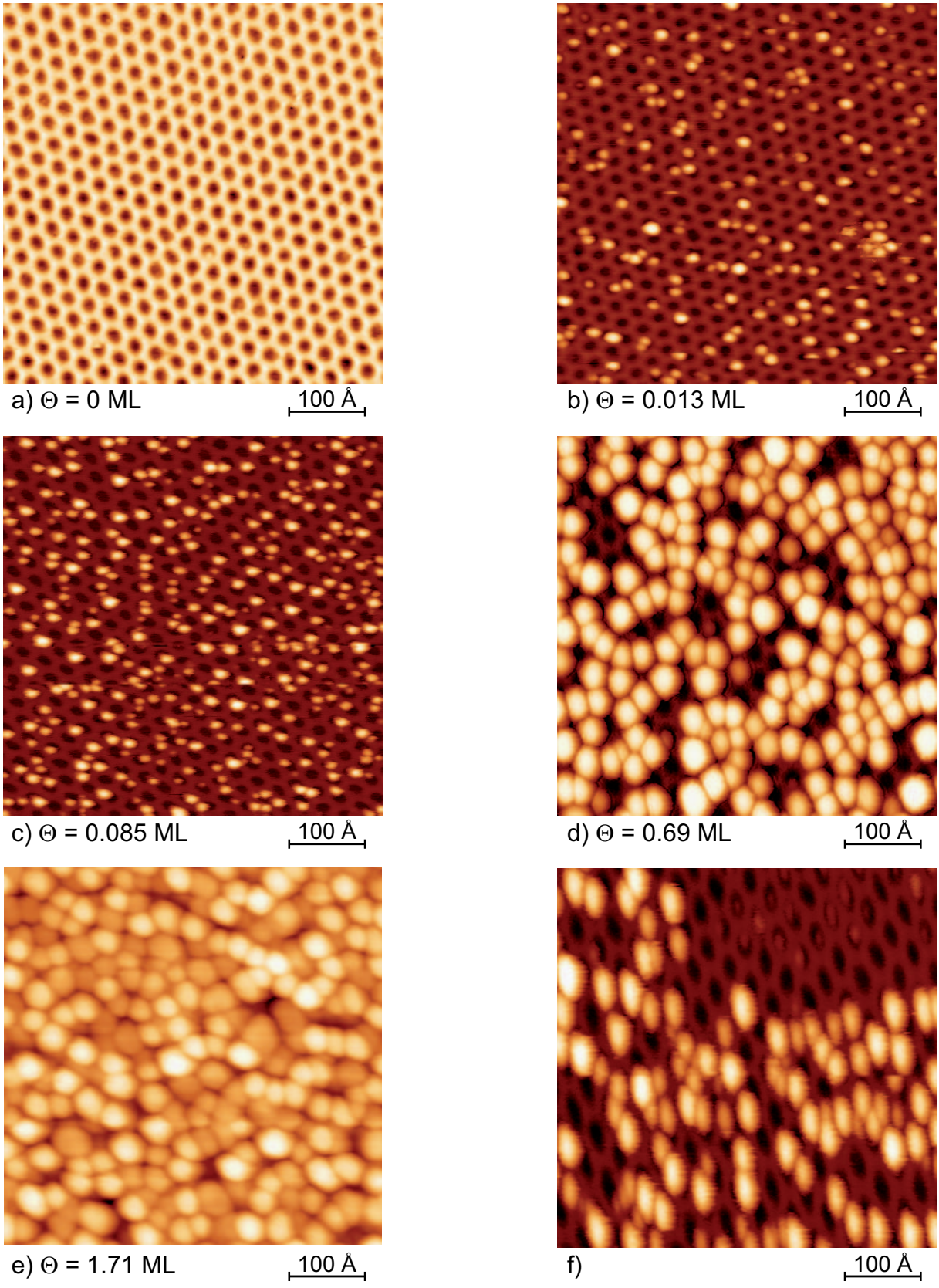

Figure 6.2: STM images of Cobalt deposited on *h*-BN/Rh(111) at $T_{\text{dep}} = 200\,\text{K}$ ($V_t = -2\,\text{V}$, $I_t = 50\,\text{pA}$). a.) Clean *h*-BN mesh b.-e.) Diverse coverages of Co f.) Rectangular region swiped by the STM tip during a previous image scan. Reducing the tip-sample distance ($V_t = -2\,\text{V}$, $I_t = 1000\,\text{pA}$), the tip aggregates the Co clusters. Images have not been corrected for thermal drift. is too small.

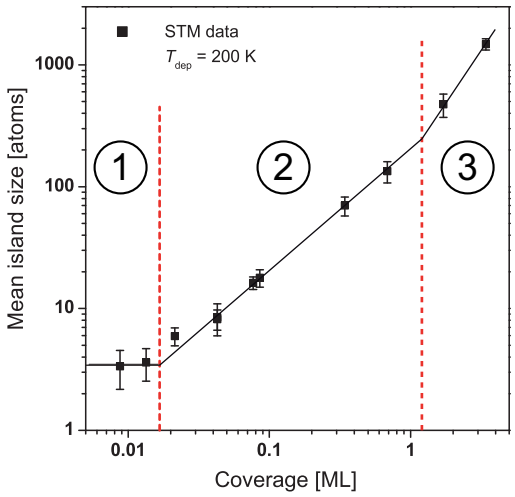

Figure 6.3: Mean island size as a function of Co coverage. The growth shows three separate regions. 1. At low coverage, the system is in the pure nucleation regime. Additional adatoms nucleate new islands and the average island size stays constant. 2. The growth regime is characterized by linear increase of the mean island size with increasing coverage. 3. The coalescence regime sets in above $\Theta = 1.0$ ML and results in the reduction of the island number, and thus in a faster-than linear increase of the mean island size. Continuous lines are guides to the eye.

islands). For a totally isotropic nucleation, the occurrence ratio would be proportional to the surface ratio of bridge vs. hole sites. Bridge sites account for $A_b = (64 \pm 10)\,\%$ of the image surface (thus $A_h = (36 \pm 10)\,\%$ for holes). The position of counted clusters is thus really isotropically random within the error bars which indicates that a possible binding energy difference between hole sites and bridge sites is small. Using the above data, we can estimate an upper bound for the binding energy difference. Similarly to the stacking fault behavior of Co/Ru(0001) (see Sect. 5.8, p. 91), we assume that the nucleation ratio in holes versus on bridge sites follows a Boltzmann term of the site free energy difference (see Eq. 5.4, p. 93). Naturally, the ratio of island types (hole/bridge) must be normalized with the ratio of bridge/hole surfaces. We get

$$\frac{N_h A_b}{N_b A_h} \approx \exp\left(\frac{2\Delta F}{kT}\right) \tag{6.1}$$

Using the value and uncertainty for the areas measured above yields $\Delta F = (-3 \pm 7)\,\text{meV}$. The negative sign indicates that atoms are more strongly bound on bridge sites. Evidently, this value has a huge uncertainty and cannot be relied upon. In fact, the uncertainty of the measure most likely stems from the 34.2 % of islands discarded and not from the surface measure uncertainty. One can easily imagine that a preferred nucleation site exists on the rim of the holes where the diffusing adatom experiences a step of $\approx 0.5\,\text{Å}$ height. All islands nucleated at the rim would be counted as indeterminate and strongly bias the above calculation. Accrediting all islands previously not countedÍ, to the in-hole count ($N_h = 55.2\,\%$), would lead to $\Delta F = 13.5\,\text{meV}$. Adding a supplemental error margin to this value, we can conclude that the free energy difference for Co on h-BN/Rh(111) between hole and bridge sites is $|\Delta F| < 15\,\text{meV}$. As expected from the random locations of the dots on the surface, this energy difference is small.

Fig. 6.2 f. shows how the STM tip, when scanned too close to the surface, removes cobalt clusters. This leaves a characteristic square footprint of the previously scanned region. Imaging cobalt cluster on h-BN with the STM thus requires the choice of a high tunneling resistance, with a large

tip-sample distance. In practice, scanning with tunneling currents below 100 pA and sample voltages $1\,\mathrm{V} < |V_t| < 2\,\mathrm{V}$ have proven effective. The fact that we don't see an accumulation of cobalt on either one side of the depleted region indicates that the Co material is aggregated to the tip. This hints at a very weak bonding between the cobalt and the *h*-BN surface. The swiped region shows some small dots remaining inside of mesh holes, which may indicate that regions with a stronger bonding exist at selected locations of the mesh, namely the hole edges. This supports the model of the previous paragraph claiming that a preferred adsorption site exists at the hole rime with a free energy difference between hole and bridge sites of $\Delta F \approx 13.5\,\mathrm{meV}$.

A clearer picture of the growth process is obtained by using the island density to plot the mean size as a function of Co coverage as shown in Fig. 6.3. The plot can be divided into three regions.

1. The pure nucleation regime. It is characterized by a constant mean island size of $\langle s \rangle = 3.5$ atoms. The newly deposited adatoms form new growth nuclei. Only little aggregation occurs. The stable island number scales linearly with the coverage. The high mean size indicates that at least the monomer is mobile at $T_{\mathrm{dep}} = 200\,\mathrm{K}$.

2. The growth regime is characterized by a linear increase of mean island size with augmenting coverage (fit: $\langle s \rangle = 193\ \Theta^{0.96}$). Most additional deposited Co is aggregated by existing stable islands.

3. The coalescence regime. The actual island density decreases. This results in a more rapid increase of the island size (fit on the two last points: $\langle s \rangle \propto \Theta^{1.61}$).

6.4 Cluster heights

A strong correlation between island height and island diameter is found (not shown). This has previously been reported for the growth of Co on *h*-BN/Ni(111) [112]. Although, this is expected from a pure 3D island growth point-of-view, we cannot distinguish between a convolution of the tip shape with the island and the island shape itself. In fact, we can confirm that the visible diameter is most certainly due to tip convolution as the integrated volume of visible islands is larger than the amount of Co deposited. This strongly limits the information content in the island diameters extracted from STM images.

The *apparent* relative height in contrast is known to a precision better than 0.1 Å. We emphasize the term apparent, as the STM probes the local density of electronic states (LDOS) and not the topographic height. In fact, our measurements show that the corrugation of the mesh can vary from one image to the other from ≈ 0.3 Å up to ≈ 1 Å in rare cases. This difference is ascribed to differing electronic states of tip atoms and mesh atoms. In order to get relevant island height data, we need to first determine what the effect of the apparent corrugation is on the apparent height of islands. In this sense, we show in Fig. 6.4 a. the height distribution of the two populations of islands, namely in-hole and on-bridge. The data is taken from an experiment with 0.05 ML Co deposited on the clean mesh at 200 K. For islands in the mesh holes, the distribution shows a maximum at 2.7 Å and a full width at half maximum (FWHM) of 1.2 Å while for islands on bridge sites the maximum is at 3.1 Å and the FWHM is 1.6 Å (heights are measured with respect to the bridge level). The corrugation of the boron nitride layer was ≈ 0.85 Å on the corresponding images.

The difference in peak position for the two populations is 0.4 Å although the same corrugation as measured on the mesh would be expected if islands have the same height distributions and electronic effects are negligible. Two explanations come to mind for this discrepancy. First, if the island bottom is really vertically shifted by 0.85 Å when comparing in-hole and on-bridge dots, the mean height of the two types of islands must be different. This would yield in-hole islands with a height of 3.6 Å. We

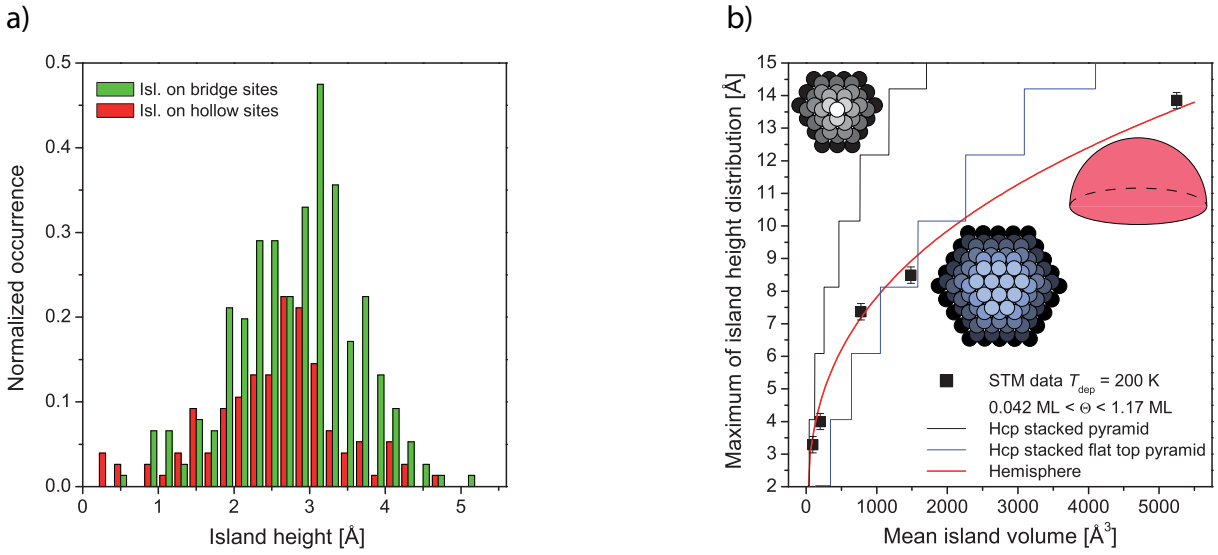

Figure 6.4: a. Island height distribution for 0.05 ML Co deposited on *h*-BN/Rh(111) at $T_{\text{dep}} = 200$ K. The height is measured with respect to bridge site level. Islands on bridge site (green) and on hole sites (red) are counted separately. The clean mesh corrugation in the corresponding images was 0.8 Å while the position difference between the two peaks is only 0.4 Å. See text for explanations.
b. Most probable island height as a function of mean island volume. The different island sizes are obtained in experiment by varying the Co deposition amount at $T_{\text{dep}} = 200$ K. The volume is calculated as the mean island size times the Co-hcp lattice cell (11.07 Å^3). Fitting models are the hcp-stacked pyramid (black), the hcp-stacked pyramid with a flat top of minimum 12 atoms (blue) and the continuous hemisphere (red). The model suggests that Co islands take a nearly perfect hemispherical shape.

have shown that the binding energy is very similar on hole and on bridge sites, thus it is not expected that islands show such a radically different growth behavior on the two types of sites. The second possibility is that the important apparent mesh corrugation is a purely electronic effect of the tip-sample interaction and that the physical position of the bottom of islands is shifted by the 0.5 Å mesh corrugation measured in [111] and calculated in [121]. Supposing islands of the same mean height, this would explain the measured height difference between in-hole and on-bridge dots within the error bars. In this case, we could conclude that the electronic effects biasing the measure of the hole depth are relieved when tunneling through the cobalt. This second possibility is supported by the fact that other purely electronic tunnel effect can be observed on the system (see Sect. 6.8.1). With the present data we cannot unequivocally distinguish between these two cases. In further studies presented below, we have used the island height measured with the bridge site level as reference for all islands. This introduces a systematic error of 0.5 Å for the height of islands in holes but permits to study a much larger quantity of islands. A mean or peak height measured on a complete image has thus an error bar ±0.25 Å.

6.4.1 Determining the island shape

We can extract information on the island shape *without* using the visible island diameter. At a given temperature ($T_{\mathrm{dep}} = 200$ K), we study how the most probable island height evolves with increasing coverage. As we know the mean island size for each coverage, we can plot the most probable height as a function of island volume. Squares on Fig. 6.4 b. show the values obtained experimentally for Co coverages from $\Theta = 0.042$ ML to $\Theta = 1.17$ ML. We have shown in Fig. 6.3 that the mean island size increases accordingly from $\langle s \rangle = 16$ atoms to $\langle s \rangle = 474$ atoms. The corresponding volume is calculate by multiplying $\langle s \rangle$ by the hcp-cobalt lattice cell ($v = 11.08\,\text{Å}^3$).

As expected, the island height is a monotonic increasing function of island volume. To understand which shape is responsible for this behavior, we make two assumptions.

1. Islands have an approximate vertical axis of revolution.

2. The island shape scales without changing its aspect ratio

The first assumption is supported by several arguments. First and foremost we observe nearly circular islands. Although STM tip convolution is expected to round atomic island corners, the overall 2D shape of the island is expected to be visible. Second, as monomer diffusion on top of islands is an activated process, edge diffusion can also be supposed activated. This eventually results in compact, nearly round, islands.

We support the second assumption, i.e. that the overall shape stays constant, for two separate cases. The 3D island growth may either be the result of kinetic limited processes or the result of a thermal equilibrium. For kinetic limited processes, we assure that the same processes are activated for the complete plotted values by making all measurements at the same temperature ($T_{\mathrm{dep}} = 200$ K) and at the same deposition flux. We thus expect a similar shape given by the kinetics for different island sizes. In the case of thermal equilibrium, the shape's aspect ratio is given by the ratio of the Co/h-BN interface energy with the Co/vacuum surface energy. We thus expect the shape to scale with island size.

6.4.2 Atomistic models

The simplest 3D island shape expected to occur in hcp stacked atoms is the hexagonal based pyramid. The minimum number of atoms s needed to build a pyramid of a given height h (in atomic steps) is[1]

[1] In the fcc stacked, triangular based pyramid, the size function is $s(h) = n(n+1)(n+2)/6$. Interestingly, the limit for h tending to infinity is $h^3/4$ in the hcp case and $h^3/6$ in the fcc case. The fruit vendor at the market is thus better off stacking

$$s(h) = \left(4h^3 + 6h^2 + 4h + 1 - (-1)^h\right)/16 \tag{6.2}$$

where the $(-1)^h$ accounts for the two types of hexagons alternating at the pyramid's base. This pyramid ends with a single atom on top which is expected to be quite unstable (as we experience when using such a pyramid as an STM tip). As an alternative, more realistic model, we use a flat top pyramid. The stacking is the same as before, but the last three layers are discarded which results in the topmost layer showing 12 atoms (see inset in Fig. 6.4 b.). In this case the size function is

$$s^*(h) = s(h+3) - s(3) \tag{6.3}$$

The resulting height versus volume for both functions are plotted on the graph using the hcp-Co inter-planar distance of 2.035 Å for conversion. Evidently, the height functions are discontinuous because the apparent height of the pyramid changes upon addition of the one last atom at the top. We observe that the sharp pyramid fits the small islands very well but for larger islands, the model predicts too high clusters. The flat top pyramid model fits the medium sized islands best while being less accurate for the smaller and larger ones. Finally, in order to reach the largest islands, a flat top pyramid model with the first 5 layers removed is necessary (not shown). This gives a pyramid with a mesa of 27 atoms on its highest level. The fit for small island sizes is correspondingly worse. These results indicate that the simple flat top pyramid model is not explaining all observed island heights. It seems that the topmost atomic layer grows with increasing cluster size.

6.4.3 Continuous model

As an alternative to the atomistic model shown above, we can use a continuous shape model. We suppose that islands are half-ellipsoids with a circular base. Only the height direction is either compressed or inflated. The volume function is then

$$V(r,h) = \frac{2\pi}{3}\, r^2\, h = \frac{2\pi}{3}\, \gamma\, r^3 \tag{6.4}$$

with r the radius of the basis, h the island height (both in Å) and γ the scaling coefficient between r and h. γ is supposed constant because of the shape scaling assumption we made above. $\gamma = 1$ corresponds to the hemisphere. Using γ as a fit parameter on the experimental data yields $\gamma = 0.99$. This means that the experimentally observed islands scale like a hemisphere! The height function for the hemisphere is shown as a red line on Fig. 6.4 b. We observe that this function fits all available data precisely. Unfortunately we cannot determine if the hemispherical shape of the dots stems from thermal equilibrium or from kinetic limited processes. In the light of this finding, we observe that even at high Co coverages, the surface foot print of the islands is small (radius = height). This confirms again that the actual diameter of islands is much smaller than the apparent diameter. It also explains, to some degree, why the islands do not coalesce although they seem to be touching on images with higher coverages.

6.5 Island size distribution

We have now clearly established how the island height scales with the volume. We can use this information to study the island size distribution. In fact, the island height distributions are easy to obtain from images at different growth conditions, independently of STM tip convolution. Fig. 6.5 shows the normalized size distribution for the deposition of 0.085 ML Co at three temperatures. The characteristic shape of the distributions shown in previous chapters for 2D islands is maintained. Deposition

his oranges in an hcp manner than in an fcc manner.

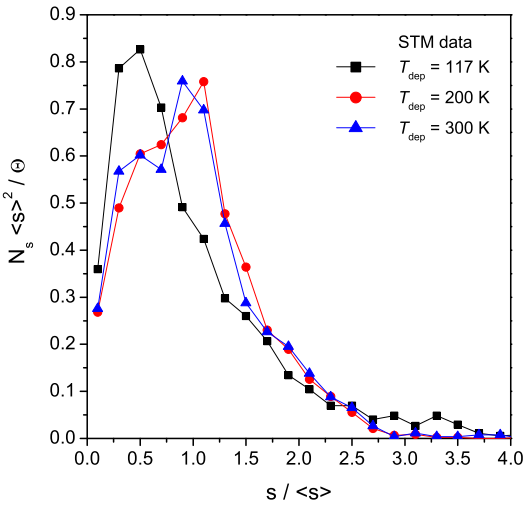

Figure 6.5: Island size distribution for Co deposited at three different temperatures. The size is calculated with the hemispherical shape model using the height distribution.

at $T_{\mathrm{dep}} = 117$ K yields a maximum of 0.85 for a size of $0.5\langle s\rangle$. This peak is slightly higher and narrower than expected from 2D nucleation theory for $i = 1$ (see e.g. Ref. [23]). For deposition at 200 K and 300 K, the distributions are very similar. They exhibit a maximum of 0.75 at the mean size. Comparing these distributions with theoretical predictions for 2D islands supports the fact that the monomer is the critical cluster size up to 300 K.

Gwo et al. [127] report that Co clusters on Si_3N_4 exhibit "magic cluster" sizes. Islands of these sizes are supposed more stable and thus more frequently found on the surface. To get a broad collection of cluster sizes, they study different coverages of Co at the same growth conditions. We have performed an equivalent size analysis (not shown) of a sample of 2200 islands for different coverage values deposited at $T_{\mathrm{dep}} = 200$ K. The data does not show any evidence of the "magic cluster" sizes reported by Gwo et al. The existence of such "magic" sizes supposes islands in thermodynamic equilibrium. This hints at the fact that the shape of Co clusters on *h*-BN are the result of kinetically limited processes and not thermodynamic equilibrium.

6.5.1 Island height and area correlation

If all clusters are immobile during the growth phase, a strong correlation between the island size and its capture area is expected [128]. If larger clusters are mobile in contrast, the measured correlation should be much smaller as the clusters aggregate monomers while moving on the surface and their final position is almost random. The simplest approach to estimate the monomer capture surface of a nucleus is to calculate its associated Voronoi area [129]. Several more refined approaches have been proposed, for example by Bartelt et al. [130] who introduce an edge capture cell, taking into account the spatial extension of islands. In the present work we want to investigate if a correlation exists between the Co island size and the capture area. For this purpose the Voronoi tessellation approach is sufficient. In Fig. 6.6 we present a Voronoi construction for 0.1 ML Co deposited at 150 K on the clean mesh. The center of mass of 470 islands have been extracted from one image and, after

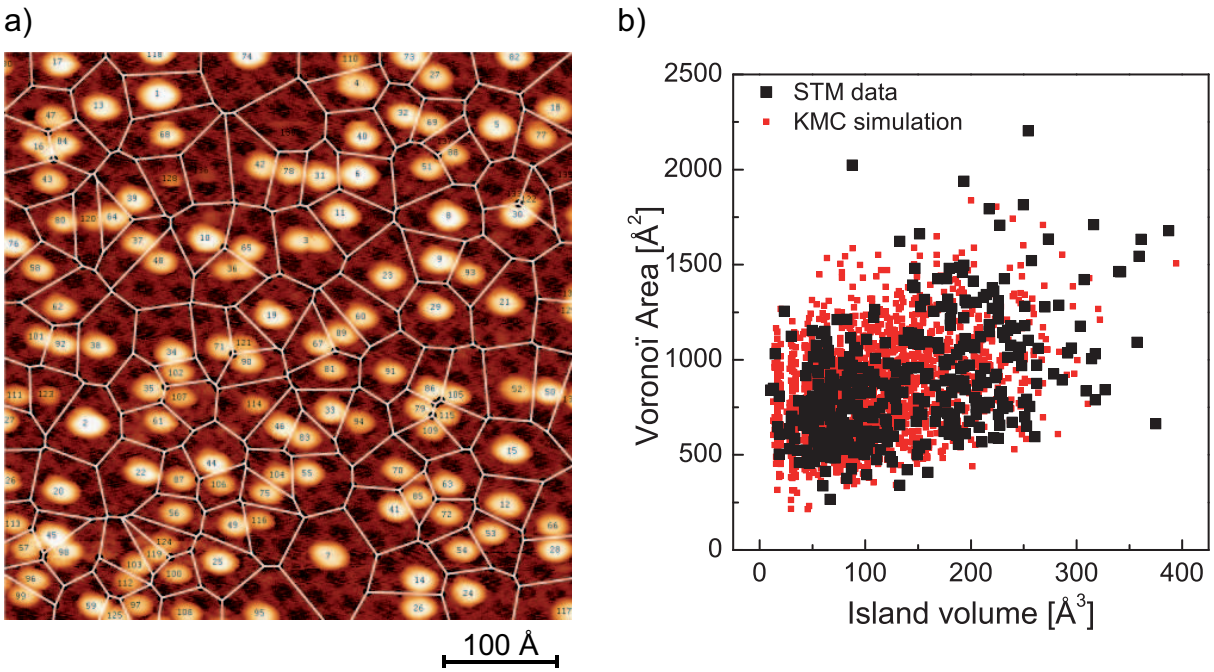

Figure 6.6: a. Example of Voronoi tessellation applied to the islands of an STM image. The area of each Voronoi polygon is calculated and associated to the corresponding island.
b. Voronoi area as a function of island size for 0.1 ML Co deposited on the clean mesh at 150 K (black squares). The result is compared to a KMC simulation of 2D islands with parameters chosen to produce compact islands of the same mean size as in the experiment.

tessellation, the area of the corresponding Voronoi polygon has been calculated. The experimental data is shown as black squares in Fig. 6.6 b. Although the data seems to have strong random character, a linear trend is apparent. In order to quantify if the random character is inherent to the stochastic nature of the growth or if it can be ascribed to large cluster mobility, we perform KMC simulations. The simulations are done for compact 2D islands with parameters chosen as to obtain the same mean island size as measured in the experiment. In the simulation all cluster sizes except the monomer are immobile.

Comparison of the KMC simulation with the experimental data shows an excellent agreement. The slope of the linear trend is obviously the same. Also the random spread of Voronoi areas for a given island size is of the same order of magnitude. This lets us conclude that large clusters are immobile on the surface at 150 K.

6.6 Island densities

The second step of our investigation consists in studying the island density as a function of the deposition temperature in order to extract the diffusion barriers of Co monomers and possibly larger clusters. We have shown above that the system is in the island saturation regime between coverages of ≈ 0.02 ML and ≈ 1.0 ML. We chose to deposit 0.085 ML of Co because lower coverages render island recognition easier. The STM images in Fig. 6.7 show that the shape of the cobalt clusters is independent of deposition temperatures. On the contrary, the cluster density decreases with increasing temperature; the mean size augments accordingly. The adsorption sites are random independently of T_{dep}. For cobalt deposition above 500 K, the surface does not exhibit any clusters. This indicates that the sticking coefficient decreases with increasing temperature and that desorption of the Co monomers occurs during deposition.

The island densities extracted from the STM images are calculated using the rhodium surface unit cell ($c = 6.264\,\text{Å}^2$) as a reference. The densities are presented in the Arrhenius plot of Fig. 6.8. The plot suggests three regions. It shows an almost linear decrease of island density with increasing temperature for deposition temperatures between 117 K and 200 K. Between 200 K and 300 K, the data seems to follow another linear relation, but with a much steeper slope. Finally, at temperatures above 300 K a third linear regime is observed.

6.6.1 Diffusion parameters from 3D scaling law

In order to fit the data and extract diffusion parameters, the scaling law (Eq. 3.5) has to be adapted to 3D, Volmer-Weber growth. In this case both the exponent and the prefactor are changed to account for the smaller base of the islands. Assuming hemispherical islands and $i = 1$, we get [20]

$$n_x \propto \left(\frac{D}{F}\right)^{-2/7} \tag{6.5}$$

Fitting the island density data for $T_{\mathrm{dep}} < 200$ K gives the monomer migration barrier $E_{\mathrm{m}} = (23 \pm 3)$ meV. In order, to extract the corresponding attempt frequency, we need to know the proportionality factor η between the $(D/F)^{-2/7}$ term and the island density. In the 2D case, when solving rate equations analytically [20] gives $\eta = \Theta^{1/3}$ for $i = 1$, which yields $\eta = 0.44$ for 0.085 ML. In contrast KMC simulation results [22] suggest a value closer to $\eta = 0.25$. In the 3D case, the prefactor theoretically is $\eta = \Theta^{2/7}$ [20], which for our coverage yields $\eta = 0.49$. Fitting with this value gives an attempt frequency $\nu_0 = 7 \times 10^5$ Hz. Using the 2D value for η in contrast gives $\nu_0 = 6 \times 10^4$ Hz. The difference of over one order of magnitude between the two approaches suggests that this value has to be treated with precaution.

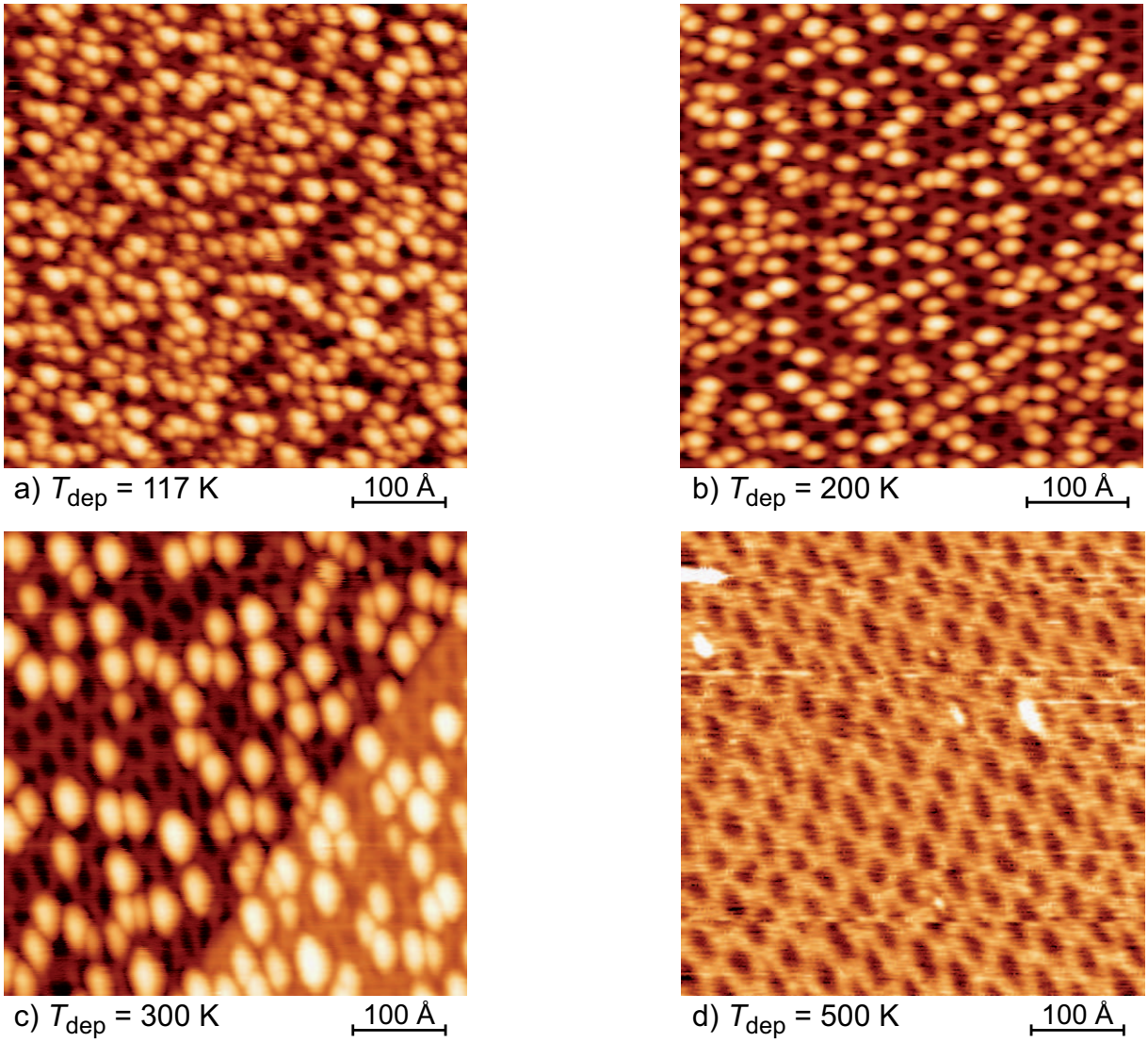

Figure 6.7: STM images of 0.085 ML Co deposited on the clean *h*-BN/Rh(111) surface at different temperatures. Images a.–c. clearly show a decrease in island density with increasing deposition temperature. At $T_{dep} = 500$ K no cobalt can be seen on the surface. This indicates that the sticking coefficient is low and desorption occurs.

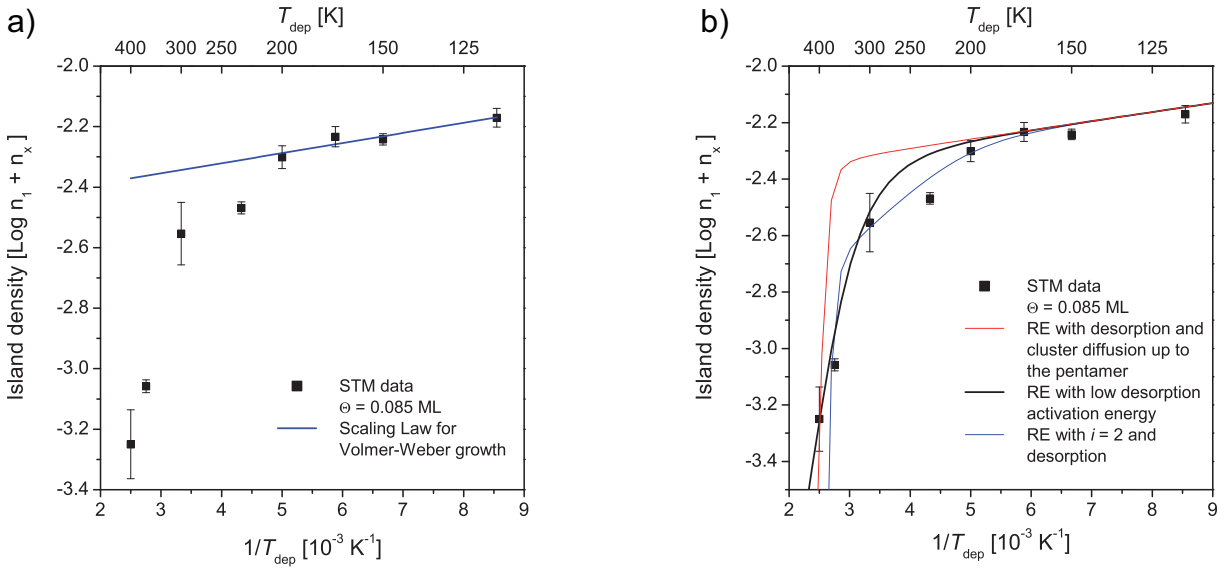

Figure 6.8: Island densities after deposition of 0.085 ML of Co on the clean boron nitride superlattice.
a. The densities shows a linear decrease in the Arrhenius representation for deposition temperatures below 200 K. The data is fitted with the scaling law for 3D growth and $i = 1$. The parameters are $E_m = 23$ meV and $\nu_0 = 7 \times 10^5$ Hz
b. Island densities fitted with rate equation models. All models include a desorption term. Diffusion of clusters up to the pentamer are included with different desorption energies (red & black curves). Dissociation of the dimer ($i = 2$) is included for the blue curve.

These migration parameters for the monomer are quite surprising. First, the migration activation energy of 23 meV is very small. We recall that equivalent values for metal-on-metal systems are typically 10 times larger. Evidently the Co monomer is only weakly physisorbed to the boron nitride surface as suggested by the desorption at high temperature and the fact that the STM tip can remove the Co from the surface by simply scanning over it. This suggests that the corrugated potential surface experienced by the monomer upon diffusion may have only a weak amplitude. The diffusion attempt frequency at $\nu_0 \approx 1 \times 10^6$ Hz is also very small. The Meyer-Neldel rule [131] predicts a monotonic increasing relation between the migration barrier and the attempt frequency. Thus smaller energy barriers are associated with smaller attempt frequencies which could explain the small value found in experiment. From the transition state theory point of view [132], a small prefactor is explained by a small difference in vibrational free energy between the transition state (saddle-point) and the equilibrium state (binding site).

The low activation energy for diffusion implies that the temperature dependence of the hopping frequency for a monomer is small. This is surprising and may indicate that the traditional monomer diffusion model is not applicable here. Long-range interactions between adatoms, e.g. mediated by a metal surface-state [133], have for example been known to alter diffusion behavior. Evidently the *h*-BN does not exhibit a surface state, but long-range interactions are still possible, for example by local surface strain. Such long-range interactions result in some characteristic inter-cluster distances being more probable. We have studied the nearest-neighbor cluster distances using a Delaunay triangulation of the island positions. No remarkable distance feature has been found. This suggests that long range interactions are not the origin of the low monomer migration barrier. In the following calculations we will thus continue to use the traditional monomer diffusion model.

6.6.2 Modeling desorption

In order to understand the Arrhenius plot for the full temperature range studied, we need to model desorption (incomplete condensation) as observed on the STM images. In the following, we assume that only monomers can desorb. The quantity of adsorbate which is visible on the image is an equilibrium between monomer migration on the surface, leading to nucleation, and desorption. The characteristic time τ_{desorp} a monomer stays adsorbed on the surface before being re-evaporated can be written as a Boltzmann term

$$\frac{1}{\tau_{\text{desorp}}} = \nu_{\text{desorp}} = \nu_{0\,\text{desorp}} \exp\left(\frac{-E_{\text{desorp}}}{kT}\right) \tag{6.6}$$

with an associated energy barrier and attempt frequency for desorption E_{desorp}, $\nu_{0\,\text{desorp}}$. Equivalently a characteristic time before attachment of a diffusing monomer to a stable island can be estimated to $\tau = \ln(n_x^{-1})/(n_x D)$[70] on a surface with a density n_x of stable islands (in the growth regime, thus neglecting nucleation). The regime where $\tau_{\text{desorp}} \gg \tau$ corresponds to complete condensation case while $\tau_{\text{desorp}} \ll \tau$ corresponds to no sticking of the adsorbate.

The temperature dependence of these terms has been first studied by using rate equations by Kisliuk et al. [134] and integrated by Venables et al. [135]. Here, we write the usual rate equations for cluster diffusion (see Eq. 4.19, p. 73) and add desorption to the monomer term:

$$\frac{\mathrm{d}n_1}{\mathrm{d}t} = (\ldots) - \nu_{\text{desorp}} n_1 \tag{6.7}$$

Because we find that clusters up to the pentamer diffuse on the surface (see next section) we write the rate equation up to size 5. The rate equation's general form is not modified when changing from 2D to 3D Volmer-Weber growth[20]. The only adjustment necessary is the adaptation of the capture coefficients σ to the 3D case. Obviously, for the monomer, dimer and trimer no change is necessary as their shape is indistinguishable between 2D and 3D growth modes. For larger stable islands in contrast the σ_x will be different as only the bottom layer of the 3D cluster offers a capture surface to the diffusing monomer. As we are not aware of capture coefficients having been calculated for 3D islands, we use the lattice approximation for 2D islands [9]. For small clusters, i.e. at low temperature, the difference is small, while at high temperature the system is expected to be dominated by the desorption process so the overall effect of this approximation should be small.

We numerically integrate the above rate equations with this knowledge and fit the experimental island densities as seen in Fig. 6.8 b. At deposition temperatures below 200 K the desorption term is negligible. Simulations show that also the cluster diffusion up to the pentamer size has a negligible effect on the island density up to ≈ 300 K. Thus below 200 K only the monomer migration barrier and its associated attempt frequency determine the fit, giving $E_{\text{m}} = (20 \pm 3)$ meV and $\nu_0 = 6 \times 10^{(3\pm0.5)}$ Hz. The migration barrier is equal within the error bars to the one found by the scaling law. The attempt frequency is much smaller but we recall the arguments above about the uncertainty of this value.

We simulate desorption with a supposed attempt frequency of $\nu_{0\,\text{desorp}} = 1 \times 10^{13}$ Hz and fit the data with the desorption energy barrier as parameter. The result is plotted as the red continuous line in Fig. 6.8 b. We see that the steep decrease of island density upon start of desorption ($E_{\text{desorp}} =$ 900 meV) is reproduced, but that the model does not explain the island densities measured between 200 K and 300 K. Using both the desorption barrier and the attempt frequency as fitting parameters yields the black curve. This is calculated with $E_{\text{desorp}} = 170$ meV and $\nu_{0\,\text{desorp}} = 6 \times 10^3$ Hz. The fit of the data is excellent throughout the measured temperature range. Such a small desorption energy is surprising. Auwärter et al. [112] have also observed desorption for Co/*h*-BN/Ni(111). Their methodology only permits to calculate an energy difference between the desorption and the migration activation

barriers which yields $\Delta E = 140$ meV. This is very close to our values ($\Delta E = E_{\mathrm{desorp}} - E_{\mathrm{m}} = 147$ meV) which strongly supports this model.

The Arrhenius plot shows a knee at 200 K. This may indicate that, starting at this temperature the dimer dissociates (although the island size distribution at 300 K which we presented above indicates that the dimer is stable). To get a complete picture of possible processes which could be responsible for the observed island densities, we add a dimer dissociation term to the above rate equations. We fit the data with the dimer dissociation activation energy and the corresponding attempt frequency as parameters. This yields the blue curve in Fig. 6.8 b. with parameters $E_2 = 170$ meV and $\nu_{02} = 6 \times 10^3$ Hz (other parameters are as in the first simulation above). This model fits the experimental island densities well throughout the temperature range studied. We note that the attempt frequency is close to the one of monomer and cluster diffusion. In contrast, the dissociation energy is small when compared with the Co dimer on other surface ($E_2 \approx 420$ meV for Co/Pt(111)).

6.7 Cluster mobility

We finally investigate the diffusion of small clusters. The idea is to deposit a low coverage of Co at a temperature where monomer diffusion is frozen, guaranteing statistical growth and particularly a high density of monomers. Upon annealing, the onset of diffusion for different species can be observed by monitoring the mean island size. In the case of Co on h-BN/Rh(111), we cannot proceed to deposition in the statistical growth regime because the experimental setup cannot reach a temperature low enough. In fact, using the diffusion parameters found above, we estimate the onset of monomer diffusion at 25 K.

We thus modify the original experiment and deposit 0.01 ML of Co at 200 K. At this temperature the monomer is clearly mobile, and we expect a zero monomer density on the surface after deposition has ended. We then anneal the surface to different temperatures and follow the evolution of the mean island size. If all clusters are immobile and dimers are stable, no evolution of the mean island size should be observed. We show corresponding results in Fig. 6.9.

After deposition at 200 K, the mean island size is 3.3 atoms. When annealing to 350 K, the mean size increases to 8.8 atoms. This indicates that a process is activated in this temperature range which was frozen at 200 K. The shape of $\langle s \rangle$ as a function of annealing temperature resembles the stepwise increase which was observed for Co/Pt(111) (see Sect. 4.12, p. 71). The size increase by more than 5 atoms is in contrast much larger than the steps in the Co/Pt(111) experiment. The fact that the island mean size stays approximatively constant when annealing to 300 K and 350 K excludes the typical Ostwald ripening [45] behavior. We have previously shown that the island size distribution is characteristic for an $i = 1$ behavior up to 300 K. We thus suspect that cluster diffusion is activated before dimer dissociation sets in and is responsible for the observed mean size increase. This is also supported by the fact that the adatoms are weakly bound to the boron nitride layer. Deposition of the same coverage at 140 K yields a smaller mean island size, as expected when the monomer is mobile. Deposition at 350 K shows a much larger mean island size. This emphasizes the difference between deposition, with a continuous flux of adatoms, and annealing.

In order to get a quantitative understanding of this annealing experiment, we simulate the system using the rate equation introduced in the previous section. Rate equations are known for not reproducing island size distribution faithfully. To minimize the potential error in our simulations, we simulate the deposition process at 200 K in a KMC. The KMC model does not allow for 3D growth, so 2D islands were simulated. We still expect the size distribution to be exact because the very low coverage only results in small islands, with relevant cluster sizes < 6. Growth in the third direction and a change in the capture behavior is negligible for these small islands. The KMC simulation was performed with the diffusion parameters determined above, namely $E_{\mathrm{m}} = 20$ meV and $\nu_0 = 6 \times 10^3$ Hz.

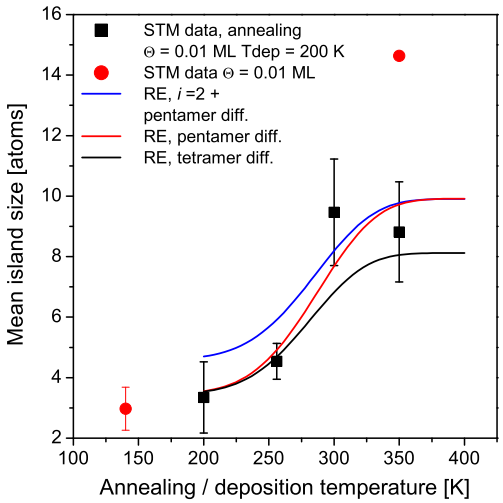

Figure 6.9: Mean island size after deposition of 0.01 ML Co on the clean mesh surface. (black squares) deposition at 200 K and subsequent annealing to different temperatures. (red dots) deposition of the same coverage at other temperatures without annealing

With these parameters, the experimental mean island size is obtained for a coverage of 0.007 ML instead of the 0.01 ML of the experiment. This difference can be explained by the uncertainty on the coverage in the experiment. In fact, deposition times in the experiment are ≈ 2 s and thus induce a high potential error.

We numerically integrate the rate equations for an annealing time of 1800 s at temperatures between 200 K and 400 K. As no monomers are present on the surface at any time during annealing, desorption is absent, thus the coverage is constant. The large increase in mean size observed experimentally does not permit to distinguish the onset of diffusion of different cluster sizes, we thus set all activation energies for mobile clusters to the same value. The model including cluster diffusion up to the tetramer results in the black curve shown in Fig. 6.9. The activation barriers are $E_{\mathrm{m}2} = E_{\mathrm{m}3} = E_{\mathrm{m}4} = 230$ meV using the same attempt frequency as for monomer diffusion ($\nu_0 = 6 \times 10^3$ Hz). We observe that the mean sizes at 260 K and at 350 K are well reproduced. In contrast, the annealing experiment to 300 K shows a much higher island density. Including pentamer diffusion yields the red curve in Fig. 6.9. This model faithfully reproduces the experimental data points with all cluster diffusion energy barriers $E_{\mathrm{m,j}} = 230$ meV, $j = (2\ldots5)$. Again the attempt frequency of the monomer diffusion was used. Acknowledging our previous remark about the uncertainty of the attempt frequency, we also calculated the onset of cluster diffusion if they experience a more "usual" value of $\nu_0 = 1 \times 10^{13}$ Hz. In this case, the mean island size shows a steeper increase with increasing annealing temperatures and yields an activation energy $E_{\mathrm{m,j}} = 700$ meV, $j = (2\ldots5)$. The very low prefactor of $\nu_0 = 6 \times 10^3$ Hz is unconventional. Thus the migration barrier of $E_{\mathrm{m,j}} = 700$ meV associated with the normal prefactor of $\nu_0 = 1 \times 10^{13}$ Hz seems more probable, but from the present experiments we cannot conclude which of the two case is more correct.

The blue curve in Fig. 6.9 shows the result when simulating annealing with the dimer dissociating (parameters correspond to the simulation in the Arrhenius plot). The remarkable feature is that the mean island size is much larger at 200 K. At this temperature dimer dissociation is activated so both

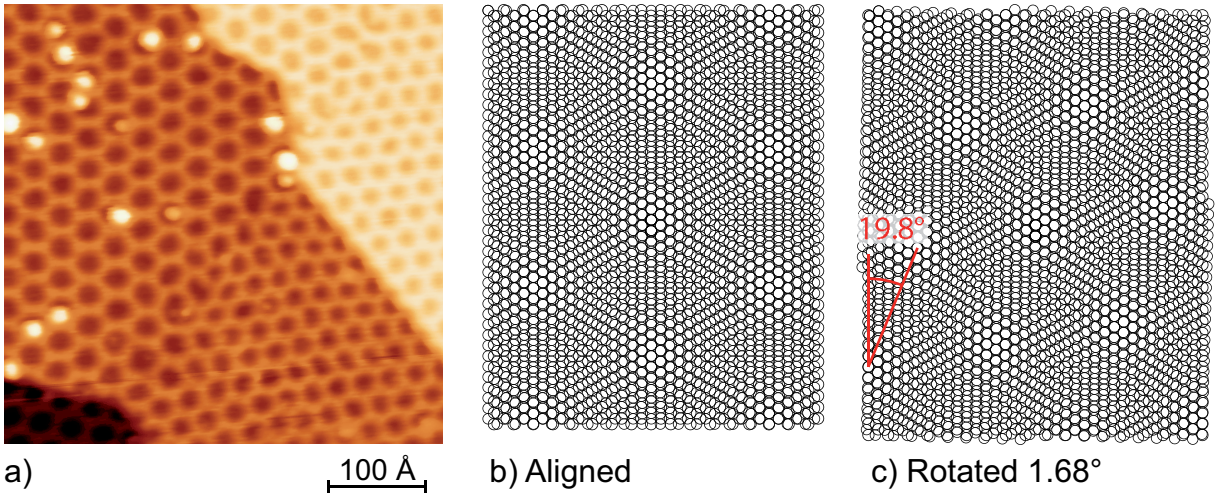

Figure 6.10: STM image of 0.01 ML Co deposited on the clean *h*-BN/Rh(111) at 200 K and annealed to 300 K. The traditional hexagonal superlattice with a lattice parameter of 32 Å is visible on the upper left part of the image. A superlattice with a different mesh size (28.5 Å) and rotated orientation of 19.8° is visible on the lower right side of the image. The Moiré construction explains the two lattice by a rotation of the *h*-BN layer by 1.68° with respect to the Rh(111) substrate. It also shows that the interatomic distance between B and N atoms does not change between the two lattices.

monomers and dimers eventually disappear from the surface, aggregating into larger islands. The discrepancy with experiment acts as an additional argument that $i = 1$.

6.8 Relative rotation of the boron nitride overlayer and other STM observations

Following Co deposition on the *h*-BN surface at $T_{\mathrm{dep}} > 300$ K, coexistence of a different superlattice with the one reported by Corso et al. [111] was observed. This different lattice was never observed on the clean mesh. Fig. 6.10 a. shows the meeting of the two types of superlattices. For this image, 0.01 ML Co were deposited at 200 K and subsequently annealed to 300 K (experiment corresponding to the previous section). The upper-left part of the image shows the traditional *h*-BN mesh with 32.2 Å [120] lattice constant. The lower right part shows a similar lattice with a lattice constant of 28.5 Å and a rotated orientation of 19.78°. The periodicity of the two lattices looks very different although the lattice constant has only 12 % difference. This is an optical illusion due to the fact that the holes in the mesh are much smaller in the smaller lattice. The dislocation line separating the two regions has been found to be a preferred nucleation site for adatoms. Along the line numerous clusters of smaller size than observed on the remaining surface are observed. The Co island density is also larger by ≈ 20 % on the denser lattice.

We know [122, 121] that the original superlattice is a Moiré pattern of the *aligned* superposition of a 13×13 *h*-BN unit cells on 12×12 Rh(111) atoms. The new superlattice also has a 6-fold symmetry, which indicates that the possible strain experienced by the *h*-BN layer is isotropic. We assume in the following that the rhodium substrate does not experience strain. Using the Moiré construction detailed in Ref. [136], we can calculate the rotation angle α of the overlayer versus the substrate. In order to do this, we need to know the rotation angle β between the Moiré pattern and a dense direction of the substrate. We have no direct way to determine the atomic orientation of the substrate covered by *h*-BN with the STM. However knowing that the standard *h*-BN mesh aligns with the dense directions of the substrate, provides us with the needed reference. We know the angle between the two super-

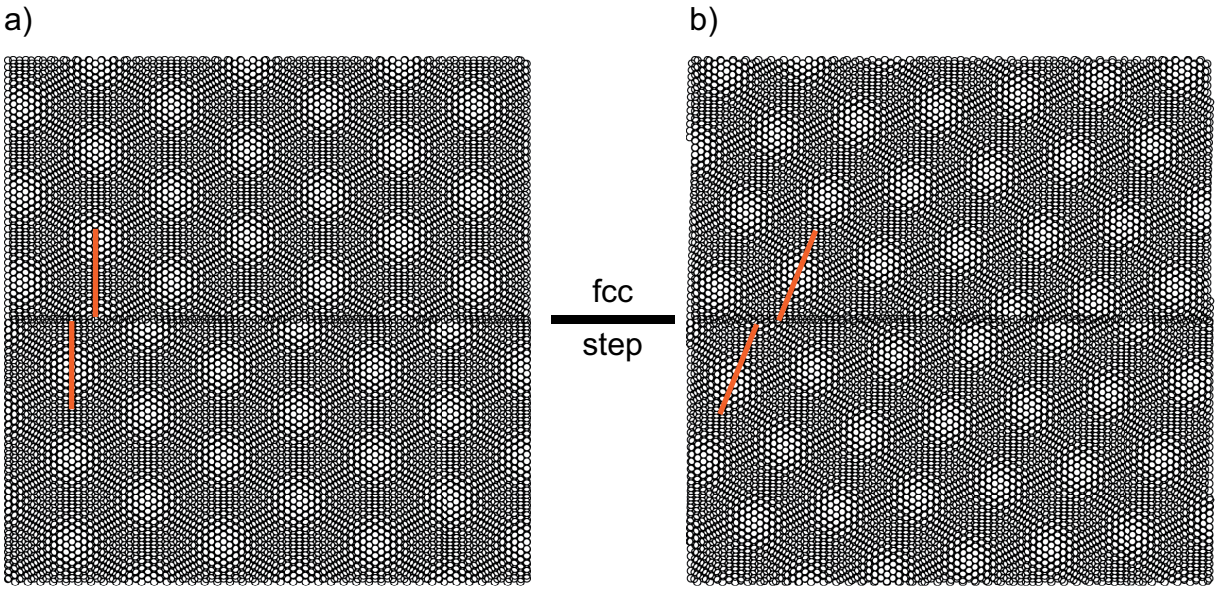

Figure 6.11: Moiré pattern as exhibited for *h*-BN on Rh(111) across a substrate step edge. The overlayer periodicity is constant, only the substrate layer is shifted according to the fcc step stacking model (see Fig. 5.9, p. 92).
a) Normal superlattice with aligned *h*-BN and Rh(111) dense directions.
b) New lattice with dense directions of the overlayer rotated by $1.68°$.
Note that the step direction has no effect on the Moiré pattern.

lattices $\beta = 19.8°$ and the lattice constant of the new superlattice $l = 28.5$. After some trigonometry the relative rotation can be written as [136]:

$$\alpha = \arctan\left(\frac{\sin(\beta)a_{\mathrm{Rh}}}{l + a_{\mathrm{Rh}}\cos(\beta)}\right) = 1.68° \tag{6.8}$$

This means that the *h*-BN layer is rotated by $1.68°$ with respect to the substrate. Using the above construction we can also calculate the lattice constant $a^*_{h\text{-BN}}$ of the overlayer:

$$a^*_{h\text{-BN}} = l\,\frac{\sin(\alpha)}{\sin(\beta)} = 2.47\,\text{Å} \tag{6.9}$$

In particular we notice that $a_{\mathrm{Rh}} = \frac{13.07}{12}a^*_{h\text{-BN}}$ which confirms that the 13×13 periodicity is maintained in the rotation. The two Moiré patterns in Fig. 6.10 show this result graphically.

This new form of superlattice has been observed only after deposition of cobalt. It is unclear if this is a coincidence or if the cobalt plays an active role in the creation of the new lattice. We further noticed that the Co island density is higher on regions with the modified superlattice. This indicates that diffusion of Co on the new type of superlattice is slower and thus that the migration barrier is higher. An alternative explanation is that the potential corrugation between hole and bridge sites is different on the new type of lattice. Subsequent work should clarify this in order to fully understand the diffusion of Co on *h*-BN.

We also note on the STM image (Fig. 6.10 a.) that the two types of meshes propagate over atomic step edges. This shows that a direct interaction must exist between the *h*-BN overlayer of two successive terraces. In fact, we notice that the new superlattice experiences a sideways shift of approximatively half the lattice constant when crossing a step edge. In Fig. 6.11 we propose a Moiré model which explains this shift. Between successive fcc stacked layers of the Rh(111) surface, the dense directions

is shifted perpendicularly by $a_{\mathrm{Rh}} \tan(30)/2$ (see Fig. 5.9, p. 92 for the stacking model). Fig. 6.11 shows the effect on the Moiré pattern of a shift in the substrate corresponding to an atomic step. The lattice constant of the *h*-BN overlayer is kept constant. The excellent agreement between this Moiré model and the STM images indicates that the periodicity of the *h*-BN is not broken at a substrate step-edge. This suggests that the *h*-BN forms a *continuous* layer on top of Rh(111) with B-N bonds reaching across substrate steps.

6.8.1 STM image contrast inversion

Several additional interesting observation have been made on the boron nitride superlattice during this work. Fig. 6.12 a. shows the sudden and uncontrolled contrast inversion while scanning the surface ($V_t = 0.2\,\mathrm{V}$, $I_t = 56\,\mathrm{pA}$). Similar inversions are observed for both positive and negative sample bias voltages. Nieminen et al. [137] studied the contrast inversion observed for CO molecules on Cu(111) when a CO molecule is adsorbed on the STM tip. They explain the observed height differences in STM images by the tunneling through different channels, namely through the adsorbed molecule or through vacuum. The contrast difference is attributed to opposite phases in the currents through different pathes. This explanation is coherent with our observation. In fact, it is straightforward to imagine a BN molecule attaching to the STM tip and changing the tunneling characteristics. The sudden appearance and disappearance of the contrast inversion also supports this model when a corresponding molecule adsorbs or desorbs from the STM tip. Further calculations explaining the higher rim observed around the "holes" of the mesh still need to be performed.

An second interesting observation is shown in Fig. 6.12 b. This image was taken with a constant tunneling current $I_t = 32\,\mathrm{pA}$ and stepwise varying the sample bias voltage as show on the image. We observe a continuous *reversible* contrast inversion as a function of voltage. This phenomenon is not always present, which suggests that the tunneling does not take place through the clean STM tip, but through an adsorbed molecule as explained in the previous paragraph. This voltage dependent contrast inversion was observed only when tunneling into empty-states of the sample. It can tentatively be explained in two ways. Either a molecule on the STM tip changes its configuration as a function of the local electric field in a reversible manner. Or, the phase differences between tunneling pathes are voltage dependent.

6.8.2 Moiré dislocation

Finally, 6.12 c. shows a dislocation in the *h*-BN superlattice. A dislocation in a Moiré pattern is produced by one dislocation in one of the lattices forming the Moiré [138]. This indicates that either the Rh(111) exhibits a dislocations at this point or the *h*-BN overlayer. Arguments in favor and against this second possibility exist. The fact that the overlayer grows when depositing the borazine molecules suggests that dislocations may occur in this stacking. On the other hand, the boron nitride system avoids B-B and N-N bonds which are electronically unfavorable. Thus we expect dislocations to be themselves energetically unfavorable. An atomic resolved study of these may give insight on the exact structure leading to the dislocation.

6.9 Conclusions and Outlook

In this chapter we have shown an extensive study of the growth of cobalt on the hexagonal boron nitride superlattice formed on Rh(111). We have shown that cobalt clusters on this surface grow following a Volmer-Weber growth model, resulting in almost perfectly hemispherical islands. The island formation behavior has been shown to follow the traditional nucleation–growth–coalescence phases

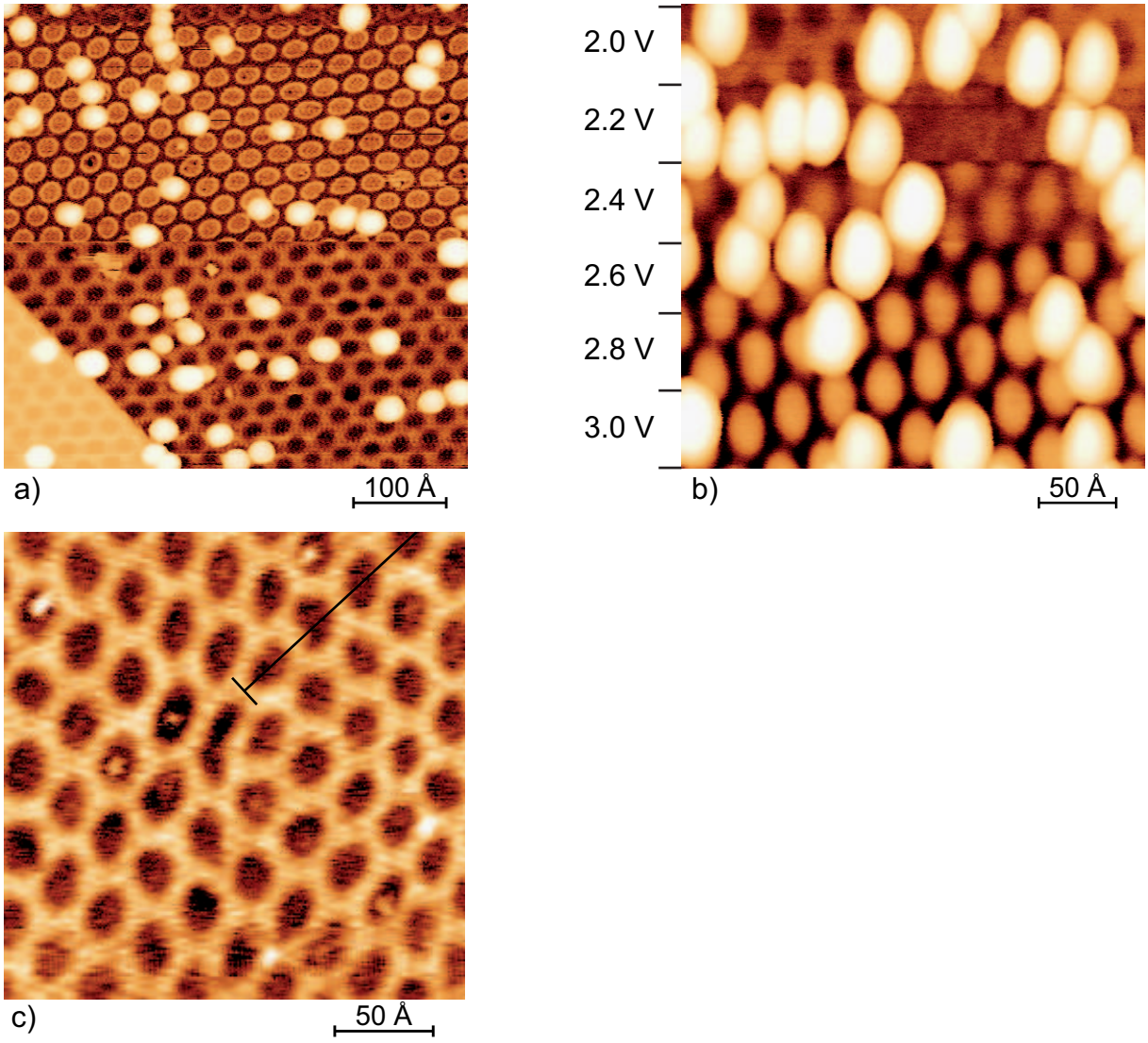

Figure 6.12: a. Uncontrolled sudden contrast reversal in the STM image ($V_t = 0.2$ V, $I_t = 56$ pA).
b. Reversible contrast inversion as a function of tunneling voltage ($I_t = 32$ pA).
c. Dislocation in the *h*-BN superlattice.

during deposition. From a statistical study of the island location with respect to the *h*-BN lattice, we were able to estimate the corrugation of the surface potential energy experienced by the diffusing Co atom to $\Delta F = 13.5$ meV. From the Arrhenius plot of the island density, we also obtain the migration barrier $E_m = 23$ meV and the attempt frequency $\nu_0 = 1 \times 10^6$ Hz although some doubt remain on the validity of the homogeneous monomer diffusion model for this system.

We were able to show that between 200 K and 300 K Co clusters with sizes up to 5 start diffusing on the surface. Using the usual attempt frequency of 10^{13} Hz yields a migration barrier for these species of $E_m = 700$ meV which can be compared to similar values from Pt/Pt(111) observations. We also confirm by several methods that the dimer is stable, at least to a temperature of 300 K.

Finally, we calculate the monomer desorption energy barrier to $E_{desorp} = 170$ meV. This astonishingly low value is in good agreement with previous experiments by Auwärter et al. [112] where the actual coverage of Co on the surface was monitored continuously during deposition at different temperatures. Following Co deposition, a new superlattice with a 12 % smaller lattice constant was observed. We unambiguously show that this stems from a rotated (1.68°) *h*-BN overlayer and that the interatomic distance of the *h*-BN remains unchanged in the rotation. By observing the modification of the Moiré pattern at the step edge, we could infer that the *h*-BN overlayer is continuous across substrate steps. We also provide possible explanations for the contrast inversion observed on STM images.

Basing on this work, we propose to study the migration of the monomer on *h*-BN by modeling the surface in a KMC simulation with a potential corrugation corresponding to the hexagonal superlattice. This should give insight about wether the diffusion activation barrier is really so low (23 meV) or if the homogeneous model is not adapted to this system. Further interesting work could focus on the magnetic properties of the Co dots on the *h*-BN . Preliminary results indicate that the blocking temperature of those dots is well below room temperature. As the islands are of hemispherical shape, the shape anisotropy energy should be much smaller than for bidimensional Co islands, which could lead to out-of-plane magnetization.

Furthermore, the magnetism of the Co dots could be studied by producing nanometer sized spin valves. Deposition of a complete pseudomorphic monolayer of Co on either Rh(111) or Ru(0001) yields a magnetic pining layer, which guarantees the spin polarization of electrons in filled state tunneling. Deposition of *h*-BN on this surface should yield an equivalent superlattice as the one observed on Rh(111), as the pseudomorphic cobalt acquires the lattice constant of the rhodium or ruthenium substrate. After deposition of cobalt clusters on this substrate, the parallel or anti-parallel alignment of the cluster magnetization with respect to the pining layer could be measured by tunneling resistance seen by the STM (see e.g. Ref. [139]).

Chapter 7

Conclusions & Outlook

In this work we have taken a look by experiment as well as by simulation on the submonolayer growth behavior of cobalt on three different surfaces: Pt(111), Ru(0001) and *h*-BN/Rh(111). The differences in adatom diffusion behavior between these three systems are remarkable. When depositing Co on platinum we have observed the reconstruction of the surface at deposition temperatures above 180 K. We were able, by comparison of the experimental data with kinetic Monte-Carlo and rate equation simulations, to understand the diffusion of the Co monomer on the heterogenous, reconstructed surface and to extract key activation barriers for many atomistic processes. In particular, the creation of the Pt surface reconstruction has been identified to stem from the insertion of Co adatoms in the topmost Pt(111) layer. This insertion creates a network of dislocations which act repulsively on the diffusing monomer and influence the island density. We were also able to show that the Co dimer is stable and thus that dimer diffusion sets in before dissociation occurs. We devised an experiment and corresponding simulations permitting the extraction of dimer and trimer diffusion activation barriers.

The deposition of cobalt on the ruthenium surface shows a more conventional, homogeneous diffusion behavior. The island density follows an Arrhenius law for all deposition temperatures above the onset of monomer diffusion. At low temperature, nucleation is dictated by a modified diffusion barrier for the monomer towards attachment. Comparison with previous works indicate that the system is very sensitive to surface impurities. For example, we observed stacking fault behavior which could be impurity driven. Taking into account the data from previous work, we evidenced the trimer as the critical cluster for surface temperatures above 250 K.

Finally, we studied the deposition of Co on the hexagonal boron nitride superlattice formed upon the thermal decomposition of borazine on Rh(111). This system contrasts with the two metal-on-metal systems above in several ways.

- The growth mode is not of the Frank-van der Merwe but of the Volmer-Weber type.
- Complete condensation is not guaranteed for deposition temperatures above ≈ 200 K.
- Larger clusters, up to the size of 5, are diffusing on the surface.

The system exhibits a nearly constant island density in a large temperature range meaning that the diffusion on the BN hexagonal mesh has a very small temperature dependency or that the homogeneous diffusion model is not applicable. We have shown that the difference in binding energy between the hole and bridge sites of the *h*-BN mesh is negligible. Thus, the obvious heterogeneity of the surface is not the cause for this surprising result.

We have developed a versatile, efficient and extendable kinetic Monte-Carlo simulation tool which permits the simulation of any binding potential landscape and geometry. Based on this framework

we used the simulation program to study attractive and repulsive randomly placed impurities. The growth of linear dislocations has also been implemented. The framework in its present state offers the possibility to simulate strain effects on the diffusing species in a most general form. For example, vicinal surfaces or Moiré superlattices as the *h*-BN on Rh(111), Ru(0001) and Pd(111), or also the nucleation on graphene could be further investigated. This will eventually lead to the determination of activation barriers for the atomistic processes involved.

In contrast, cluster diffusion has been known to be difficult to simulate with KMC. We propose a clean implementation of a numerical solution to the rate equation approach to nucleation and growth, which permits the deposition, diffusion and annealing of a system including freely selectable diffusing and critical cluster sizes.

The systems we have studied experimentally all have in common that they exhibit –or are expected to exhibit– interesting magnetic properties. Basing on our results, the controlled growth of a large and well known population of cobalt clusters is possible on these surfaces. This enables the study of magnetism by integrating methods as for example the magneto optical Kerr effect. Detailed analysis of the surface and perimeter dependence of the magnetic susceptibility have already shown remarkable results [43]. Particularly, studying the magnetic behavior of cobalt clusters on the hexagonal boron nitride and on substrates with a stronger patterning behavior should give insight into magnetism of surface supported clusters.

Appendix A

Development of image processing tools

The past 20 years have seen the development of numerous scanning probe microscopy (SPM) data recording techniques. The most prominent in scientific research is probably the STM which was used in the present work, but atomic force microscopy (AFM) or magnetic force microscopy (MFM) are also gaining momentum, particularly in industrial and biological applications. The AFM is for example used for surface quality assurance by high-end watch makers and the MFM by computer hard disc manufacturers to image the magnetic domains on their discs.

The development of these direct space investigation techniques has brought the need to process the recorded images to extract relevant scientific data. The raw image data typically show experimental artifacts which need to be removed in order to permit correct interpretation of the images. The most straightforward example is the removal of a plane. Due to experimental limitation in aligning the scanning head with the sample on a sub-Ångström length scale, recorded images of a flat surface typically show a tilted plane. It is easy to remove this tilt by subtracting a best fit plane (in the least square sense, for example) from the data in order to obtain a correct image of the surface. Evidently, this is only the simplest example and over the years several relevant techniques and tools have been developed by image processing software manufacturers.

Most SPM hardware manufacturers offer or sell an image processing tool to complement their microscope. These softwares are generally not the manufacturer's first priority and this shows on the final product. The softwares are typically user unfriendly, for example by necessitating a hardware *dongle*[1] or by limiting the application to a specific platform (typically MS Windows). Some even introduce errors in the data. As the programming sources of the software are closed, no valid review of the mathematical algorithms implemented is possible. The user must trust the software issuer on the correctness of the programming. Also, no extension can be user programmed for a specific application. If a manufacturer produces a software for a large range of applications and users, it certainly cannot concentrate on the specific needs of one subset of users.

The above reasons have led Prof. Brune and his group to develop an own image processing software. The original requirements were to offer all standard image processing tools in an easy to use and intuitive graphical user interface (GUI). The aim was also to build an extensible architecture which would facilitate the development of new tools and to produce a software capable of running on the diverse platforms in use in the group (Windows, MacOS, Linux). This last requirement led to the choice of the Java programming language [140], which was designed with cross-platform capabilities in mind. The project was started under the programming lead of M. Epple with major contributions by R. Bargmann followed by several programmers and resulted in a mature, full-featured image pro-

[1] A piece of hardware, eg. a USB stick or printer port insert, which dialogues with the software to confirm a valid licence has been bought.

a) b)

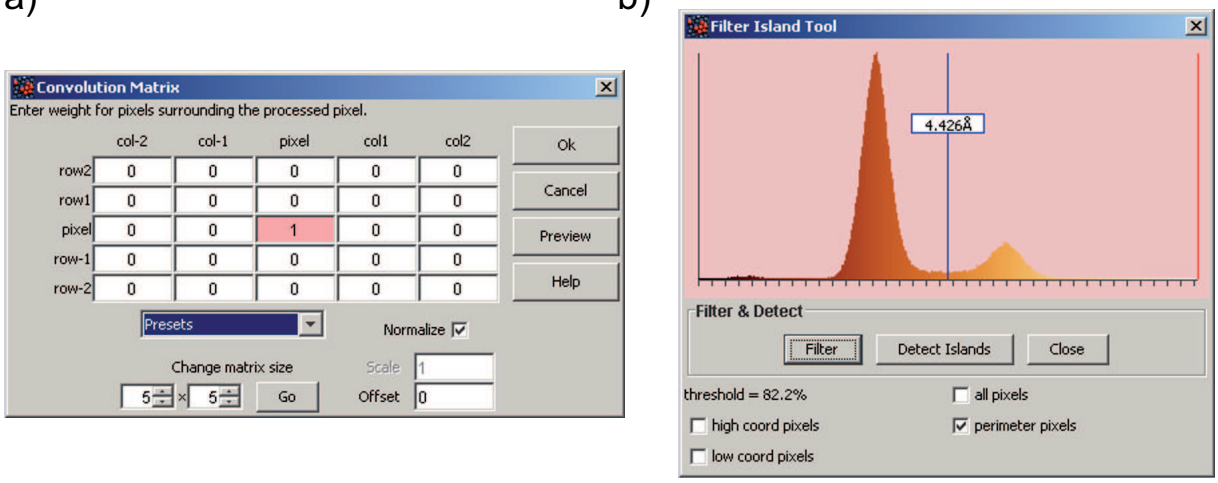

Figure A.1: Graphical user interfaces for image processing tools.
a) The *Convolution Matrix* tool convolves a given matrix with the image. The user may choose between presets from a dropdown list or enter other kernel values into the corresponding text fields. A preview shows the effect on the image and permits an iterative process to reach optimal kernel values for a desired result. The kernel matrix size can be chosen in order to enter more values.
b) The *Filter Island* tool provides an improved method to detect islands or clusters. The typical work flow consists of two steps: 1. Apply filters by convolving the image subsequently with different kernels. 2. Choose a threshold on the pixel histogram (blue line marker), above which protuberances on the surface are considered islands.

cessing and analysis software named S.I.M.P.L.E [2].

In the course of this thesis work the author has contributed to the project by developing and implementing several features. Amongst others, the color rendering of images in a choice of color scales has been introduced and existing tools improved. Moreover, several new tools were also developed which will be presented in the following.

A.1 A 2D convolution matrix

All finite linear image filters can be expressed as the discrete convolution of a matrix H, called kernel in the literature, with the pixel values of the image (see eg. Ref. [141] for an introduction). The choice of the kernel coefficients H_{ij} will determine the effect of the filter, some examples of which will be presented below. The convolution can be understood in the following way: for each image pixel, compute a new pixel value by taking the old pixel and its neighbors each multiplied by the corresponding kernel coefficient. This is intuitively equivalent to a weighted average of a pixel and its neighbors, although choosing negative coefficients will bias this idea a little.

We developed a corresponding convolution tool for S.I.M.P.L.E which is shown in Fig. A.1 a). The user interface offers to type in the coefficients directly or to use one of the proposed presets as a starting point. The size of the matrix can be adapted to the user's needs up to a size of 25×25. The central value is always the one corresponding to the processed pixel, i.e. the coefficient H_{00} (represented as a boxed value in the kernels shown thereafter). If the corresponding checkbox is selected, the coefficients are automatically normalized so that $\sum H_{ij} = 1$. Any other multiplier (the scale s) can be

[2] S.I.M.P.L.E stands for SPM Image Processing from LNS EPFL.

chosen, although this will result in data for which the height unit is no longer valid. For example, we apply the very simple kernel,

$$H = \begin{pmatrix} 0 & 0 & 0 \\ 0 & \boxed{1} & 1 \\ 0 & 0 & 0 \end{pmatrix} \tag{A.1}$$

If normalization is on, all coefficients will be multiplied by $s = 1/\sum H_{ij} = 1/2$ upon calculation. This will simply average each pixel with its right neighbor. The height data, although modified, keeps a valid unit. For example a pixel at position i, j has height $P_{i,j} = 1$ Å and its neighbor $P_{i+1,j} = 1.6$ Å. The result of the above kernel gives $Q_{i,j} = 1.3$ Å and it is still relevant to call the unit Å. If normalization is off, the coefficients are multiplied by a freely chosen scale s. Evidently, the height value loses its unit. In the above example, if choosing $s = 1$, we will have $Q_{i,j} = 2.6$, which are no longer Å. In the special case where $\sum H_{ij} = 0$, the scale s is automatically set to 1.

The offset value o permits to shift the whole resulting image up or down. This is provided only for completeness and for further applications as in the present implementation it has no net effect. The lowest point of a STM image is always automatically shifted to 0 Å upon update.

After choosing the relevant coefficients, and scale, the user can preview the effect on the image with a preview button. This permits an iterative process to find optimal parameters.

A.1.1 Convolution algorithm

The algorithm is the straightforward multiplication method

$$Q_{i,j} = o + s \sum_n \sum_m H_{n,m} P_{i+n,j+m} \tag{A.2}$$

where n and m sweep over the entire matrix. The STM data are typically stored as 32bit `floating` point values, in order to minimize rounding errors, all calculations are done in `double` 64bit precision. A special case that has to be treated are the image border pixels where the neighbors fall outside the image ($i + n < 0$ or $i + n \geq I$ and corresponding for j direction). Several approaches are documented in the literature, for example taking pixels outside the image as 0 or using periodic boundary condition. We chose the solution which introduces the least artifacts when processing SPM images, namely propagating the closest border pixel value outside of the image (eg. $P_{i,k} = P_{i,0}$ if $k < 0$).

The above mentioned algorithm scales with O(M^2) (see Refs. [27, 28] for O() notation) where M is the number of elements. We are aware that a faster convolution algorithm exists, where one takes the fast Fourier transform (FFT) of both the kernel and the image, multiplies the two and performs an inverse fast Fourier transform (iFFT). This FFT algorithm scales with O($M \log M$). After testing the simpler, slower algorithm with typical image and kernel sizes we found it to perform sufficiently fast and following the KISS[3] precept decided to keep it.

A.1.2 Chosen presets

We present below a choice of presets offered to the user which will be of interest for later explanations. The visual effect of each preset including its kernel can be seen on Fig. A.2.

Identity transformation

Fig. A.2 a): The identity transformation leaves the image unchanged. This kernel is the identity element of the discrete convolution. It is given here to show the original image.

[3] Keep It Simple & Stupid

a) Original image

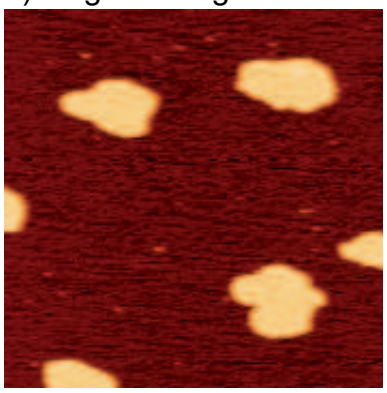

$$\begin{pmatrix} 0 & 0 & 0 \\ 0 & \boxed{1} & 0 \\ 0 & 0 & 0 \end{pmatrix}$$

b) 1st derivative (x dir.)

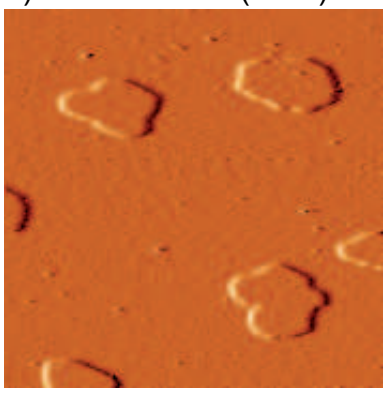

$$\begin{pmatrix} 0 & 0 & 0 \\ -1/2 & \boxed{1/2} & 0 \\ 0 & 0 & 0 \end{pmatrix}$$

c) Line sharpen

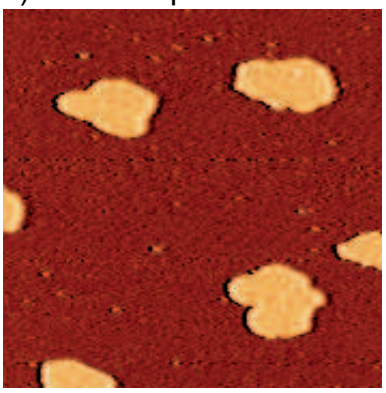

$$\begin{pmatrix} 0 & 0 & 0 & 0 & 0 \\ -1 & -1 & \boxed{5} & -1 & -1 \\ 0 & 0 & 0 & 0 & 0 \end{pmatrix}$$

d) Shadow effect

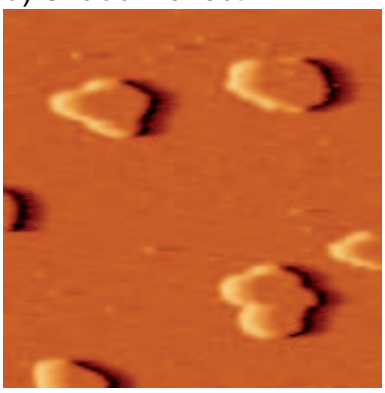

$$\begin{pmatrix} 0 & 0 & 0 & \dots & 0 & 0 & 0 \\ -1 & -1 & -1 & \dots & -1 & -1 & \boxed{16} \\ 0 & 0 & 0 & \dots & 0 & 0 & 0 \end{pmatrix}$$

e) 2nd derivative (optimized)

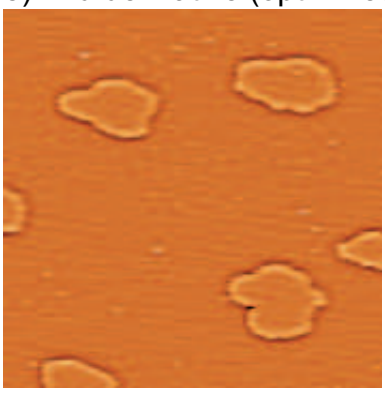

$$\begin{pmatrix} -1 & -1 & -1 & -1 & -1 & -1 & -1 \\ -1 & -3 & -3 & -3 & -3 & -3 & -1 \\ -1 & -3 & -2 & -2 & -2 & -3 & -1 \\ -1 & -3 & -2 & \boxed{89} & -2 & -3 & -1 \\ -1 & -3 & -2 & -2 & -2 & -3 & -1 \\ -1 & -3 & -3 & -3 & -3 & -3 & -1 \\ -1 & -1 & -1 & -1 & -1 & -1 & -1 \end{pmatrix}$$

f) Gaussian blur (σ=2)

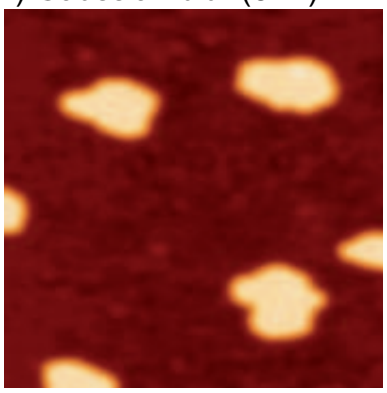

$$\begin{pmatrix} \ddots & \vdots & \vdots & \vdots & \vdots & \vdots & \iddots \\ \dots & 0.0146 & 0.0212 & 0.0241 & 0.0212 & 0.0146 & \dots \\ \dots & 0.0212 & 0.0309 & 0.0351 & 0.0309 & 0.0212 & \dots \\ \dots & 0.0241 & 0.0351 & \boxed{0.0397} & 0.0351 & 0.0241 & \dots \\ \dots & 0.0212 & 0.0309 & 0.0351 & 0.0309 & 0.0212 & \dots \\ \dots & 0.0146 & 0.0212 & 0.0241 & 0.0212 & 0.0146 & \dots \\ \iddots & \vdots & \vdots & \vdots & \vdots & \vdots & \ddots \end{pmatrix}$$

$$H_{ij} = \frac{1}{2\pi\sigma^2} \exp\left(-\frac{i^2+j^2}{2\sigma^2}\right)$$

Figure A.2: A list of convolution kernels with their effect on a test image.

1st derivative

Fig. A.2 b): This kernel calculates the discrete first derivative in the x direction. It gives as an output the differences of two adjacent pixels and thus acts as a crude high-pass filter. It can be used to calculate the gradient vector of the image if also applied in the y direction. Obviously, the centered version

$$\begin{pmatrix} 0 & 0 & 0 \\ -1/2 & \boxed{0} & 1/2 \\ 0 & 0 & 0 \end{pmatrix} \tag{A.3}$$

gives similar results.

Line sharpening

Fig. A.2 c): This kernel gives the visual illusion that the image is sharpened in the x direction. Actually one can understand this kernel as the difference of two kernels (convolution is distributive). Namely, the identity kernel and a second derivative in the x direction using:

$$\begin{pmatrix} 0 & 0 & 0 & 0 & 0 \\ 1 & 1 & \boxed{-4} & 1 & 1 \\ 0 & 0 & 0 & 0 & 0 \end{pmatrix} \tag{A.4}$$

This second derivative kernel is already an improved version as it spans to the second nearest neighbor sites. Using this information, we can read the kernel as "take the original image and subtract the second derivative". One can easily be convinced that this yields sharper object borders. It also introduces a dip artifact (see Fig. A.2 c.) at the lower rim of objects and a bump artifact at the upper rim. This effect is heavily used in commercial video transfer to DVD to make low quality pictures look sharper on high resolution output devices.

Shadow effect

Fig. A.2 d): This long kernel (16×1) produces the well known shadow effect much appreciated by some authors for their STM images.

Second derivative

Fig. A.2 e): This is a kernel of the same type as the sharpening presented above. It calculates the modulus of the second derivative but this time with no preferred direction. The identity is added again but has only little effect as all other coefficients are much larger.

This kernel has been optimized for and will be used in the Filter Island tool below for island and cluster detection.

Gaussian blur

Fig. A.2 f): Blurring an image is equivalent to applying a low pass filter. This is for example interesting in reducing high frequency noise. One widely used method is *Gaussian blur* which is presented here. Convolution is made between the image and a kernel whose coefficients follow a normalized 2D Gaussian (see also equation on Fig. A.2). The given σ measures the amount of blur (the smaller the σ the sharper the image). Although this method theoretically is not finite meaning that weights reach to infinity on each side, it can reasonably be used with a finite number of coefficients. In our

application, for example, the condition $\sum H_{i,j} > 99.5\%$ is used which gives a kernel of size 7×7 for $\sigma = 1$ and 13×13 for $\sigma = 2$.

We are aware that a faster algorithm than 2D convolution exists for the Gaussian blur. It can be shown that applying a 1D Gaussian kernel on each line of the original image and on each column of the result is equivalent to a 2D Gaussian convolution. This takes less memory to compute and is faster than the simple multiplication algorithm. Again, our tests have shown that no relevant user benefit can be expected from the faster algorithm so it was not implemented.

A.2 Island detection with image filtering

As has been shown many times in the present work, one is interested in the clusters or islands when studying submonolayer nucleation and growth. Typically one wants to extract from the images information like the number of islands, their size, their maximum height, their mean height, their position etc. In order to do this, the original S.I.M.P.L.E program included an *Island Tool*.

In this tool, the user graphically chooses a threshold height. All pixels of the image above this threshold are considered part of an island (this is also called flooding in other applications). The program then detects which pixels are adjacent, forming a closed surface. These are counted as an island and added to a list.

The above algorithm works well for islands with similar heights on a flat substrate. This is typically the case for metal on metal systems with Frank–van der Merwe growth conditions. In the case of Co deposited on h-BN, the islands that form are not 2D. Furthermore, they are of very different heights. This makes the traditional island detection method inefficient (see Fig. A.3 a. and b.). This fact motivated us to develop an improved island tool which detects islands efficiently in such cases.

The new tool which is shown in Fig. A.1 b) uses a three step process:

1. Filter the image using relevant kernels
2. Apply the standard island detection algorithm
3. Revert the image to the original state and use height data from the unfiltered image for output in the island list

Evidently all the "magic" lies in determining the interesting filter kernels to apply to reach the desired result, namely well separated islands with similar heights. Inspired by the work on edge detection done by Canny et al. [142] we propose the following kernels:

1. Apply a Gaussian blur. This step reduces high frequency noise which would render the next step inefficient. Typical images used in the h-BN study have 1 pixel ≈ 2 Å. In this case a Gaussian blur with $\sigma = 1$ has been found to give satisfactory results.
2. Subtract an optimized second derivative from the previous image (see kernel in Fig. A.2 e.). This will have two desired effects: First, the top of island appears almost flat as the second derivative does not vary rapidly locally on islands. Second, the island borders where the second derivative is strongly positive, will appear much lower and thus facilitate detection by the threshold method.

The work flow described above is shown in Fig. A.3 a)→c)→d). The image in a) shows the original data. The filter kernels were applied on c). Finally, Fig. A.3 d) shows an overlay of the detected island borders on the original image.

We have developed an efficient and easy to use method to detect 3D islands on surfaces. The image is filtered using well chosen kernels. The result makes detection simple by emphasizing island borders. Since its implementation, the filtered island detection tool is in use on a daily basis.

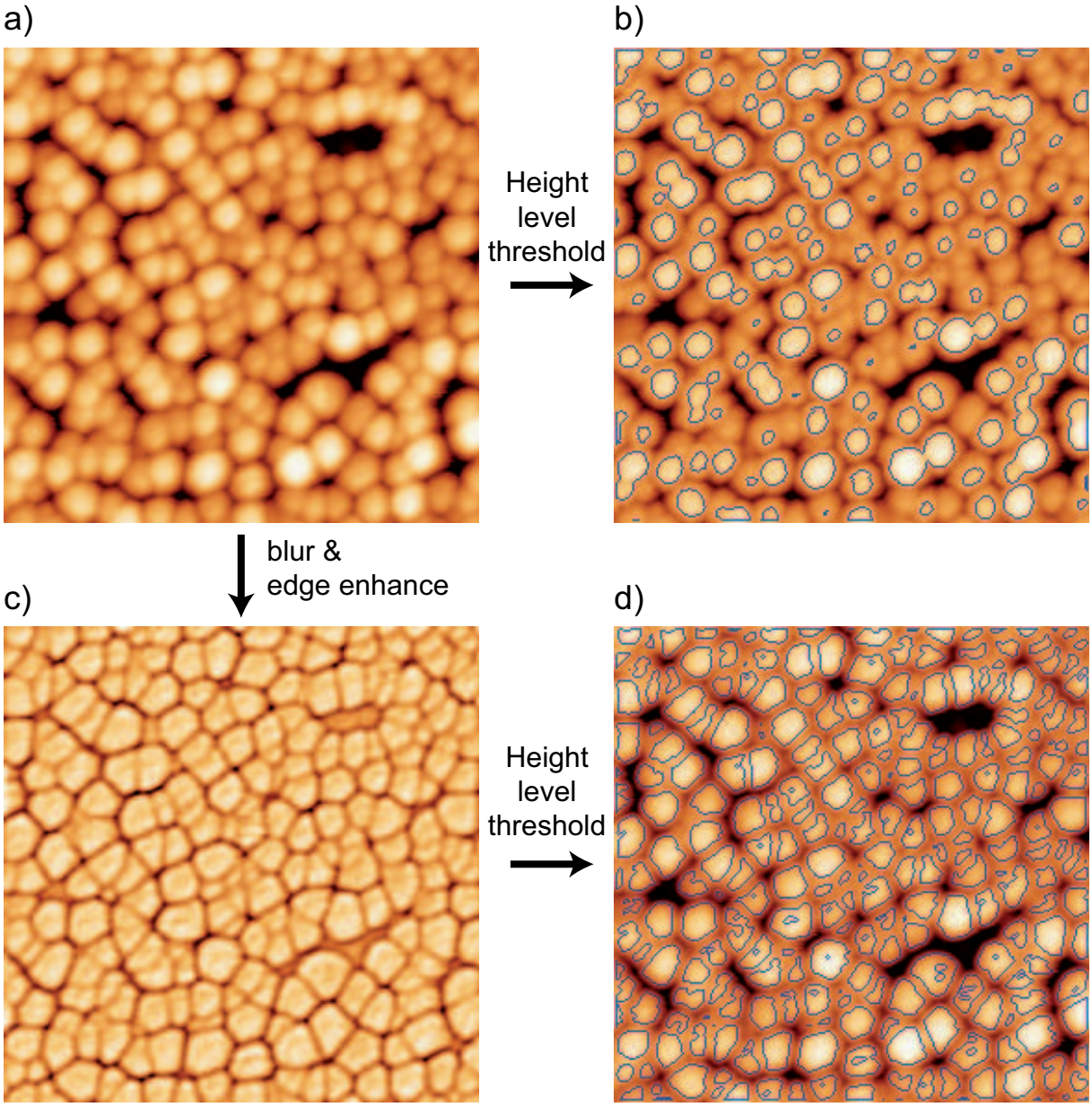

Figure A.3: Comparison of island detection using standard detection (a→b) versus the newly developed *Filter Island* tool (a→c→d). The standard detection technique cannot resolve many low level islands. Closely sitting, high islands are coalesced and detected as single large islands. The new tool, by an intelligent choice of filtering, resolves all islands efficiently and equally independent of the height.

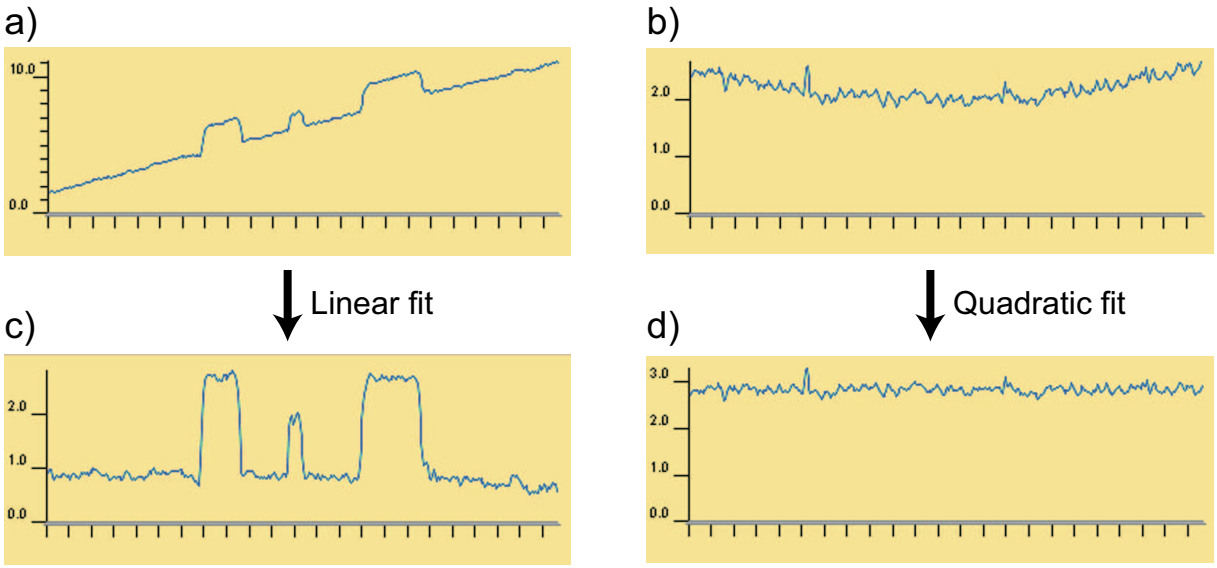

Figure A.4: The *Lines Fit* tool fits each scan line separately with a linear or quadratic function and subtracts this fit from the line.

A.3 Line-by-line linear and quadratic fitting

In perfect STM imaging conditions, the difference of two subsequent scan lines is given only by the surface being scanned. Unfortunately, experimental artifacts can be introduced. A typical example is the recording of image at low temperature with liquid nitrogen cooling. Liquid nitrogen, in contrast to helium, has a high viscosity. This, in combination with a pulsed flow through the cryostat, may lead to low frequency oscillations which are visible in the recorded images. Scan lines of a flat surface will show a slight curvature which varies in time, and thus change from line to line.

This artifact can be corrected by fitting each line separately with a fit function and subtracting this function from the line values. We have developed a tool to perform this correction. The user may choose between fitting each line with a linear or a quadratic function. Evidently, to be correct, the fit must be applied to a region which is supposed flat by the observer. This is typically an atomic terrace. In order to restrict the points for the fit to those of a terrace, the user can graphically choose a height range.

The least square fit is performed using the Levenberg-Marquardt [143, 144] algorithm with simple polynomial of first and second order test functions. The programmatic implementation uses the LMA Java package [145] in conjunction with the linear algebra JAMA [146] package. After fitting, the constant value of the polynomial is set to 0 at the center point of the line. This assures that the mean height value of each line is retained while the artifacts are effectively removed. When applying the algorithm to images with horizontal atomic steps, the steps would be removed if the constant of the polynomial was maintained. Fig. A.4 shows the algorithm applied successfully to scan lines using linear and quadratic fit functions. Note that the program automatically shifts the whole image in order to have the lowest point at 0 Å after applying an algorithm. This is why the lines seem not to keep their mean height.

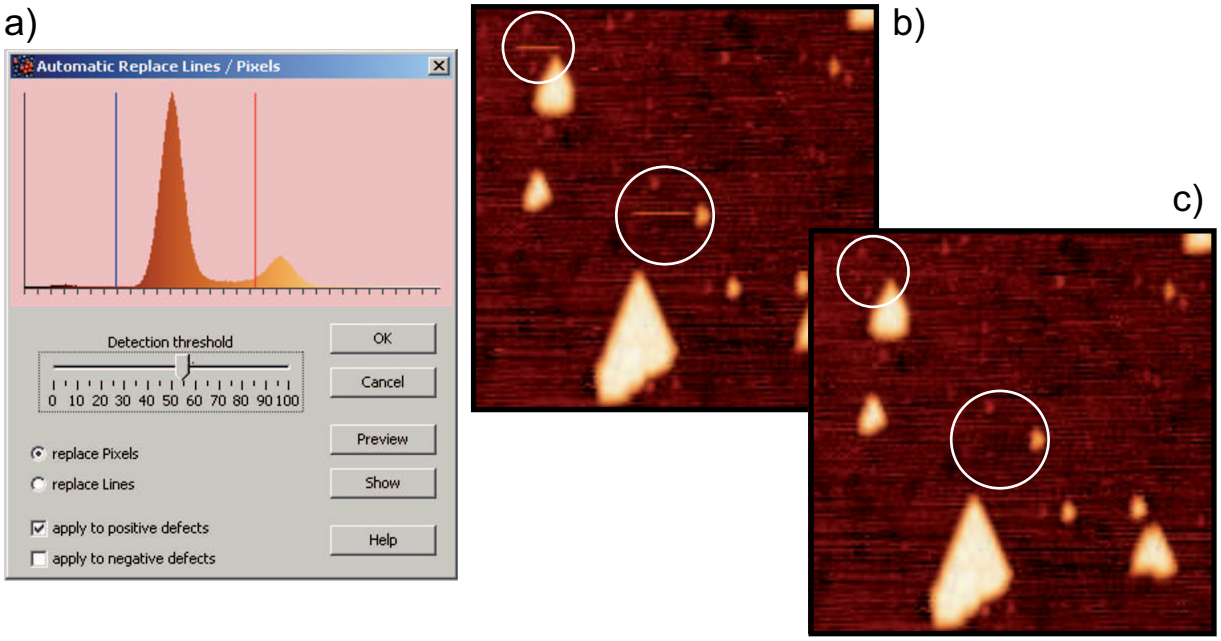

Figure A.5: The *Automatic Replace Line / Pixel* tool permits the correction for esthetic purposes of STM tip instabilities appearing on images. The algorithm detects such instabilities by calculating for each pixel a local second derivative in the y direction (perpendicular to the scan direction). The pixel is replaced by a mean value of it's neighbors above and below if this derivative is above a threshold.

A.4 Correcting STM tip instabilities

The information recorded with the STM is the local density of states (LDOS). The recorded data thus depend both on the electronic state of the tip and of the sample. It is well known that the tunneling probability decreases exponentially with the tip–sample distance. Because of this, the point through which tunneling occurs is made of one or a few atoms at the tip apex.

During the experiments one sees that the tip can abruptly change its shape, resulting in different tunneling characteristics. This is understood as a rearrangement of the atoms at the tip. Surprisingly, this change is often rapidly followed by the reverse evolution, resulting in the previous tunneling characteristics. In STM images, these tip instabilities appear as small pieces of a scanning line with a remarkably different (higher or lower) height than surrounding pixels. Examples of such conformation changes are encircled in Fig. A.5. Taking into account the tip scanning speed one can estimate the time the tip stayed in a different state to less than $10\,\mu$s. It is suggested that these higher regions are pure artifacts of the tip state and thus do not contain any physical information of the sample surface. This is generally confirmed when scanning the same surface region a second time, in which case the higher regions do not appear. Unfortunately, these tip instabilities introduce errors when analyzing images, for example when trying to detect islands or when calculating mean heights.

In order to correct this tip artifact on the images we have developed a tool that automatically detects and removes the incriminated pixels. The tool is shown in Fig. A.5. The selection algorithm uses the fact that such tip instabilities produce errors which have an extension of exactly one scanning line. If an instability lasts for two lines, it is considered a feature of the surface and cannot be corrected. In effect, the tool calculates a second derivative in the y direction of the image for each pixel. If this value is above a threshold chosen by the user, the pixel is selected for replacement. Replacement is done by computing an average from the pixel above and below in the y direction.

In the histogram graph in the upper part of the tool, the user chooses a height region on which the algorithm should have an effect. This permits for example to restrict the application to pixels of an atomic terrace, effectively excluding islands which feature a different height. By corresponding checkboxes, the user can choose if the correction algorithm should apply to higher ("positive") and/or lower ("negative") pixels compared to their neighbors pixels. Furthermore, the user has the choice to replace individual pixels or complete lines. In the latter case, the detection threshold is compared to a mean value of the second derivative along the complete line. Evidently, the knowledgeable user will be wary of using this tool with too low thresholds as it can easily introduce user generated artifacts or remove valuable scientific data. In order to simplify the judgment for the user the pixels that will be replaced are indicated in red while moving the fader which chooses the threshold.

A.5 STM image 3D rendering: a bridge to POV-Ray

Scientific communication towards a non-specialist audience, for example in the search for funding or when trying to promote a field to the general public, requires producing appealing visuals. In the field of SPM, this task is somewhat easier as the main instrument produces images which represent real-world objects, easier to grasp for an untrained eye than for example reciprocal space images or data on graphs. As the objects represented on the images are actual 3-dimensional objects, for AFM or STM topographic images at least, it comes as no surprise that already in the first ever publication about STM [6] the data was represented in pseudo 3D perspective.

Acknowledging the importance of 3D rendering of topographic images, we developed a corresponding feature for S.I.M.P.L.E . The rendering of surfaces and objects in 3D, including surface properties, shadows, ambient lighting and reflectance is a programming art in itself which we did not try to master as an aside. Instead, the choice was made to tap the power of an existing 3D rendering and ray tracing program: POV-Ray [147].

POV-Ray, which stands for *Persistence Of Vision Ray tracer*, is a full featured, free, open source 3D software package developed by a worldwide team of dedicated volunteers. Its capabilities include the modeling of 3D objects using a proprietary scene description language as well as a ray tracer with advanced capabilities as radiance or smoke rendering. The tool we developed uses only a small part of this power, but the user has all the tools in hand to extend the rendering files produced for the ray tracer.

Rendering of topographic data from the image processing software is a two step process: First, the user chooses relevant parameters in the user interface (see the GUI on Fig. A.6), then the source files are produced and the ray tracer is called to render the files. The resulting image is shown in the software. The 3D data forming the surface is extracted from a gray scale version of the topographic image. This gray scale image is interpreted as a height map, where brighter pixels indicate higher regions. The user can choose if he wants to use the real height data or the color data (which are not necessarily linear with the actual height). The user can also choose a magnification of the height data. This is almost always necessary when rendering images with atomic height regions, as the x and y direction are orders of magnitude larger than the z (height) data.

The user also chooses properties of the topographic surface to render. Typically, one can use a color map taken from the STM image which is projected on the surface or a uniform color. The reflectance (phong value) of the surface can be chosen between a matte (0) and very reflective, reminiscent of a shiny plastic material (1). A light source with its corresponding color is placed in space and finally the observer –the camera– location is chosen. Final render results are shown in Fig. A.6. Both images are rendered with the colored STM image as a surface map and reflectance set to 0.1. Differences lie in the camera location, background color and light color (left: RGB$[1.0, 0.47, 0.6]$, right: RGB$[1.0, 1.0, 1.0]$).

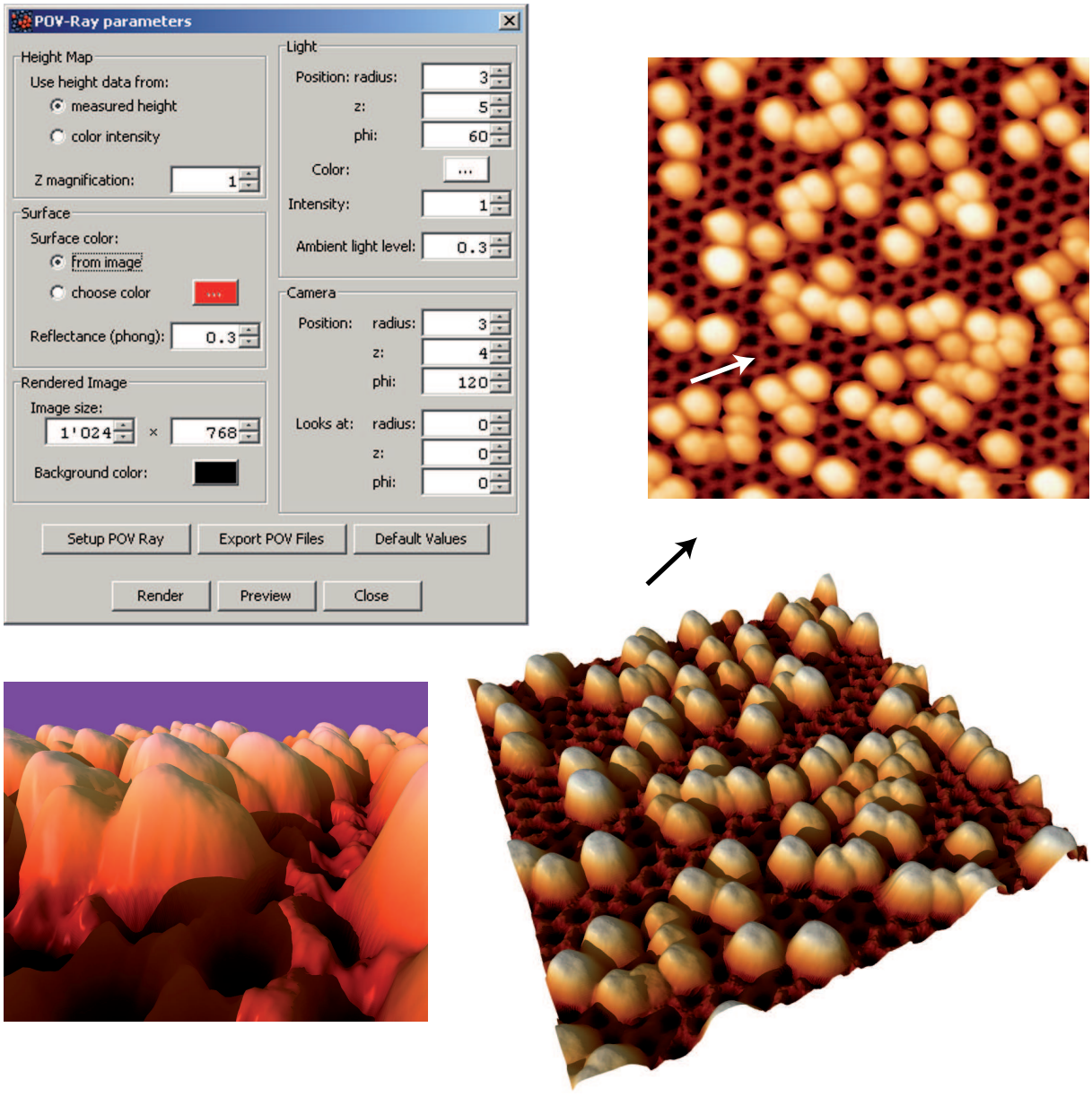

Figure A.6: The *POV-Ray* tool provides a software bridge to the 3D rendering software of the same name. From the original image (top), two possible renders are shown. View points are indicated by arrows on the orignal image.

Acronyms & Symbols

AFM	Atomic force microscope
BST	Binary search tree
c-BN	Cubic boron nitride
CVD	Chemical vapor deposition
CPU	Central processing unit
DFT	Density functional theory
DLA	Diffusion limited aggregation
EMT	Effective medium theory
fcc	Face centered cubic
FIM	Field ion microscope
FM	Ferromagnetic
FWHM	Full width at half maximum
GUI	Graphical user interface
h-BN	hexagonal boron nitride
hcp	Hexagonal close packed
KMC	Kinetic Monte-Carlo
LDA	Local density approximation
LDOS	Local density of states
LEED	Low-energy electron diffraction
ℓHe	Liquid helium
MAE	Magnetic anisotropy energy
MBE	Molecular beam epitaxy
MD	Molecular dynamics
ML	Monolayer
MOKE	Magneto-optical Kerr effect
ODE	Ordinary differential equation
OO	Object oriented
PRNG	Pseudo-random number generator
RE	Mean field Rate Equations
RHEED	Reflection high-energy electron diffraction
RMS	Root mean square
RT	Room temperature i.e. 300 K
SPLEEM	Spin-polarized low-energy electron microscopy
SPM	Scanning probe microscope
STM	Scanning tunneling microscopy
UHV	Ultrahigh vacuum
UHVCVD	Ultrahigh vacuum chemical vapor deposition

a	Nearest-neighbor interatomic distance on the close-packed surface [Å]
A_b	Ratio of the h-BN/Rh(111) surface covered by bridge regions
A_h	Ratio of the h-BN/Rh(111) surface covered by hole regions
B	Magnetic flux density [T]
b	Natural interatomic distance of the adsorbate element [Å]
c	Atomic unit cell on the close packed surface [$\mathrm{Å}^2$]
C	Area of a closed cell on the terrace delimited by repulsive dislocations [c]
d	Distance on the surface [a] (see a above)
d	Thickness of the magnetic material [m]
D	Tracer diffusion coefficient, in general [$\mathrm{Å}^2/s$] but here mainly [c/s] (see c above)
d_forward	Distance in front of a dislocation line which must be pristine to allow arm growth [a]
d_insert	Distance up to which an insertion event modifies the surface binding energy [a]
E	Energy (see text for details) [eV]
E_2	Dimer dissociation barrier [eV]
$E_3..E_i$	Cohesion energy of Trimer,...,Critical cluster Dimer dissociation barrier [eV]
E_attach	Migration barrier for attachment [eV]
E_b	Binding energy [eV]
E_desorp	Activation energy for monomer desorption [eV]
$E_\mathrm{dl\text{-}grow}$	Activation energy for dislocation growth [eV]
$E_\mathrm{dl\text{-}nucl}$	Activation energy for dislocation nucleation [eV]
E_ex	Activation energy for exchange process [eV]
E_F	Fermi level [eV]
$E_{\mathrm{in}\uparrow}$, $E_{\mathrm{in}\downarrow}$	Migration barrier towards, or away from, a site with lower binding energy [eV]
E_insert	Activation energy for insertion process [eV]
E_m	Monomer migration barrier [eV]
E_m2, E_m3 ...	Dimer, Trimer migration barrier [eV]
ΔE_pot	Potential energy difference between two points of the surface [eV]
E_step	Surface site binding energy difference, for a level difference of 1[eV]
F	Deposition flux [ML/s]
ΔF	Difference in free energy between monomers on hcp and fcc sites [eV]
F_i	Interface free energy [eV]
F_f	Surface free energy of the heteroepitaxial layer [eV]
F_s	Substrate surface free energy [eV]
H	Convolution matrix kernel
h	Island height [atomic levels] or [Å]
i	Critical cluster size [atoms]
I_t	STM tunneling set-current [pA]
k	Boltzmann constant $= 8.617 \times 10^{-5}$ [eV/K]
l	Lattice constant of the h-BN superlattice [Å]
ℓ	Vicinal surface step width [Å] or [a]
ℓ_0	Crossover step width [Å] or [a]
M	Magnetization
M	Number of elements to estimate algorithm scaling behavior
m	Density of impurities [ML]
n_∞	Density of stable islands on an infinite terrace [ML]
n_0	Island density in the step edge dominated regime [ML]
n_1, n_2, n_3	Monomer, Dimer, Trimer density [ML]

n_x	Density of stable islands [ML]
N_b	Ratio of total islands on bridge sites
n_ex	Density of exchange sites or exchanged atoms [ML]
$n_\mathrm{grow}^\mathrm{sat}$	Dislocation growth saturation density [ML]
N_h	Ratio of total islands on hole sites
$n_\mathrm{nucl}^\mathrm{sat}$	Dislocation nucleation saturation density [ML]
N_s	Number of islands of size s
o	Offset factor the convolution calculation [Å]
$P_{i,j}$	Pixel value at image position (i,j) [Å]
p	Island perimeter [Å] or [a] (see a above)
$Q_{i,j}$	Pixel value after processing at image position (i,j) [Å]
r	Exponent of coverage in the exchange model
R	Radius of hemispherical islands
ΔS	Entropy difference between two points on the surface [eV/K]
s	Island size or surface [Å^2] or [atoms]
s	Scale factor in the elements of the convolution matrix
s_max	Maximum diffusing island size [atoms]
t	Time [s]
δT	Absolute error on the temperature measure [K]
T_ann	Annealing temperature [K]
T_char	Characteristic temperature describing the onset of a particular process [K]
T_dep	Deposition temperature [K]
T_desorp	Onset temperature for desorption [K]
T_mes	Temperature of measurement [K]
U	Uniformly distributed random variable
$U_\mathrm{di,k}$	Direct impingement rate on islands contributing to islands of size k [ML/s]
v	Volume of the atomic unit cell in the crystallographic structure [Å^3]
V_t	STM tunneling sample bias tension [V]
W	Periodic surface potential corrugation in the Frenkel-Kontorova model [eV]
α	Linear parameter in island size vs. perimeter fit function (see also below)
α	In the Moiré construction, relative rotation of the two layers [deg]
β	Exponent in island size vs. perimeter fit function (see also below)
β	Angle between a dense direction of the substrate and the Moiré pattern [deg]
γ	Scaling coefficient between the ellipsoid height and base radius
η	Prefactor in the island density scaling law (Eq. 3.5), $\eta \approx 0.25$
η	Ellipticity of light in the Kerr effect
Θ	Adatom coverage [ML]
θ	Rotation angle of the polarization of light in the Kerr effect [rad]
θ_F	Rotation angle of the polarization of light in the Faraday effect [rad]
$\kappa_1, \kappa_2, \kappa_3 \ldots$	Monomer, Dimer, Trimer… direct impingement coefficient
κ_ex	Direct impingement coefficient for exchanged and immobile atoms
ν	Verdet constant [rad/T m]
ν_0	Hopping attempt frequency [Hz]
ν_{02}, ν_{03}	Dimer, Trimer dissociation attempt frequency [Hz]
$\nu_{0\,\mathrm{ex}}$	Attempt frequency for exchange process [Hz]
$\nu_{0\,\mathrm{desorp}}$	Attempt frequency for desorption process [Hz]
ν_char	Characteristic rate describing the onset of a particular process [Hz]

ν_{ex}	Rate for exchange process [Hz]
$\nu_{\mathrm{ex\,eff}}$	Effective exchange rate at a given time or coverage, depends on n_1 [Hz]
ρ_{s}	Density of states of the sample
$\sigma_1, \sigma_2, \sigma_3 \ldots$	Monomer, Dimer, Trimer… capture coefficient for a diffusing monomer
σ_x	Average capture coefficient for all stable islands
$\sigma_{i,j}$	Capture coefficient for islands of size i and j diffusing towards each other
σ_{ex}	Capture coefficient for exchanged and immobile atoms
τ	Characteristic mean time between occurrences of a process [s]
Ψ	Electronic wave function

References

[1] D. M. Eigler and E. K. Schweizer, "Positioning single atoms with a scanning tunneling microscope," *Nature*, vol. 344, pp. 524–526, 1990. [Online]. Available: http://dx.doi.org/10.1038/344524a0

[2] K. Bromann, C. Félix, H. Brune, W. Harbich, R. Monot, J. Buttet, and K. Kern, "Controlled deposition of size-selected Ag nanoclusters," *Science*, vol. 274, p. 956, 1996. [Online]. Available: http://dx.doi.org/10.1126/science.274.5289.956

[3] M. L. Plumer, J. v. Ek, and D. Weller, Eds., *The Physics of Ultra-High-Density Magnetic Recording*, ser. Springer Series in Surface Sciences. Berlin: Springer, 2001, vol. 41.

[4] H. G. Boyen, G. Kastle, F. Weigl, B. Koslowski, C. Dietrich, P. Ziemann, J. P. Spatz, S. Riethmuller, C. Hartmann, M. Moller, G. Schmid, M. G. Garnier, and P. Oelhafen, "Oxidation-resistant gold-55 clusters," *Science*, vol. 297, no. 5586, pp. 1533–1536, 2002. [Online]. Available: http://dx.doi.org/10.1126/science.1076248

[5] N. Weiss, T. Cren, M. Epple, S. Rusponi, G. Baudot, S. Rohart, A. Tejeda, V. Repain, S. Rousset, P. Ohresser, F. Scheurer, P. Bencok, and H. Brune, "Uniform magnetic properties for an ultrahigh-density lattice of noninteracting Co nanostructures," *Phys. Rev. Lett.*, vol. 95, p. 157204, 2005. [Online]. Available: http://dx.doi.org/10.1103/PhysRevLett.95.157204

[6] G. Binnig, H. Rohrer, C. Gerber, and E. Weibel, "Surface studies by scanning tunneling microscopy," *Phys. Rev. Lett.*, vol. 49, p. 57, 1982. [Online]. Available: http://dx.doi.org/10.1103/PhysRevLett.49.57

[7] G. Zinsmeister, "Theory of thin film condensation. part B: Solution of the simplified condensation equation," *Thin Solid Films*, vol. 2, no. 5-6, pp. 497–507, 1968. [Online]. Available: http://dx.doi.org/10.1016/0040-6090(68)90063-1

[8] G. Zinsmeister, "Theory of thin film condensation. part D: Influence of a variable collision factor," *Thin Solid Films*, vol. 7, p. 51, 1971. [Online]. Available: http://dx.doi.org/10.1016/0040-6090(71)90013-7

[9] J. A. Venables, "Rate equation approaches to thin film nucleation kinetics," *Philos. Mag.*, vol. 17, p. 697, 1973. [Online]. Available: http://dx.doi.org/10.1080/14786437308219242

[10] P. Gambardella, S. Rusponi, M. Veronese, S. S. Dhesi, C. Grazioli, A. Dallmeyer, I. Cabria, R. Zeller, P. H. Dederichs, K. Kern, C. Carbone, and H. Brune, "Giant magnetic anisotropy of single Co atoms and nanoparticles on Pt," *Science*, vol. 300, pp. 1130–1133, 2003. [Online]. Available: http://dx.doi.org/10.1126/science.1082857

[11] C. J. Chen, *Introduction to Scanning Tunneling Microscopy*, 2nd ed., ser. Monographs on the Physics and Chemistry of Materials. Oxford: Oxford University Press, USA, 2007.

[12] M.-C. Blüm, "Supramolecular assembly, chirality, and electronic properties of rubrene studied by STM and STS," Ph.D. dissertation, Ecole Polytechnique Fédérale de Lausanne, 2006. [Online]. Available: http://library.epfl.ch/theses/?nr=3487

[13] J. Bardeen, "Tunneling from a many-particle point of view," *Phys. Rev. Lett.*, vol. 6, p. 57, 1961. [Online]. Available: http://dx.doi.org/10.1103/PhysRevLett.6.57

[14] J. Tersoff and D. R. Hamann, "Theory and application for the scanning tunneling microscope," *Phys. Rev. Lett.*, vol. 50, p. 1998, 1983. [Online]. Available: http://dx.doi.org/10.1103/PhysRevLett.50.1998

[15] N. Weiss, "Propriétés magnétiques de nanostructures de cobalt adsorbées," Ph.D. dissertation, EPFL, 2004. [Online]. Available: http://library.epfl.ch/theses/?nr=2980

[16] Z. Q. Qiu and S. D. Bader, "Surface magneto-optic Kerr effect," *Review of Scientific Instruments*, vol. 71, no. 3, p. 1243, 2000. [Online]. Available: http://dx.doi.org/10.1063/1.1150496

[17] M. Treier, "Design and construction of a device for magneto-optical Kerr effect measurements in uhv," Ecole Polytechnique Fédérale de Lausanne, Tech. Rep., 2005.

[18] J. Giesecke, "Internship report," Tech. Rep., 2007.

[19] F. El Gabaly, S. Gallego, C. Munoz, L. Szunyogh, P. Weinberger, C. Klein, A. K. Schmid, K. F. McCarty, and J. de la Figuera, "Imaging spin-reorientation transitions in consecutive atomic Co layers on Ru(0001)," *Phys. Rev. Lett.*, vol. 96, no. 14, pp. 147 202–4, 2006. [Online]. Available: http://dx.doi.org/10.1103/PhysRevLett.96.147202

[20] J. W. Evans, P. A. Thiel, and M. C. Bartelt, "Morphological evolution during epitaxial thin film growth: Formation of 2D islands and 3D mounds," *Surf. Sci. Rep.*, vol. 61, pp. 1–128, 2006. [Online]. Available: http://dx.doi.org/10.1016/j.surfrep.2005.08.004

[21] C. Ratsch and J. A. Venables, "Nucleation theory and the early stages of thin film growth," *J. Vac. Sci. Technol. A*, vol. 21, no. 5, pp. S96–S109, 2003. [Online]. Available: http://dx.doi.org/10.1116/1.1600454

[22] H. Brune, "Microscopic view of epitaxial metal growth: nucleation and aggregation," *Surf. Sci. Rep.*, vol. 31, pp. 121–229, 1998. [Online]. Available: http://dx.doi.org/10.1016/S0167-5729(97)00015-0

[23] M. C. Bartelt and J. W. Evans, "Exact island-size distributions for submonolayer deposition: Influence of correlations between island size and separation," *Phys. Rev. B*, vol. 54, p. R17359, 1996. [Online]. Available: http://dx.doi.org/10.1103/PhysRevB.54.R17359

[24] Mathematica. [Online]. Available: http://www.wolfram.com/

[25] M. El Ouali, "Kinetic Monte Carlo simulation of diffusion and nucleation phenomena on the (111) surface of an fcc structure," Ecole Polytechnique Fédérale de Lausanne, Tech. Rep., 2002.

[26] K. A. Fichthorn and W. H. Weinberg, "Theoretical foundations of dynamical Monte Carlo simulations," *J. Chem. Phys.*, vol. 95, no. 2, pp. 1090–1096, 1991. [Online]. Available: http://dx.doi.org/10.1063/1.461138

[27] E. W. Weisstein. "Landau symbols." from mathworld–a wolfram web resource. [Online]. Available: http://mathworld.wolfram.com/LandauSymbols.html

[28] P. E. Black. (2005) Big-O notation. [Online]. Available: http://www.nist.gov/dads/HTML/bigOnotation.html

[29] W. H. Press, S. A. Teukolsky, W. T. Vetterling, and B. P. Flannery, *Numerical Recipes in C*, 2nd ed. Melbourne: Cambridge University Press, 1996. [Online]. Available: http://www.nr.com/

[30] M. Matsumoto and T. Nishimura, "Mersenne twister: A 623 dimensionally equidistributed uniform pseudorandom number generator," *ACM Transactions on Modeling and Computer Simulation*, vol. 8, no. 1, p. 3, 1998. [Online]. Available: http://www.math.sci.hiroshima-u.ac.jp/~m-mat/MT/emt.html

[31] G. Marsaglia and R. G. Brown. Diehard battery of tests of randomness. [Online]. Available: http://www.phy.duke.edu/~rgb/General/dieharder.php

[32] World Wide Web Consortium. [Online]. Available: http://www.w3.org/XML/

[33] L. Thomason, Y. Berquin, and A. Ellerton. TinyXML: a simple, small, C++ XML parser. [Online]. Available: http://www.grinninglizard.com/tinyxml/

[34] H. Brune, M. Giovannini, K. Bromann, and K. Kern, "Self-organized growth of nanostructure arrays on strain-relief patterns," *Nature*, vol. 394, pp. 451 – 453, 1998. [Online]. Available: http://dx.doi.org/10.1038/28804

[35] R. J. Needs and M. Mansfield, "Calculations of the surface stress tensor and surface energy of the (111) surfaces of iridium, platinum and gold," *J. Phys.: Condens. Matter*, vol. 1, no. 41, p. 7555, 1989. [Online]. Available: http://dx.doi.org/10.1088/0953-8984/1/41/006

[36] C. E. Bach, M. Giesen, H. Ibach, and T. L. Einstein, "Stress relief in reconstruction," *Phys. Rev. Lett.*, vol. 78, no. 22, p. 4225, 1997. [Online]. Available: http://link.aps.org/abstract/PRL/v78/p4225

[37] R. J. Needs, M. J. Godfrey, and M. Mansfield, "Theory of surface stress and surface reconstruction," *Surf. Sci.*, vol. 242, p. 215, 1991. [Online]. Available: http://dx.doi.org/10.1016/0039-6028(91)90269-X

[38] M. Bott, M. Hohage, T. Michely, and G. Comsa, "Pt(111) reconstruction induced by enhanced Pt gas-phase chemical potential," *Phys. Rev. Lett.*, vol. 70, p. 1489, 1993. [Online]. Available: http://dx.doi.org/10.1103/PhysRevLett.70.1489

[39] A. R. Sandy, S. G. J. Mochrie, D. M. Zehner, G. Grübel, K. G. Huang, and D. Gibbs, "Reconstruction of the Pt(111) surface," *Phys. Rev. Lett.*, vol. 68, p. 2192, 1992. [Online]. Available: http://dx.doi.org/10.1103/PhysRevLett.68.2192

[40] P. Grütter and U. Dürig, "Quasidendritic growth of Co induced by localized reconstruction of Pt(111)," *Surf. Sci.*, vol. 337, p. 147, 1995. [Online]. Available: http://dx.doi.org/10.1016/0039-6028(95)00541-2

[41] E. Lundgren, B. Stanka, W. Koprolin, M. Schmid, and P. Varga, "An atomic-scale study of the Co induced dendrite formation on Pt(111)," *Surf. Sci.*, vol. 423, no. 2-3, pp. 357–363, 1999. [Online]. Available: http://dx.doi.org/10.1016/S0039-6028(98)00931-5

[42] P. Gambardella, A. Dallmeyer, K. Maiti, M. C. Malagoli, W. Eberhardt, K. Kern, and C. Carbone, "Ferromagnetism in one-dimensional monatomic metal chains," *Nature*, vol. 416, pp. 301 – 304, 2002. [Online]. Available: http://dx.doi.org/10.1038/416301a

[43] S. Rusponi, T. Cren, N. Weiss, M. Epple, P. Buluschek, L. Claude, and H. Brune, "The remarkable difference between surface and perimeter atoms in the magnetic anisotropy of 2D nanostructures," *Nat. Mater.*, vol. 2, pp. 546–551, 2003. [Online]. Available: http://dx.doi.org/10.1038/nmat930

[44] P. Grütter and U. T. Dürig, "Scanning tunneling microscopy of Co on Pt(111)," *J. Vac. Sci. Technol. B*, vol. 12, pp. 1768–1771, 1994. [Online]. Available: http://link.aip.org/link/?JVB/12/1768/1

[45] H. Brune, G. S. Bales, C. Boragno, J. Jacobsen, and K. Kern, "Measuring surface diffusion from nucleation island densities," *Phys. Rev. B*, vol. 60, p. 5991, 1999. [Online]. Available: http://dx.doi.org/10.1103/PhysRevB.60.5991

[46] H. Brune, "Metals on metals," in *Physics of Covered Solid Surfaces*, ser. Landolt Börnstein New Series, Group III: Condensed Matter, H. P. Bonzel, Ed. Berlin: Springer, 2001, vol. 42 Subvolume A, Part 1, pp. 217–258.

[47] S. C. Wang and G. Ehrlich, "Adatom motion to lattice steps: A direct view," *Phys. Rev. Lett.*, vol. 70, p. 41, 1993. [Online]. Available: http://dx.doi.org/10.1103/PhysRevLett.70.41

[48] S. C. Wang and G. Ehrlich, "Atom condensation at lattice steps and clusters," *Phys. Rev. Lett.*, vol. 71, p. 4174, 1993. [Online]. Available: http://dx.doi.org/10.1103/PhysRevLett.71.4174

[49] K. W. Jacobsen, J. K. Nørskov, and M. J. Puska, "Interatomic interactions in the effective-medium theory," *Phys. Rev. B*, vol. 35, no. 14, p. 7423, 1987. [Online]. Available: http://link.aps.org/abstract/PRB/v35/p7423

[50] P. Stoltze, "Simulations of surface defects," *J. Phys.-Condens. Mat.*, vol. 6, p. 9495, 1994. [Online]. Available: http://dx.doi.org/10.1088/0953-8984/6/45/004

[51] J. Jacobsen, K. W. Jacobsen, P. Stoltze, and J. K. Nørskov, "Island shape-induced transition from 2D to 3D growth for Pt/Pt(111)," *Phys. Rev. Lett.*, vol. 74, p. 2295, 1995. [Online]. Available: http://dx.doi.org/10.1103/PhysRevLett.74.2295

[52] R. F. Sabiryanov, M. I. Larsson, K. J. Cho, W. D. Nix, and B. M. Clemens, "Surface diffusion and growth of patterned nanostructures on strained surfaces," *Phys. Rev. B*, vol. 67, no. 12, p. 125412, 2003. [Online]. Available: http://link.aps.org/abstract/PRB/v67/e125412

[53] O. Robach, C. Quiros, P. Steadman, K. F. Peters, E. Lundgren, J. Alvarez, H. Isern, and S. Ferrer, "Magnetic anisotropy of ultrathin cobalt films on Pt(111) investigated with X-ray diffraction: Effect of atomic mixing at the interface," *Phys. Rev. B*, vol. 65, p. 054423, 2002. [Online]. Available: http://dx.doi.org/10.1103/PhysRevB.65.054423

[54] A. Atrei, U. Bardi, M. Galeotti, G. Rovida, M. Torrini, and E. Zanazzi, "Alloying at the Co/Pt(111) interface: a study by crystallographic low energy electron diffraction," *Surf. Sci.*, vol. 339, p. 323, 1995. [Online]. Available: http://dx.doi.org/10.1016/0039-6028(95)00631-1

[55] S. Rusponi, S. R. Longwitz, P. Buluschek, E. Vargoz, C. Goyhenex, K. Kern, and H. Brune, "Step-wise increase of the mean island size in ripening by cluster diffusion," to be published.

[56] M. Bott, M. Hohage, M. Morgenstern, T. Michely, and G. Comsa, "New approach for determination of diffusion parameters of adatoms," *Phys. Rev. Lett.*, vol. 76, p. 1304, 1996. [Online]. Available: http://dx.doi.org/10.1103/PhysRevLett.76.1304

[57] K. Kyuno, A. Gölzhäser, and G. Ehrlich, "Growth and the diffusion of platinum atoms and dimers on Pt(111)," *Surf. Sci.*, vol. 397, p. 191, 1998. [Online]. Available: http://dx.doi.org/10.1016/S0039-6028(97)00732-2

[58] H. Brune, H. Röder, C. Boragno, and K. Kern, "Microscopic view of nucleation on surfaces," *Phys. Rev. Lett.*, vol. 73, p. 1955, 1994. [Online]. Available: http://dx.doi.org/10.1103/PhysRevLett.73.1955

[59] C. Goyhenex, "Adatom and dimer migration in heteroepitaxy: Co/Pt(1 1 1)," *Surf. Sci.*, vol. 600, no. 1, pp. 15–22, 2006. [Online]. Available: http://dx.doi.org/10.1016/j.susc.2005.08.043

[60] K. D. Shiang and T. T. Tsong, "Molecular-dynamics study of self-diffusion: Iridium dimers on iridium surfaces," *Phys. Rev. B*, vol. 49, pp. 7670–7678, 1994. [Online]. Available: http://dx.doi.org/10.1103/PhysRevB.49.7670

[61] G. S. Bales and D. C. Chrzan, "Dynamics of irreversible island growth during submonolayer epitaxy," *Phys. Rev. B*, vol. 50, no. 9, p. 6057, 1994. [Online]. Available: http://dx.doi.org/10.1103/PhysRevB.50.6057

[62] G. S. Bales, "Crossover scaling during submonolayer epitaxy on vicinal surfaces," *Surf. Sci.*, vol. 356, p. L439, 1996. [Online]. Available: http://dx.doi.org/10.1016/0039-6028(96)00675-9

[63] M. Mansfield and R. J. Needs, "Application of the Frenkel-Kontorova model to surface reconstructions," *J. Phys.: Condens. Matter*, vol. 2, pp. 2361–2374, 1990. [Online]. Available: http://dx.doi.org/10.1088/0953-8984/2/10/004

[64] J. A. Meyer and R. J. Behm, "Place exchange as a mechanism for adlayer island nucleation during epitaxial growth and resulting scaling behavior," *Surf. Sci.*, vol. 322, p. L275, 1995. [Online]. Available: http://dx.doi.org/10.1016/0039-6028(95)90010-1

[65] D. D. Chambliss and K. E. Johnson, "Nucleation with a critical cluster size of zero: Submonolayer Fe inclusion in Cu(100)," *Phys. Rev. B*, vol. 50, p. 5012, 1994. [Online]. Available: http://dx.doi.org/10.1103/PhysRevB.50.5012

[66] F. Nouvertné, U. May, M. Bamming, A. Rampe, U. Korte, G. Güntherodt, R. Pentcheva, and M. Scheffler, "Atomic exchange processes and bimodal initial growth of Co/Cu(001)," *Phys. Rev. B*, vol. 60, p. 14382, 1999. [Online]. Available: http://dx.doi.org/10.1103/PhysRevB.60.14382

[67] R. Pentcheva, K. A. Fichthorn, M. Scheffler, T. Bernhard, R. Pfandzelter, and H. Winter, "Non-Arrhenius behavior of the island density in metal heteroepitaxy: Co on Cu(001)," *Phys. Rev. Lett.*, vol. 90, no. 7, p. 076101, 2003. [Online]. Available: http://link.aps.org/abstract/PRL/v90/e076101

[68] G. L. Kellogg, "Direct observations of adatom-surface-atom replacement: Pt on Ni(110)," *Phys. Rev. Lett.*, vol. 67, p. 216, 1991. [Online]. Available: http://dx.doi.org/10.1103/PhysRevLett.67.216

[69] G. L. Kellogg and P. Feibelman, "Surface self-diffusion on Pt(001) by an atomic exchange mechanism," *Phys. Rev. Lett.*, vol. 64, p. 3143, 1990. [Online]. Available: http://dx.doi.org/10.1103/PhysRevLett.64.3143

[70] M. C. Bartelt and J. W. Evans, "Scaling analysis of diffusion-mediated island growth in surface adsorption processes," *Phys. Rev. B*, vol. 46, p. 12675, 1992. [Online]. Available: http://dx.doi.org/10.1103/PhysRevB.46.12675

[71] M. C. Bartelt and J. W. Evans, "Nucleation and growth of square islands during deposition: sizes, coalescence, separations and correlations," *Surf. Sci.*, vol. 298, p. 421, 1993. [Online]. Available: http://dx.doi.org/10.1016/0039-6028(93)90057-Q

[72] A. Zangwill and E. Kaxiras, "Submonolayer island growth with adatom exchange," *Surf. Sci.*, vol. 326, p. L483, 1995. [Online]. Available: http://dx.doi.org/10.1016/0039-6028(95)00046-1

[73] S. Liu, L. Bönig, J. Detch, and H. Metiu, "Submonolayer growth with repulsive impurities: Island density scaling with anomalous diffusion," *Phys. Rev. Lett.*, vol. 74, p. 4495, 1995. [Online]. Available: http://dx.doi.org/10.1103/PhysRevLett.74.4495

[74] J. V. Barth, H. Brune, G. Ertl, and R. J. Behm, "Scanning tunneling microscopy on the reconstructed Au(111) surface: Atomic structure, long-range rotational domains, and surface defects," *Phys. Rev. B*, vol. 42, p. 9307, 1990. [Online]. Available: http://dx.doi.org/10.1103/PhysRevB.42.9307

[75] T. Michely, M. Hohage, S. Esch, and G. Comsa, "The effect of surface reconstruction on the growth mode in homoepitaxy," *Surf. Sci.*, vol. 349, p. L89, 1996. [Online]. Available: http://dx.doi.org/10.1016/0039-6028(95)01042-4

[76] M. Hohage, T. Michely, and G. Comsa, "Pt(111) network reconstruction: structure, growth and decay," *Surf. Sci.*, vol. 337, p. 249, 1995. [Online]. Available: http://dx.doi.org/10.1016/0039-6028(95)00623-0

[77] R. Kalousek, M. Schmid, A. Hammerschmid, E. Lundgren, and P. Varga, "Slowing down adatom diffusion by an adsorbate: Co on Pt(111) with and without preadsorbed CO," *Phys. Rev. B*, vol. 68, p. 233401, 2003. [Online]. Available: http://dx.doi.org/10.1103/PhysRevB.68.233401

[78] S. Ovesson, A. Bogicevic, and B. I. Lundqvist, "Origin of compact triangular islands in metal-on-metal growth," *Phys. Rev. Lett.*, vol. 83, p. 2608, 1999. [Online]. Available: http://dx.doi.org/10.1103/PhysRevLett.83.2608

[79] H. Brune, H. Röder, K. Bromann, K. Kern, J. Jacobsen, P. Stoltze, K. Jacobsen, and J. Nørskov, "Anisotropic corner diffusion as origin for dendritic growth on hexagonal substrates," *Surf. Sci.*, vol. 349, pp. L115–L122, 1996. [Online]. Available: http://dx.doi.org/10.1016/0039-6028(95)01347-4

[80] S. C. Wang and G. Ehrlich, "Structure, stability, and surface diffusion of clusters: Ir_x on Ir(111)," *Surf. Sci.*, vol. 239, p. 301, 1990. [Online]. Available: http://dx.doi.org/10.1016/0039-6028(90)90232-W

[81] K. Kyuno and G. Ehrlich, "Diffusion and dissociation of platinum clusters on Pt(111)," *Surf. Sci.*, vol. 437, p. 29, 1999. [Online]. Available: http://dx.doi.org/10.1016/S0039-6028(99)00659-7

[82] H. Röder, E. Hahn, H. Brune, J. P. Bucher, and K. Kern, "Building one- and two-dimensional nanostructures by diffusion-controlled aggregation at surfaces," *Nature*, vol. 366, p. 141, 1993. [Online]. Available: http://dx.doi.org/10.1038/366141a0

[83] S. Berning, "Efficient implementation of trimer cluster diffusion for kinetic Monte Carlo simulation," Ecole Polytechnique Fédérale de Lausanne, Tech. Rep., 2005.

[84] C. Goyhenex, to be published.

[85] P. Feibelman and T. Michely, "Pt-dimer dissociation on Pt(111)," *Surf. Sci.*, vol. 492, pp. L723–L728, 2001. [Online]. Available: http://dx.doi.org/10.1016/S0039-6028(01)01459-5

[86] G. Moulas, S. Ouazi, S. Rusponi, K. Halleux, P. Buluschek, and H. Brune, to be published.

[87] A. V. Ruban, H. L. Skriver, and J. K. Nørskov, "Surface segregation energies in transition-metal alloys," *Phys. Rev. B*, vol. 59, p. 15990, 1999. [Online]. Available: http://dx.doi.org/10.1103/PhysRevB.59.15990

[88] D. Sander, "The magnetic anisotropy and spin reorientation of nanostructures and nanoscale films," *J. Phys.-Condens. Mat.*, vol. 16, pp. R603–R636, 2004. [Online]. Available: http://dx.doi.org/10.1088/0953-8984/16/20/R01

[89] J. W. Evans and M. C. Bartelt, "Nucleation and growth in metal-on-metal homoepitaxy: Rate equations, simulations and experiments," *J. Vac. Sci. Technol. A*, vol. 12, p. 1800, 1994. [Online]. Available: http://dx.doi.org/10.1116/1.579009

[90] M. C. Bartelt, A. K. Schmid, J. W. Evans, and R. Q. Hwang, "Island size and environment dependence of adatom capture: Cu/Co islands on Ru(0001)," *Phys. Rev. Lett.*, vol. 81, no. 9, p. 1901, 1998. [Online]. Available: http://link.aps.org/abstract/PRL/v81/p1901

[91] J. Vrijmoeth, C. Günther, J. Schröder, R. Q. Hwang, and R. J. Behm, "Morphology and structure of ultrathin Co- and Au-films grown on Ru(0001) substrates," in *Magnetism and Structure in Systems of Reduced Dimension*, R. F. C. Farrow, Ed. New York: Plenum Press, 1993, p. 55.

[92] C. Günther, S. Günther, E. Kopatzki, R. Q. Hwang, J. Schröder, J. Vrijmoeth, and R. J. Behm, "Microscopic aspects of thin metal film epitaxial growth on metallic substrates," *Ber. Bunsenges. Phys. Chem.*, vol. 97, p. 522, 1993.

[93] R. Q. Hwang, C. Günther, J. Schröder, S. Günther, E. Kopatzki, and R. J. Behm, "Nucleation and growth of thin metal films on clean and modified metal substrates studied by scanning tunneling microscopy," *J. Vac. Sci. Technol. A*, vol. 10, p. 1970, 1992. [Online]. Available: http://dx.doi.org/10.1116/1.578012

[94] F. El Gabaly, J. M. Puerta, C. Klein, A. Saa, A. K. Schmid, K. F. McCarty, J. I. Cerda, and J. de la Figuera, "Structure and morphology of ultrathin Co/Ru(0001) films," *New J. Phys.*, vol. 9, no. 80, p. 1, 2007. [Online]. Available: http://dx.doi.org/10.1088/1367-2630/9/3/080

[95] G. L. Kellogg, "Hydrogen promotion of surface self-diffusion on Rh(100) and Rh(311)," *Phys. Rev. B*, vol. 55, no. 11, p. 7206, 1997. [Online]. Available: http://link.aps.org/abstract/PRB/v55/p7206

[96] R. Stumpf, "H-enhanced mobility and defect formation at surfaces: H on be(0001)," *Phys. Rev. B*, vol. 53, no. 8, p. R4253, 1996. [Online]. Available: http://link.aps.org/abstract/PRB/v53/pR4253

[97] S. Horch, H. T. Lorensen, S. Helveg, E. Lægsgaard, I. Stensgaard, K. W. Jacobsen, J. K. Nørskov, and F. Besenbacher, "Enhancement of surface self-diffusion of platinum atoms by adsorbed hydrogen," *Nature*, vol. 398, p. 134, 1999. [Online]. Available: http://dx.doi.org/10.1038/18185

[98] J. Nara, T. Sasaki, and T. Ohno, "Adsorption and diffusion of Si atoms on the H-terminated Si(001) surface: Si migration assisted by H mobility," *Phys. Rev. Lett.*, vol. 79, no. 22, p. 4421, 1997. [Online]. Available: http://link.aps.org/abstract/PRL/v79/p4421

[99] G. L. Kellogg, "Hydrogen inhibition of exchange diffusion on Pt(100)," *Phys. Rev. Lett.*, vol. 79, no. 22, p. 4417, 1997. [Online]. Available: http://link.aps.org/abstract/PRL/v79/p4417

[100] T. R. Linderoth, S. Horch, L. Petersen, S. Helveg, M. Schønning, E. Lægsgaard, I. Stensgaard, and F. Besenbacher, "Energetics and dynamics of Pt dimers on Pt(110)-(1x2)," *Phys. Rev. B*, vol. 61, p. R2448, 2000. [Online]. Available: http://dx.doi.org/10.1103/PhysRevB.61.R2448

[101] M. C. Bartelt and J. W. Evans, "Dendritic islands in metal-on-metal epitaxy I. shape transtitions and diffusion at island edges," *Surf. Sci.*, vol. 314, p. L829, 1994. [Online]. Available: http://dx.doi.org/10.1016/0039-6028(94)90203-8

[102] G. Ehrlich and F. G. Hudda, "Atomic view of surface self-diffusion: Tungsten on tungsten," *J. Chem. Phys.*, vol. 44, p. 1039, 1966. [Online]. Available: http://dx.doi.org/10.1063/1.1726787

[103] R. L. Schwoebel and E. J. Shipsey, "Step motion on crystal surfaces," *J. Appl. Phys.*, vol. 37, p. 3682, 1966. [Online]. Available: http://dx.doi.org/10.1063/1.1707904

[104] C. Busse, C. Polop, M. Müller, K. Albe, U. Linke, and T. Michely, "Stacking-fault nucleation on Ir(111)," *Phys. Rev. Lett.*, vol. 91, no. 5, p. 056103, 2003. [Online]. Available: http://link.aps.org/abstract/PRL/v91/e056103

[105] S. C. Wang and G. Ehrlich, "Atomic behavior at individual binding sites: Ir, re, and W on Ir(111)," *Phys. Rev. Lett.*, vol. 68, no. 8, p. 1160, 1992. [Online]. Available: http://link.aps.org/abstract/PRL/v68/p1160

[106] C. Polop, A. Lammerschop, C. Busse, and T. Michely, "Dependence of stacking-fault nucleation on cluster mobility," *Phys. Rev. B*, vol. 71, p. 125423, 2005. [Online]. Available: http://dx.doi.org/10.1103/PhysRevLett.91.056103

[107] S. A. de Vries, W. J. Huisman, P. Goedtkindt, M. J. Zwanenburg, S. L. Bennett, I. K. Robinson, and E. Vlieg, "Surface atomic structure of the reconstructions of Ag(111) and Cu(111)," *Surf. Sci.*, vol. 414, no. 1-2, pp. 159–169, 1998. [Online]. Available: http://dx.doi.org/10.1016/S0039-6028(98)00509-3

[108] M. Giesen and H. Ibach, "Homoepitaxial growth on nominally flat and stepped Cu(1 1 1) surfaces: island nucleation in fcc sites vs. hcp stacking fault sites," *Surf. Sci.*, vol. 529, no. 1-2, pp. 135–143, 2003. [Online]. Available: http://dx.doi.org/10.1016/S0039-6028(03)00077-3

[109] S. Degen, C. Becker, and K. Wandelt, "Thin alumina films on $Ni_3Al(111)$: A template for nanostructured Pd cluster growth," *Faraday Discuss.*, vol. 125, pp. 343–356, 2004. [Online]. Available: http://dx.doi.org/10.1039/b303244b

[110] A. T. N'Diaye, S. Bleikamp, P. J. Feibelman, and T. Michely, "Two-dimensional Ir cluster lattice on a graphene Moiré on Ir(111)," *Phys. Rev. Lett.*, vol. 97, no. 21, pp. 215 501–4, 2006. [Online]. Available: http://link.aps.org/abstract/PRL/v97/e215501

[111] M. Corso, W. Auwärter, M. Muntwiler, A. Tamai, T. Greber, and J. Osterwalder, "Boron nitride nanomesh," *Science*, vol. 303, pp. 217–220, 2004. [Online]. Available: http://dx.doi.org/10.1126/science.1091979

[112] W. Auwärter, M. Muntwiler, T. Greber, and J. Osterwalder, "Co on h-BN/Ni(1 1 1): from island to island-chain formation and Co intercalation," *Surf. Sci.*, vol. 511, no. 1-3, pp. 379–386, 2002. [Online]. Available: http://dx.doi.org/10.1016/S0039-6028(02)01545-5

[113] [Online]. Available: http://en.wikipedia.org/wiki/Image:Boron-nitride-(hexagonal)-top-3D-balls.png

[114] F. Banhart, M. Zwanger, and H. J. Muhr, "The formation of curled concentric-shell clusters in boron nitride under electron irradiation," *Chemical Physics Letters*, vol. 231, no. 1, pp. 98–104, 1994. [Online]. Available: http://dx.doi.org/10.1016/0009-2614(94)01215-6

[115] N. G. Chopra, R. J. Luyken, K. Cherrey, V. H. Crespi, M. L. Cohen, S. G. Louie, and A. Zettl, "Boron nitride nanotubes," *Science*, vol. 269, no. 5226, pp. 966–967, 1995. [Online]. Available: http://dx.doi.org/10.1126/science.269.5226.966

[116] E. Bengu and L. D. Marks, "Single-walled BN nanostructures," *Phys. Rev. Lett.*, vol. 86, no. 11, p. 2385, 2001. [Online]. Available: http://link.aps.org/abstract/PRL/v86/p2385

[117] A. Nagashima, N. Tejima, Y. Gamou, T. Kawai, and C. Oshima, "Electronic states of monolayer hexagonal boron nitride formed on the metal surfaces," *Surf. Sci.*, vol. 357-358, p. 307, 1996. [Online]. Available: http://dx.doi.org/10.1016/0039-6028(96)00134-3

[118] A. Nagashima, N. Tejima, Y. Gamou, T. Kawai, and C. Oshima, "Electronic dispersion relations of monolayer hexagonal boron nitride formed on the Ni(111) surface," *Phys. Rev. B*, vol. 51, no. 7, p. 4606, 1995. [Online]. Available: http://link.aps.org/abstract/PRB/v51/p4606

[119] W. Auwärter, T. J. Kreutz, T. Greber, and J. Osterwalder, "XPD and STM investigation of hexagonal boron nitride on Ni(111)," *Surf. Sci.*, vol. 429, p. 229, 1999. [Online]. Available: http://dx.doi.org/10.1016/S0039-6028(99)00381-7

[120] S. Berner, M. Corso, R. Widmer, O. Groening, R. Laskowski, P. Blaha, K. Schwarz, A. Goriachko, H. Over, S. Gsell, M. Schreck, H. Sachdev, T. Greber, and J. Osterwalder, "Boron nitride nanomesh: Functionality from a corrugated monolayer," *Angew. Chem. Int. Ed.*, vol. 46, no. 27, pp. 5115–5119, 2007. [Online]. Available: http://dx.doi.org/10.1002/anie.200700234

[121] R. Laskowski, P. Blaha, T. Gallauner, and K. Schwarz, "Single-layer model of the hexagonal boron nitride nanomesh on the Rh(111) surface," *Phys. Rev. Lett.*, vol. 98, no. 10, pp. 106 802–4, 2007. [Online]. Available: http://link.aps.org/abstract/PRL/v98/e106802

[122] O. Bunk, M. Corso, D. Martoccia, R. Herger, P. R. Willmott, B. D. Patterson, J. Osterwalder, J. F. van der Veen, and T. Greber, "Surface X-ray diffraction study of boron-nitride nanomesh in air," *Surf. Sci.*, vol. 601, no. 2, pp. L7–L10, 2007. [Online]. Available: http://dx.doi.org/10.1016/j.susc.2006.11.018

[123] A. Goriachko, Y. B. He, M. Knapp, H. Over, M. Corso, T. Brugger, S. Berner, J. Osterwalder, and T. Greber, "Self-assembly of a hexagonal boron nitride nanomesh on Ru(0001)," *Langmuir*, vol. 23, no. 6, pp. 2928–2931, 2007. [Online]. Available: http://dx.doi.org/10.1021/la062990t

[124] M. Morscher, M. Corso, T. Greber, and J. Osterwalder, "Formation of single layer h-BN on Pd(1 1 1)," *Surf. Sci.*, vol. 600, no. 16, pp. 3280–3284, 2006. [Online]. Available: http://dx.doi.org/10.1016/j.susc.2006.06.016

[125] T. Brugger, Ph.D. dissertation, University of Zürich, to be published.

[126] A. Lehnert, Ph.D. dissertation, Ecole Polytechnique Fédérale de Lausanne, to be published.

[127] S. Gwo, C.-P. Chou, C.-L. Wu, Y.-J. Ye, S.-J. Tsai, W.-C. Lin, and M.-T. Lin, "Self-limiting size distribution of supported cobalt nanoclusters at room temperature," *Phys. Rev. Lett.*, vol. 90, no. 18, p. 185506, 2003. [Online]. Available: http://link.aps.org/abstract/PRL/v90/e185506

[128] P. A. Mulheran and J. A. Blackman, "The origins of island size scaling in heterogeneous film growth," *Phil. Mag. Lett.*, vol. 72, p. 55, 1995. [Online]. Available: http://dx.doi.org/10.1080/09500839508241614

[129] D. Weaire and N. Rivier, "Soap, cells and statistics - random patterns in two dimensions," *Contemporary Physics*, vol. 25, no. 1, pp. 59 – 99, 1984. [Online]. Available: http://dx.doi.org/10.1080/00107518408210979

[130] M. C. Bartelt, C. R. Stoldt, C. J. Jenks, P. A. Thiel, and J. W. Evans, "Adatom capture by arrays of two-dimensional Ag islands on Ag(100)," *Phys. Rev. B*, vol. 59, no. 4, p. 3125, 1999. [Online]. Available: http://link.aps.org/abstract/PRB/v59/p3125

[131] G. Boisvert, L. J. Lewis, and A. Yelon, "Many body nature of the Meyer-Neldel compensation law for diffusion," *Phys. Rev. Lett.*, vol. 75, p. 469, 1995. [Online]. Available: http://dx.doi.org/10.1103/PhysRevLett.75.469

[132] L. T. Kong and L. J. Lewis, "Transition state theory of the preexponential factors for self-diffusion on Cu, Ag, and Ni surfaces," *Phys. Rev. B*, vol. 74, no. 7, pp. 073 412–4, 2006. [Online]. Available: http://link.aps.org/abstract/PRB/v74/e073412

[133] N. Knorr, H. Brune, M. Epple, A. Hirstein, A. M. Schneider, and K. Kern, "Long-range adsorbate interactions mediated by a two-dimensional electrons gas," *Phys. Rev. B*, vol. 65, p. 115420, 2002. [Online]. Available: http://dx.doi.org/10.1103/PhysRevB.65.115420

[134] P. Kisliuk, "The sticking probabilities of gases chemisorbed on the surfaces of solids," *Journal of Physics and Chemistry of Solids*, vol. 3, no. 1-2, pp. 95–101, 1957. [Online]. Available: http://dx.doi.org/10.1016/0022-3697(57)90054-9

[135] J. A. Venables, G. D. T. Spiller, and M. Hanbücken, "Nucleation and growth of thin films," *Rep. Prog. Phys.*, vol. 47, p. 399, 1984. [Online]. Available: http://dx.doi.org/10.1088/0034-4885/47/4/002

[136] T. Wiederholt, H. Brune, J. Wintterlin, R. J. Behm, and G. Ertl, "Formation of two-dimensional sulfide phases on Al(111): an STM study," *Surf. Sci.*, vol. 324, p. 91, 1995. [Online]. Available: http://dx.doi.org/10.1016/0039-6028(94)00732-2

[137] J. A. Nieminen, E. Niemi, and K.-H. Rieder, "Interference between competing tunneling channels and chemical resolution of STM," *Surf. Sci.*, vol. 552, no. 1-3, pp. L47–L52, 2004. [Online]. Available: http://dx.doi.org/10.1016/j.susc.2004.01.043

[138] H. Hashimoto and R. Uyeda, "Detection of dislocation by the Moiré pattern in electron micrographs," *Acta Crystallographica*, vol. 10, p. 143, 1957. [Online]. Available: http://dx.doi.org/10.1107/S0365110X57000456

[139] S. Rusponi, N. Weiss, T. Cren, M. Epple, and H. Brune, "High tunnel magnetoresistance in spin-polarized scanning tunneling microscopy of Co nanoparticles on Pt(111)," *Appl. Phys. Lett.*, vol. 87, p. 162514, 2005. [Online]. Available: http://dx.doi.org/10.1063/1.2077856

[140] The Java programming language software development kit. [Online]. Available: http://java.sun.com

[141] W. K. Pratt, *Digital Image Processing*. New York: Wiley & Sons, 1978.

[142] J. F. Canny, "A computational approach to edge detection," *IEEE Trans. Patt. Anal. Mach. Intell.*, vol. 8, pp. 679–714, 1986.

[143] K. Levenberg, "A method for the solution of certain non-linear problems in least squares." *Quart. Appl. Math.*, vol. 2, p. 164, 1944.

[144] D. W. Marquardt, "An algorithm for least-squares estimation of nonlinear parameters," *SIAM J. Appl. Math.*, vol. 11, no. 2, pp. 431–441, 1963. [Online]. Available: http://link.aip.org/link/?SMM/11/431/1

[145] J. Holopainen. (2007) A Levenberg-Marquardt fit package for the Java language. [Online]. Available: http://users.utu.fi/jaolho/

[146] B. Miller, J. Hicklin, C. Moler, P. Webb, R. F. Boisvert, R. Pozo, and K. Remington. (2005) JAMA: A Java matrix package. [Online]. Available: http://math.nist.gov/javanumerics/jama/

[147] Persistence of Vision Team and C. Cason, "Pov-ray: Persistence of vision ray tracer," 2005. [Online]. Available: http://www.povray.org/

Remerciements

J'aimerais en premier lieu remercier le Prof. Harald Brune de m'avoir accueilli dans son groupe de recherche, de m'avoir offert la possibilité d'effectuer ce travail de thèse et de m'avoir fait confiance pendant les nombreuses années durant lesquelles nous avons collaboré.

Je remercie aussi les membres du jury de thèse Prof. G. Meylan, Prof. T. Michely, Prof. J. Osterwalder et Prof. A. Pasquarello d'avoir accepté la tâche de juger ce travail.

Un merci tout particulier au Dr Stefano Rusponi pour son aide incessante au laboratoire, ceci sans jamais perdre le sourire, pour sa compétence, sa patience et aussi particulièrement pour l'immense travail de relecture de ce manuscrit. Le travail avec lui a toujours été agréable et enrichissant.

Plusieurs autres personnes ont directement participé à l'obtention des résultats présentés dans cette thèse, je remercie plus particulièrement pour leur aide : Mehdi El Ouali, Laurent Claude, Johannes Giesecke, Romain Dequesne, Thomas Brugger et Anne Lehnert.

Je remercie aussi tous les collègues doctorants et post-docs de l'institut pour les discussions de physique ainsi que pour les agréables pauses passées ensembles. Au risque d'en oublier, je tente une liste: Max Epple, Uta Schlickum, Manuela Kobas, Régis Decker, Régis Stephan, Raphaël Vallotton, Safia Ouazi, Géraud Moulas, Markus Etzkorn, Nicolas Weiss, Stéphane Pons, Pierre Convers, Pietro Gambardella et Stephan Fedrigo.

Évidemment ce travail n'aurait pas été possible sans le concours de l'équipe technique et administrative de l'institut, toujours efficace et serviable: Gilles Grandjean, Pascal Cattin, Philippe Zürcher, Philippe Guex, Michel Fazan, Claude Amendola, José Grandjean, Philippe Cordey, Martial Doy, Claire-Lise Bandelier, Chantal Roulin, Florence Choulat, André Schläfli.

Merci aussi à tous mes amis de m'avoir accompagné pendant ces années.
Un merci tout particulier à Brigitte pour nos longues discussions sur les méandres de la vie.

Un merci du fond du cœur à mon père et à ma mère
pour leur soutien inconditionnel qui m'a permis de devenir qui je suis.

Et puis un merci plein de tendresse à Marie pour son amour et tout le reste.

Curriculum vitæ

Philipp M. Buluschek
Born on 27.12.1975 in Zürich, Switzerland
German nationality

Education:

2003–2007	Ph.D. studies / Research and teaching assistant Ecole Polytechnique Fédérale de Lausanne (EPFL), Switzerland
2001–2003	Research associate, EPFL
1994–2001	Studies in physics (M.Sc.), EPFL
1981–1994	School and gymnasium, Lausanne, Switzerland

Languages (fluent): French, German, English

Publications:

P. Buluschek, S. Rusponi, E. Vargoz, M. El Ouali and H. Brune. "Heteroepitaxial nucleation on a surface unstable towards reconstruction: Co/Pt(111)". *In preparation for Physical Review Letters*, (2007)

S. Rusponi, T. Cren, N. Weiss, M. Epple, P. Buluschek, L. Claude and H. Brune. "The remarkable difference between surface and perimeter atoms in the magnetic anisotropy of 2D nanostructures". *Nature Materials, 2, pp.564 (2003)*

P. Buluschek, D. Grützmacher, A. Dommann and H. Brune. "A Hot Electron Emission Array". *in Top Nano 21 Report 2003, Commission for Technology and Innovation (CTI), Bern, (2003)*

V. Desarnaulds, P. Buluschek. "Détermination des temps de réverbération souhaitables dans les églises par corrélation entre appréciations subjectives et mesures objectives". *in Proceedings of Congrès Français d'Acoustique*, (2000)